Surveying Star Formation in the Galaxy

by

Adam G. Ginsburg

B.S., Rice University, 2007

M.S., University of Colorado, Boulder, 2009

A thesis submitted to the

Faculty of the Graduate School of the

University of Colorado in partial fulfillment

of the requirements for the degree of

Doctor of Philosophy

Department of Astrophysical and Planetary Sciences

2013

This thesis entitled:
Surveying Star Formation in the Galaxy
written by Adam G. Ginsburg
has been approved for the Department of Astrophysical and Planetary Sciences

John Bally

Prof. Jeremy Darling

Prof. Jason Glenn

Prof. Neal Evans

Prof. Michael Shull

Date

The final copy of this thesis has been examined by the signatories, and we find that both the content and the form meet acceptable presentation standards of scholarly work in the above mentioned discipline.

Ginsburg, Adam G. (Ph.D., Astrophysics)

Surveying Star Formation in the Galaxy

Thesis directed by Prof. John Bally

I studied the formation of massive stars and clusters via millimeter, radio, and infrared observations. The Bolocam Galactic Plane Survey (BGPS) was the first millimeter-wave blind survey of the plane of our Galaxy. I wrote the data reduction pipeline for this survey and produced the final publicly released data products. I ran extensive tests of the pipeline, using simulations to probe its performance.

The BGPS detected over 8000 1.1 mm sources, the largest sample at this wavelength ever detected. As a single-wavelength continuum survey, the BGPS serves as a finder chart for millimeter and radio observations. I therefore performed follow-up surveys of BGPS sources in CO 3-2 and H_2CO, and others did similar follow-ups to measure velocities and distances towards these sources.

H_2CO observations of ultracompact HII regions and other millimeter-bright sources were used to measure the local molecular gas density. These measurements hint that density within molecular clouds does not follow a simple lognormal distribution. They also show that star-forming clouds all contain gas at density $\gtrsim 10^4$ cm^{-3}.

I used the BGPS source catalog to identify the most massive compact clumps within the galaxy, identifying 18 with masses $M > 10^4$ $M_\odot$ in the first quadrant of the Galactic plane. As these objects are all actively star-forming, the starless timescale of massive proto-cluster clumps must be relatively short, with lifetimes $\lesssim 0.6$ Myr.

Dedication

To stars and gas, for holding still for a picture.

Acknowledgements

To the people who have helped: family, friends, and colleagues.

Specific help on these projects came from Jim Braatz, Glen Langston, Phil Perrilat, Esteban Araya, Devin Silvia, and Jeff Mangum. Software was developed in collaboration with Jordan Mirocha and Thomas Robitaille. Co-authors who contribute to the works in this paper include: James Aguirre, Jeremy Darling, John Bally, Cara Battersby, Eli Bressert, Erik Rosolowsky, Miranda Dunham, Manuel Merello, Timothy Ellsworth-Bowers, Jason Glenn, Neal Evans, Guy Stringfellow, Jonathan Williams, Wayne Schlingman, Yancy Shirley, Paul Harvey

Contents

Chapter

Tables

Table

Figures

Figure

Chapter 1

Introduction

1.1 Preface

This thesis describes the research I have performed with a wide variety of collaborators, mostly centered on the Bolocam Galactic Plane Survey team led by John Bally and Jason Glenn. The BGPS data reduction process, at the core of this work, was done in collaboration with James Aguirre and Erik Rosolowsky.

However, the work proceeded somewhat haphazardly: I came into the BGPS team as a (perhaps foolish) student enthusiastic about data reduction. I never planned to take over the BGPS data, but it happened a few years into my time at CU. This thesis is therefore somewhat scattered: some of the observations reported here were taken as 'follow-up' to the BGPS before it was completed.

This document primarily consists of a number of published papers centered around a common theme of radio and millimeter observations of the Galaxy, with the common driving question being 'How do stars form?' I have therefore added thesis-specific introductions to each section to describe where they fit in to the bigger picture of this document. I've also included sections describing work that is not yet published but (hopefully) soon will be.

1.2 Star Formation in the Galaxy

It has been known for at least half a century that stars form from the gravitational collapse of clouds of cool material. The gas that will eventually form stars is typically observed as dark features

obscuring background stars. The brighter nebulae, which have been studied for far longer (Messier, 1764), contain hot and diffuse gas. These nebulae, while spectacular, are not the construction materials of new stars. However, they mark the locations where new stars have formed - nebulae are often stellar nurseries.

To track down the cool star-forming material, it is necessary to observe at longer wavelengths. Infrared observations can pierce through obscuring material, as dust becomes more transparent at longer wavelengths. With near- and mid-infrared observations, such as those enabled by HgCdTe detectors like those in the NICFPS and TripleSpec instruments at Apache Point Observatory and the InSb detectors used on the Spitzer Space Telescope, it is possible to observe obscured young stars. These objects have just ignited fusion in their cores and represent the youngest generation of new stars.

But this material has already formed stars. To see the truly cold material, that which still has potential to form new stars, we need to examine gas that is not heated at all by stars. Assuming we want to look for gas that can form a star like our sun and that the density of the gas to form is $\sim 10^4$ H_2 particles per cubic centimeter (an assumption left unjustified for now), the Jeans scale requires a temperature $T \sim 10$ K, which means we need to look at wavelengths $\lambda \gtrsim 100\mu$m in order to observe this gas.

Gas at these densities turns out to be quite rare. While there are thousands of stars within 100 pc of the sun, the closest known star-forming globules are at distances greater than 100 pc. While this sparsity is explained in part by our current position in the Galaxy (we're buzzing along its outskirts at 250 km s^{-1}), it reflects the reality that star formation in the present epoch is dispersed and rare.

Even more rare are the massive stars that end their lives in supernovae. While there are hundreds of stellar nurseries within a few hundred parsecs, the nearest region of massive star formation is the Orion Molecular Cloud at a distance of 400 pc. Out to 1000 pc, though, there are still only a handful of massive star forming regions, including Monoceros R2 and Cepheus A.

These massive stars in many ways are the most important to study in order to understand

the evolution of gas and dust in the universe and our own origins. In their deaths, they produce the heavy elements required to form dust, planets, and life. Throughout their lives and deaths, massive stars dump energy into the interstellar medium and effectively control the motions and future of the gas around them.

The bigger the star, the shorter it lives, so massive stars are nearly as rare as their birth regions. They also tend to be found nearby or within these birth regions. Since they can be found near large globs of dust, finding these globs can help us discover new groups of massive stars.

This thesis summarizes surveys within our Galaxy to discover and examine regions forming new massive stars and clusters. The largest body of work described here is the Bolocam Galactic Plane Survey, the first dust continuum survey of a significant fraction of the Galactic Plane.

With that broad overview in place, the next sections describe a few of the specific problems addressed in this thesis in greater detail.

1.2.1 Gas Flow and Collapse

Stars form as the end state of the collapse of gas cores. The classic analysis used to determine when stars will form from a gas cloud is the Jeans analysis, which determines under what conditions an overdensity in a uniform isothermal medium becomes unstable to gravitational collapse. Jeans analysis defines a length scale

$$L_J = \left(\frac{\pi c_s^2}{G\rho_0}\right)^{1/2}$$

and a mass scale

$$M_J = \left(\frac{2\pi kT}{G\mu}\right)^{3/2} \rho_0^{-1/2} = \left(\frac{\pi}{G\mu}\right)^{3/2} c_s^3 \rho_0^{-1/2}$$

which defines the typical mass at which a core should form. In this equation, c_s is the sound speed in the gas, ρ_0 is the density of the medium, T is the gas temperature, μ is the mean mass per particle in proton masses, and G is the gravitational constant. More careful analyses including other factors, e.g. external pressure on the core, yield similar values.

The Jeans instability growth time scale τ_J is within a factor of a few of the free-fall collapse

time τ_{ff},

$$\tau_J = \left(\frac{1}{4\pi G\rho_0}\right)^{1/2}$$

$$\tau_{ff} = \left(\frac{3\pi}{32G\rho_0}\right)^{1/2} = \pi\sqrt{\frac{3}{8}}\tau_J$$

implying a typical mass infall rate for an isothermal core of

$$\dot{M}_J = M_J/\tau_J = \frac{1}{2}\pi^2\frac{c_s^3}{G}$$

$$\dot{M}_{ff} = \pi\sqrt{\frac{3}{32}}\frac{c_s^3}{G}$$

Under free-fall collapse at 10 K, then, a 1 $M_\odot$ star takes only $\sim 10^4$ years to form, but a 100 $M_\odot$ star takes ~ 1 Myr.

Real stars do not form so quickly, but initial accretion rates may be as high as $10^{-4}M_\odot \mathrm{yr}^{-1}$ in cores, and the accretion must be at least that fast for massive stars to form in times shorter than the lifetimes of their parent clouds.

Low-mass stars go through subsequent phases of collapse, from the initial unstable core to a hydrostatic core in which collapse no longer proceeds isothermally because the dust becomes optically thick to its own radiation. Eventually a protostar forms, surrounded by a disk and a core. The core continues to accrete onto the star through the disk until all the material is either accreted or blown away in outflows. The disk both accretes on to the star and forms planets.

This process is well-understood for low-mass stars in the broad strokes outlined here, and each phase in this process has been observationally confirmed. For massive stars, the picture is far less clear. It is still actively debated whether active stars ever have a "core" analogous to low-mass pre-stellar cores, since a 100 $M_\odot$ gas cloud unstable to collapse would also be unstable at smaller scales and would therefore be likely to fragment into many lower-mass cores.

The two main competing theoretical extremes to get around this problem are known as the "turbulent core" (McKee & Tan, 2003; Krumholz et al., 2005, 2009; Tan et al., 2006; McKee & Ostriker, 2007a) and "competitive accretion" (Klessen et al., 2000; Bonnell & Bate, 2002; Bonnell et al., 2004; Bonnell & Bate, 2006; Bonnell, 2008) models. In the former, an additional support

mechanism, turbulence, prevents fragmentation in massive cores, allowing a single core with $M_{core} > M_J(thermal)$ to form into a single stellar system. By contrast, the competitive accretion model, in its most extreme form, asserts that all stars start their lives as $\sim M_J$ cores which exist within a collapsing cloud. They are then able to accrete additional material from the cloud and grow from their minimum mass to populate the initial mass function (see Section 1.2.3).

Neither theory is presently able to account for feedback from the formed stars. Massive stars drastically affect their environment when they turn on, which can be long before they are done accreting. Massive stars probably go through phases similar to low-mass stars, but they may look quite different. They are likely to ignite fusion while still accreting within a dense core; feedback will begin while most of the matter that will eventually reach the star is still in the 'core' phase.

If this happens, the massive star will begin to illuminate a hypercompact H II region, in which the extremely high surrounding densities trap the ionizing radiation. Over time, the star's luminosity will grow and the surrounding density decrease, either by accreting or being ejected, and the H II region will expand, going through an ultracompact (UC) H II phase, then a diffuse H II region, then ending its observable phase as it blends into the low-density warm interstellar medium.

Understanding these early phases is important for understanding what sets a star's final mass. In a core accretion model, $\sim 2/3$ of the gas in the original 'core' may accrete, and the other $\sim 1/3$ blow out, but the mass of the star should be very near the core mass. In the competitive accretion model, the core mass may have little influence on the final star mass, as most of the stellar mass will be Bondi-Hoyle accreted from the surrounding medium.

In order for Bondi-Hoyle (BH) accretion to be effective, though, the surrounding 'clump' medium must have a very high density. The BH accretion rate is strongly dependent on the mass of the accreting star and the sound speed of the gas:

$$\dot{M}_{BH} = \frac{4\pi\rho G^2 M^2}{c_s^3}$$

For a low-mass star in a low-density medium and a high-mass star in a high-density medium, the

values are

$$\dot{M}_{BH} = 1.6 \times 10^{-7} \left(\frac{M}{M_\odot}\right)^2 \left(\frac{n}{10^4 \mathrm{cm}^{-3}}\right) \left(\frac{c_s}{1 \mathrm{kms}^{-1}}\right)^{-3} M_\odot \mathrm{yr}^{-1}$$

$$\dot{M}_{BH} = 1.6 \times 10^{-4} \left(\frac{M}{10M_\odot}\right)^2 \left(\frac{n}{10^5 \mathrm{cm}^{-3}}\right) \left(\frac{c_s}{1 \mathrm{kms}^{-1}}\right)^{-3} M_\odot \mathrm{yr}^{-1}$$

The timescale for a $10M_\odot$ star to double its mass in a $n \sim 10^5 \mathrm{cm}^{-3}$ medium is $\sim$ 50 kyr, but drops to only 5 kyr for density $n \sim 10^6 \mathrm{cm}^{-3}$. It is therefore crucial that we measure the density of the bulk of the gas around massive stars - the mass and density of the surrounding medium are essential parameters for determining whether competitive accretion is a viable model for growing massive stars.

Throughout the thesis, I examine the local gas density on parsec scales via line ratios and simpler column-density based estimates. I also examine tracers of infall and outflow to determine accretion properties of forming stars.

1.2.2 Turbulence

Turbulence is one of the defining features of the interstellar medium. Turbulence is thought to govern many properties of the ISM, rendering it scale-free and defining the distribution of velocities, densities, temperatures, and magnetic fields in the gas between stars.

Turbulence forms in fluids when the inertial force greatly exceeds the viscosity. It creates instabilities in the fluid that start on large scales and "cascade" energy to smaller scales. Once a small enough size-scale is reached, the viscosity exceeds the interial force and the energy heats the fluid on local scales.

Turbulence is most easily modeled by a Kolmogorov spectrum, in which $\Delta v \propto \ell^{1/3}$, i.e. the typical velocity dispersion is greatest at the largest size scales. Kolmogorov turbulence strictly only describes incompressible fluids without magnetic fields, while the ISM is compressible and threaded by magnetic fields. Nonetheless, Kolmogorov turbulence is nearly consistent with some observed properties of the ISM. The Larson size-linewidth relation ($\sigma_{\mathrm{km\ s}^{-1}} \approx 1.1 L_{pc}^{0.38}$), in particular, is similar to that predicted by Kolmogorov turbulence.

Turbulence is often quoted as a source of **pressure** based on the Kolmogorov description. At size scales much smaller than the driving scale of the turbulence (the "box size" in a simulation), turbulence becomes isotropic and can add support against gravitational collapse.

However, turbulence decays rapidly. The turbulent decay timescale $\tau_{decay} \propto \ell/v$, where ℓ is the turbulent length scale and v is the velocity scale. It therefore increases with size scale as $\tau_{decay} \propto \ell^{2/3}$. Turbulence decays most quickly on the smallest sizescales.

We are therefore left with two conditions: Turbulence must be driven at large scales for turbulence to provide support against gravity[1] , and it must be constantly driven to resupply the turbulence that is transferred to heat on the smallest scales.

Once stars form, however, large-scale driving of turbulence may not be the dominant shaping mechanism for the gas. Outflows from low-mass stars, soft UV from B stars, and ionizing UV and strong winds from OB stars can drive gas motions, disrupting gas or replenishing turbulent energy. Once stars have formed in a cloud, local feedback rather than the turbulent cascade is likely to govern the future evolution of the cloud.

Because the ISM is compressible, interacting flows within the turbulent medium will result in density enhancements and voids. Many simulation studies have determined that the resulting density distribution, and correspondingly the column-density distribution, should be log-normal. Observational studies agree that in regions not yet significantly affected by gravity, the column-density distribution is log-normal. In regions where stars are actively forming, i.e. regions in which gas self-gravity has affected a significant fraction of the gas, a high-density power-law tail forms.

One theory of star formation holds that the initial mass function of stars is determined entirely by turbulence (Padoan & Nordlund, 2002; Padoan et al., 2007a; Krumholz & McKee, 2005). In this description, the highest overdensities in the turbulent medium become gravitationally unstable and separate from the turbulent flow as they collapse into proto-stellar cores. This idea has been a hot topic in the past few years, but it may be an overly simplistic view.

[1] Once stars form in a cloud and stellar feedback becomes significant, turbulence can be driven at all scales, but the turbulent support needed to slow or prevent the initial collapse of starless cores cannot be driven by local stars.

Turbulence is appealing to theorists as it is a difficult problem to address directly with observations, but it may have great predictive power. If turbulence is the dominant governing process of the ISM, then it is possible to derive a reasonably robust star-formation theory based on the excursion set theory successfully applied to cosmological structure formation (Hopkins, 2012b; Hennebelle & Chabrier, 2011; Hopkins, 2012a).

However, in reality, turbulence is just one of many processes governing the ISM and star formation. Stellar feedback, in the form of radiation, winds, supernovae, and outflows imposes a preferred driving scale on any individual region, and in many cases these processes will happen faster than turbulent processes. The notion of **initial conditions** for star formation, while theoretically appealing, may prove too strong an oversimplification when searching for a complete theory of star formation.

Throughout this thesis, I consider and measure the drivers, effects and properties of turbulence on a few different scales.

In the W5 and IRAS 05358 regions (Chapter 2 and Ginsburg et al. (2009)), I examined outflows as potential drivers of turbulence. In IRAS 05358, I concluded that the outflows could provide the observed turbulence in the ∼pc-scale 'clump', but that the central core had energy dissipation much faster than turbulence could be resupplied. In W5, I rule out protostellar outflows as a significant driver of turbulence.

In Chapter 5, I examine the density probability distribution function (PDF) in giant molecular clouds (GMCs). Because H_2CO is uniquely capable of measuring local volume density, I was able to place interesting constraints on the density PDFs in non-star-forming GMCs, namely that they are unlikely to be the simple log-normal distributions expected from isothermal incompressible turbulence.

1.2.3 Mass Functions

Perhaps the most fundamental goal of star formation studies is to determine the Initial Mass Function (IMF) of stars and what, if anything, causes it to vary. It is also one of the most

challenging statistically and observationally.

The IMF defines the probability distribution function of stellar masses at birth, and therefore differs greatly from the present-day stellar mass function that is very strongly affected by stellar death at the highest masses. In order to determine the mass function for the most massive stars, it is necessary to look at their birth places. These birth places are dusty, dense, and rare.

It remains somewhat unclear whether the IMF is a universal function or is sampled independently for individual clusters. If it is universal, there is a possibility of forming massive stars anywhere stars form. If cluster-dependent, then a massive star must form with a surrounding cluster.

Some groups now claim that the initial mass function is decided in the gas phase by the formation of cores. The Core Mass Function (CMF) measures the probability distribution function of core masses, where cores are generally identified observationally as column-density peaks in millimeter/submillimeter emission maps. The CMF has a similar functional form to the IMF, but its mean is higher by a factor ~ 3 in local star forming regions, leading to the claim that star formation proceeds from CMF $\rightarrow$ IMF with 30% efficiency. This idea has recently been explored theoretically by Chabrier & Hennebelle (2010) and Hopkins (2012b) and observationally by the Herschel Gould's Belt team (Arzoumanian et al., 2011; André et al., 2010).

Gas clouds follow a mass function that extends up to the largest possible coherent scales, giant molecular clouds with scales $\sim 50 - 100$ pc that are limited by the scale-height of the ISM in Galactic disks. Between 'cores' and GMCs, intermediate scale blobs are often called 'clumps'. The mass function of these clumps has yet to be determined.

The mass function of GMCs was determine from CO emission towards the Galactic plane and in nearby galaxies (e.g., M33) where they can be resolved. The CMF was measured in nearby ($D < 500$ pc) clouds where $30''$ beams easily resolve ~ 0.1 pc cores. However, clumps are only found in large numbers in the Galactic plane, where distances are uncertain. They cannot be resolved in other galaxies (or at least, could not prior to ALMA).

To understand star formation on a galactic scale, it is necessary to understand the transition

from large-scale giant molecular clouds and proto-stellar cores. Clouds follow a shallow mass function, with the largest clouds containing most of the gas. Cores and stars are both drawn from steep mass functions in which most of the mass is near some peak in the distribution. Presumably there must be some intermediate state of the gas that is drawn from an intermediate distribution, shallower than 'cores' but steeper than 'clouds'.

The BGPS (Chapter 3) presents the first real opportunity to explore the mass function of clumps on scales intermediate between cores and giant clouds. While I do not explicitly examine core or clump mass functions in this thesis, their measurement is an important motivation for the large-area surveys we have performed.

1.2.3.1 Star Clusters

Star clusters are also drawn from a mass function comparable to stars, but their distribution is better measured than for stars. Clusters are easily visible - and resolvable - in other galaxies, and massive clusters are less likely to be embedded than massive stars, since a bound cluster will outlive its few most massive stars. In normal galaxies, cluster populations are consistent with a Schechter distribution: a power-law $\alpha \sim 2$ with an exponential cutoff at large masses.

$$N(M)dM = C \left(\frac{M}{M_*}\right)^{-2} e^{-(M/M_*)} dM$$

Since clusters are not drawn from the same parent distribution as GMCs (which have $\alpha \sim 1$, so $N(M)dM \sim CM^{-1}dM$), it is plausible that their precursors are, instead, the intermediate-scale 'clumps' observed in the millimeter continuum. However, the clump mass function has yet to be measured, so even this first step of determining plausibility is incomplete.

Clusters are an important observational tool in astrophysics. For stellar studies, they have been used to select populations of co-eval stars. In extragalactic studies, they are frequently the smallest observable individual units. However, many recent works have pointed out that clusters may be short-lived, transient phenomena (Kruijssen et al., 2011a; Whitehead et al., 2013; Gieles et al., 2011; Whitmore, 2009). Any study of their populations must take in to account their

dissolution. The most massive clusters, however, are both the most easily observed and the longest lived, and therefore provide some of the most useful tools for understanding stars.

As with massive stars, massive clusters are rare. Only a handful of young massive clusters (YMCs) are known within our Galaxy, the most prominent being NGC 3603, the Arches cluster, and Westerlund 1 (Portegies Zwart et al., 2010). These are the only locations in the galaxy known to be forming multiple stars near the (possible) upper stellar mass limit. Despite their importance, the population of such clusters is effectively unconstrained. The incomplete knowledge of clusters is due to extinction and confusion within the Galactic plane at wavelengths where the stars are directly observable.

In Chapter 4, I search the BGPS for candidate proto-massive star clusters. Because the Galactic disk is optically thin at 1.1 mm, a complete census of proto-clusters is possible. I use the detected candidates to infer features about the population of Galactic YMCs, including their formation timescales and rates.

1.3 Outline

This thesis includes 6 chapters. Chapter 2 describes observations of the W5 star-forming region to identify outflows; this chapter is somewhat tangential to the rest. Chapter 3 describes the BGPS data reduction process and data pipeline. Chapter 4 is a Letter identifying massive proto-clusters in the BGPS. Chapter 5 is the pilot study of H_2CO towards previously-known UCHII regions. It includes the methodology and analysis of turbulent properties of Galactic GMCs. Chapter 6 expands upon Chapter 5, detailing the expansion of the H_2CO survey to BGPS-selected sources. Chapter 7 summarizes software development for this thesis and beyond. Chapter 8 concludes.

Chapter 2

Using outflows to track star formation in the W5 HII region complex

2.1 Preface

Only a few months after arriving at CU, I was given the opportunity to visit the peak of Mauna Kea to perform observations with the JCMT. I spend about 3 weeks at the telescope over the course of two years primarily mapping the W5 complex. A side-project done during these observations resulted in my Comps II project on IRAS 05358+3543. These data were taken using Jonathan Williams' Hawaii time allocation with the HARP receiver. The data were taken with essentially no plan for how they would be used. The paper may have diminished our group's overall interest in the W5 region: it turns out that star formation is probably at its end here, being quenched by massive-star feedback. However, there is a largely ignored cloud to the northwest of the well-studied W5 bubbles that has significant potential to form new stars.

The W5 study was originally intended to include a Bolocam census of cores, but the data in this region turned out to be the most problematic and contained little signal. We acquired additional data in 2009, but never got around to performing a joint analysis of the CO and continuum data. In part, at least, this is because W5 is so faint in the millimeter continuum compared to many Galactic Plane sources.

2.2 Introduction

Galactic-scale shocks such as spiral density waves promote the formation of giant molecular clouds (GMCs) where massive stars, star clusters, and OB associations form. The massive stars in

such groups can either disrupt the surrounding medium or promote further star formation. While ionizing and soft UV radiation, stellar winds, and eventually supernova explosions destroy clouds in the immediate vicinity of massive stars, as the resulting bubbles age and decelerate, they can also trigger further star formation. In the "collect and collapse" scenario (e.g. Elmegreen & Lada, 1977), gas swept-up by expanding bubbles can collapse into new star-forming clouds. In the "radiation-driven implosion" model (Bertoldi & McKee, 1990; Klein et al., 1983), pre-existing clouds may be compressed by photo-ablation pressure or by the increased pressure as they are overrun by an expanding shell. In some circumstances, forming stars are simply exposed as low-density gas is removed by winds and radiation from massive stars. These processes may play significant roles in determining the efficiency of star formation in clustered environments (Elmegreen, 1998).

Feedback from low mass stars may also control the shape of the stellar initial mass function in clusters (Adams & Fatuzzo, 1996; Peters et al., 2010). Low mass young stars generate high velocity, collimated outflows that contribute to the turbulent support of a gas clump, preventing the clump from forming stars long enough that it is eventually blown away by massive star feedback. It is therefore important to understand the strength of low-mass protostellar feedback relative to other feedback mechanisms.

Outflows are a ubiquitous indicator of the presence of ongoing star formation (Reipurth & Bally, 2001). CO outflows are an indicator of ongoing embedded star formation at a younger stage than optical outflows because shielding from the interstellar radiation field is required for CO to survive. Although Herbig- Haro shocks and H_2 knots reveal the locations of the highest-velocity segments of these outflows, CO has typically been thought of as a "calorimeter" measuring the majority of the mass and momentum ejected from protostars or swept up by the ejecta (Bachiller, 1996).

The W5 star forming complex in the outer galaxy is a prime location to study massive star formation and triggering. The bright-rimmed clouds in W5 have been recognized as good candidates for ongoing triggering by a number of groups (Lefloch et al., 1997; Thompson et al., 2004; Karr & Martin, 2003). The clustering properties were analyzed by Koenig et al. (2008) using Spitzer

infrared data, and a number of significant clusters were discovered. The whole W5 complex may be a product of triggering, as it is located on one side of the W4 chimney thought to be created by multiple supernovae during the last ∼10 MYr (Oey et al., 2005, Figure 2.1).

Following Koenig et al. (2008), we adopt a distance to W5 of 2 kpc based on the water-maser parallax distance to the neighboring W3(OH) region (Hachisuka et al., 2006). As with W3, the W5 cloud is substantially ($\approx 1.5\times$) closer than its kinematic distance would suggest ($v_{LSR}(-40 \text{ km s}^{-1}) \approx 3$ kpc). Given this distance, Koenig et al. (2008) derived a total gas mass of $6.5\times10^4\ M_\odot$ from a 2 μm extinction map.

The W5 complex was mapped in the ^{12}CO 1-0 emission line by the Five College Radio Astronomy Observatory (FCRAO) using the SEQUOIA receiver array (Heyer et al., 1998). The same array was used to map W5 in the ^{13}CO 1-0 line (C. Brunt, private communication). Some early work searched for outflows in W5 (Bretherton et al., 2002), but the low-resolution CO 1-0 data only revealed a few, and only one was published. The higher resolution and sensitivity observations presented here reveal many additional outflows.

While W5 is thought to be associated with the W3/4/5 complex, there are other infrared sources in the same part of the sky that are not obviously associated with W5. Some of these have been noted to be in the outer arm (several kpc behind W5) by Digel et al. (1996) and Snell et al. (2002).

In section 2, we present the new and archival data used in our study. In section 3, we discuss the outflow detection process and compare outflow detectability in W5 to that in Perseus. In section 4, we discuss the physical properties of the outflows and their implications for star formation in the W5 complex. In section 5, we briefly describe the outer-arm outflows discovered.

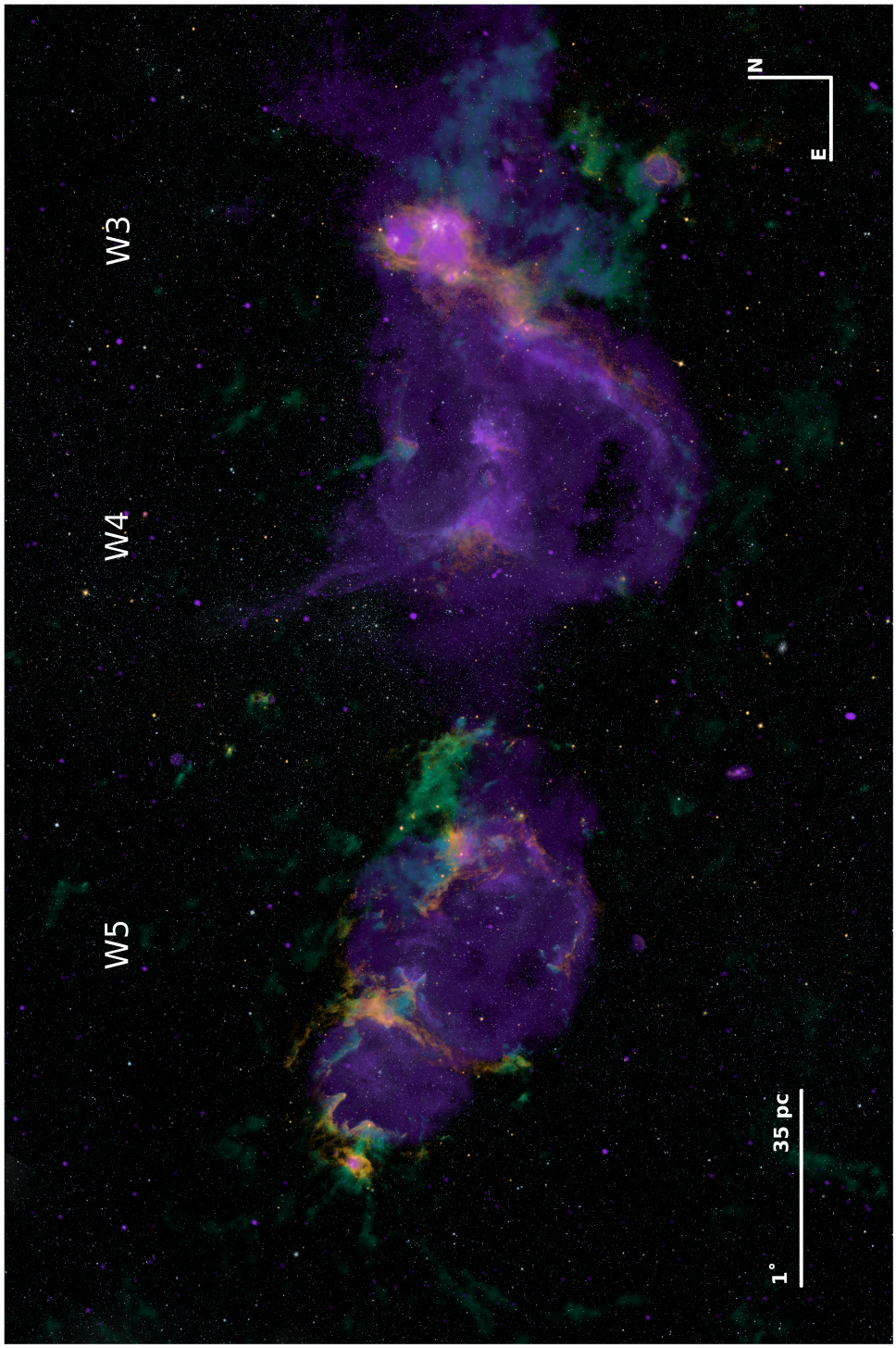

Figure 2.1 An overview of the W3/4/5 complex (also known as the "Heart and Soul Nebula") in false color. Orange shows 8 μm emission from the Spitzer and MSX satellites. Purple shows 21 cm continuum emission from the DRAO CGPS (Taylor et al., 2003); the DSS R image was used to set the display opacity of the 21 cm continuum as displayed (purely for aesthetic purposes). The green shows JCMT ^{12}CO 3-2 along with FCRAO ^{12}CO 1-0 to fill in gaps that were not observed with the JCMT. The image spans $\sim 7^{\circ}$ in galactic longitude. This overview image shows the hypothesized interaction between the W4 superbubble and the W3 and W5 star-forming regions (Oey et al., 2005).

2.3 OBSERVATIONS

2.3.1 JCMT HARP CO 3-2

CO J=3-2 345.79599 GHz data were acquired at the 15 m James Clerk Maxwell Telescope (JCMT) using the HARP array on a series of observing runs in 2008. On 2-4 January, 2008, $\sim$ 800 square arcminutes were mapped. During the run, τ_{225}, the zenith opacity at 225 GHz measured using the Caltech Submillimeter Observator tipping radiometer, ranged from 0.1 to 0.4 ($0.4 < \tau_{345GHz} < 1.6$[1]). Additional areas were mapped on 4-7 August, 16-20 and 31 October, and 1 and 12-15 Nov 2008 in similar conditions. A total of $\sim$ 3 square degrees (12000 arcmin^2) in the W5 complex were mapped (a velocity-integrated mosaic is shown in Figure 2.2).

HARP is a 16 pixel SIS receiver array acting as a front-end to the ACSIS digital auto-correlation spectrometer. In January 2008, 14 of the 16 detectors were functional. In the 2nd half of 2008, 12 of 16 were functional, necessitating longer scans to achieve similar S/N.

In January 2008, a single spectral window centered at 345.7959899 with bandwidth 1.0 GHz and channel width 488 kHz (0.42 km s^{-1}) was used. In August 2008 and later, we used 250 MHz bandwidth and 61 kHz (0.05 km s^{-1}) channel width. At this frequency, the beam FWHM is $14''$ (0.14 pc at a distance of 2 kpc) [2] .

A raster mapping strategy was used. In 2008, the array was shifted by 1/2 of an array spacing ($58.2''$) between scans. Data was sampled at a rate of $0.6s$ per integration. Two perpendicular scans were used for each field observed. Most fields were $10\times10'$ and took $\sim$ 45 minutes. When only 12 receptors were available, 1/4 array stepping ($29.1''$) was used with a sample rate of $0.4s$ per integration.

Data were reduced using the SMURF package within the STARLINK software distribution [3] . The SMURF command MAKECUBE was used to generate mosaics of contiguous sub-fields. The data were gridded on to cubes with $6''$ pixels and smoothed with a σ = 2-pixel gaussian, resulting

[1] http://docs.jach.hawaii.edu/JCMT/SCD/SN/002.2/node5.html
[2] http://docs.jach.hawaii.edu/JCMT/OVERVIEW/tel_overview/
[3] http://starlink.jach.hawaii.edu/

in a map FWHM resolution of 18″ (0.17 pc). A linear fit was subtracted from each spectrum over emission-free velocities (generally -60 to -50 and -20 to -10 km s^{-1}) to remove the baseline. The final map RMS was $\sigma_{T_A^*} \sim 0.06 - 0.11K$ in 0.42 km s^{-1} channels.

The sky reference position (off position) in January 2008 was J2000 2:31:04.069 +62:59:13.81. In later epochs, off positions closer to the target fields were selected from blank sky regions identified in January 2008 in order to increase observing efficiency. A main-beam efficiency $\eta_{mb} = 0.60$ was used as per the JCMT website to convert measurements to T_{mb}, though maps and spectra are presented in the original T_A^* units.

2.3.2 FCRAO Outer Galaxy Survey

The FCRAO Outer Galaxy Survey (OGS) observed the W5 complex in ^{12}CO (Heyer et al., 1998) and ^{13}CO 1-0 (C. Brunt, private communication). The ^{13}CO data cube achieved a mean sensitivity of 0.35 K per 0.13 km s^{-1} channel, or 0.6 K km s^{-1} integrated. The ^{13}CO cube was integrated over all velocities and resampled to match the BGPS map using the MONTAGE[4] package. The FWHM beam size was θ_B =50.″(0.48 pc). The integrated ^{12}CO data cube, with a sensitivity $\sigma = 1K$ km s^{-1}, is displayed with region name identifications in Figure 2.3.

2.3.3 Spitzer

Spitzer IRAC and MIPS 24 μm images from Koenig et al. (2008) were used for morphological comparison. The reduction and extraction techniques are detailed in their paper.

2.4 Analysis

2.4.1 Outflow Detections

Outflows were identified in the CO data cubes by manually searching through position-velocity space for line wings using STARLINK's GAIA display software. Outflow candidates were identified by high velocity wings inconsistent with the local cloud velocity distribution, which ranged

[4] http://montage.ipac.caltech.edu/

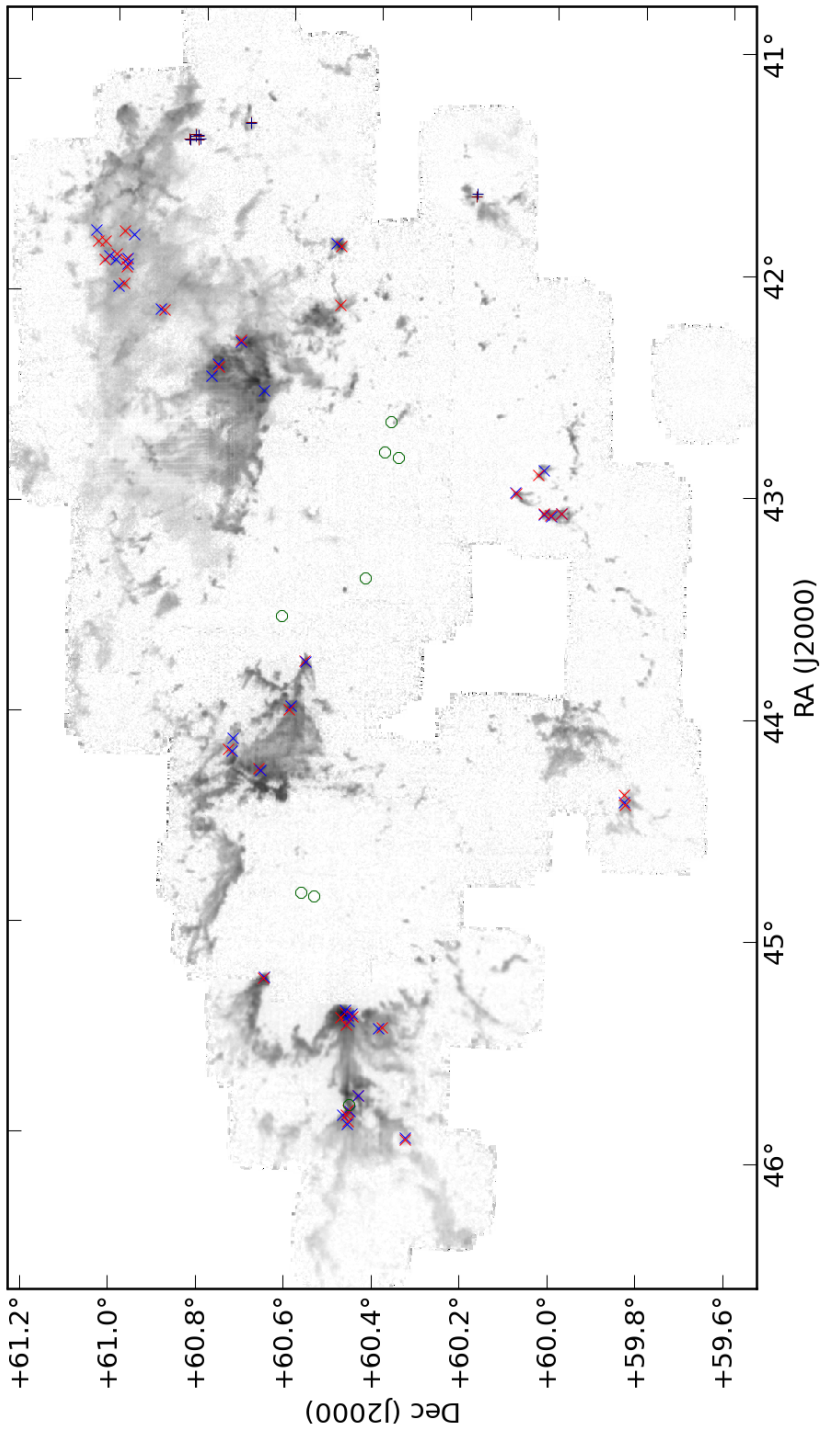

Figure 2.2 A mosaic of the CO 3-2 data cube integrated from -20 to -60 km s^{-1}. The grayscale is linear from 0 to 150 K km s^{-1}. The red and blue X's mark the locations of redshifted and blueshifted outflows. Dark red and dark blue plus symbols mark outflows at outer arm velocities. Green circles mark the location of all known B0 and earlier stars in the W5 region from SIMBAD.

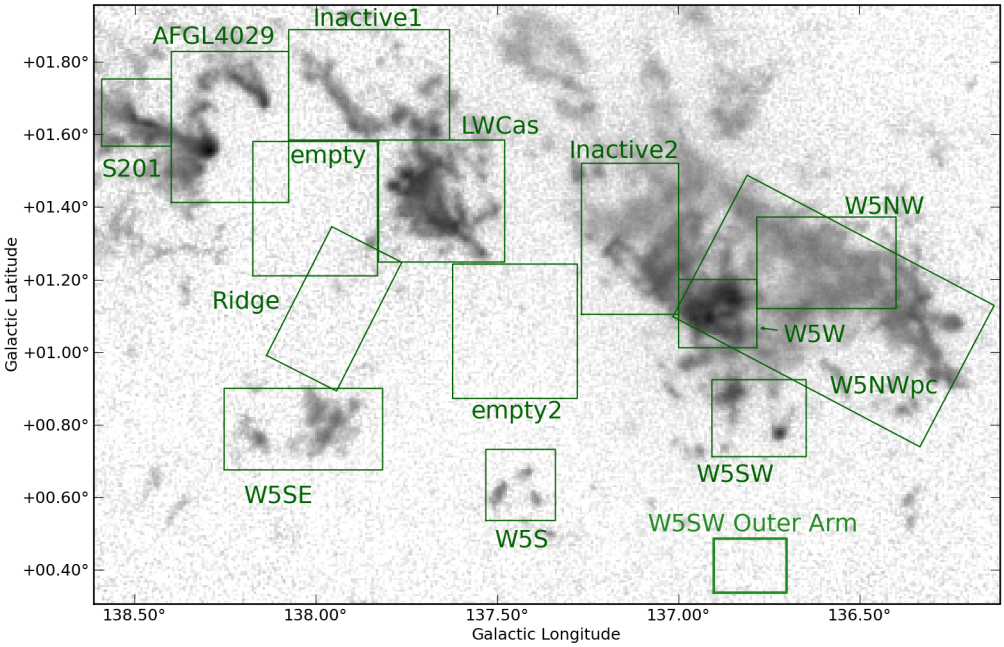

Figure 2.3 Individual region masks overlaid on the FCRAO ^{12}CO integrated image. The named regions, S201, AFGL4029, LWCas, W5NW, W5W, W5SE, W5S, and W5SW, were all selected based on the presence of outflows within the box. The inactive regions were selected from regions with substantial CO emission but without outflows. The 'empty' regions have essentially no CO emission within them and are used to place limits on the molecular gas within the east and west 'bubbles'. W5NWpc is compared directly to the Perseus molecular cloud in Section 2.4.1.1

from a width of 3 km s^{-1} to 7 km s^{-1}. Once an outflow candidate was identified in the position-velocity diagrams, the velocity range over which the wing showed emission in the position-velocity diagram (down to $T_A^* = 0$) was integrated over to create a map from which the approximate outflow size and position was determined (e.g. Figures 2.4 and 2.5).

Unlike Curtis et al. (2010) and Hatchell & Dunham (2009), we did not use an 'objective' outflow identification method because of the greater velocity complexity and poorer spatial resolution of our observations. The outflow selection criteria in these papers requires the presence of a sub-mm clump in order to identify a candidate driving source (and therefore a targeted region in which to search for outflows), making a similar objective identification impossible for our survey. As discussed later in Section 2.5, the regions associated with outflows have wide lines and many are double-peaked. Additionally, many smaller areas associated with outflows have collections of gaussian-profiled clumps that are not connected to the cloud in position-velocity diagrams but are not outflows. In particular, W5 is pockmarked by dozens of small cometary globules that are sometimes spatially coincident with the clouds but slightly offset in velocity.

While Arce et al. (2010) described the benefits of 3D visualization using isosurface contours, we found that the varying signal-to-noise across large-scale ($\sim$ 500 pixel^2) regions with significant extent in RA/Dec and limited velocity dynamic range made this method diffult for W5. There were many low-intensity outflows that were detectable by careful searches through position-velocity space that are not as apparent using isosurface methods. Out of the 55 outflows reported here, only 14 [5] would be considered obvious, high-intensity, high-velocity flows from their spectra alone; the rest could not be unambiguously detected without a search through position-velocity space.

In the majority of sources, the individual outflow lobes were unresolved, although some showed hints of position-velocity gradients at low significance and in many the red and blue flows are spatially separated. Only Outflow 1's lobes were clearly resolved (Figure 2.4). Some of the most suggestive gradients occurred where the outflow merged with its host molecular cloud in position-

[5] Outflows 15, 20, 24, the cluster of outflows 26-32, 47, 48, 52, and 53 could all have readily been detected by pointed single-dish measurements.

velocity space, making the gradient difficult to distinguish (e.g., Outflow 12, Figure 2.6). Bipolar pairs were selected when there were red and blue flows close to one another. The classification of a bipolar flow was either 'yc' (yes - confident), 'yu' (yes - unconfident), or 'n' (no) in Table 2.2. This identification is discussed in the captions for each outflow figure in the online supplement. The AFGL 4029 region has many red and blue lobes but confusion prevented pairing.

In cases where only the red- or blue-shifted lobe was visible, the surrounding pixels were searched for lower-significance and lower-velocity counterparts. For cases in which emission was detected, a candidate counterflow was identified and incorporated into the catalog. However, in 12 cases, the counterflow still evaded detection, either because of confusion or because the counterflow is not present in CO.

The outflow positions are overlaid on the CO 3-2 image in Figure 2.2 to provide an overview of where star formation is most active. The figures in Section 2.6.2 show outflow locations overlaid on small-scale images.

Because our detection method involved searching for high-velocity outflows by eye, there should be no false detections. However, it is possible that some of these outflows are generated by mechanisms other than protostellar jets and winds since we have not identified their driving sources.

One possible alternative driving mechanism is a photoevaporation flow, which could be accelerated up to the sound speed of the ionized medium, $c_{II} \approx 10$ km s^{-1}. Gas accelerating away from the cloud would not be detected as an outflow because it would be rapidly ionized. However, gas driven inward would be accelerated and remain molecular. It could exhibit red and / or blue flows depending on the line of sight orientation. While there are viable candidates for this form of outflow impersonator, such flows can only have peak velocities $v \lesssim c_{II}/4 \approx 2.5$ km s^{-1} in the strong adiabatic shock limit, so that any gas seen with higher velocity tails are unlikely to be radiation-driven.

Another plausible outflow impostor is the high-velocity tail in a turbulent distribution. However, for a typical molecular cloud, the low temperatures would require very high mach-number

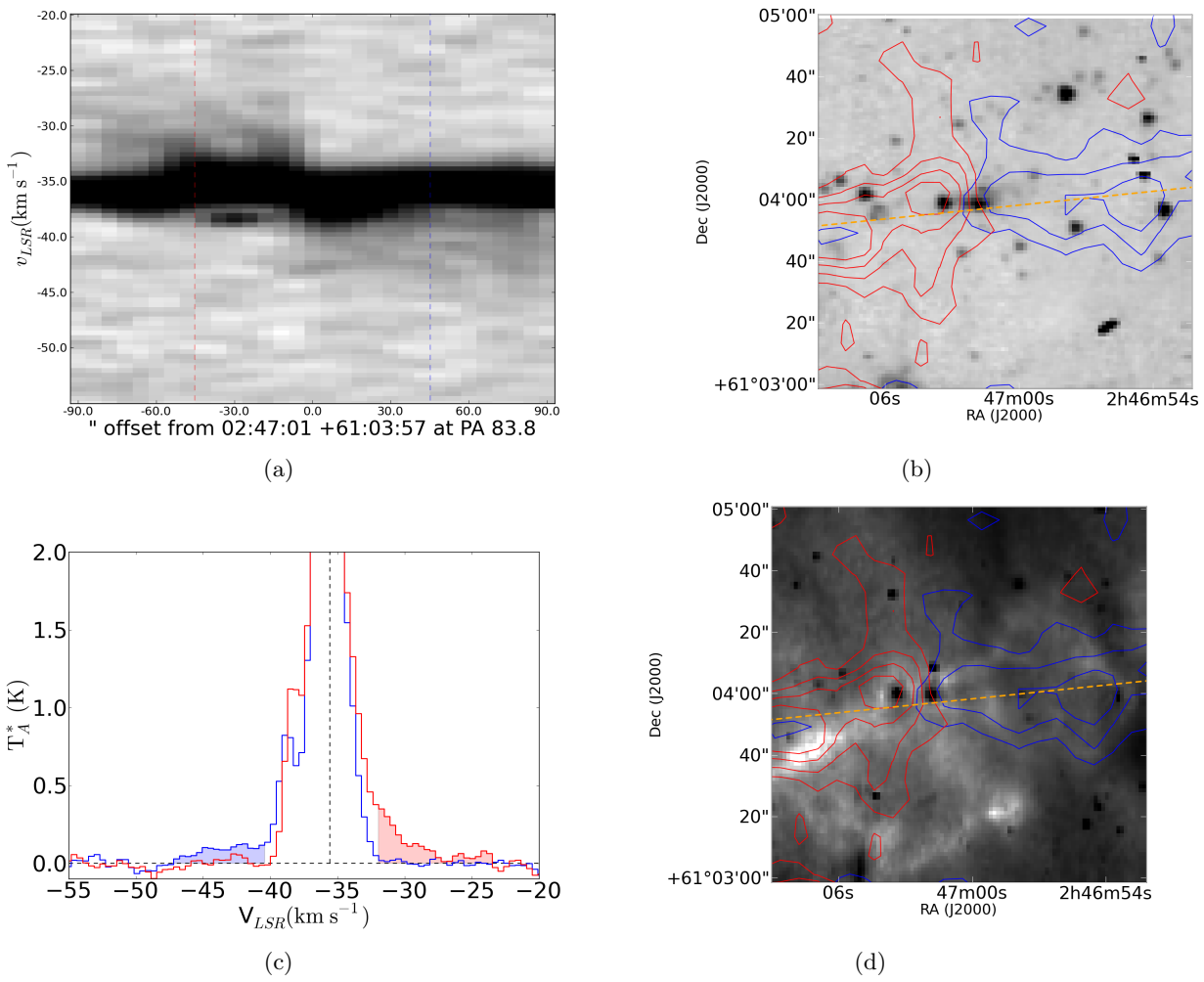

Figure 2.4 Position-velocity diagrams (a), spectra (c), and contour overlays of Outflow 1 on Spitzer 4.5 μm (b) and 8 μm (d) images. This outflow is clearly resolved and bipolar. *(a)*: Position-velocity diagram of the blue flow displayed in arcsinh stretch from T_A^* =0 to 3 K. Locations of the red and blue flows are indicated by vertical dashed lines. The location of the position-velocity cut is indicated by the orange dashed line in panels (b) and (d), although the position-velocity cut is longer than those cut-out images. *(b)* Spitzer 4.5 μm image displayed in logarithmic stretch from 30 to 500 MJy sr^{-1}. *(c)*: Spectrum of the outflow integrated over the outflow aperture and the velocity range specified with shading. The velocity center (vertical dashed line) is determined by fitting a gaussian to the ^{13}CO spectrum in an aperture including both outflow lobes. In the few cases in which ^{13}CO 1-0 was unavailable, a gaussian was fit to the ^{12}CO 3-2 spectrum. *(d)*: Contours of the red and blue outflows superposed on the Spitzer 8 μm image displayed in logarithmic stretch. The contours are generated from a total intensity image integrated over the outflow velocities indicated in panel (c). The contours in both panels (b) and (d) are displayed at levels of 0.5,1,1.5,2,3,4,5,6 K km s^{-1} ($\sigma \approx 0.25$ K km s^{-1}). The contour levels and stretches specified in this caption apply to all of the figures in the supplementary materials except where otherwise noted.

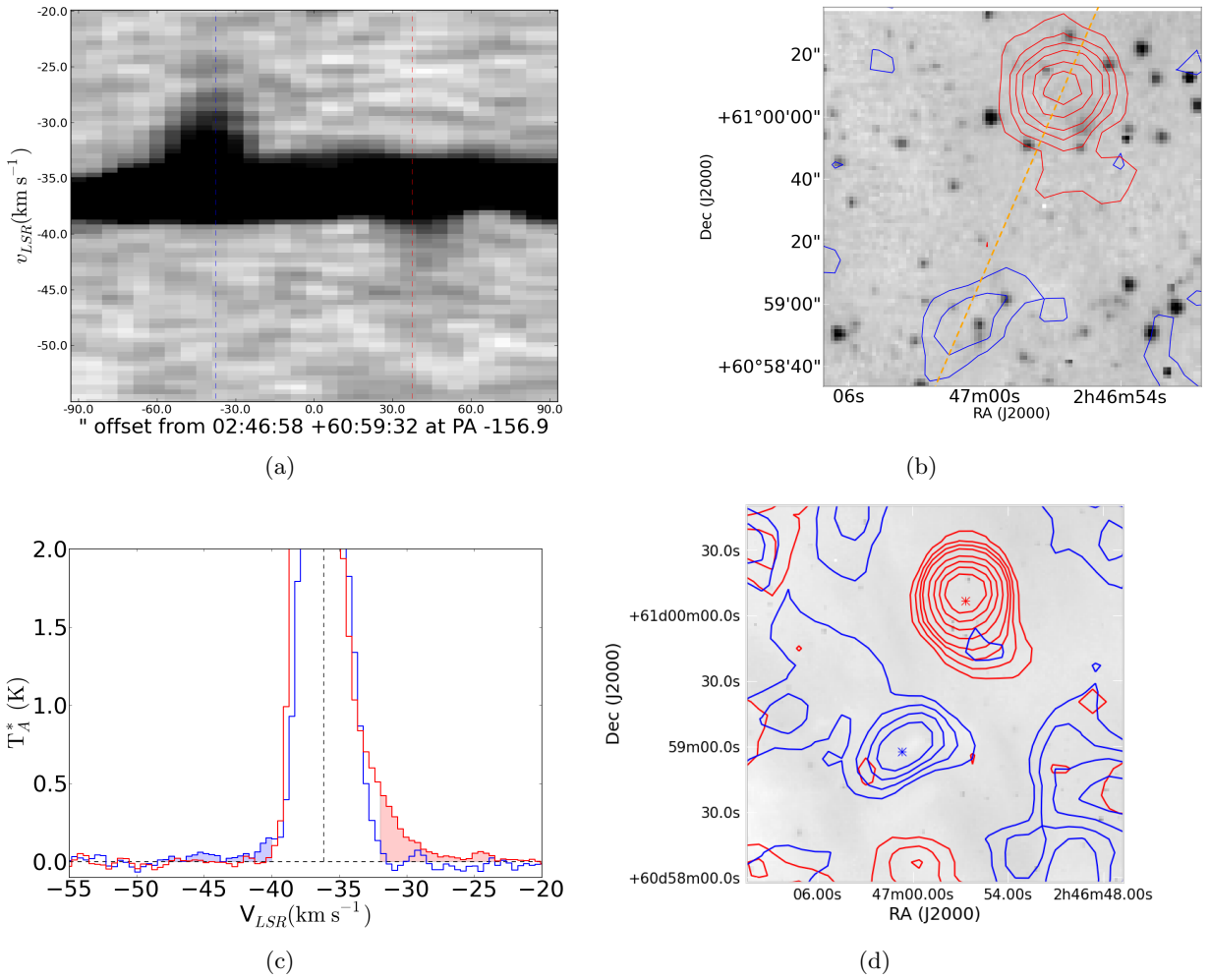

Figure 2.5 Position-velocity diagram, spectra, and contour overlays of Outflow 2 (see Figure 2.4 for a complete description). While the two lobes are widely separated, there are no nearby lobes that could lead to confusion, so we regard this pair as a reliable bipolar outflow identification.

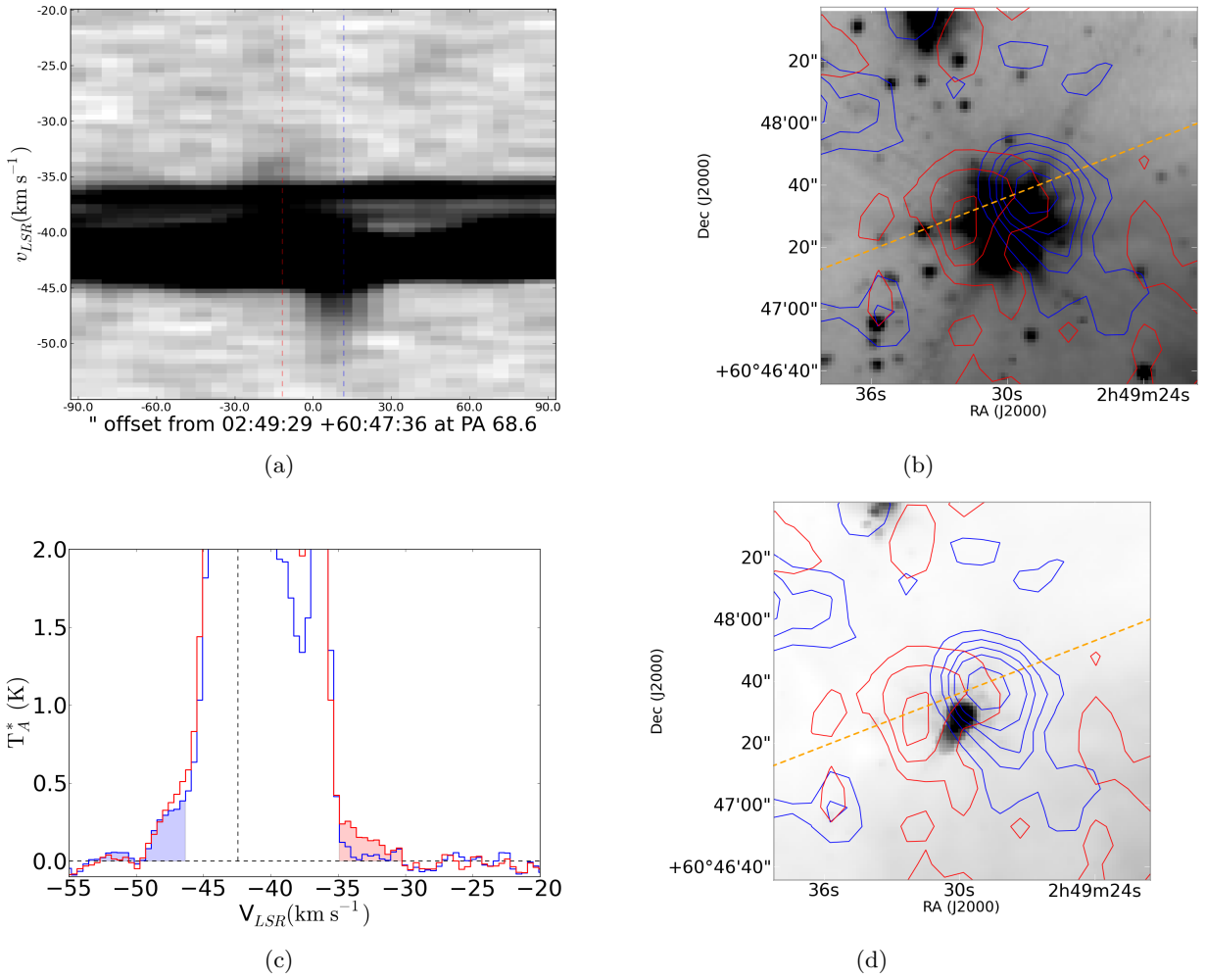

(a) (b) (c) (d)

Figure 2.6 Position-velocity diagram, spectra, and contour overlays of Outflow 12. Much of the red outflow is lost in the complex velocity profile of the molecular cloud(s), but it is high enough velocity to still be distinguished.

shocks ($\mathcal{M} \gtrsim 10$ assuming $T_{cloud} \sim 20$ K and $v_{flow} \sim 3$ km s^{-1}) that in idealized turbulence should be rare and short-lived. It is not known how frequent such high-velocity excursions will be in non-ideal turbulence with gravity (A. Goodman, P. Padoan, private communication). Finally, it is less likely for turbulent intermittency to have nearly coincident red and blue lobes, so intermittency can be morphologically excluded in most cases.

2.4.1.1 Comparison to Perseus CO 3-2 observations

We used the HARP CO 3-2 cubes from Hatchell et al. (2007) to evaluate our ability to identify outflows. We selected an outflow that was well-resolved and unconfused, L1448, and evaluated it at both the native sensitivity of the Hatchell et al. (2007) observations and degraded in resolution and sensitivity to match our own. We focus on L1448 IRS2, labeled Outflow 30 in Hatchell et al. (2007). Figure 2.7 shows a comparison between the original quality and degraded data.

Integrating over the outflow velocity range, we measure each lobe to be about $1.6' \times 0.8'$ (0.14×0.07pc). Assuming a distance to Perseus of 250 pc (e.g. Enoch et al., 2006a), we smooth by a factor of 8 by convolving the cube with a FWHM = $111''$ gaussian, then downsample by the same factor of 8 to achieve $6''$ square pixels at 2 kpc. The resulting noise was reduced because of the spatial and spectral smoothing and was measured to be ≈ 0.05 K in 0.54 km s^{-1} channels, which is comparable to the sensitivity in our survey. It is still possible to distinguish the outflows from the cloud in position-velocity space. Each lobe is individually unresolved (long axis $\sim 12''$ compared to our beam FWHM of $18''$), but the two are separated by $\gtrsim 20''$ and therefore an overall spatial separation can still be measured. Because they are just barely unresolved at this distance, the lobes' surface brightnesses are approximately the same at 2 kpc as at 250 pc; if this outflow were seen at a greater distance it would appear fainter.

Hatchell et al. (2007) detected 4 outflows within this map, plus an additional confused candidate. We note an additional grouping of outflowing material in the north-middle of the map (centered on coordinate 150×150 in Figure 2.7). In the smoothed version, only three outflows are detected in the blue and two in the red, making flow-counterflow association difficult. The

north-central blueshifted component appears to be the counterpart of the red flow when smoothed, although it is clearly the counterpart of the northwest blue flow in the full-resolution image.

We are therefore able to detect any outflows comparable to L1448 (assuming a favorable geometry), but are likely to see clustered outflows as single or possibly extended lobes and will count fewer lobes than would be detected at higher resolution. Additionally, it is clear from this example that two adjacent outflows with opposite polarity are not necessarily associated, and therefore the outflows' source(s) may not be between the two lobes.

In order to determine overall detectability of outflows compared to Perseus, we compare to Curtis et al. (2010) in Figure 2.8. Out of 29 outflows in their survey with measured 'lobe lengths', 22 (71%) were smaller than 128″ which would be below our 18″ resolution if observed at 2 kpc. Even the largest lobes (HRF26R, HRF28R, HRF44B) would only extend $\sim 60''$ at 2 kpc. Each lobe in the largest outflow in our survey, Outflow 1, is $\sim 80''$ ($660''$ at 250pc), but no other individual outflow lobes in W5 are clearly resolved. However, as seen in Figure 2.8, many bipolar lobes are **separated** by more than the telescope resolution, and the overall lobe separation distribution (as opposed to the lobe length, which is mostly unmeasured in our sample) in W5 is quite similar to the separation distribution in Perseus. The 2-sample KS test gives a 25% probability that they are drawn from the same distribution (the null hypothesis that they are drawn from the same distribution cannot be rejected).

On average, the Curtis et al. (2010) outflow velocities are similar to ours (Figure 2.9). We detect lower velocity outflows because we do not set a strict lower velocity limit criterion. We do not detect the highest velocity outflows most likely because of our poorer sensitivity to the faint high-velocity tips of outflows, although it is also possible that no high-velocity ($v > 20$ km s^{-1}) flows exist in the W5 region. Note that the histogram compares quantities that are not directly equivalent: the outflows in Curtis et al. (2010) and our own data are measured out to the point at which the outflow signal is lost, while the 'region' velocities are full-width half-max (FWHM) velocities.

Finally, we use the detectability of outflows in Perseus to inform our expectations in W5.

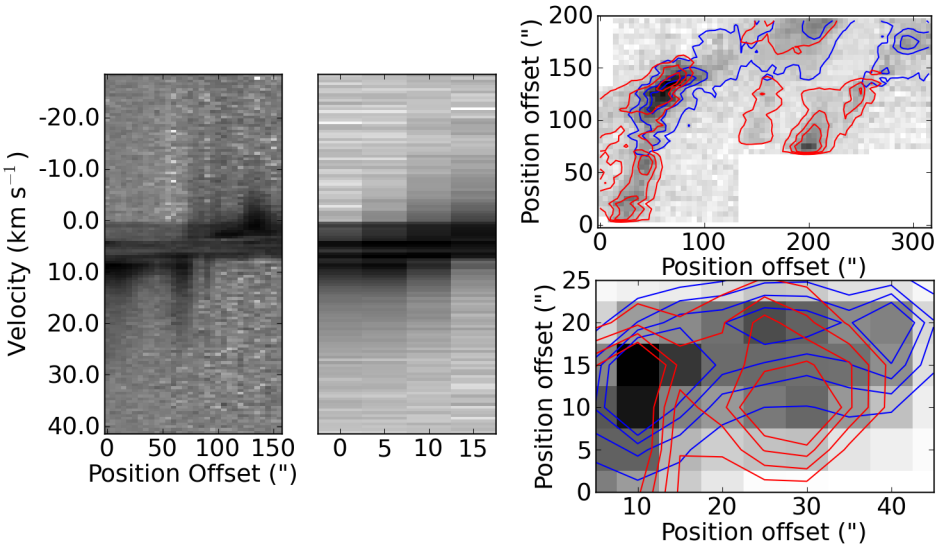

Figure 2.7 Comparison of L1448 seen at a distance of 250 pc (left) versus 2 kpc (middle) with sensitivity 0.5 K and 0.05K per 0.5 km s^{-1} channel respectively. *Far Left*: Position-velocity diagram (log scale) of the outflow L1448 IRS2 at its native resolution and velocity. L1448 IRS2 is the rightmost outflow in the contour plots. The PV diagram is rotated 45° from RA/Dec axes to go along the outflow axis. *Middle Left*: Position-velocity diagram (log scale) of the same outflow smoothed and rebinned to be eight times more distant. *Top Right*: The integrated map is displayed at its native resolution (linear scale). The red contours are of the same data integrated from 6.5 to 16 km s^{-1} and the blue from -6 to 0 km s^{-1}. Contours are at 1,3, and 5 K km s^{-1} ($\sim 6, 18, 30\sigma$). Axes are offsets in arcseconds. Because we are only examining the relative detectability of outflows at two distances, we are not concerned with absolute coordinates. *Bottom Right*: The same map as it would be observed at eight times greater distance. Axes are offsets in arcseconds assuming the greater distance. Contours are integrated over the same velocity range as above, but are displayed at levels 0.25,0.50,0.75,1.00 K km s^{-1} ($\sim 12, 24, 48, 60\sigma$). The entire region is detected at high significance, but dominated by confusion. It is still evident that the red and blue lobes are distinct, but they are each unresolved.

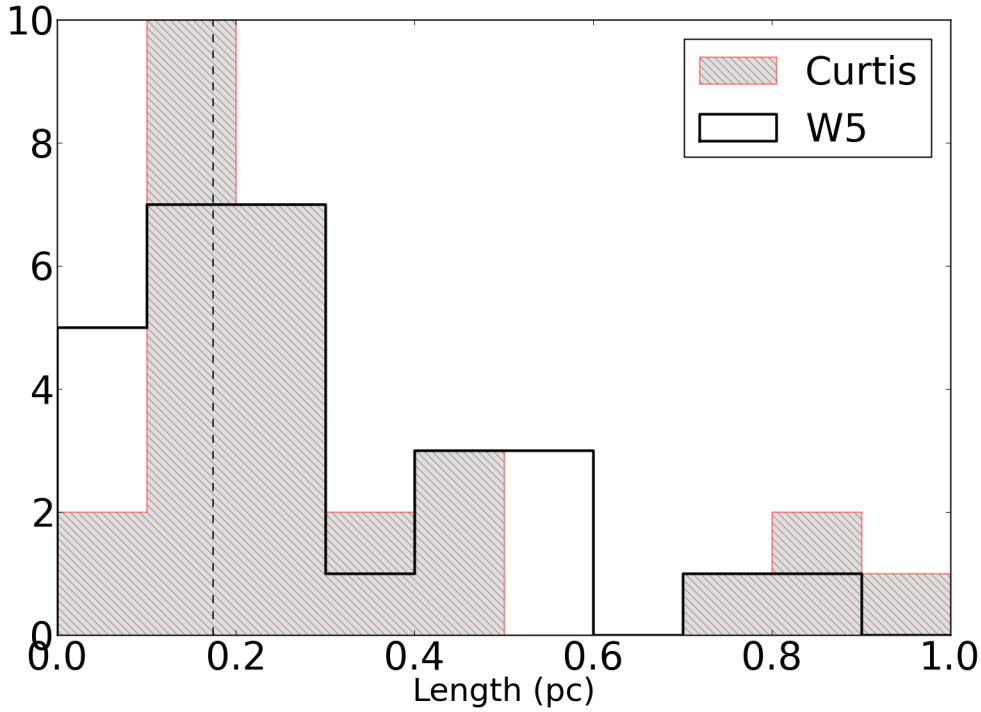

Figure 2.8 Histogram of the measured outflow lobe separations. The grey hatched region shows Curtis et al. (2010) values. The vertical dashed line represents the spatial resolution of our survey. The two distributions are similar.

Since it appears that we can detect outflows from low-mass protostars with sub-stellar to $\sim 30 L_{\odot}$ luminosities at the distance of W5 and these objects should be the most numerous in a standard initial mass function, the distribution of physical properties in W5 outflows should be similar to those in Perseus. However, because W5 is a somewhat more massive cloud ($M_{W5} \approx 5 M_{Perseus}$ [6]), we might expect the high-end of the distribution to extend to higher values of outflow mass, momentum, and energy. Since we will likely see clustered outflows confused into a smaller number of distinct lobes, we expect a bias towards higher values of the derived quantities but a lower detection rate.

2.4.1.2 Velocity, Column Density, and Mass Measurements

Throughout this section, we assume that the CO lines are optically thin and thermally excited. The measured properties are presented in Table 2.2. These assumptions are likely to be invalid, so we also discuss the consequences of applying 'typical' optical depth corrections to the derived quantities. Because we do not measure optical depths and the optical depth correction for CO 3-2 is less well quantified than for CO 1-0 (Curtis et al., 2010; Cabrit & Bertout, 1990)[7] , we only present the uncorrected measurements in Table 2.3.

The outflow velocity ranges were measured by examining both RA-velocity and Dec-velocity diagrams interactively using the STARLINK GAIA data cube viewing tool. The velocity limits are set to include all outflow emission that is distinguishable from the cloud (i.e. the velocity at which outflow lobes dominate over the gaussian wing of the cloud emission) down to zero emission. An outflow size (or lobe size, following Curtis et al., 2010) was determined by integrating over the blue and red velocity ranges and creating an elliptical aperture to include both peaks; the position and size therefore have approximately beam-sized ($\approx 18''$) accuracy. The integrated outflow maps are shown as red and blue contours in Figure 2.5. The velocity center was computed by fitting a

[6] M_{W5} is estimated from ^{13}CO. We also estimate the total molecular mass in W5 using the X-factor and acquire $M_{W5} = 5.0 \times 10^4\ M_{\odot}$, in agreement with Karr & Martin (2003), who estimated a molecular mass of 4.4×10^4 from ^{12}CO using the same X-factor. Koenig et al. (2008) estimated a total gas mass of 6.5×10^4 from a 2MASS extinction map. The total molecular mass in Perseus is $M_{Perseus} \sim 10^4$ (Bally et al., 2008)

[7] In Curtis et al. (2010), this correction factor ranged from 1.8 to 14.3; Arce et al. (2010) did not enumerate the optical depth correction they used but it is typically around 7 (Cabrit & Bertout, 1990).

gaussian to the FCRAO ^{13}CO spectrum averaged over the elliptical aperture.

The column density is estimated from ^{12}CO J=3-2 assuming local thermal equilibrium (LTE) and optically thin emission using the equation $N(\mathrm{H_2}) = 5.3 \times 10^{18} \eta_{mb}^{-1} \int T_A^*(v) dv$ for $T_{ex} = 20$ K. The derivation is given in the Appendix. The column density in the lobes is likely to be dominated by low-velocity gas and therefore our dominant uncertainty may be missing low-velocity emission rather than poor assumptions about the optical depth.

The scalar momentum and energy were computed from

$$p = M \frac{\sum T_A^*(v)(v - v_c)\Delta v}{\sum T_A^*(v)\Delta v} \tag{2.1}$$

$$E = \frac{M}{2} \frac{\sum T_A^*(v)(v - v_c)^2\Delta v}{\sum T_A^*(v)\Delta v} \tag{2.2}$$

where v_c is the ^{13}CO 1-0 centroid velocity. The same assumptions used in determining column density are applied here.

We estimate an outflow lifetime by taking half the distance between the red and blue outflow centroids divided by the maximum measured velocity difference ($\Delta v_{max} = (v_{max,red} - v_{max,blue})/2$), $\tau_{flow} = L_{flow}/(2\Delta v_{max})$, where L_{flow} refers to the length of the flow. This method assumes that the outflow inclination is 45°; if it is more parallel to the plane of the sky, we overestimate the age, and vice-versa. The momentum flux is then $\dot{P} = p/\tau$. Similarly, we compute a mass loss rate by dividing the total outflow mass by the dynamical age, which yields what is likely a lower limit on the mass loss rate (if the lifetime is underestimated, the mass loss rate is overestimated, but the outflow mass is always a lower limit because of optical depth and confusion effects).

The dynamical ages are highly suspect since the red and blue lobes are often unresolved or barely resolved, and diffuse emission averaged with the lobe emission can shift the centroid position. Additionally, it is not clear what portion of the outflow corresponds to the centroid: the bow shock or the jet could both potentially dominate the outflow emission. Curtis et al. (2010) discuss the many ways in which the dynamical age can be in error. Our mass loss rates are similar to those in Perseus **without** correcting our measurements for optical depth, while our outflow masses are an order of magnitude lower. It therefore appears that our dynamical age estimates must be too

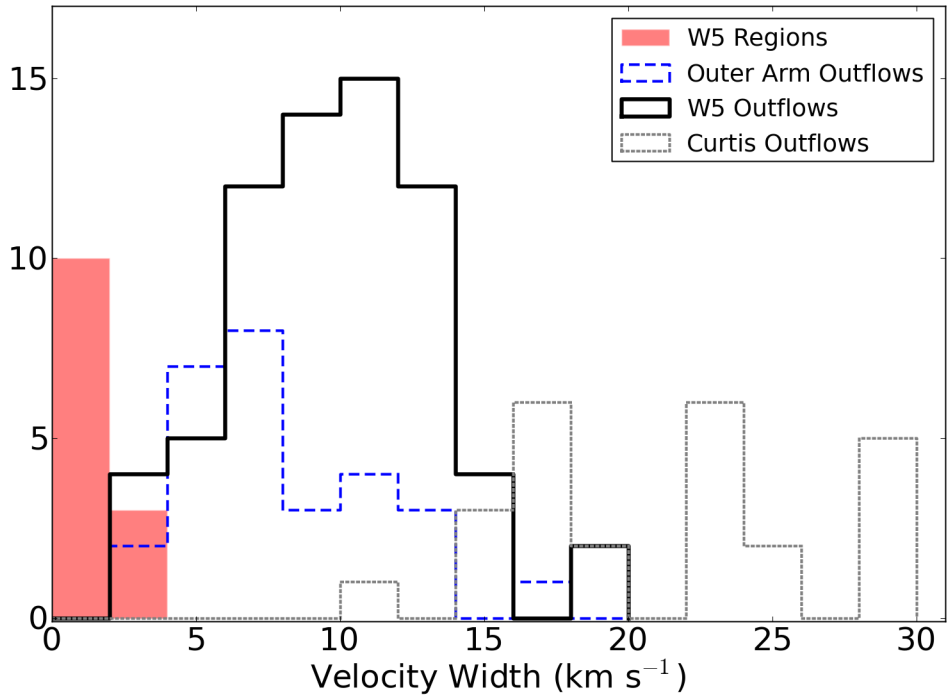

Figure 2.9 Histogram of the outflow line widths. *Black lines*: histogram of the measured outflow widths (half-width zero-intensity, measured from the fitted central velocity of the cloud to the highest velocity with non-zero emission). *Blue dashed lines*: outflow half-width zero-intensity (HWZI) for the outer arm (non-W5) sample. *Solid red shaded*: The measured widths (HWHM) of the sub-regions as tabulated in Table 2.1. *Gray dotted*: Outflow v_{max} (HWZI) values for Perseus from Curtis et al. (2010).

low, since we have no reason to expect protostars in W5 to be undergoing mass loss at a greater rate than those in Perseus. However, given more reliable dynamical age estimates from higher resolution observations of shock tracers, the mass loss rates could be corrected and compared to other star-forming regions.

Because the emission was assumed to be optically thin, the mass, column, energy, and momentum measurements we present are strictly lower limits. While some authors have computed correction factors to ^{12}CO 1-0 optical depths (e.g. Cabrit & Bertout, 1990), the corrections are different for the 3-2 transition (1.8 to 14.3, Curtis et al., 2010). Additionally, CO 3-2 may require a correction for sub-thermal excitation because of its higher critical density (the CO 3-2 critical density is 27 times higher than CO 1-0; see Appendix 2.9 for modeling of this effect).

Additionally, most of the outflow mass is at the lowest distinguishable velocities in typical outflows (e.g. Arce et al., 2010). It is therefore plausible that in the more turbulent W5 region, a greater fraction of the outflow mass is blended (velocity confused) with the cloud and therefore not included in mass, momentum, and energy measurements. This omission could be greater than the underestimate due to poor opacity assumptions.

The total mass of the W5 outflows is $M_{tot} \approx 1.5 M_{\odot}$, substantially lower, even with an optical depth correction of 10×, than the 163 $M_{\odot}$ reported in Perseus (Arce et al., 2010). Arce et al. (2010) also include a correction factor of 2.5 to account for higher temperatures in outflows and a factor of 2 to account for emission blended with the cloud. The temperature correction is inappropriate for CO 3-2 (see Appendix 2.9, Figure 2.27), but the resulting total outflow mass in W5 with an optical depth correction and a factor of 2 confusion correction is about 30 $M_{\odot}$. In order to make our measurements consistent with a mass of 160 $M_{\odot}$, a density upper limit in the outflowing gas of $n(\mathrm{H_2}) < 10^{3.5}\mathrm{cm}^{-3}$ is required, since a lower gas density results in greater mass for a given intensity (see Appendix 2.9, Figure 2.28). However, we expect the total outflow mass in W5 to be greater than in Perseus because of the greater cloud mass, implying that the density in the flows must be even lower, or additional corrections are needed.

The total outflow momentum is $p_{tot} \approx 10.9 M_{\odot}$ km s^{-1}, versus a quoted 517 $M_{\odot}$ km s^{-1} in

Perseus (Arce et al., 2010). Arce et al. (2010) included inclination and dissociative shock corrections for the momentum measurements on top of the correction factors already applied to the mass. If these corrections are removed from the Perseus momentum total (except for optical depth, which is variable in their data and therefore cannot be removed), the uncorrected outflow momentum in Perseus would be about 74 $M_{\odot}$ km s^{-1}. The W5 outflow momentum, if corrected with a 'typical' optical depth in the range 7-14, would match or exceed this value. If an additional CO 3-2 excitation correction (in the range 1-20) is applied, the W5 outflow momentum would significantly exceed that in Perseus.

Assuming a turbulent line width $\Delta v \sim 3$ km s^{-1} (approximately the smallest FWHM line-width observed), the total turbulent momentum in the ambient cloud is $p = M_{tot}\Delta v = 1.3 \times 10^5 M_{\odot}$ km s^{-1}, which is $\sim 10^5$ times the measured outflow momentum - the outflows detected in our survey cannot be the sole source of the observed turbulent line widths, even if corrected for optical depth and missing mass.

Table 2.1 presents the turbulent momentum for each sub-region computed by multiplying the measured velocity width by the integrated ^{13}CO mass. Even if the outflow measurements are orders of magnitude low because of optical depth, cloud blending, sub-thermal excitation, and other missing-mass considerations, outflows contribute negligibly to the total momentum of high velocity gas in W5. This result is unsurprising, as there are many other likely sources of energy in the region such as stellar wind bubbles and shock fronts between the ionized and molecular gas. Additionally, in regions unaffected by feedback from the HII region (e.g. W5NW), cloud-cloud collisions are a possible source of energy.

Figure 2.10 displays the distribution of measured properties and compares them to those derived in the COMPLETE (Arce et al., 2010) and Curtis et al. (2010) HARP CO 3-2 surveys of Perseus. Our derived masses are substantially lower than those in Arce et al. (2010) even if corrected for optical depth, but our momenta are similar to the CPOC (COMPLETE Perseus Outflow Candidate) sample and our energies are higher, indicating a bias towards detecting mass at high velocities. The bias is more heavily towards high velocities than the CO 1-0 used in Arce

et al. (2010). The discrepancy between our values and those of Arce et al. (2010) and Curtis et al. (2010) can be partly accounted for by the optical depth correction applied in those works: ^{13}CO was used to correct for opacity at low velocities, where most of the outflow mass is expected. Those works may also have been less affected by blending because of the smaller cloud line widths in Perseus.

The momentum flux and mass loss rate are compared to the values derived in Perseus by Hatchell et al. (2007) and Curtis et al. (2010) in Figures 2.11 and 2.12. Both of our values are computed using the dynamical timescale τ_d measured from outflow lobe separation, while the Hatchell et al. (2007) values are derived using a more direct momentum-flux measurement in which the momentum flux contribution of each pixel in the resolved outflow map is considered. The derived momentum fluxes (Figure 2.11) are approximately consistent with the Curtis et al. (2010) Perseus momentum fluxes; Curtis et al. (2010) measure momentum fluxes in a range $1\times10^{-6} < \dot{P} < 7\times10^{-4}$ $M_\odot$ km s^{-1} yr^{-1}, higher than our measured $6 \times 10^{-7} < \dot{P} < 1 \times 10^{-4}$ $M_\odot$ km s^{-1} yr^{-1} by approximately the opacity correction they applied. As seen in Figure 2.11, the Hatchell et al. (2007) momentum flux measurements in Perseus cover a much lower range $6\times10^{-8} < \dot{P} < 2\times10^{-5}$ $M_\odot$ km s^{-1} yr^{-1} and are not consistent with our measurements. This disagreement is most likely because of the difference in method. The W5 outflows exhibit substantially higher mass-loss rates and momentum fluxes if we assume a factor of 10 opacity correction, as expected from our bias toward higher-velocity, higher-mass flows.

2.4.2 Structure of the W5 molecular clouds: A thin sheet?

The W5 complex extends $\sim 1.6^\circ \times 0.7^\circ$ within 20° of parallel with the galactic plane. At the assumed distance of 2 kpc, it has a projected length of $\sim$ 60 pc (Figure 2.2). In the 8 μm band (Figure 2.1), the region appears to consist of two blown-out bubbles with $\sim 10 - 15$ pc radii centered on $\ell = 138.1, b = 1.4$ and $\ell = 137.5, b = 0.9$. While the bubbles are filled in with low-level far-infrared emission, there is no CO detected down to a $3-\sigma$ limit of 3.0 K km s^{-1} (^{12}CO 1-0), 2.4 K km s^{-1} (^{12}CO 3-2, excepting a few isolated clumps), and 1.5 K km s^{-1} (^{13}CO 1-0). Using

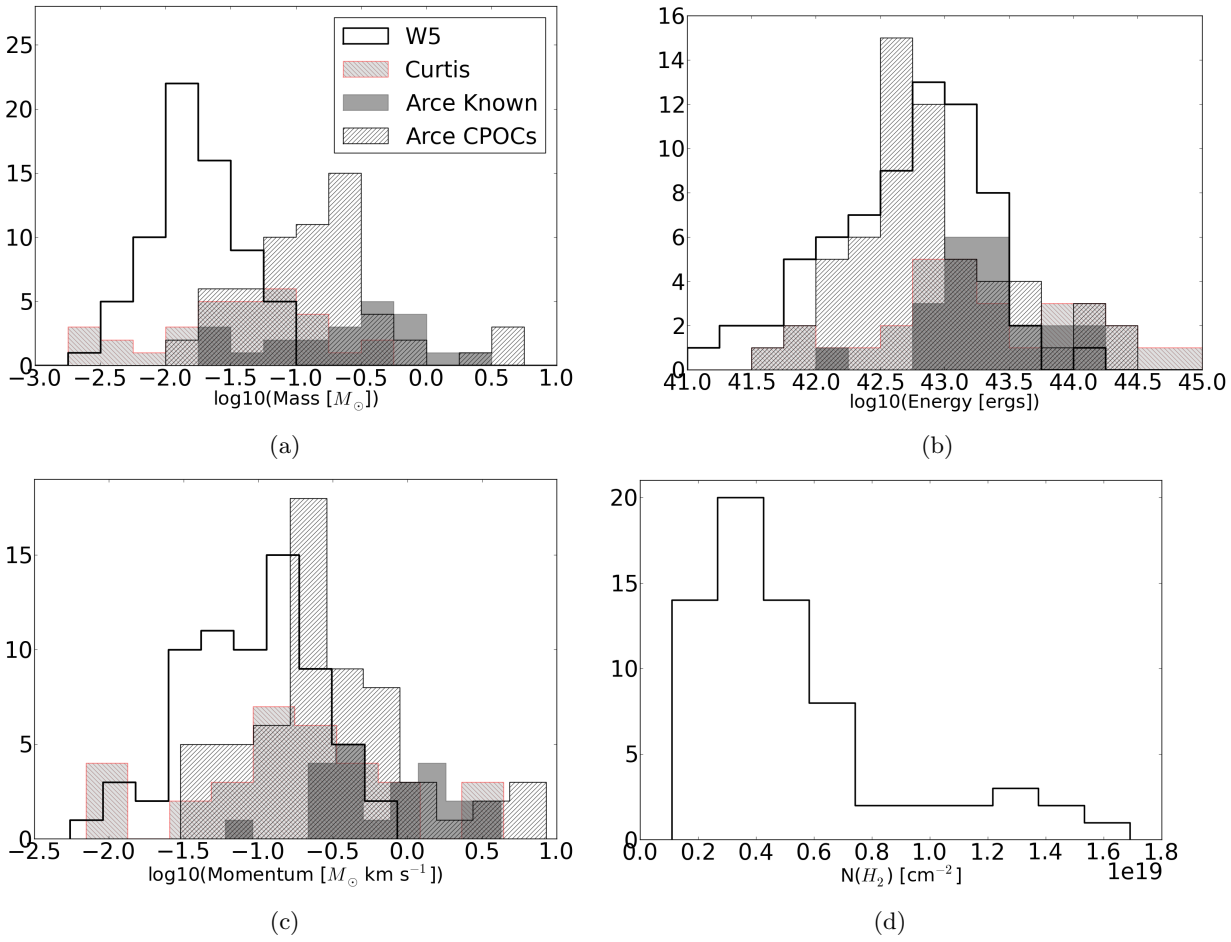

Figure 2.10 Histograms of outflow physical properties. The solid unfilled lines are the W5 outflows (this paper), the forward-slash hashed lines show Arce et al. (2010) CPOCs , the dark gray shaded region shows Arce et al. (2010) values for known outflows in Perseus, and the light gray, backslash-hashed regions show Curtis et al. (2010) CO 3-2 outflow properties. The outflow masses measured in Perseus are systematically higher partly because both surveys corrected for line optical depth using ^{13}CO. The medians of the distributions are 0.017, 0.044, 0.33, and 0.14 $M_\odot$ for W5, Curtis, Arce Known, and Arce CPOCs respectively, which implies that an optical depth and excitation correction factor of 2.5-20 would be required to make the distributions agree (although W5, being a more massive region, might be expected to have more massive and powerful outflows). It is likely that CO 3-2 is sub-thermally excited in outflows, and CO outflows may be destroyed by UV radiation in the W5 complex while they easily survive in the lower-mass Perseus region, which are other factors that could push the W5 mass distribution lower.

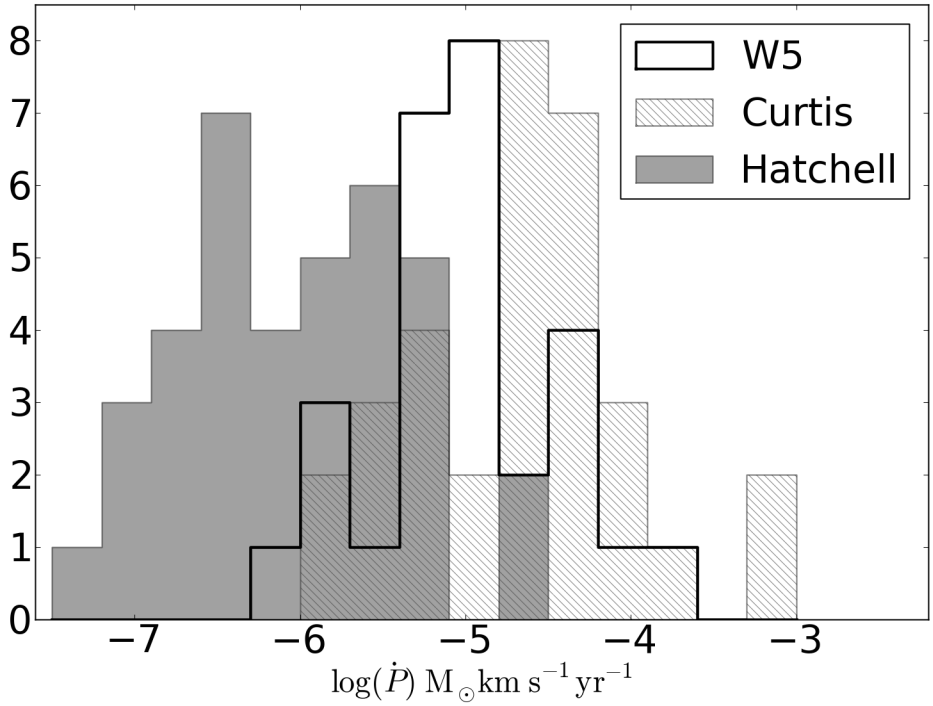

Figure 2.11 Histogram of the measured outflow momentum fluxes. The black thick line shows our data, the grey shaded region shows the Hatchell et al. (2007) data, and the hatched region shows Curtis et al. (2010) values. Our measurements peak squarely between the two Perseus JCMT CO 3-2 data sets, although the Curtis et al. (2010) results include an opacity correction that our data do not, suggesting that our results are likely consistent with Curtis et al. (2010) but inconsistent with the Hatchell et al. (2007) direct measurement method.

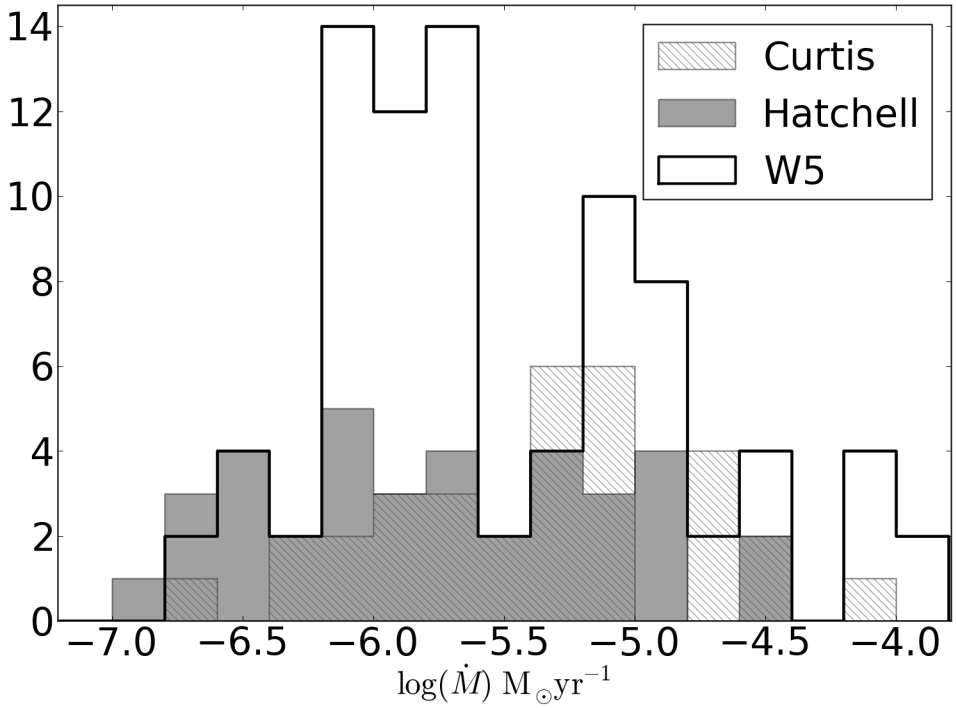

Figure 2.12 Histogram of the measured mass loss rate. The black thick line shows our data, while the grey shaded region shows the Hatchell et al. (2007) data, which is simply computed by $\dot{M} = \dot{P} \times 10/5$ km s^{-1}, where the factor of 10 is a correction for opacity. Our mass loss rates are very comparable to those of Hatchell et al. (2007), but different methods were used so the comparison may not be physically meaningful. Curtis et al. (2010) (hatched) used a dynamical time method similar to our own and also derived similar mass loss rates, although their mass measurements have been opacity-corrected using the ^{13}CO 3-2 line. Because our mass loss rates agree reasonably with Perseus, but our outflow mass measurements are an order of magnitude low, we believe our dynamical age estimates to be too small.

the X-factor (the CO-to-H_2 conversion factor) for ^{12}CO $N(H_2) = 3.6 \times 10^{20} \mathrm{cm}^{-2}/(\mathrm{K\ km\ s}^{-1})$, we derive an upper limit $N(H_2) < 1.1 \times 10^{21} \mathrm{cm}^{-2}$, or $A_V \lesssim 0.6$. Individual 'wisps' and 'clumps' of CO can sometimes be seen, particularly towards the cloud edges, but in general the bubbles are absent of CO gas.

Given such low column limits, the W5 cloud must be much smaller along the line of sight than its $\sim$ 50 pc size projected on the sky. Alternately, along the line-of-sight, the columns of molecular gas are too low for CO to self-shield, and it is therefore destroyed by the UV radiation of W5's O-stars. In either case, there is a significant excess of molecular gas in the plane of the sky compared to the line of sight, which makes W5 an excellent location to perform unobscured observations of the star formation process. The implied thin geometry of the W5 molecular cloud may therefore be similar to the bubbles observed by Beaumont & Williams (2010), but on a larger scale.

There is also morphological evidence supporting the face-on hypothesis. In the AFGL 4029 region (Section 2.5.2) and all along the south of W5, there are ridges with many individual cometary 'heads' pointing towards the O-stars that are unconfused along the line of sight. This sort of separation would not be expected if we were looking through the clouds towards the O-stars. W5W, however, presents a counterexample in which there are two clouds along the line of sight that may well be masking a more complex geometry.

2.5 Sub-regions

Individual regions were selected from the mosaic for comparison. All regions with multiple outflows and indicators of star formation activity were named and included as regions for analysis. Additionally, three "inactive" regions were selected based on the presence of ^{13}CO emission but the lack of outflows in the ^{12}CO 3-2 data. Finally, two regions devoid of CO emission were selected as a baseline comparison and to place upper limits on the molecular gas content of the east and west 'bubbles'. The regions are identified on the integrated ^{13}CO image in Figure 2.3.

Average spectra were taken of each "region" within the indicated box. Gaussians were fit

to the spectrum to determine line-widths and centers (Figure 2.13, Table 2.1). Gaussian fits were necessary because in many locations there are at least two velocity components, so the second moment (the "intensity-weighted dispersion") is a poor estimator of line width. Widths ranged from $v_{FWHM} = 2.3$ to 6.2 km s^{-1} (Figure 2.9).

Table 2.1. Gaussian fit parameters of sub-regions

Region	Velocity 1 (km s^{-1})	Width 1 (FWHM, km s^{-1})	Amplitude 1 (K)	Velocity 2 (km s^{-1})	Width 2 (FWHM, km s^{-1})	Amplitude 2 (K)		
S201	-38.04	3.149	2.35	-	-	-		
AFGL4029	-38.91	3.3605	1.48	-	-	-		
LWCas	-38.83	3.478	2.33	-	-	-		
W5W	-41.37	3.8775	3.07	-36.16	3.8305	1.90		
W5NW	-36.37	3.854	1.6	-	-	-		
W5NWpc	-36.37	3.713	1.19	-41.81	4.3475	0.47		
W5SW	-42.78	4.136	0.6	-36.34	4.183	0.22		
W5S	-40.15	2.914	0.34	-35.76	2.2795	0.40		
Inactive1	-42.91	2.6555	0.75	-39.38	4.2065	0.42		
Inactive2	-38.94	3.7365	1.2	-	-	-		
empty	-37.81	5.217	0.04	-	-	-		
^{13}CO fits							^{13}CO mass ($M_\odot$)	^{13}CO momentur ($M_\odot$ km s^{-}
S201	-37.97	2.5615	0.56	-	-	-	1300	3500
AFGL4029	-38.66	2.35	0.35	-	-	-	2600	6100
LWCas	-38.75	2.679	0.51	-	-	-	3700	10000
W5W	-41.23	2.773	1.09	-36.51	3.5485	0.47	4500	13000
W5NW	-36.1	3.431	0.7	-	-	-	5300	18000
W5NWpc	-36.18	3.3135	0.42	-41.44	3.619	0.14	15000	50000
W5SW	-42.6	3.807	0.1	-36.15	4.2535	0.05	790	3000
W5S	-39.9	2.444	0.07	-35.48	2.209	0.08	320	790
Inactive1	-42.58	2.5145	0.1	-38.97	2.82	0.07	1400	3500

Table 2.1 (cont'd)

Region	Velocity 1 (km s^{-1})	Width 1 (FWHM, km s^{-1})	Amplitude 1 (K)	Velocity 2 (km s^{-1})	Width 2 (FWHM, km s^{-1})	Amplitude 2 (K)			
Inactive2	-38.82	3.196	0.37	-	-	-	3100	9900	3.2×10
empty	-38.44	4.7705	0.02	-	-	-	340	1600	7.8×10

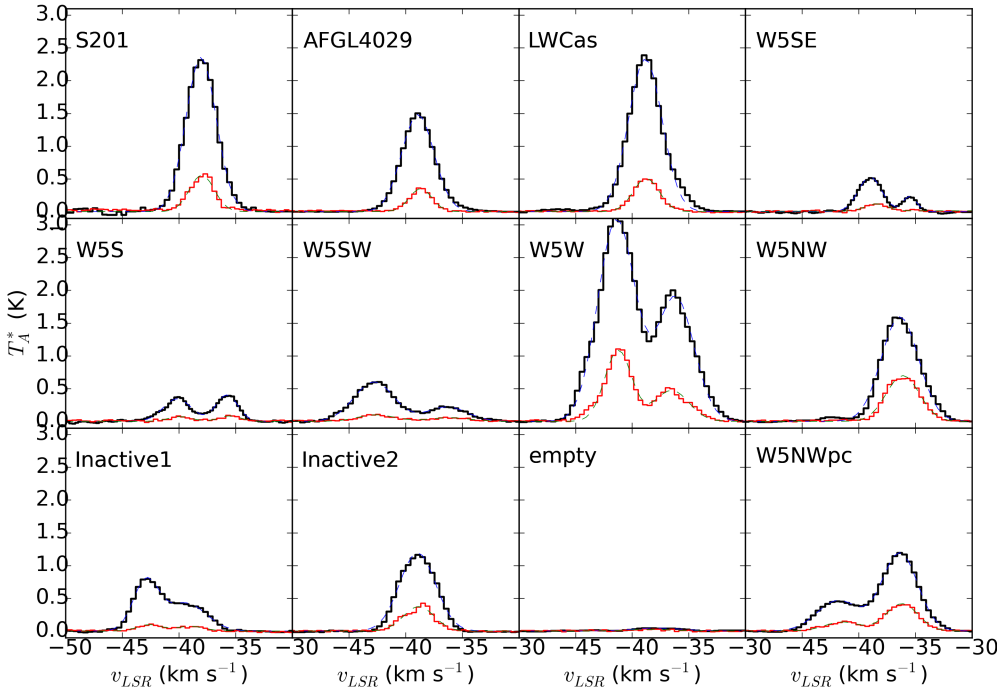

Figure 2.13 Spatially averaged spectra of the individual regions analyzed. ^{12}CO 3-2 is shown by thick black lines and ^{13}CO 1-0 is shown by thin red lines. Gaussian fits are overplotted in blue and green dashed lines, respectively. The fit properties are given in Table 2.1.

2.5.1 Sh 2-201

Sh 2-201 is an HII region and is part of the same molecular cloud as the bright-rimmed clouds in W5E, but it does not share a cometary shape with these clouds (Figure 2.14). Instead, it is internally heated and has its own ionizing source (Felli et al., 1987). The AFGL 4029 cloud edge is at a projected distance of $\sim$ 7 pc from the nearest exposed O-star, and the closest illuminated point in the Spitzer 8 and 24 μm maps is at a projected distance of $\sim$ 5 pc. The star forming process must therefore have begun before radiation driven shocks from the W5 O-stars could have impacted the cloud.

2.5.2 AFGL 4029

AFGL 4029 is a young cluster embedded in a cometary cloud (Figure 2.15). There is one clear bipolar outflow and 6 single-lobed flows that cannot be unambiguously associated with an opposite direction counterpart. The cluster is mostly unresolved in the data presented here and is

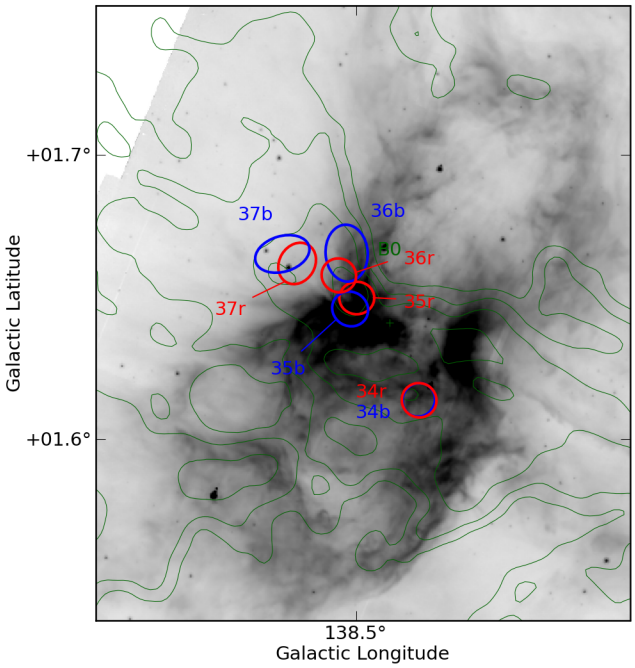

Figure 2.14 Small scale map of the Sh 2-201 region plotted with CO 3-2 contours integrated from -60 to -20 km s^{-1} at levels 3,7.2,17.3,41.6, and 100 K km s^{-1}. The IRAC 8 μm image is displayed in inverted log scale from 800 to 8000 MJy sr^{-1}. Contours of the CO 3-2 cube integrated from -60 to -20 km s^{-1} are overlaid at logarithmically spaced levels from 3 to 100 K km s^{-1} (3.0,7.2,17.3,41.6,100; $\sigma \approx 0.7$ K km s^{-1}). The ellipses represent the individual outflow lobe apertures mentioned in Section 2.4.1.2.

clearly the most active CO clump in W5. It contains a cluster of at least 30 B-stars (Deharveng et al., 1997). The outflows from this region have a full width $\Delta v \approx 30$ km s^{-1}, which is entirely inconsistent with a radiation-driven inflow or outflow since it is greater than the sound speed in the ionized medium.

The northeast cometary cloud is strongly affected by the W5 HII region. It has an outflow in the head of the cloud (Figure 2.16), and the cloud shows a velocity gradient with distance from the HII region. The polarity of the gradient suggests that the cometary cloud must be on the far side of the ionizing O-star along the line of sight assuming that the HII region pressure is responsible for accelerating the cloud edge.

2.5.3 W5 Ridge

The W5 complex consists of two HII region bubbles separated by a ridge of molecular gas (Figure 2.17). This ridge contains the LW Cas optical nebula, a reflection nebula around the variable star LW Cas, on its east side and an X-shaped nebula on the west. The east portion of LW Cas Nebula is bright in both the continuum and CO J=3-2 but lacks outflows (see Figure 2.17). The east portion also has the highest average peak antenna temperature, suggesting that the gas temperature in this region is substantially higher than in the majority of the W5 complex (higher spatial densities could also increase the observed T_A, but the presence of nearby heating sources make a higher temperature more plausible). It is possible that high gas temperatures are suppressing star formation in the cloud. Alternately, the radiation that is heating the gas may destroy any outflowing CO, which is more likely assuming the two Class I objects identified in this region by Koenig et al. (2008) are genuine protostars.

The ridge is surprisingly faint in HI 21 cm emission compared to the two HII regions (Figure 2.18) considering its 24 μm surface brightness. The integrated HI intensity from -45 to -35 km s^{-1} is $\sim$ 800 K km s^{-1}, whereas in the HII region bubble it is around 1000 K km s^{-1}. The CO-bright regions show lower levels of emission similar to the ridge at 700-800 K km s^{-1}. However, the ridge contains no CO gas and very few young stars (Figure 7 in Koenig et al., 2008). It is possible

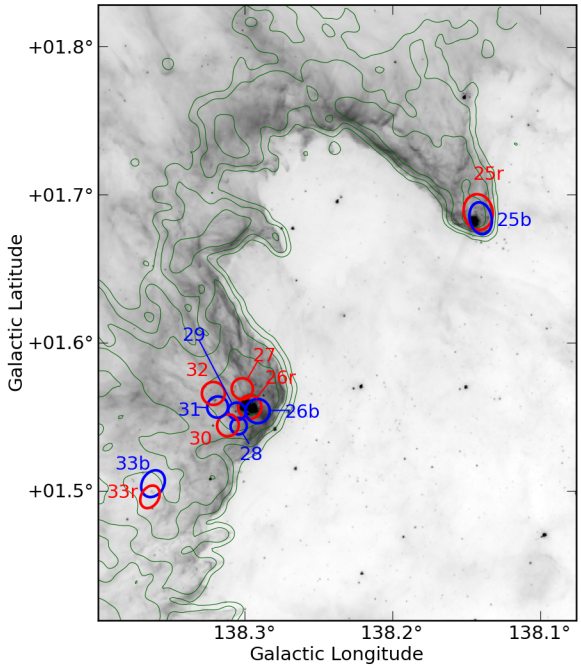

Figure 2.15 Small scale map of the AFGL 4029 region plotted with CO 3-2 contours integrated from -60 to -20 km s^{-1} at levels 3,7.2,17.3,41.6, and 100 K km s^{-1}. The IRAC 8 μm image is displayed in inverted log scale from 800 to 8000 MJy sr^{-1}. Contours of the CO 3-2 cube integrated from -60 to -20 km s^{-1} are overlaid at logarithmically spaced levels from 3 to 100 K km s^{-1} (3.0,7.2,17.3,41.6,100; $\sigma \approx 0.7$ K km s^{-1}). Outflows 26-32 are ejected from a forming dense cluster. A diagram displaying the kinematics of the northern cometary cloud is shown in Figure 2.16.

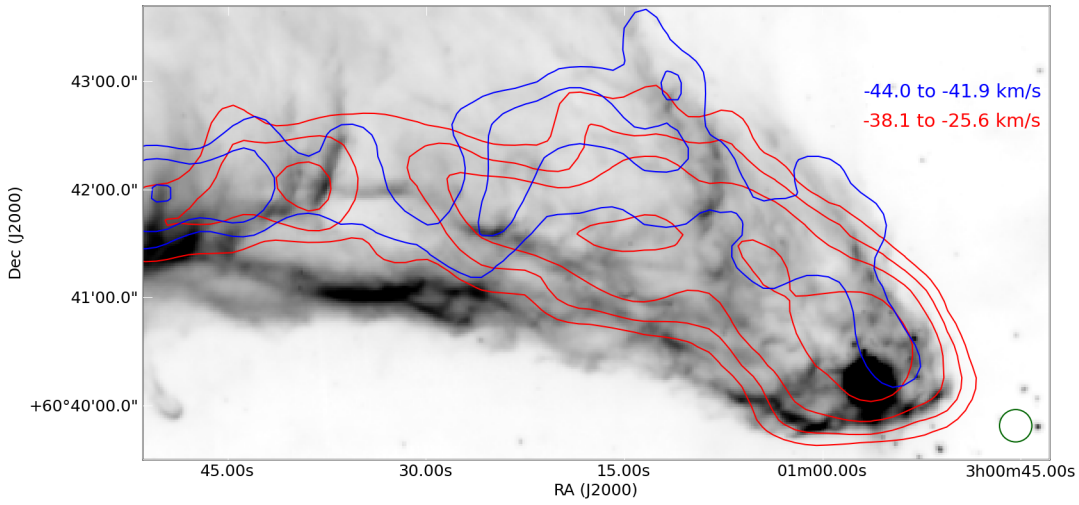

Figure 2.16 The northeast cometary cloud. Contours are shown at 0.5,1,2, and 5 K km s^{-1} integrated over the ranges -44.0 to -41.9 km s^{-1} (blue) and -38.1 to -35.6 km s^{-1} (red). There is a velocity gradient across the tail, suggesting that the front edge is being pushed away along the line of sight.

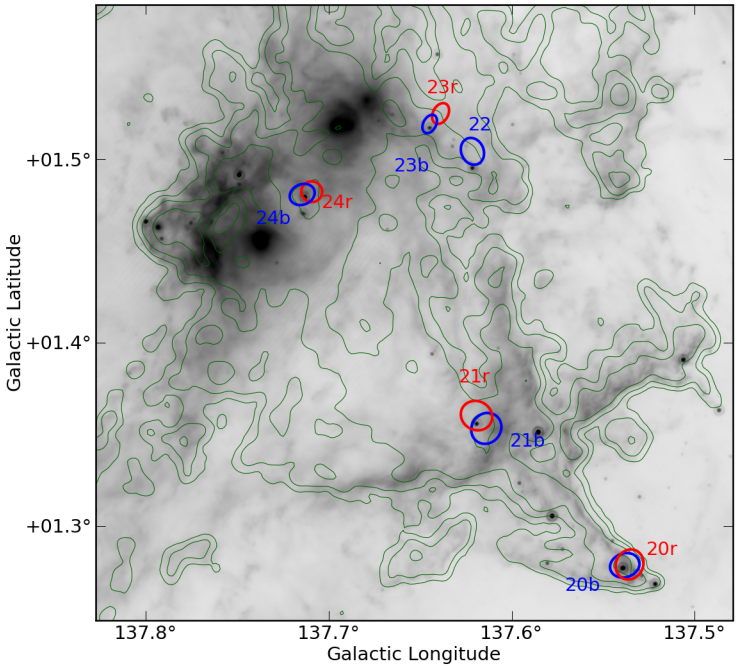

Figure 2.17 Small scale map of the LW Cas nebula plotted with CO 3-2 contours integrated from -60 to -20 km s^{-1} at levels 3,7.2,17.3,41.6, and 100 K km s^{-1}. The feature containing outflows 20 and 21 is the X-shaped ridge referenced in Section 2.5.3. This sub-region is notable for having very few outflows associated with the most significant patches of CO emission. The gas around it is heated on the left side by the O7V star HD 18326 ($D_{proj} = 8.5$ pc), suggesting that this gas could be substantially warmer than the other molecular clouds in W5.

that the ridge contains cool HI but has very low column-densities along the direction pointing towards the O-stars, in which case the self-shielding is too little to prevent CO dissociation. This ridge may therefore be an excellent location to explore the transition from molecular to atomic gas under the influence of ionizing radiation in conditions different from high-density photodissociation (photon-dominated) regions.

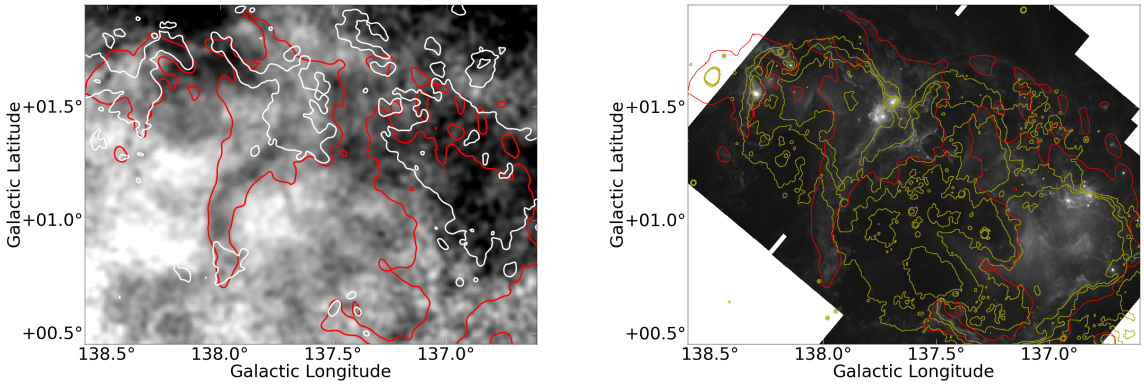

Figure 2.18 *Top:* The DRAO 21 cm HI map integrated from -45 to -35 km s^{-1} displayed in grayscale from 700 (black) to 1050 (white) K km s^{-1} with IRAS 100 μm contours (red, 40 MJy sr^{-1}) and ^{12}CO 1-0 contours integrated over the same range (white, 4 K km s^{-1}) overlaid. The ridge of IRAS 100 μm emission at $\ell = 138.0$ coincides with a relative lack of HI emission at these velocities, suggesting either that there is less or colder gas along the ridge. *Bottom:* The Spitzer 24 μm map with 21 cm continuum contours at 6, 8, and 10 MJy sr^{-1} overlaid. The IRAS contours are also overlaid to provide a reference for comparing the two figures and to demonstrate that the HII region abuts the cold-HI area. The moderate excess of continuum emission implies a somewhat higher electron density along the line of sight through the ridge.

We examine Outflow 20 as a possible case for pressure-driven implosion (radiation, RDI, or gas pressure, PDI) by examining the relative timescales of the outflow driving source and the HII-region-driven compression front. A typical molecular outflow source (Class 0 or I) has a lifetime of $\sim 5 \times 10^5$ years (Evans et al., 2009). Given that there is an active outflow at the head of this cloud, we use 0.5 MYr as an upper limit. The approximate distance from this source to the cloud front behind it is $\sim$ 3.3 pc. If we assume the cloud front has been pushed at a constant speed $v \leq c_{II} \approx 10$km s^{-1}, we derive a lower limit on its age of 0.3 MYr. While these limits allow for the protostar to be older than the compression front by up to 0.2 MYr, it is likely that the compression front moved more slowly (e.g., 3 km s^{-1} if it was pushed by a D-type shock front) and that the

protostar is not yet at the end of its lifetime - it is very plausible that this soure was born in a radiation-driven implosion.

2.5.4 Southern Pillars

There are 3 cometary clouds that resemble the "elephant trunk" nebula in IC 1396 (Figure 2.19). Each of these pillars contains evidence of at least one outflow in the head of the cloud (see the supplementary materials, outflows 16-19 and 38) These pillars are low-mass and isolated; there is no other outflow activity in southern W5. However, because of the bright illumination on their northern edges and robust star formation tracers, these objects present a reasonable case for triggered star formation by the RDI mechanism.

The kinematics of these cometary clouds suggest that they have been pushed in different directions by the HII region (Figure 2.19). The central cometary cloud (Figure 2.19b) has two tails. The southwest tail emission peaks around -39.5 km s^{-1} and the southeast tail peaks at -41.5 km s^{-1}, while the head is peaked at an intermediate -40.5 km s^{-1}. These velocity shifts suggest that the gas is being accelerated perpendicular to the head-tail axis and that the southeast tail is on the back side of the cometary head, while the southwest tail is on the front side. The expanding HII region is crushing this head-tail system.

The southeast cometary cloud (Figure 2.19a) peaks at -35.0 km s^{-1}. There are no clearly-separated CO tails as in the central cloud, but there is a velocity shift across the tail, in which the west (right) side is blueshifted compared to the east (left) side, which is the opposite sense from the central cometary cloud.

The southwest cometary cloud (Figure 2.19c) peaks at -40.3 km s^{-1} and has weakly defined tails similar to the central cloud. Both of its tails are at approximately the same velocity (-42.5 km s^{-1}).

The kinematics of these tails provide some hints of their 3D structure and location in the cloud. Future study to compare the many cometary flows in W5 to physical models and simulations is warranted. Since these flows are likely at different locations along the line of sight (as required for

their different velocities), analysis of their ionized edges may allow for more precise determination of the full 3D structure of the clouds relative to their ionizing sources.

2.5.5 W5 Southeast

The region identified as W5SE has very little star formation activity despite having significant molecular gas ($M_{^{13}CO} \sim 800 M_{\odot}$). While there are two outflows and two Class I objects (Koenig et al., 2008) in the southeast of the two clumps ($\ell = 138.15, b = 0.77$, Figure 2.20), the main clump ($\ell = 138.0, b = 0.8$) has no detected outflows. The CO emission is particularly clumpy in this region, with many independent, unresolved clumps both in position and velocity. In the 8 and 24 micron Spitzer images, it is clear that these clouds are illuminated from the northwest. This region represents a case in which the expanding HII region has impacted molecular gas but has not triggered additional star formation. The high clump-to-clump velocity dispersion observed in this region may be analogous to the W5S cometary clouds (Section 2.5.4) but without condensed clumps around which to form cometary clouds.

2.5.6 W5 Southwest

There is an isolated clump associated with outflows in the southwest part of W5 (Figure 2.21) at $v_{LSR} \sim -45$ km s^{-1}. While this clump is likely to be associated with the W5 region, it shows little evidence of interaction with the HII region. If it is eventually impacted by the expanding ionization front (i.e. if it is within the W5 complex), this clump will be an example of "revealed", not triggered, star formation.

The other source in W5SW is a cometary cloud with a blueshifted head and redshifted tail (Figure 2.22; Outflow 13). The head contains a redshifted outflow; no blueshifted counterpart was detected (the velocity gradient displayed in Figure 2.22 is smaller than the outflow velocity and is also redshifted away from the head). The lack of a blueshifted counterpart may be because the flow is blowing into ionized gas where the CO is dissociated.

Because of its evident interaction with the HII region, this source is an interesting candidate

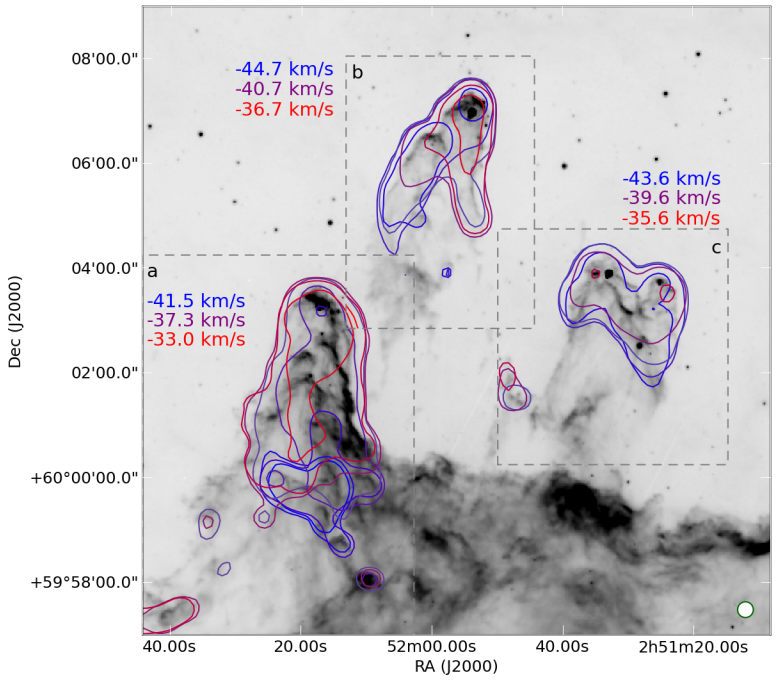

Figure 2.19 CO 3-2 contours overlaid on the Spitzer 8 μm image of the W5S cometary clouds described in Section 2.5.4. Contours are color-coded by velocity and shown for 0.84 km s^{-1} channels at levels of 1 K (a, b) and 0.5 K (c). The velocity ranges plotted are (a) -41.5 to -33.0 km s^{-1} (b) -44.7 to -36.7 km s^{-1} (c) -43.6 to -35.6 km s^{-1}. The labels show the minimum, maxmimum, and middle velocities to guide the eye. The grey boxes indicate the regions selected for CO contours; while there is CO emission associated with the southern 8 μm emission, we do not display it here. The velocity gradients are discussed in Section 2.5.4.

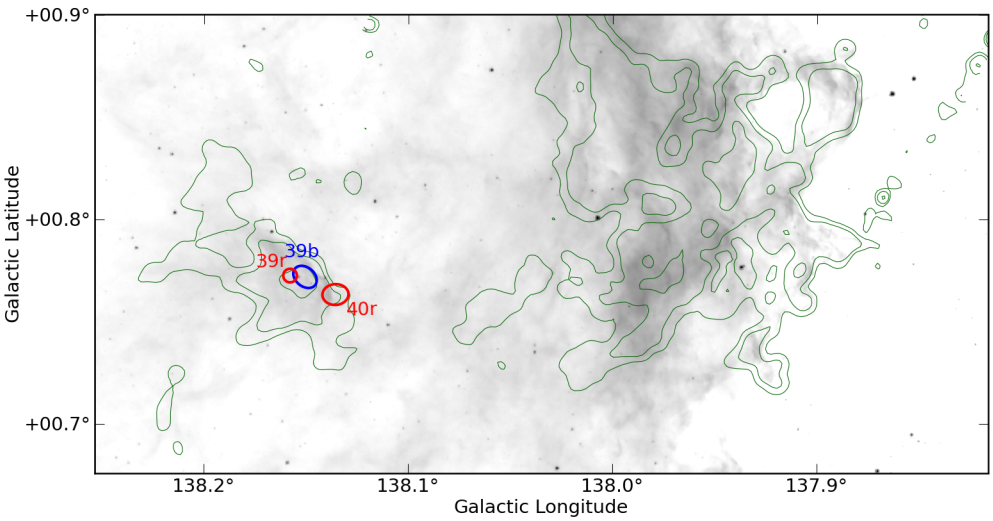

Figure 2.20 Small scale map of the W5 SE region showing the star-forming clump containing outflows 39 and 40 and the non-star-forming clump at $\ell = 138.0, b = 0.8$. CO 3-2 contours integrated from -60 to -20 km s^{-1} are displayed at levels 3,7.2,17.3,41.6, and 100 K km s^{-1}.

for a non-protostellar outflow impersonator. However, because the head is blueshifted relative to the tail, we can infer that the head has been accelerated towards us by pressure from the HII region, implying that it is in the foreground of the cloud. Given this geometry, a radiation-driven flow would appear blueshifted, not redshifted, as the detected flow is. Additionally, the outflow is seen as fast as 7.5 km s^{-1} redshifted from the cloud, which is a factor of 2 too fast to be driven by radiation in a standard D-type shock. Finally, the outflow velocity is much greater than seen in a simulation of a cometary cloud by Gritschneder et al. (2010), while the head-to-tail velocity gradient is comparable.

2.5.7 W5 West / IC 1848

There is a bright infrared source seen in the center of W5W (IRAS 02459+6029; Figure 2.23), but the nearest CO outflow lobe is ≈ 1 pc away. The nondetection may be due to confusion in this area: there are two layers of CO gas separated by $\sim$5 km s^{-1}, so low-velocity outflow detection is more difficult. Unlike the rest of the W5 complex, this region appears to have multiple independent confusing components along the line of sight (Figure 2.13), and therefore the CO data provide much less useful physical information (multiple components are also observed in the ^{13}CO data, ruling out self-absorption as the cause of the multiple components).

2.5.8 W5 NW

The northwest cluster containing outflows 1-8 is at a slightly different velocity (~ -35 km s^{-1}) than the majority of the W5 cloud complex (~ -38 km s^{-1}; Figure 2.24), but it shares contiguous emission with the neighboring W5W region. It contains many outflows and therefore is actively forming stars (Figure 2.25). However, this cluster exhibits much lower CO brightness temperatures and weaker Spitzer 8 μm emission than the "bright-rimmed clouds" seen near the W5 O-stars. We therefore conclude that the region has not been directly impacted by any photoionizing radiation from the W5 O-stars.

The lack of interaction with the W5 O-stars implies that the star formation in this region,

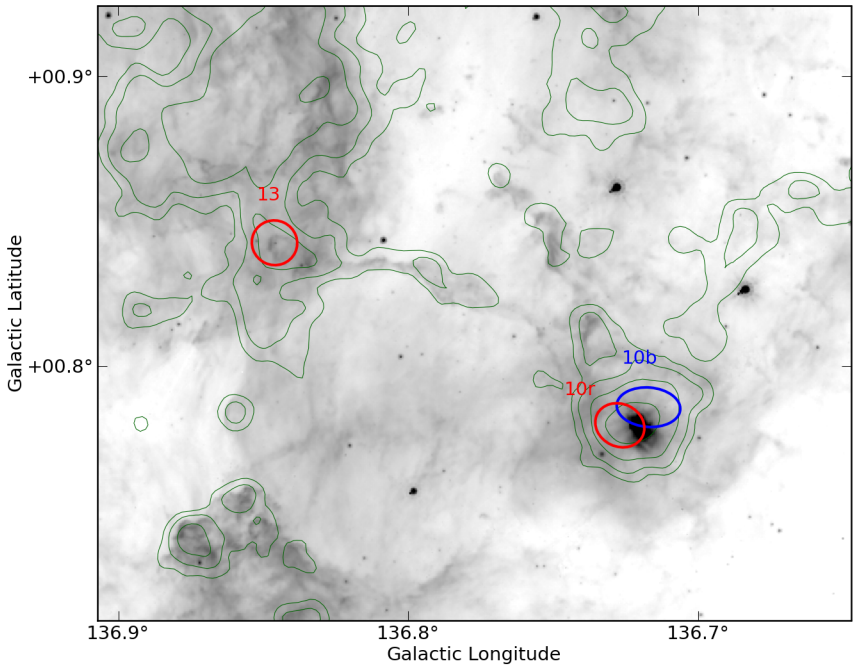

Figure 2.21 Small scale map of the W5 SW region plotted with CO 3-2 contours integrated from -60 to -20 km s^{-1} at levels 3,7.2,17.3,41.6, and 100 K km s^{-1}. Outflow 13 is at the head of a cometary cloud (Figure 2.22) and therefore has clearly been affected by the expanding HII region, but the region including bipolar Outflow 10 shows no evidence of interaction with the HII region.

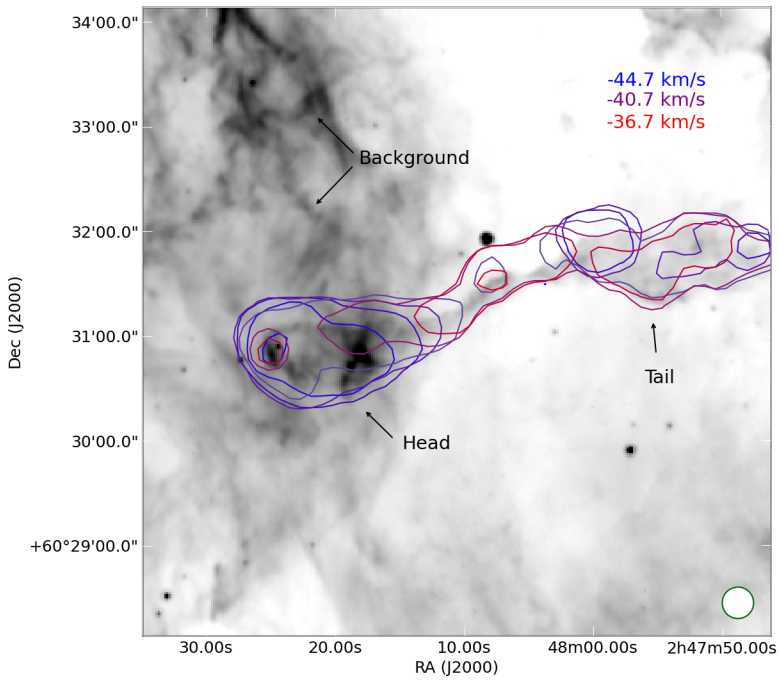

Figure 2.22 The cometary cloud in the W5 Southwest region (Outflow 13). Contours are shown at 1 K for 0.84 km s^{-1} wide channels from -37.2 km s^{-1} (blue) to -30.5 km s^{-1} (red). The head is clearly blueshifted relative to the tail and contains a spatially unresolved redshifted outflow.

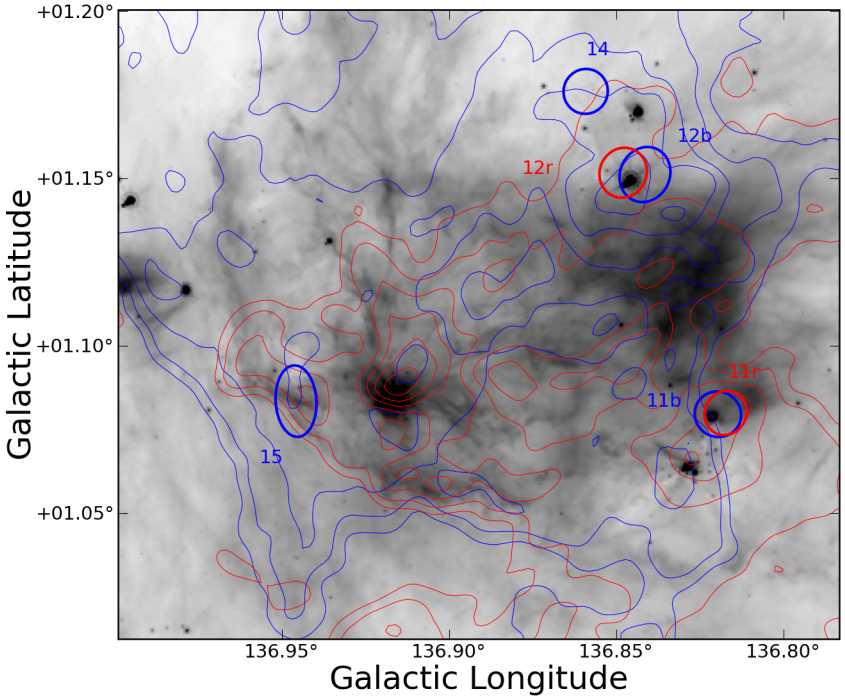

Figure 2.23 Small scale map of the W5 W region. The IRAC 8 μm image is displayed in inverted log scale from 800 to 8000 MJy sr^{-1}. Contours of the CO 3-2 cube integrated from -50 to -38 km s^{-1} (blue) and -38 to -26 km s^{-1} (red) are overlaid at levels 5,10,20,30,40,50,60 K km s^{-1} $\sigma \approx 0.5$ K km s^{-1}. The lack of outflow detections is partly explained by the two spatially overlapping clouds that are adjacent in velocity.

though quite vigorous, has not been directly triggered. Therefore not all of the current generation of star formation in W5 has been triggered on small or intermediate scales (e.g., radiation-driven implosion). Even the "collect and collapse" scenario seems unlikely here, as the region with the most outflows also displays some of the smoothest morphology (Figures 2.2 and 2.25); in "collect and collapse" the expansion of an HII region leads to clumping and fragmentation, and the spaces between the clumps should be relatively cleared out.

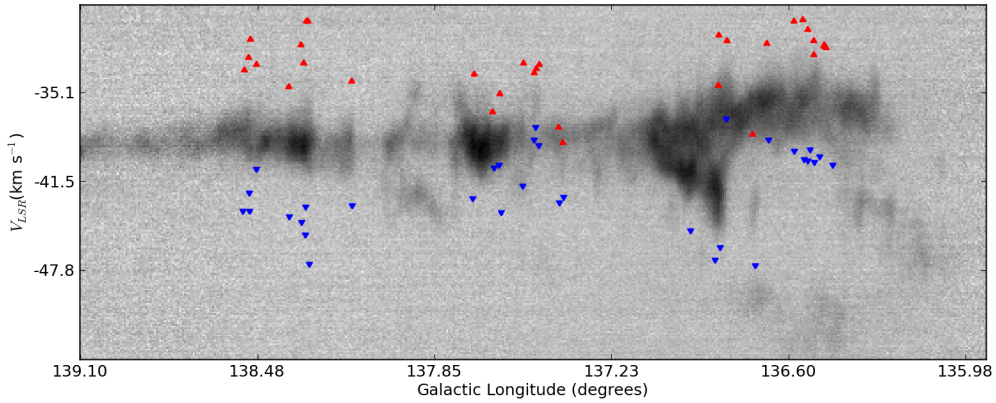

Figure 2.24 Integrated longitude-velocity diagram of the W5 complex from $b = 0.25$ to $b = 2.15$ in ^{12}CO 1-0 from the FCRAO OGS. The W5NW region is seen at a distinct average velocity around $\ell = 136.5$, $v_{LSR} = -34$ km s^{-1}. The red and blue triangles mark the longitude-velocity locations of the detected outflows. In all cases, they mark the low-velocity start of the outflow.

2.6 Discussion

2.6.1 Comparison to other outflows

The outflow properties we derive are similar to those in the B0-star forming clump IRAS 05358+3543 ($M \approx 600 M_\odot$ Ginsburg et al., 2009), in which CO 3-2 and 2-1 were used to derive outflow masses in the range 0.01-0.09 $M_\odot$. However, some significantly larger outflows, up to 1.6 pc in one direction were detected, while the largest resolved outflow in our survey was only 0.8 pc (one direction).

As noted in Section 2.4.1.1, the total molecular mass in W5 is larger than Perseus, $M_{W5} \sim 4.5 \times 10^4 M_\odot$ while $M_{Perseus} \sim 10^4 M_\odot$ (Bally et al., 2008). The length distribution of outflows

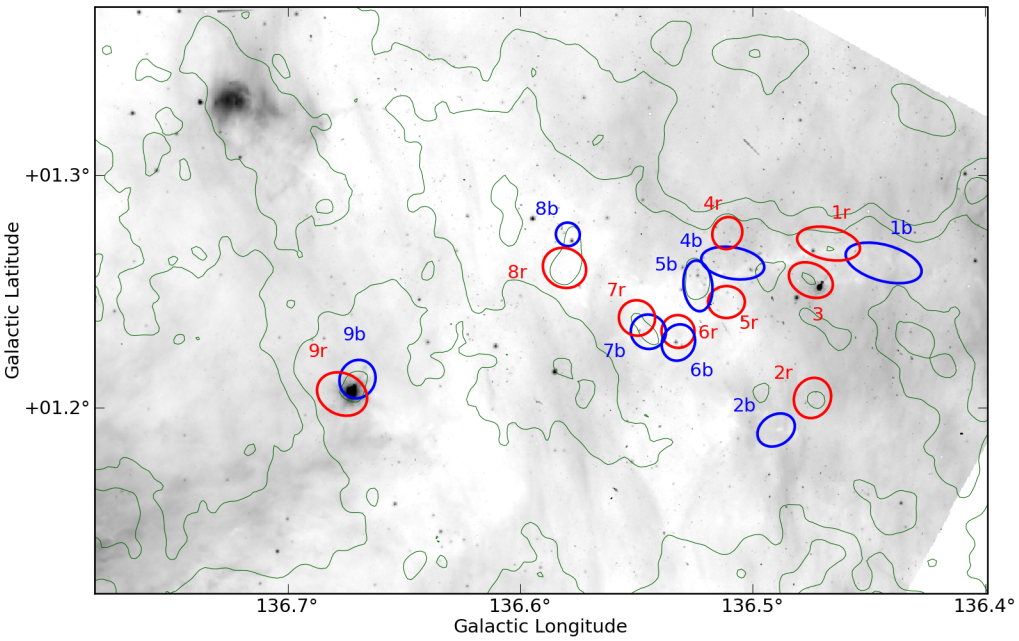

Figure 2.25 Small scale map of the W5 NW region plotted with CO 3-2 contours integrated from -60 to -20 km s^{-1} at levels 3,7.2,17.3,41.6, and 100 K km s^{-1}. Despite its distance from the W5 O-stars, $D_{proj} \approx 20$ pc, this cluster is the most active site of star formation in the complex as measured by outflow activity.

(Figure 2.8) is strikingly similar, while other physical properties have substantially different mean values with or without correction factors included.

The W5NW region is more directly comparable to Perseus, with a total mass of $\sim 1.5 \times 10^4$ $M_\odot$ (Table 2.1) and a similar size. In Figure 2.3, we show both the W5NW region, which contains all of the identified outflows, and the W5NWpc region, which is a larger area intended to be directly comparable in both mass and spatial scale to the Perseus molecular cloud. The W5NWpc region contains more than an order of magnitude more turbulent energy than the Perseus complex ($E_{turb,Per} = 1.6 \times 10^{46}$ ergs, Arce et al., 2010) despite its similar mass. Even the smaller W5NW region has $\sim 5\times$ more turbulent energy than the Perseus complex, largely because of the greater average line width ($\sigma_{FWHM,W5NW} \approx 3.5$ km s^{-1}). As with the whole of W5, there is far too much turbulent energy in W5NW to be provided by outflows alone, implying the presence of another driver of turbulence.

Figure 2.26 shows the W5NWpc region and Perseus molecular cloud on the same scale, though in two different emission lines. The Perseus cloud contains many more outflows and candidates (70 in Perseus vs. 13 in W5NWpc) despite a much larger physical area surveyed in W5. While it is likely that many of the W5W outflows will break apart into multiple flows at higher resolution, it does not seem likely that each would break apart into 5 flows, as would be required to bring the numbers into agreement. Since the highest density of outflows in Perseus is in the NGC 1333 cloud, it may be that there is no equivalently evolved region in W5NWpc. The W5W region may be comparably massive, but it is also confused and strongly interacting with the W5 HII region - either star formation is suppressed in this region, or outflows are rendered undetectable. In the latter case, the most likely mechanisms for hiding outflows are molecular dissociation by ionizing radiation and velocity confusion.

Another possibility highlighted in Figure 2.26 is that the W5NW region is interacting with the W4 bubble. The cloud in the top right of Figure 2.26 is somewhat cometary, has higher peak brightness temperature, and is at a slightly different velocity (-45 km s^{-1}) than W5NW. The velocity difference of ~ 8 km s^{-1} could simply be two clouds physically unassociated along the line

of sight, or could indicate the presence of another expanding bubble pushing two sheets of gas away from each other. Either way, the northwest portion of the W5NW region is clumpier than the area in which the outflows were detected, and it includes no outflow detections.

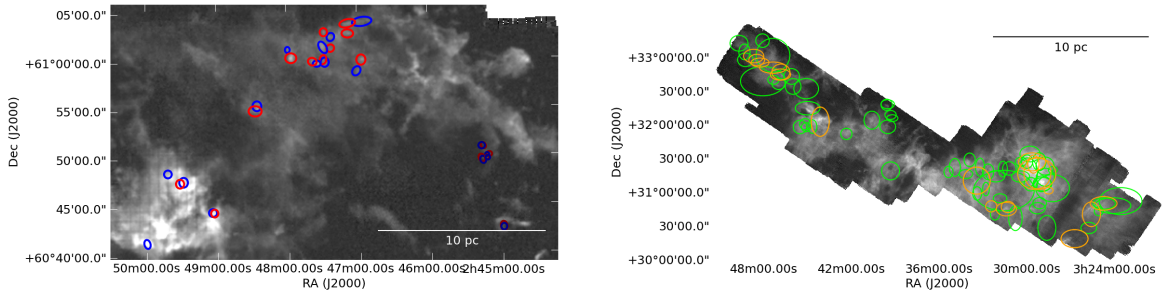

Figure 2.26 (a) An integrated CO 3-2 image of the W5W/NW region with ellipses overlaid displaying the locations and sizes of outflows. The dark red and blue ellipses in the lower right are associated with outer-arm outflows. W5W is the bottom-left, CO-bright region. W5NW is the top-center region containing the cluster of outflows. (b) An integrated CO 1-0 image of the Perseus molecular cloud from the COMPLETE survey (Arce et al., 2010). Note that the spatial scale is identical to that of (a) assuming that W5 is 8 times more distant than Perseus. The green ellipses represent Arce et al. (2010) CPOCs while the orange represent known outflows from the same paper.

2.6.2 Star Formation Activity

CO outflows are an excellent tracer of ongoing embedded star formation (e.g. Shu et al., 1987). We use the locations of newly discovered outflows to qualitatively describe the star formation activity within the W5 complex and evaluate the hypothesis that star formation has been triggered on small or intermediate scales.

Class 0/I objects are nearly always associated with outflows in nearby star-forming regions (e.g. Perseus Curtis et al., 2010; Hatchell et al., 2007). However, Koenig et al. (2008) detected 171 Class I sources in W5 using Spitzer photometry. Since our detection threshold for outflow appears to be similar to that in Perseus (Section 2.4.1.1), the lower number of outflow detections is surprising, especially considering that some of the detected outflows are outside the Spitzer-MIPS field (MIPS detections are required for Class I objects, and flows 1-4 are outside that range) or are in the outer arm (flows 39-54). Additionally, we should detect outflows from Class 0 objects that would not be identified by Spitzer colors.

There are a number of explanations for our detection deficiency. The Class I objects detected within the HII region "bubble" most likely have outflows in which the CO is dissociated similar to jet systems in Orion (e.g. HH46/47, a pc-scale flow in which CO is only visible very near the protostar; Chernin & Masson, 1991; Stanke et al., 1999). This hypothesis can be tested by searching for optical and infrared jets associated with these objects, which presumably have lower mass envelopes and therefore less extinction than typical Class I objects. Additionally, there are many outflow systems that are are likely to be associated with clusters of outflows rather than individual outflows as demonstrated in Section 2.4.1.1, where we were able to identify fewer outflows when 'observing' the Perseus objects at a greater distance. There are 24 sources in the Koenig et al. (2008) Class I catalog within 15″ (one JCMT beam at 345 GHz) of another, and in many cases there are multiple Koenig et al. (2008) Class I sources within the contours of a single outflow system.

2.6.3 Evaluating Triggering

In the previous section, we discussed in detail the relationship between each sub-region and the HII region. Some regions are observed to be star-forming but not interacting with the HII region (W5NW, Sh 2-201), while others are interacting with the HII region but show no evidence or reduced evidence of star formation (W5SE, W5W, LW Cas). At the very least, there is significant complexity in the triggering mechanisms, and no one mechanism or size scale is dominant. If we were to trust outflows as unbiased tracers of star formation, we might conclude that the majority of star formation in W5 is untriggered (spontaneous), but such a conclusion is unreliable because both radiatively triggered star formation and "revealed" star formation may not exhibit molecular outflows (although ionized atomic outflows should still be visible around young stars formed through these scenarios).

In Section 2.5.3, we analyzed a particular case in which the RDI mechanism could plausibly have crushed a cloud to create the observed protostar. It is not possible to determine whether interaction with the HII region was a necessary precondition for the star's formation, but it at least accelerated the process. The other cometary clouds share this property, but in total there are only

5 cometary clouds with detected outflows at their tips, indicating that this mechanism is not the dominant driver of star formation in W5.

The 'collect and collapse' scenario might naively be expected to produce an excess of young stars at the interaction front between the HII region and the molecular cloud. However, because such interactions naturally tend to form instabilities, this scenario produces cloud morphologies indistinguishable from those of RDI. There is not an obvious excess of sources associated with cloud edges over those deep within the clouds (e.g., Figure 2.2). We therefore cannot provide any direct evidence for this triggering scenario.

The overall picture of W5 is of two concurrent episodes of massive-star formation that have lead to adjacent blown-out bubbles. Despite the added external pressure along the central ridge, it is relatively deficient in both star formation activity and dense gas, perhaps because of heating by the strong ionizing radiation field. The lack of star formation along that central ridge implies that much of the gas was squeezed and heated, but it was not crushed into gravitationally unstable fragments. While some star formation may have been triggered in W5, there is strong evidence for pre-existing star formation being at least a comparable, if not the dominant, mechanism of star formation in the complex.

2.7 Outflow systems beyond W5

Fifteen outflows were detected at velocities inconsistent with the local W5 cloud velocities. Of these, 8 are consistent with Perseus arm velocities ($v_{LSR} > -55$ km s^{-1}) and could be associated with different clouds within the same spiral arm. The other 7 have central velocities $v_{LSR} < -55$ km s^{-1} and are associated with the outer arm identified in previous surveys (e.g. Digel et al., 1996). The properties of these outflows are given in Tables 2.5 and 2.6; the distances listed are kinematic distances assuming $R_0 = 8.4$ kpc and $v_0 = 254$ km s^{-1} (Reid et al., 2009).

Of these outflows, all but one are within $2'$ of an IRAS point source. Outflow 54 is the most distant in our survey at a kinematic distance $d = 7.5$ kpc ($v_{lsr} = -75.6$ km s^{-1}) and galactocentric distance $D_G = 14.7$ kpc. It has no known associations in the literature.

Outflows 41 - 44 are associated with a cloud at $v_{LSR} \sim -62$ km s^{-1} known in the literature as LDN 1375 and associated with IRAS 02413+6037. Outflows 53 and 55 are at a similar velocity and associated with IRAS 02598+6008 and IRAS 02425+6000 respectively. All of these sources lie roughly on the periphery of the W5 complex.

Outflows 45 - 52 are associated with a string of IRAS sources and HII regions to the north of W5 and have velocities in the range $-55 < v_{LSR} < -45$. They therefore could be in the Perseus arm but are clearly unassociated with the W5 complex. Outflows 45 and 46 are associated with IRAS 02435+6144 and they may also be associated with the Sharpless HII region Sh 2-194. Outflows 47 and 48 are associated with IRAS 02461+6147, also known as AFGL 5085. Outflows 49 and 50 are nearby but not necessarily associated with IRAS 02475+6156, and may be associated with Sh 2-196. Outflows 51 and 52 are associated with IRAS 02541+6208.

2.8 Conclusions

We have identified 40 molecular outflow candidates in the W5 star forming region and an additional 15 outflows spatially coincident but located in the outer arm of the Galaxy.

- The majority of the CO clouds in the W5 complex are forming stars. Star formation is not limited to cloud edges around the HII region. Because star formation activity is observed outside of the region of influence of the W5 O-stars, it is apparent that direct triggering by massive star feedback is not responsible for all of the star formation in W5.

- The W5 complex is seen nearly face-on as evidenced by a strict upper limit on the CO column through the center of the HII-region bubbles. It is therefore an excellent region to study massive star feedback and revealed and triggered star formation.

- Outflows contribute negligibly to the turbulent energy of molecular clouds in the W5 complex. This result is unsurprising near an HII region, but supports the idea that massive star forming regions are qualitatively different from low-mass star-forming regions in which the observed turbulence could be driven by outflow feedback. Even in regions far separated

from the O-stars, there is more turbulence and less energy injection from outflows than in, e.g., Perseus.

- Despite detecting a significant number of powerful outflows, the total outflowing mass detected in this survey ($\sim$ 1.5 $M_{\odot}$ without optical depth correction, perhaps $10 - 20$ $M_{\odot}$ when optical depth is considered) was somewhat smaller than in Perseus, a low to intermediate mass star forming region with $\sim 1/6$ the molecular mass of W5.

- The low mass measured may be partly because the CO 3-2 line is sub-thermally excited in outflows. Therefore, while CO 3-2 is an excellent tracer of outflows for detection, it does not serve as a 'calorimeter' in the same capacity as CO 1-0.

- Even considering excitation and optical depth corrections, it is likely that the mass of outflows in W5 is less than would be expected from a simple extrapolation from Perseus based on cloud mass. CO is likely to be photodissociated in the outflows when they reach the HII region, accounting for the deficiency around the HII region edges. However, in areas unaffected by the W5 O-stars such as W5NW, the deficiency may be because the greater turbulence in the W5 clouds suppresses star formation or hides outflows.

- Velocity gradients across the tails of many cometary clouds have been observed, hinting at their geometry and confirming that the outflows seen from their heads must be generated by protostars within.

- Outflows have been detected in the Outer Arm at galactocentric distances $\gtrsim$ 12 kpc. These represent some of the highest galactocentric distance star forming regions discovered to date.

Table 2.2: CO 3-2 Outflow Measured Properties

Outflow Number	Latitude	Longitude	Ellipse Major $''$	Ellipse Minor $''$	Ellipse PA $^\circ$	Velocity center (km s^{-1})	Velocity min (km s^{-1})	max (km s^{-1})	$\int T_A^* dv$ (K km s^{-1})	Bipolar? [a]
1b	136.4437	1.2622	60	27	342	-36.1	-47.6	-40.3	1.0	yc
1r	136.4674	1.2705	49	24	346	-36.1	-31.9	-23.4	1.5	yc
2b	136.4899	1.1904	30	23	299	-35.7	-48.0	-39.7	0.7	yc
2r	136.4743	1.2042	31	28	332	-35.7	-31.7	-23.0	1.3	yc
3	136.475	1.2548	35	25	332	-31.8	-31.8	-26.8	1.3	n
4b	136.5038	1.2623	26	22	35	-36.2	-44.1	-40.1	0.8	yu
4r	136.5109	1.2751	25	22	332	-36.2	-32.4	-28.6	0.9	yu
5r	136.5126	1.2453	24	22	10	-35.3	-31.4	-28.8	0.8	yu
5b	136.5236	1.2524	39	22	3	-35.3	-45.0	-39.2	1.4	yu
6b	136.532	1.228	28	25	332	-35.3	-44.8	-40.0	0.4	yc
6r	136.5327	1.2333	28	20	318	-35.3	-30.6	-24.0	1.0	yc
7b	136.5453	1.2318	24	19	332	-34.9	-47.5	-39.9	1.7	yc
7r	136.5506	1.2383	27	23	314	-34.9	-29.9	-22.7	1.3	yc
8b	136.5799	1.2755	18	14	332	-34.5	-41.5	-39.3	0.6	yc
8r	136.581	1.2601	34	30	332	-34.5	-29.6	-23.9	1.4	yc
9b	136.67	1.2123	30	27	332	-35.0	-44.5	-38.5	1.4	yc
9r	136.6766	1.2059	40	31	332	-35.0	-31.6	-26.7	0.3	yc
10b	136.7172	0.7859	39	24	353	-42.8	-52.6	-47.5	3.3	yc
10r	136.7271	0.7797	31	26	332	-42.8	-38.1	-33.1	4.1	yc
11b	136.8195	1.082	25	24	331	-34.2	-40.7	-37.0	3.1	yc
11r	136.8173	1.0799	24	22	331	-34.2	-31.4	-20.4	1.5	yc
12b	136.8414	1.1512	30	26	332	-40.4	-53.3	-46.2	1.5	yc
12r	136.8479	1.1517	27	25	332	-40.4	-34.6	-30.1	0.9	yc
13	136.8461	0.8426	28	27	332	-31.0	-31.0	-23.5	1.0	n
14	136.8591	1.176	24	23	332	-47.1	-54.5	-47.1	0.8	n
15	136.9443	1.0841	28	18	348	-45.0	-55.0	-45.0	3.1	n
16b	137.3929	0.5977	23	18	333	-40.7	-47.0	-42.6	0.7	yu
16r	137.3981	0.6121	22	19	357	-40.7	-38.7	-35.2	1.9	yu
17b	137.4084	0.6762	20	18	293	-40.3	-57.9	-43.0	2.3	yc
17r	137.412	0.6775	20	18	308	-40.3	-37.6	-30.4	1.1	yc
18b	137.4925	0.6289	16	15	333	-35.5	-39.2	-37.6	1.1	yc
18r	137.4908	0.6292	18	17	307	-35.5	-33.4	-31.0	2.0	yc
19b	137.4815	0.6409	20	17	1	-36.0	-41.9	-38.9	1.3	yc
19r	137.4798	0.6404	20	16	301	-36.0	-33.1	-25.9	0.7	yc
20r	137.5368	1.2792	24	21	332	-37.4	-33.0	-22.5	5.2	yc
20b	137.539	1.279	27	23	17	-37.4	-52.0	-41.8	3.4	yc
21b	137.6152	1.3543	31	28	322	-39.5	-52.0	-43.7	4.5	yc
21r	137.6169	1.3585	31	18	4	-39.5	-35.2	-30.0	1.2	yc
22	137.6213	1.506	27	21	293	-40.3	-46.0	-40.3	2.1	n
23b	137.6389	1.5251	21	14	331	-38.5	-42.5	-40.5	1.6	yc
23r	137.6449	1.5194	19	12	331	-38.5	-36.5	-32.0	1.9	yc
24r	137.7094	1.4824	20	20	331	-38.2	-33.8	-25.4	4.2	yc
24b	137.7146	1.4809	25	19	292	-38.2	-50.0	-42.7	4.4	yc
25b	138.1398	1.6858	39	26	282	-38.8	-49.5	-43.2	0.6	yc

Continued on next page

Outflow Number	Latitude	Longitude	Ellipse Major $''$	Ellipse Minor $''$	Ellipse PA $^\circ$	Velocity center (km s^{-1})	Velocity min (km s^{-1})	max (km s^{-1})	$\int T_A^* dv$ (K km s^{-1})	Bipolar? [a]
25r	138.142	1.6884	43	35	11	-38.8	-34.3	-27.5	1.7	yc
26b	138.2913	1.5538	29	29	355	-38.7	-52.0	-47.4	1.2	yc
26r	138.2966	1.5564	28	28	330	-38.7	-30.0	-20.0	4.2	yc
27	138.3017	1.5689	26	25	330	-30.0	-30.0	-22.0	1.8	n
28	138.3042	1.5437	20	19	330	-43.3	-46.1	-43.3	1.4	n
29	138.3053	1.5537	22	20	330	-45.3	-51.6	-45.3	2.5	n
30	138.3115	1.5443	26	26	330	-33.0	-33.0	-29.2	1.2	n
31	138.3184	1.5566	26	25	330	-44.4	-49.1	-44.4	1.1	n
32	138.3213	1.5658	27	27	330	-31.7	-31.7	-27.0	1.4	n
33b	138.3618	1.5073	28	26	330	-39.4	-49.5	-44.0	1.3	yc
33r	138.3642	1.4959	29	21	330	-39.4	-34.7	-25.8	2.0	yc
34r	138.4779	1.6137	22	21	330	-36.9	-33.1	-29.1	0.5	yc
34b	138.4768	1.6142	21	20	330	-36.9	-43.6	-40.6	0.8	yc
35r	138.4998	1.6496	22	20	4	-37.5	-31.3	-24.1	1.4	yc
35b	138.5021	1.6458	23	21	330	-37.5	-49.5	-43.6	1.3	yc
36b	138.5034	1.6654	35	26	5	-37.5	-50.4	-42.3	1.2	yc
36r	138.5061	1.6576	22	21	330	-37.5	-32.6	-26.7	1.4	yc
37r	138.5208	1.6618	27	22	330	-38.5	-33.5	-31.4	0.6	yc
37b	138.5241	1.6667	23	23	18	-38.5	-47.0	-43.6	0.6	yc
38b	137.4983	0.6062	16	15	333	-36.1	-39.2	-38.5	0.8	yc
38r	137.4977	0.6055	15	14	307	-36.1	-33.7	-32.5	0.5	yc
39b	138.1506	0.7724	23	16	321	-38.8	-45.3	-41.0	2.0	yc
39r	138.1591	0.7713	17	13	304	-38.8	-36.6	-34.7	0.7	yc
40	138.1356	0.7634	22	18	4	-36.0	-36.0	-27.6	2.2	n

Measured properties of the outflows.

[a] Is the outflow part of a bipolar pair? yc = yes, confident; yu = yes, uncertain; n = no

Table 2.3: CO 3-2 Outflow Derived Properties

Outflow Number	Mass ($M_\odot$)	Momentum ($M_\odot$ km s^{-1})	Energy (10^{42} ergs)	Dynamical Age (10^4 years)	Momentum Flux 10^{-6} $M_\odot$ km s^{-1} yr^{-1}
1b	0.034	0.26	21.1	7.0	7.2
1r	0.04	0.24	17.3	7.0	7.2
2b	0.011	0.07	4.9	5.4	4.4
2r	0.025	0.17	13.0	5.4	4.4
3	0.025	0.12	5.8	-	-
4b	0.01	0.06	4.0	7.2	1.5
4r	0.011	0.04	1.8	7.2	1.5
5r	0.01	0.04	2.0	4.5	4.0
5b	0.025	0.14	8.0	4.5	4.0
6b	0.007	0.04	3.0	1.7	8.1
6r	0.013	0.09	6.8	1.7	8.1
7b	0.017	0.13	10.5	2.4	10.9
7r	0.018	0.13	9.7	2.4	10.9
8b	0.003	0.02	0.9	4.9	4.5
8r	0.032	0.2	13.2	4.9	4.5
9b	0.025	0.13	7.2	3.9	4.2
9r	0.009	0.04	1.8	3.9	4.2
10b	0.068	0.41	25.7	3.9	22.0
10r	0.074	0.45	28.0	3.9	22.0
11b	0.042	0.17	7.2	0.7	35.3
11r	0.017	0.09	5.9	0.7	35.3
12b	0.026	0.14	8.7	1.8	15.2
12r	0.014	0.13	12.7	1.8	15.2
13	0.016	0.1	5.8	-	-
14	0.01	0.06	4.1	-	-
15	0.036	0.24	17.3	-	-
16b	0.006	0.03	1.2	11.1	0.7
16r	0.018	0.05	1.3	11.1	0.7
17b	0.019	0.12	9.4	1.4	10.6
17r	0.009	0.03	0.7	1.4	10.6
18b	0.006	0.02	0.5	1.4	4.0
18r	0.013	0.04	1.0	1.4	4.0
19b	0.011	0.05	2.4	0.7	9.6
19r	0.005	0.01	0.2	0.7	9.6
20r	0.059	0.5	46.3	0.5	156.0
20b	0.047	0.33	26.6	0.5	156.0
21b	0.086	0.58	41.4	1.7	39.1
21r	0.014	0.08	4.3	1.7	39.1
22	0.027	0.1	4.3	-	-
23b	0.011	0.03	0.9	4.5	1.3
23r	0.01	0.03	1.0	4.5	1.3
24r	0.037	0.3	26.1	1.7	34.1
24b	0.047	0.28	18.3	1.7	34.1

Continued on next page

Outflow Number	Mass ($M_\odot$)	Momentum ($M_\odot$ km s^{-1})	Energy (10^{42} ergs)	Dynamical Age (10^4 years)	Momentum Flux 10^{-6} $M_\odot$ km s^{-1} yr^{-1}
25b	0.014	0.09	6.8	1.0	42.8
25r	0.056	0.35	23.0	1.0	42.8
26b	0.023	0.24	26.1	1.1	98.3
26r	0.072	0.85	106.0	1.1	98.3
27	0.026	0.09	4.5	-	-
28	0.012	0.07	4.6	-	-
29	0.024	0.06	2.1	-	-
30	0.018	0.12	8.0	-	-
31	0.016	0.03	0.7	-	-
32	0.023	0.18	14.5	-	-
33b	0.022	0.14	10.1	3.0	11.4
33r	0.026	0.2	16.1	3.0	11.4
34r	0.005	0.03	1.7	0.7	8.4
34b	0.007	0.03	1.2	0.7	8.4
35r	0.013	0.12	11.6	1.3	18.7
35b	0.014	0.12	11.0	1.3	18.7
36b	0.025	0.19	15.8	2.7	10.7
36r	0.014	0.1	6.8	2.7	10.7
37r	0.008	0.04	1.6	2.1	4.3
37b	0.007	0.06	4.2	2.1	4.3
38b	0.005	0.01	0.4	0.9	2.3
38r	0.002	0.01	0.1	0.9	2.3
39b	0.017	0.07	2.8	7.5	1.0
39r	0.004	0.01	0.3	7.5	1.0
40	0.019	0.08	3.5	-	-

Derived properties of the outflows in the optically thin limit.

Typical optical depth corrections for ^{12}CO 3-2 are in the range 7-14 (Curtis et al., 2010).

The correction for velocity confusion is $\gtrsim 2$ but poorly constrained (Arce et al., 2010).

Finally, an excitation correction in the range 1-20 is likely required as described in the Appendix.

The mass and momentum values can be multiplied by these factors to acquire the corrected values.

The energy is weighted more heavily towards high-velocity, low-optical-depth gas, so the correction factor is likely to be lower.

Table 2.4. Totals of outflow properties

BGPS source	1.1mm mass $M_\odot$	Intensity (K km s^{-1})	Outflow Column (cm^{-2})	Outflow Mass ($M_\odot$)	Momentum ($M_\odot$ km s^{-1})	Energy (ergs)	
G136.456+01.268	19.81	1.657	5.45×10^{18}	0.0507	0.357	2.76×10^{43}	
G136.474+01.268	15.06	0.832	2.74×10^{18}	0.0162	0.115	8.9×10^{42}	
G136.500+01.258	38.16	2.166	7.11×10^{18}	0.03802	0.2055	1.188×10^{43}	
G136.512+01.194	85.65	1.512	4.97×10^{18}	0.02772	0.1536	9.44×10^{42}	
G136.536+01.232	88.86	2.744	9.03×10^{18}	0.04309	0.3245	2.575×10^{43}	
G136.671+01.210	71.31	2.667	8.78×10^{18}	0.0589	0.3405	2.088×10^{43}	
G136.719+00.782	81.3	4.28	1.407×10^{19}	0.0661	0.36	2.142×10^{43}	
G136.828+01.064	224.1	2.51	8.25×10^{18}	0.0361	0.222	1.569×10^{43}	
G136.842+00.838	21.84	0.813	2.67×10^{18}	0.0138	0.0851	5.67×10^{42}	
G136.846+01.168	67.96	2.05	6.74×10^{18}	0.0377	0.265	2.09×10^{43}	Totals
G136.849+01.150	133.2	1.34	4.4×10^{18}	0.01831	0.1516	1.322×10^{43}	
G136.948+01.092	202.8	1.45	4.76×10^{18}	0.0218	0.139	9.71×10^{42}	
G137.394+00.610	26.68	5.38	1.768×10^{19}	0.0998	0.783	6.77×10^{43}	
G137.409+00.674	41.22	1.06	3.48×10^{18}	0.0205	0.112	6.45×10^{42}	
G137.479+00.640	107.5	1.839	6.047×10^{18}	0.02244	0.1463	1.1647×10^{43}	
G137.538+01.278	87.68	0.545	1.793×10^{18}	0.008201	0.04483	2.473×10^{42}	
G137.617+01.350	128.2	1.358	4.466×10^{18}	0.01642	0.0656	2.989×10^{42}	
G137.632+01.508	48.13	2.29	7.52×10^{18}	0.025	0.143	9.06×10^{42}	
G137.665+01.526	65.13	3.16	1.04×10^{19}	0.03374	0.2716	2.321×10^{43}	
G137.707+01.490	71.2	1.763	5.78×10^{18}	0.0481	0.364	3.04×10^{43}	
G138.144+01.684	201.7	3.63	1.193×10^{19}	0.0599	0.704	8.64×10^{43}	
G138.295+01.556	824.4	6.957	2.289×10^{19}	0.09247	0.6825	5.3999×10^{43}	
G138.502+01.646	361.7	4.899	1.613×10^{19}	0.07083	1.4379	3.47758×10^{44}	

of outflow mass, momentum, and energy.

Table 2.5. Outer Arm CO 3-2 Outflows - Measured Properties

Outflow Number	Latitude	Longitude	Ellipse Major $''$	Ellipse Minor $''$	Ellipse PA $^\circ$	Kinematic Distance (pc)	R_G[a] (pc)	Velocity center (km s^{-1})	Velocity min	max	$\int T_A^* dv$ (K km s^{-1})
41r	136.364	0.9606	25	18	2	5510	13000	-61.8	-59.2	-56.5	0.5
41b	136.3634	0.9568	23	17	353	5510	13000	-61.8	-71.6	-64.3	3.0
42r	136.3522	0.9786	20	14	2	5500	12900	-62.1	-59.8	-57.6	0.6
42b	136.3548	0.9798	20	19	332	5500	12900	-62.1	-67.8	-64.4	0.5
43r	136.3495	0.9612	17	15	63	5510	13000	-61.8	-59.0	-56.1	0.8
43b	136.353	0.9621	12	12	333	5510	13000	-61.8	-66.3	-64.6	1.0
44r	136.3554	0.9576	13	13	23	5500	12900	-61.8	-59.0	-55.4	2.1
44b	136.3545	0.9567	14	14	333	5500	12900	-61.8	-68.0	-64.5	2.0
45r	136.1219	2.0816	34	25	297	3750	11400	-46.5	-43.1	-40.5	0.6
45b	136.1233	2.0803	35	25	306	3750	11400	-46.5	-57.3	-50.0	1.9
46	136.1166	2.0983	26	25	332	3790	11400	-50.2	-52.6	-50.2	0.5
47b	136.3857	2.2687	34	27	332	3220	11000	-42.0	-55.0	-46.7	3.5
47r	136.3861	2.267	35	23	304	3220	11000	-42.0	-37.3	-25.1	5.0
48b	136.374	2.2628	29	21	332	3250	11000	-43.2	-51.4	-47.0	1.5
48r	136.3736	2.2615	29	22	332	3250	11000	-43.2	-39.5	-22.2	8.9
49r	136.4663	2.4678	29	23	290	3610	11300	-45.7	-42.2	-33.0	2.2
49b	136.4661	2.4693	31	23	292	3610	11300	-45.7	-52.2	-49.1	0.9
50b	136.5087	2.5108	31	25	332	3380	11100	-43.5	-48.5	-46.5	0.8
50r	136.5118	2.5083	28	23	10	3380	11100	-43.5	-40.6	-37.5	1.0
51b	137.058	2.9858	28	23	293	4350	11900	-51.8	-55.5	-53.0	0.8
51r	137.0567	2.9864	34	25	8	4350	11900	-51.8	-50.6	-40.9	3.5
52r	137.0662	2.9999	37	26	43	4390	12000	-52.2	-49.1	-41.0	7.8
52b	137.0683	3.0013	38	29	15	4390	12000	-52.2	-65.8	-55.2	4.1
53b	138.6143	1.5611	26	26	330	5450	13000	-59.7	-71.1	-61.7	5.5

Table 2.5 (cont'd)

Outflow Number	Latitude	Longitude	Ellipse Major $''$	Ellipse Minor $''$	Ellipse PA $^\circ$	Kinematic Distance (pc)	R_G[a] (pc)	Velocity center (km s^{-1})	Velocity min	max	$\int T_A^* dv$ (K km s^{-1})
53r	138.6158	1.563	25	23	330	5450	13000	-59.7	-57.6	-54.5	1.3
54r	136.382	0.8392	29	20	343	7480	14700	-75.6	-73.2	-68.9	2.6
54b	136.3824	0.838	20	17	332	7480	14700	-75.6	-83.1	-77.9	2.0
55b	136.7623	0.4548	27	16	343	5230	12700	-60.9	-65.2	-62.7	5.4
55r	136.7579	0.4522	24	18	343	5230	12700	-60.9	-59.0	-53.2	6.0

[a]Galactocentric Radius

Table 2.6. Outer Arm CO 3-2 Outflows - Derived Properties

Outflow Number	Mass ($M_\odot$)	Momentum ($M_\odot$ km s^{-1})	Energy (10^{42} ergs)	Dynamical Age (10^4 years)	Momentum Flux 10^{-6} $M_\odot$ km s^{-1} yr^{-1}
41r	0.037	0.11	3.5	3.6	30.2
41b	0.196	0.96	54.6	3.6	30.2
42r	0.029	0.06	1.3	4.3	3.9
42b	0.03	0.11	3.9	4.3	3.9
43r	0.033	0.13	5.1	7.3	2.9
43b	0.024	0.08	2.8	7.3	2.9
44r	0.062	0.21	7.9	1.8	27.7
44b	0.067	0.28	12.6	1.8	27.7
45r	0.037	0.18	8.6	1.2	62.3
45b	0.126	0.55	28.3	1.2	62.3
46	0.028	0.1	3.7	-	-
47b	0.187	1.32	101.0	0.6	553.0
47r	0.232	1.84	164.0	0.6	553.0
48b	0.054	0.33	20.8	0.4	754.0
48r	0.341	2.4	229.0	0.4	754.0
49r	0.106	0.77	62.7	1.4	71.1
49b	0.047	0.22	10.8	1.4	71.1
50b	0.037	0.14	5.5	3.8	7.4
50r	0.038	0.14	5.5	3.8	7.4
51b	0.058	0.13	3.0	1.0	152.0
51r	0.303	1.33	72.7	1.0	152.0
52r	0.829	4.3	250.0	1.4	479.0
52b	0.472	2.5	150.0	1.4	479.0
53b	0.626	3.16	194.0	4.7	73.2

Table 2.6 (cont'd)

Outflow Number	Mass ($M_\odot$)	Momentum ($M_\odot$ km s^{-1})	Energy (10^{42} ergs)	Dynamical Age (10^4 years)	Momentum Flux 10^{-6} $M_\odot$ km s^{-1} yr^{-1}
53r	0.124	0.31	8.5	4.7	73.2
54r	0.461	1.24	37.5	1.8	135.0
54b	0.212	1.14	64.0	1.8	135.0
55b	0.411	1.66	68.0	7.5	28.3
55r	0.404	0.47	6.6	7.5	28.3

2.9 W5 Appendix: Optically Thin, LTE dipole molecule

While many authors have solved the problem of converting CO 1-0 beam temperatures to H_2 column densities (Garden et al., 1991; Bourke et al., 1997; Cabrit & Bertout, 1990; Lada & Fich, 1996), there are no examples in the literature of a full derivation of the LTE, optically thin CO-to-H_2 conversion process for higher rotational states. We present the full derivation here, and quantify the systematic errors generated by various assumptions.

We begin with the assumption of an optically thin cloud such that the radiative transfer equation (Wilson et al., 2009, eqn 1.9) simplifies to

$$\frac{dI_\nu}{\mathrm{d}s} = -\kappa_\nu I_\nu \tag{2.3}$$

The absorption and stimulated emission terms yield

$$\kappa_\nu = \frac{h\nu_{ul}B_{ul}n_u}{c}\varphi(\nu) - \frac{h\nu_{ul}B_{lu}n_l}{c}\varphi(\nu) \tag{2.4}$$

where $\varphi(\nu)$ is the line shape function ($\int \varphi(\nu)\mathrm{d}\nu \equiv 1$), n is the density in the given state, ν is the frequency of the transition, B is the Einstein B coefficient, and h is Planck's constant.

By assuming LTE (the Boltzmann distribution) and using Kirchoff's Law and the definition of the Einstein A and B values, we can derive a more useful version of this equation

$$\kappa_\nu = \frac{c^2}{8\pi\nu_{ul}^2}n_u A_{ul}\left[\exp\left(\frac{h\nu_{ul}}{k_B T_{ex}}\right) - 1\right]\varphi(\nu) \tag{2.5}$$

where k_B is Boltzmann's constant.

The observable T_B can be related to the optical depth, which is given by

$$\int \tau_\nu \mathrm{d}\nu = \frac{c^2}{8\pi\nu_{ul}^2}A_{ul}\left[\exp\left(\frac{h\nu_{ul}}{k_B T_{ex}}\right) - 1\right]\int \varphi(\nu)\mathrm{d}\nu \int n_u \mathrm{d}s \tag{2.6}$$

Rearranging and converting from density to column ($\int n\mathrm{d}s = N$) gives an equation for the column density of the molecule in the upper energy state of the transition:

$$N_u = \frac{8\pi\nu_{ul}^2}{c^2 A_{ul}}\left[\exp\left(\frac{h\nu_{ul}}{k_B T_{ex}}\right) - 1\right]^{-1}\int \tau_\nu \mathrm{d}\nu \tag{2.7}$$

In order to relate the brightness temperature to the optical depth, at CO transition frequencies the full blackbody formula must be used and the CMB must also be taken into account. Wilson et al. (2009) equation 15.29

$$T_B(\nu) = \frac{h\nu}{k_B}\left(\left[e^{h\nu/k_BT_{ex}}-1\right]^{-1} - \left[e^{h\nu/k_BT_{CMB}}-1\right]^{-1}\right)(1-e^{-\tau_\nu}) \tag{2.8}$$

is rearranged to solve for τ_ν:

$$\tau_\nu = -\ln\left[1 - \frac{k_BT_B}{h\nu}\left(\left[e^{h\nu/k_BT_{ex}}-1\right]^{-1} - \left[e^{h\nu/k_BT_{CMB}}-1\right]^{-1}\right)^{-1}\right] \tag{2.9}$$

We convert from frequency to velocity units with $\mathrm{d}\nu = \nu/c\mathrm{d}v$, and plug Equation 2.9 into Equation 2.7 to get

$$N_u = \frac{8\pi\nu_{ul}^3}{c^3A_{ul}}\left[\exp\left(\frac{h\nu_{ul}}{k_BT_{ex}}\right)-1\right]^{-1}\int -\ln\left[1 - \frac{k_BT_B}{h\nu_{ul}}\left(\left[e^{h\nu_{ul}/k_BT_{ex}}-1\right]^{-1} - \left[e^{h\nu_{ul}/k_BT_{CMB}}-1\right]^{-1}\right)^{-1}\right]\mathrm{d}v \tag{2.10}$$

which is the full LTE upper-level column density with no approximations applied.

The first term of the Taylor expansion is appropriate for $\tau << 1$ ($\ln[1+x] \approx x - \frac{x^2}{2} + \frac{x^3}{3}\ldots$)

$$N_u = \frac{8\pi\nu_{ul}^3}{c^3A_{ul}}\left[\exp\left(\frac{h\nu_{ul}}{k_BT_{ex}}\right)-1\right]^{-1}\int \frac{k_BT_B}{h\nu_{ul}}\left(\left[e^{h\nu_{ul}/k_BT_{ex}}-1\right]^{-1} - \left[e^{h\nu_{ul}/k_BT_{CMB}}-1\right]^{-1}\right)^{-1}\mathrm{d}v \tag{2.11}$$

which simplifies to

$$N_u = \frac{8\pi\nu_{ul}^2k_B}{c^3A_{ul}h}\frac{e^{h\nu_{ul}/k_BT_{CMB}}-1}{e^{h\nu_{ul}/k_BT_{CMB}}-e^{h\nu_{ul}/k_BT_{ex}}}\int T_B\mathrm{d}v \tag{2.12}$$

This can be converted to use μ_e (0.1222 for ^{12}CO; Muenter, 1975), the electric dipole moment of the molecule, instead of A_{ul}, using Wilson et al. (2009) equation 15.20 $\left((A_{ul} = (64\pi^4)/(3hc^3))\,\nu^3\mu_e^2\right)$:

$$N_u = \frac{3}{8\pi^3\mu_e^2}\frac{k_B}{\nu_{ul}}\frac{2J_u+1}{J_u}\frac{e^{h\nu_{ul}/k_BT_{cmb}}-1}{e^{h\nu_{ul}/k_BT_{CMB}}-e^{h\nu_{ul}/k_BT_{ex}}}\int T_B\mathrm{d}v \tag{2.13}$$

The total column can be derived from the column in the upper state using the partition function and the Boltzmann distribution

$$n_{tot} = \sum_{J=0}^{\infty} n_J = n_0\sum_{J=0}^{\infty}(2J+1)\exp\left(-\frac{J(J+1)B_eh}{k_BT_{ex}}\right) \tag{2.14}$$

This equation is frequently approximated using an integral (e.g. Cabrit & Bertout, 1990), but a more accurate numerical solution using up to thousands of rotational states is easily computed

$$n_J = \left[\sum_{j=0}^{j=j_{max}} (2j+1)\exp\left(-\frac{j(j+1)B_e h}{k_B T_{ex}}\right)\right]^{-1} (2J+1)\exp\left(-\frac{J(J+1)B_e h}{k_B T_{ex}}\right) \quad (2.15)$$

The effects of using the approximation and the full numerical solution are shown in figure 2.27.

The CO 3-2 transition is also less likely to be in LTE than the 1-0 transition. The critical density ($n_{cr} \equiv A_{ul}/C_{ul}$) of ^{12}CO 3-2 is 27 times higher than that for 1-0. We have run RADEX (van der Tak et al., 2007a) LVG models of CO to examine the impact of sub-thermal excitation on column derivation. The results of the RADEX models are shown in Figure 2.28. They illustrate that, while it is quite safe to assume the CO 1-0 transition is in LTE in most circumstances, a similar assumption is probably invalid for the CO 3-2 transition in typical molecular cloud environments.

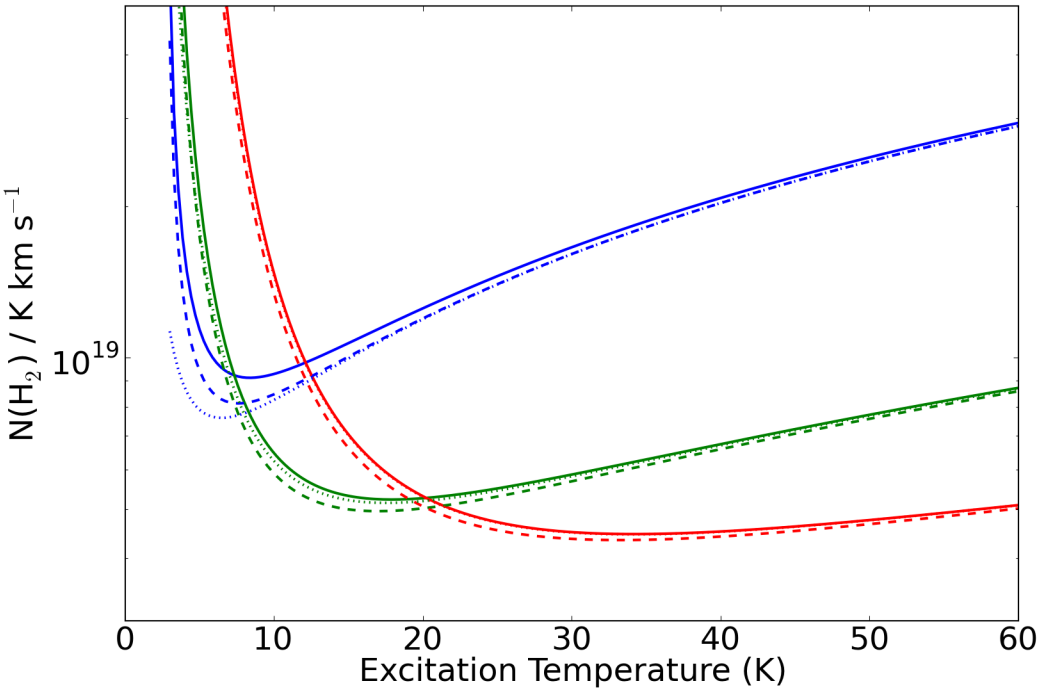

Figure 2.27 The LTE, optically thin conversion factor from T_B (K km s^{-1}) to N(H_2) (cm^{-2}) assuming $X_{^{12}CO} = 10^{-4}$ plotted against T_{ex}. The dashed line shows the effect of using the integral approximation of the partition function (e.g. Cabrit & Bertout, 1990). It is a better approximation away from the critical point, and is a better approximation for higher transitions. The dotted line shows the effects of removing the CMB term from Equation 2.8; the CMB populates the lowest two excited states, but contributes nearly nothing to the $J = 3$ state. Top (blue): J=1-0, Middle (green): J=2-1, Bottom (red): J=3-2.

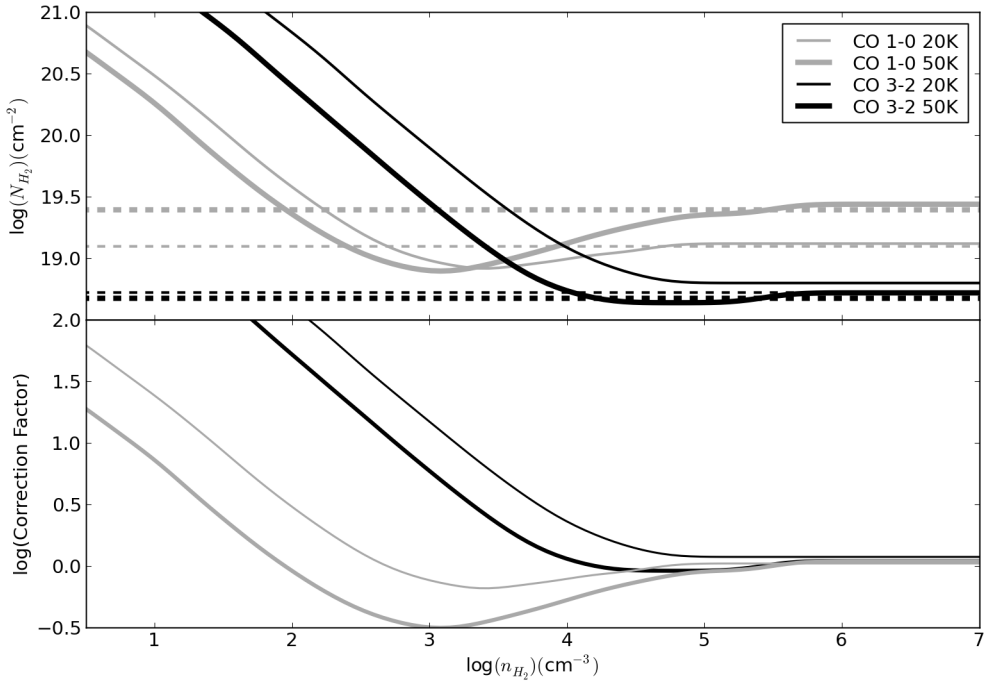

Figure 2.28 *Top*: The derived N(H_2) as a function of n_{H_2} for $T_B = 1$ K. The dashed lines represent the LTE-derived $N(H_2)/T_B$ factor, which has no density dependence and, for CO 3-2, only a weak dependence on temperature. We assume an abundance of ^{12}CO relative to H_2 $X_{CO} = 10^{-4}$. *Bottom*: The correction factor (N$(H_2)_{RADEX}$ / N$(H_2)_{LTE}$) as a function of n_{H_2}. For $T_K = 20$ K, the "correction factor" at 10^3 cm^{-3} (typical GMC mean volume densities) is ~ 15, while at 10^4 cm^{-3} (closer to n_{crit} but perhaps substantially higher than GMC densities) it becomes negligible. The correction factor is also systematically lower for a higher gas kinetic temperature. For some densities, the "correction factor" dips below 1, particularly for CO 1-0. This effect is from a slight population inversion due to fast spontaneous decay rates from the higher levels and has been noted before (e.g. Goldsmith, 1972).

Chapter 3

The Bolocam Galactic Plane Survey

3.1 Preface

The Bolocam Galactic Plane Survey consumed the bulk of my time on this thesis. A great deal of that time was dedicated to development of the BGPS Pipeline (Section 7.2). That software is described in Aguirre et al. (2011) and this chapter.

3.1.1 Version 1

The Bolocam Galactic Plane Survey (BGPS) Version 1 (v1.0) was released in 2009 and published in Aguirre et al. (2011) and Rosolowsky et al. (2010). Aguirre et al. (2011) summarizes a great deal of the work on the BGPS pipeline, in particular the reduction strategy we implemented. However, since that paper was written in cooperation with James Aguirre, the text is not reproduced here and instead references to the paper are included within the description of v2.0 below.

3.2 Introduction

Surveys of the Galactic plane have great legacy value and open broad regions of discovery space, e.g. the infrared IRAS (Cao et al., 1997), MSX (Price et al., 2001), GLIMPSE (Churchwell et al., 2009), and MIPSGAL (Carey et al., 2009) surveys. Until the recent advent of hundred-bolometer millimeter arrays, blind surveys of large regions of the sky were impractical. However, instruments like Bolocam, AzTEC, MAMBO, SIMBA, SCUBA, and LABOCA have changed the

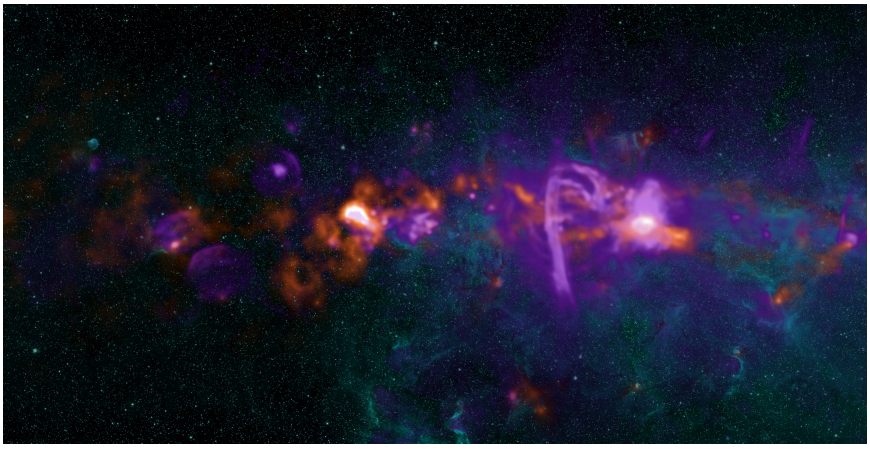

Figure 3.1 The 'cover figure' for the BGPS: The Galactic Center seen at 1.1 mm (orange), 20 cm (purple), and 8 μm.

field, and the Herschel Space Observatory has opened the Terahertz window with the Hi-Gal Galactic plane survey (Molinari et al., 2010). These Galactic plane surveys have lasting legacy value.

The ground-based millimeter surveys are well-suited to detecting compact, dense structures throughout the Galactic plane. Because of the low opacity of dust at millimeter wavelenths, the entire Galactic plane is optically thin, allowing for flux-limited studies of dust clumps.

The Herschel Space Observatory and the Hi-Gal survey have provided access to the peak of the dust spectral energy distribution at modest ($\sim 30''$) resolution. With these data becoming available, the need for long-wavelength data at comparable resolution remains important: long-wavelength data are essential for constraining the dust emissivity, one of the free parameters in spectral energy distribution (SED) fits. Shetty et al. (2009a,b) demonstrated the need for long-wavelength data to accurately determine both β, the dust emissivity spectral index, and temperature.

Millimeter-wave dust emission has the advantage of being relatively insensitive to temperature. When looking at cold gas, $T \lesssim 20$ K, all of the Herschel bands differ from a Rayleigh-Jeans temperature approximation. Longer wavelength observations are still affected by temperature assumptions but less severely. The 1.1 mm band is in many cases the longest wavelength unaffected by free-free emission, providing the least environmentally-biased view of optically thin dust emission and therefore total dust mass.

The millimeter/sub-millimeter regime has been the last decade of wavelength space to become available to astronomers. While optical and radio observations from the ground see through a transparent atmosphere, millimeter observations are plagued by a bright foreground that dominates the astrophysical signal by orders of magnitude. This signal must be removed in order to create maps of astrophysical emission.

Chapin et al. (2013) presented a summary of the techniques used to separate astrophysical and atmospheric signals in bolometric observations. The Bolocam observations reported in this paper were conducted with a fast-scanning strategy that places the 'fixed' astrophysical emission at a different sampling frequency than the varying foreground atmosphere. This approach is one of the most efficient and flexible and has been used predominantly over alternatives like a nodding

secondary in most recent large-scale observing campaigns (Aguirre et al., 2011; Schuller, 2012).

While fast-scanning provides some separation between astrophysical and atmospheric signal, the atmospheric signal is still predominant and must be excised. Most approaches to removing atmospheric signal will also remove astrophysical signal with an angular scale comparable to the detector array. In order to recover signal on these large angular scales, the most commonly used approach for bright Galactic signals is an iterative reconstruction process, in which a model of the astrophysical signal is subtracted from the observed timestream repeatedly. This process was first used on Bolocam data by Enoch et al. (2006b) and refined in Aguirre et al. (2011).

This paper presents v2.0 of the Bolocam Galactic Plane Survey (BGPS), with a complete data release available at `irsa.ipac.caltech.edu/data/BOLOCAM_GPS/`. In Paper I (Aguirre et al., 2011), the initial processing of the BGPS v1.0 was described in detail. It was noted in Section 5 of that paper that there was a discrepancy between our survey and previously published results. This discrepancy raised the possibility of a flux calibration error in the Version 1 (hereafter v1.0) results: we correct this error in this paper. In addition to resolving this discrepancy, we have made significant improvements to the data pipeline, measured important features of the pipeline including its angular transfer function, improved the pointing accuracy, and added new observations.

The BGPS v1.0 data has been public since 2009, and has been used extensively. It was used to examine the properties of maser sources (Pandian et al., 2012; Chen et al., 2012), outflow sources (Ioannidis & Froebrich, 2012), and high-mass star-forming regions (Reiter et al., 2011; Battersby et al., 2011; Dunham et al., 2011). It has served as the basis for studies of forming clusters (Alexander & Kobulnicky, 2012; Ginsburg et al., 2012) and intermediate-mass stars (Arvidsson et al., 2010). The BGPS and other surveys have served as finder charts for large-scale millimeter line studies of the Galactic plane (Schenck et al., 2011; Schlingman et al., 2011; Ginsburg et al., 2011a). There are also further upcoming studies of clump LSR velocities and distances based on this data (Shirley, 2013; Ellsworth-Bowers et al., 2013). These and many other studies demonstrate the need for, and benefits of, publicly available blind legacy surveys.

The paper is as follows: We resolve the flux calibration discrepancy in Section 3.3. In Section

6.3, we discuss new observations included in the v2.0 data. Section 3.5 describes changes to the data reduction process and new data products. Section 3.6 and Section 3.8 measure the angular transfer function of the BGPS v2.0 pipeline and properties of extracted sources respectively. The paper concludes with a brief discussion of some results and a summary.

3.3 Calibration

3.3.1 Why was there a multiplicative offset in the v1.0 data release?

In Aguirre et al. (2011), we reported that a 'correction factor' of about 1.5 on average was needed to bring our data into agreement with other 1 mm data sets. We discovered that the published v1.0 BGPS images have a different calibration reported in their FITS headers than was used in processing the data. The calibration used in the released data was borrowed from a previous observing run, during which a different bias voltage was used, and differed from the pipeline-derived calibration by a factor ≈ 1.5, completely explaining the discrepancy.

3.3.2 Comparing v1.0 and v2.0 calibration

We checked the data for consistency with the measured calibration offset. In order to compare flux densities in identical sources, we performed aperture photometry on the v2.0 data based on the locations of v1.0 sources using both the 'source masks' from Bolocat v1.0 (Rosolowsky et al., 2010) and circular apertures centered on the Bolocat v1.0 peaks. Source masks, also known as label masks, are images in which the value of a pixel is either 0 for no source or the catalog number of a source if there is a source associated with a pixel.

We measured the multiplicative offset between v1.0 and v2.0 by comparing these aperture-extracted fluxes. For each aperture size, we measured the best-fit line between the v1.0 and v2.0 data using a total least squares (TLS[1]) method weighted by the flux measurement errors as reported in the catalogs. The agreement with $S_{\rm v2.0} = 1.5\ S_{\rm v1.0}$, as expected based on Section 3.3.1 is generally

[1] `https://code.google.com/p/agpy/source/browse/trunk/agpy/fit_a_line.py`, see also `http://astroml.github.com/book_figures/chapter8/fig_total_least_squares.html`

within 10%, although the larger apertures show a slight excess with $S_{\rm v2.0} \approx$ (1.6-1.7) $S_{\rm v1.0}$, which is expected from the improved extended flux recovery in v2.0 (see Section 3.6). The v2.0/v1.0 flux ratio is weakly dependent on the source flux, with generally higher v2.0/v1.0 ratios for brighter sources.

3.3.3 Comparison to Other Surveys

In Section 5.5 of Aguirre et al. (2011), we compared the BGPS v1.0 data to other data sets from similar-wavelength observations. We repeat those comparisons here using the v2.0 data.

We compare to 3 data sets in the same $\sim$ 1 mm atmospheric window. Two data sets from MAMBO II, the Motte et al. (2007, M07) Cygnus X survey and the Rathborne et al. (2006, R06) IRDC survey, overlap with the BGPS. The SIMBA 1.3 mm survey of the $\ell = 44^\circ$ region is the largest survey in the 1 mm band that overlaps with ours (Matthews et al., 2009, M09).

The surveys we compare to have different angular transfer functions. In order to account for the difference, we allow for a large angular scale offset between the observations. We fit a line of the form $y = mx + b$ to the data, where x and y represent the pixel values gridded to $7.2''$ pixels. The b value allows for a local offset, i.e. a non-zero b value indicates a substantial difference in the angular transfer function. Since such an additive offset is unlikely to apply across the entire observed region, we also fit the offset for small sub-regions in the M07 and M09 data, focusing on DR21 and a region centered on G45.5+0.1 respectively.

The results of that comparison are displayed in Table 3.1, which includes the original comparison from Aguirre et al. (2011)[2] . BGPS v2.0 is in much better agreement with the other data sets than v1.0, but it retains a significant additive offset, particularly with respect to MAMBO. The additive offset is explained by a difference in the angular transfer function; the MAMBO observing strategy of fast position switching allows structures on the scale of the array to be preserved, while Bolocam's fast-scan strategy does not. The differing observing strategy explains why there is an

[2] In Aguirre et al. (2011), there was a minor error in the table: M07 and M09 were swapped. This has been corrected in Table 3.1.

Table 3.1. Flux comparison with R06, M07, and M09

Comparison Survey	Pixels > 3 MJy sr^{-1}		Pixels > 10 MJy sr^{-1}		Pixels > 20 MJy sr^{-1}	
BGPS v1.0	m	b	m	b	m	b
R06	1.39	−2.00	1.46	−2.79	1.53	−4.77
M07	1.51	4.13	1.44	13.78	1.36	27.45
M07DR21	1.36	28.03	1.31	37.91	1.25	49.44
M09	1.32	−0.22	1.25	4.94	1.21	9.88
M09a	1.50	−5.15	1.51	−4.82	1.53	−5.11
BGPS v2						
R06	1.05	3.67	1.02	5.03	1.00	7.05
M07	1.16	6.51	1.12	12.75	1.08	21.04
M07DR21	1.09	21.98	1.07	27.61	1.04	34.21
M09	0.73	1.33	0.69	6.75	0.66	13.45
M09a	0.96	−3.21	0.94	−0.69	0.89	2.91

The table values m and b are given for a linear fit of the form $y = mx + b$.
References: Rathborne et al. (2006, R06), Motte et al. (2007, M07), Matthews et al. (2009, M09).
M09a refers to the G45.5+0.1 region, and M07DR21 refers to the DR21 region

additive offset between Bolocam and MAMBO, but no such offset for SIMBA, which was used in a fast-scan mode similar to Bolocam. The varying backgrounds in separate regions account for some of the remaining multiplicative offset. When individual sub-regions are compared, the additive and multiplicative offsets more clearly separate into independent components, i.e. a line with an additive offset is a better fit to the data.

To enable a comparison of flux density between the surveys, we must account for the different spectral bandpasses of the instruments. The relative flux density measured between the instruments depends on the spectral index α_ν of the observed source; $\alpha_\nu = 2$ corresponds to a perfect black body on the Rayleigh-Jeans tail. In Table 3.2 we show the relative flux densities expected for Bolocam, MAMBO and SIMBA; they differ by at most 19% for spectral indices $\alpha_\nu < 5$. Bolocam flux densities are expected to be higher because it has a higher effective central frequency than either of the other instruments.

In Aguirre et al. (2011), we measured Bolocam/MAMBO and Bolocam/SIMBA ratios in the range $0.66 < R < 0.83$, indicating a clear disagreement between the surveys. With the v2.0 data, we measure ratios $0.97 < R_{SIMBA} < 1.08$ and $0.89 < R_{MAMBO} < 0.99$. These numbers still indicate that the BGPS is too faint by $\lesssim 20\%$ relative to the expectations laid out in Table 3.2, but with a systematic calibration error no better than 20% in each survey, the agreement is reasonable.

3.4 Expansion of the BGPS and Observations

Thirteen nights of additional data were acquired from December 15th, 2009 to January 1st, 2010. The target fields and areas covered are listed in Table 3.3 as boxes in Galactic latitude and longitude, with position angles to the Galactic plane indicated. The original observations are described in Section 2 of Aguirre et al. (2011).

The new target fields were selected from visual inspection of FCRAO OGS ^{12}CO integrated maps, Dame et al. (2001) ^{12}CO maps, and IRAS 100 μm maps. The fields were selected primarily to provide even spacing in RA in order to maximize observing efficiency, and were therefore not blindly selected.

Table 3.2. Relative flux expectation for Bolocam, MAMBO, and SIMBA given different input source spectral indices

α_ν	Bolocam/MAMBO	Bolocam/SIMBA
1.0	1.06274	1.06348
1.5	1.07926	1.08246
2.0	1.09746	1.10382
2.5	1.11448	1.12488
3.0	1.12877	1.14393
3.5	1.13962	1.1601
4.0	1.14685	1.17301
4.5	1.15057	1.18264
5.0	1.15108	1.18918

Response functions are computed using an atmospheric transmittance corresponding to 1 mm of precipitable water vapor

Table 3.3. Observations

Target	Longitude	Latitude	Longitude Size	Latitude Size	Position Angle
IRAS 22172	102.91	-0.64	1.67	1.07	0
l106	105.81	0.15	1.48	1.33	0
l111w	108.23	-0.43	3.35	2.78	0
l111n	110.50	2.18	4.19	2.21	0
l111s	111.07	-1.64	2.32	1.10	0
l119	119.40	3.08	3.29	0.83	330
l123	123.68	2.65	2.87	1.07	12
l126	125.70	1.93	1.06	1.08	0
l129	129.21	0.11	1.82	1.63	0
camob1	141.20	-0.31	2.79	3.40	0
l154	154.83	2.38	1.68	1.27	0
l169	169.42	-0.32	4.08	2.05	0
sh235	172.94	2.50	4.60	1.34	0
l181	181.11	4.40	2.19	1.20	0
l182	182.36	0.23	3.25	1.18	28
l195	195.92	-0.66	3.04	1.18	56
l201	201.57	0.30	1.32	1.37	0
ngc2264	202.97	2.21	2.20	1.32	0
orionBnorth	204.01	-11.86	2.17	1.33	335
orionB	206.73	-16.21	2.36	2.35	30
orionAspine	212.45	-19.24	4.35	2.48	0
monr2	213.54	-12.13	2.70	2.78	0
l217	217.69	-0.24	1.91	1.04	0

Additionally, the Orion A and B and Mon R2 clouds were observed in observing campaigns by collaborators. These complexes are not directly part of the BGPS, but are included in this data release reduced in the same manner as the Galactic plane data. They are much closer than typical BGPS sources and their selection for mapping is very biased, but we include them in the archival data. Parts of the Orion A nebula remain proprietary as of this release, but are expected to be released upon publication of Kauffmann et al (in prep). The California nebula has also been observed and the data published in Harvey et al. (2013).

Finally, some archival CSO data was recovered and added to the BGPS. These data include maps of M16 and M17. M17 is an extraordinarily bright 1.1 mm source that was poorly covered in the BGPS because it is below $b = -0.5$.

The Bolocat cataloging tool was run on these new fields and they have been included in the v2.0 catalog. Some of their properties are displayed in Section 3.8. A total of 548 new sources not covered in the v1.0 survey were extracted.

3.5 Data Reduction and Data Products

3.5.1 Sky Subtraction

We compared a few different methods for atmospheric subtraction and astrophysical image reconstruction, but settled on an approach very similar to that used in v1.0. This subsection recounts the minor changes from v1.0 and explores some alternative approaches.

The PCA method (Enoch et al., 2007) with iterative flux density restoration was used for v2.0 as for v1.0. In the PCA atmosphere removal method, the n eigenvectors corresponding to the highest values along the diagonal of the covariance matrix (the most correlated components) are nulled. We nulled 13 PCA components in both v1.0 and v2.0. The selection of 13 components produced the best compromise between uniform background noise and fully restored peak signal. Simulations show that the point source recovery is a very weak function of number of PCA components nulled (nPCA), while extended flux recovery is a strong function of nPCA. However, residual atmospheric

signal was substantially reduced with higher nPCA. In v2.0, 20 iterations were used instead of the 50 used in v1.0; in both surveys, convergence was clearly achieved by 20 iterations, and generally individual iterations are indistinguishable by ~ 5 iterations.

The iterative process adopts the non-negative flux density above some cutoff as a model of the astrophysical sky and subtracts that flux density from the timestream before repeating the atmospheric subtraction. This approach allows large angular scale structures to be recovered by removing them from the timestreams before they can contribute to the correlated signal. In v2.0, it was more succesful than in v1.0 at removing negative bowls (see Section 3.8.2). Negative bowls are introduced because the atmospheric subtraction process assumes that the mean level of any timestream, and therefore any map, is zero; the iterative process allows this assumption to be violated, creating maps with net positive signal.

The negative bowls are significantly reduced in v2.0. This change is attributed to a few effects that all operate in the same direction. The deconvolution process, in which a positive-definite model of the emission without sub-beam-scale noise is created from a real image, was made more stable in v2.0 by performing a local signal-to-noise cut using the noise maps described in Section 3.5.2.1; in v1.0 there was no reliable noise map available during the iterative map making process. Better image co-alignment reduced inter-observation spatial offsets. Improvement in the bolometer gain calibration, which is done on a per-observation basis in v2.0, improved the convergence of the iterative map maker. These changes are individually minor, but together resulted in significant improvements to the map quality.

The quadratic planar fit sky subtraction method discussed in Sayers et al. (2010) was implemented and tested for 1.1mm Galactic plane data in the v2.0 pipeline, but was not used for the final data products. In principle, this method should do a substantially better job at removing smooth atmospheric signal from timestreams than PCA cleaning because it is based on physically expected atmospheric variation. The spatial recovery was better than the aggressive 13-PCA approach, but as with a simpler median subtraction approach (subtracting the median timestream from all bolometers), a great deal of spurious signal from the atmosphere remained in the maps,

and the noise properties were highly non-uniform, rendering source extraction difficult. It was also more computationally expensive and did not remove correlated electronic readout noise, which PCA subtraction did. The Sayers et al. (2010) approach is likely more effective at 143 GHz because the atmosphere is better-behaved at lower frequencies. We speculate that it is also more effective for deep extragalactic fields in which more repeat observations of the same field are able to distinguish atmospheric from real signal on the angular scales of the array.

3.5.2 New Map Types

In the v2.0 data release, there are two new map types released: noise maps and median maps. A variant of the noise maps was produced in v1.0, while the median maps are an entirely new data product.

3.5.2.1 Noise Maps

Residual bolometer timestreams are automatically generated as part of the iterative map-making process. The residual is the result of subtracting the astrophysical model (which is smooth, noiseless, and non-negative) from the atmosphere-subtracted data timestream. The resulting timestream should only contain the remaining astrophysical noise. However, maps of the residual timestream contain sharp edge features because the astrophysical model is sharp-edged (i.e., transitions from 0 to a non-zero value from one pixel to the next). These sharp transitions are mitigated in the presence of noise.

We therefore created noise maps by taking the local standard deviation of the residual map. Pixels in the original map that were not sampled (i.e., represented by `NaN` in the FITS data file) are ignored when computing this local standard deviation and their values are set to be an arbitrarily high number (100 Jy/beam) such that pixels near the map edge are assumed to have extremely high noise (which is reasonable, since these pixels are affected by a variety of artifacts rendering them unreliable measurements of the true astrophysical flux). The local noise is computed within a $FWHM = 10$-pixel gaussian, which enforces a high noise level within $\sim 2'$ of the map edge. This

method produces good noise maps (i.e., in agreement with the standard deviation calculated from blank regions of the signal map) and was used both within the iterative process and for cataloging.

We show the noise per pixel for each square degree in the inner galaxy in Figure 3.2. The noise level in each outer-galaxy field is summarized in Figure 3.3. Because the outer galaxy coverage is irregular, we show the noise per observed region rather than dividing the regions into degree-scale sub-regions.

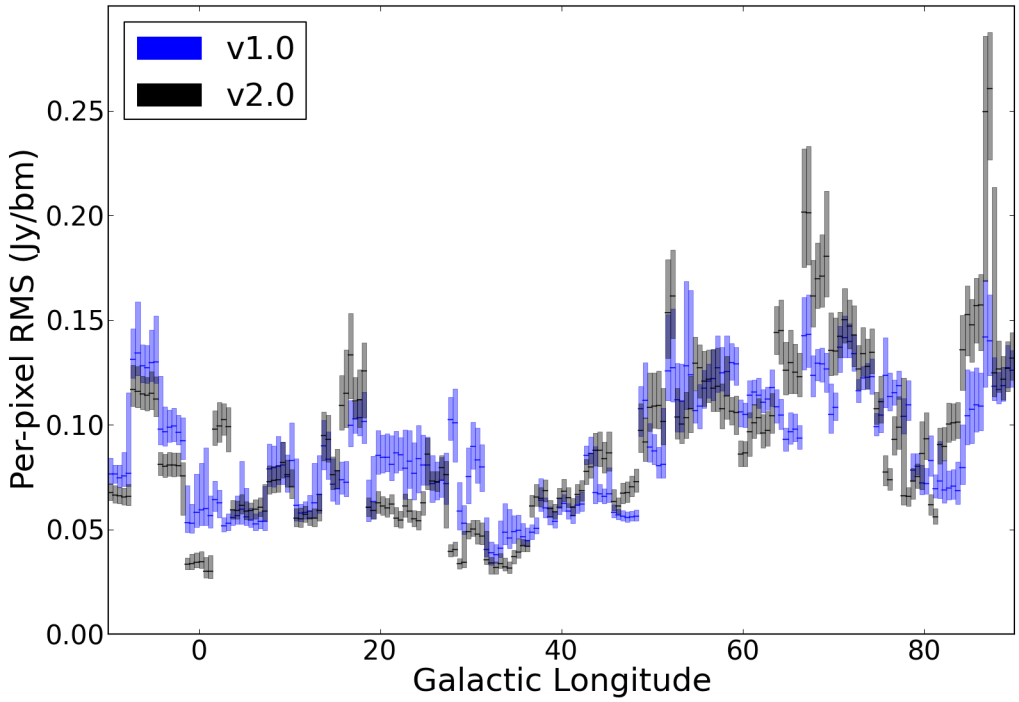

Figure 3.2 RMS noise per 0.5 degrees in longitude in the range $|b| < 0.5$. The solid lines show the median noise values, while the shaded regions highlight the 1-σ (68%) interval (quantiles 16-84).

3.5.3 Median Maps

Some artifacts (cosmic ray hits, instrumental artifacts) inevitably remained at the end of the process. In order to mitigate these effects, "median maps" were created. The value of each spatial pixel was set to the median value of the timestream points that intersected that pixel; pixels with fewer than 3 data points were set to `NaN`. The noise in the median maps was in some cases lower than that in the weighted mean maps, particularly for fields with fewer total observations. They

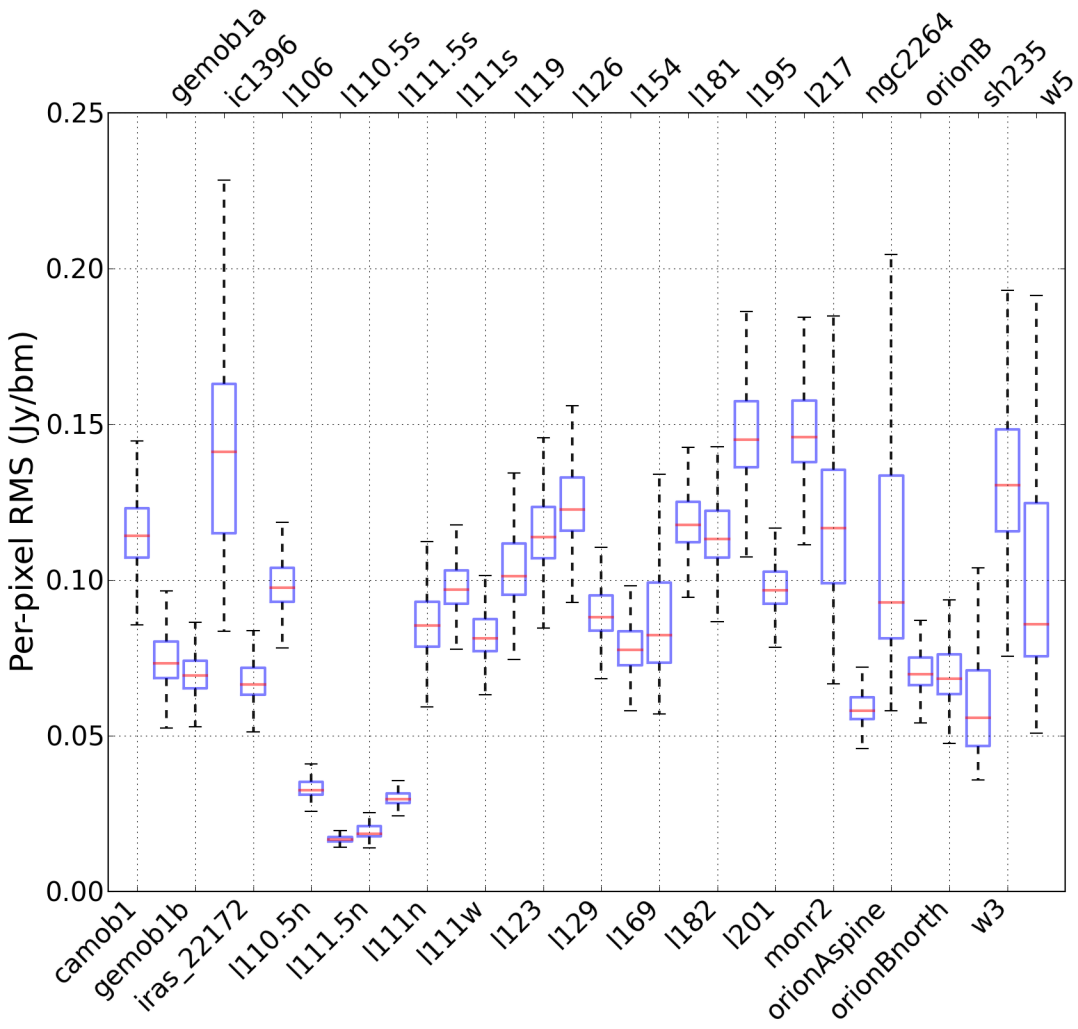

Figure 3.3 The noise in each outer galaxy field is shown with box plots. The red lines indicate the median, the boxes show the 25%-75% range, and the black dashed lines ('whiskers') show the 16%-84% (1-σ) range. Unlike Figure 3.2, the field size for each region varies, which is why there is a much broader spread in the widths of the individual noise distributions.

uniformly have mitigated instrument-related artifacts such as streaking. These maps are released in addition to the weighted-mean maps, which often have higher signal-to-noise.

3.5.4 Pointing

In order to get the best possible pointing accuracy in each field, all observations of a given area were median-combined using the MONTAGE package, which performs image reprojections, to create a pointing master map (Berriman et al., 2004). Each individual observation was then aligned to the master using a cross-correlation technique (Welsch et al., 2004):

(1) The master and target image were projected to the same pixel space

(2) The images were cross-correlated and the peak pixel in the cross-correlation map identified

(3) Sub-pixel alignment was measured by performing a 2nd-order Taylor expansion around the peak pixel

This method is similar to the version 1.0 method but improved by using MONTAGE to create the master images (which deals with reprojection better than IRAF), and the peak-finding method proved more robust than the previous Gaussian fitting approach. The v1.0 Gaussian fitting approach is often used in astronomy (e.g., `http://www.astro.ucla.edu/~mperrin/IDL/sources/subreg.pro`), but is biased when images are dominated by extended structure because the least-squares fitting approach will identify the broader peak that represents auto-correlation of astrophysical structure rather than correlation between the two images. In v1.0, we attempted to mitigate this issue by subtracting off a 'background' component before fitting the Gaussian peak, but this method was not robust.

The improved approach to pointing in general resulted in typical RMS offsets between the individual frames and the master of $\sim 2\,''$. The improvement in the point spread function is readily observed (see Section 3.8.2)

3.5.5 Pointing Comparison

We carefully re-examined the pointing throughout the BGPS using a degree-by-degree cross-correlation analysis between the v1.0, v2.0, and Herschel Hi-Gal 350 μm data. The Herschel data were unsharp-masked (high-pass filtered) by subtracting a version of the data smoothed with a $\sigma = 120''$ Gaussian. The result was then convolved with a $\sigma = 8.9''$ Gaussian to match the beam sizes.

Errors on the offsets were measured utilizing the Fourier scaling theorem to achieve sub-pixel resolution (inspired by Guizar-Sicairos & Fienup, 2008). The errors on the best-fit shift were determined using errors estimated from the BGPS data and treating the filtered Hi-Gal data as an ideal model. The tools for this process, along with a test suite demonstrating their applicability to extended structures in images, are publicly available at `https://github.com/keflavich/image_registration`.

The cross-correlation technique calculated the χ^2 statistic as a function of the offset. For a reference image Y and observed image X with error per pixel σ,

$$\chi^2 = \sum \frac{(X - Y(\Delta x, \Delta y))^2}{\sigma^2}$$

where Δx and Δy are the pixel shifts. Because Y is not, in fact, an ideal model but instead is a noisy image, we increase σ by the rms of the difference between the aligned images, using a corrected $\sigma_c^2 = \sigma_{BGPS}^2 + RMS(X - Y(\Delta x_b, \Delta y_b))$, where $\Delta x_b, \Delta y_b$ are the best-fit shifts.

For the majority of the examined 1-square-degree fields, the signal dominated the noise and we were able to measure the offsets to sub-pixel accuracy. A plot of the longitude / latitude offsets between v2.0 and v1.0 and Herschel Hi-Gal is shown in Figure 3.4.

Table 3.4 lists the measured offsets in arcseconds between images for all 1 degree fields from $\ell = 351^\circ$ to $\ell = 65^\circ$. The offsets represent the Galactic longitude and latitude shifts in arcseconds from the reference (left) to the 'measured' field (right).

Table 3.5 shows the means of the columns in Table 3.4, weighted by the error in the measurements and by the number of sources. Weighting by the number of sources is used for comparison

with other works that attempt to measure the pointing offset on the basis of catalog source position offsets. None of the measured offsets are significant; in all cases the scatter exceeds the measured offset.

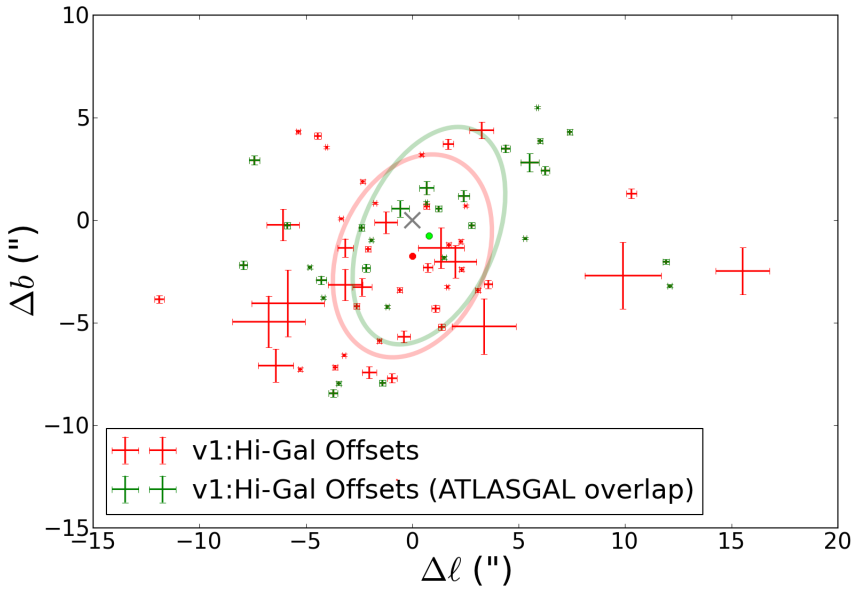

(a)

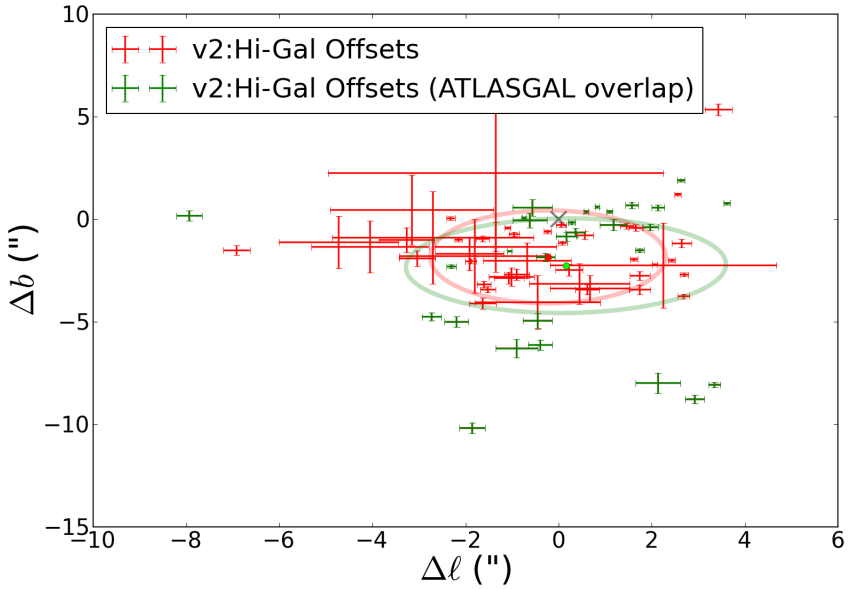

(b)

Figure 3.4 Plots of the latitude and longitude offsets of individual 1-degree fields in v1.0 (a) and v2.0 (b) as compared with Herschel Hi-Gal. Offsets were measured using a cross-correlation technique described in the text. The error bars correspond to $\Delta\chi^2 < 2.3$, or $1-\sigma$ for Gaussian distributed noise and 2 degrees of freedom. The circles and ellipses represent the mean and standard deviation (unweighted) offsets in the whole survey (red) and the $(351^\circ < \ell) \cup (\ell < 20^\circ)$ ATLASGAL-overlap regions (green). In both cases, the mean offset is consistent with zero (shown as a black `x`), but many individual fields show significant offsets. Note that the scales are different; there are far fewer outliers in the v2.0-Herschel comparison (b) and the average offset is much closer to zero. The errors are larger in the non-ATLASGAL overlap region because there is less signal in the $35^\circ < \ell < 65^\circ$ range.

Table 3.4. Cross-Correlation Offsets

Field Name	$\Delta\ell$(HG-v2)	Δb(HG-v2)	$\Delta\ell$(v1-v2)	Δb(v1-v2)	$\Delta\ell$(HG-v1)	Δb(HG-v1)	N(v1 sources)
l351	0.37(−0.21)	−0.65(0.21)	3.12(−0.16)	1.83(0.14)	−2.17(−0.19)	−2.33(0.19)	56
l352	1.10(−0.07)	0.37(0.07)	3.14(−0.06)	1.45(0.06)	−1.93(−0.07)	−0.97(0.07)	87
l353	3.35(−0.13)	−8.07(0.13)	−3.80(−0.08)	−12.41(0.08)	7.39(−0.12)	4.30(0.12)	65
l354	2.14(−0.48)	−7.98(0.50)	−3.71(−0.11)	−12.04(0.09)	5.51(−0.43)	2.81(0.44)	52
l355	2.92(−0.20)	−8.78(0.20)	−3.57(−0.11)	−12.12(0.09)	6.24(−0.20)	2.42(0.20)	54
l356	−0.62(−0.37)	−0.06(0.35)	−1.29(−0.22)	−0.96(0.17)	0.68(−0.34)	1.58(0.32)	42
l357	−0.56(−0.43)	0.56(0.41)	−0.06(−0.24)	−0.39(0.17)	−0.56(−0.42)	0.56(0.39)	23
l358	2.14(−0.14)	0.56(0.14)	−0.62(−0.14)	0.17(0.12)	2.78(−0.14)	−0.25(0.14)	35
l359	2.63(−0.08)	1.90(0.06)	−10.05(−0.08)	5.86(0.07)	12.10(−0.10)	−3.21(0.07)	248
l000	3.61(−0.07)	0.77(0.06)	−1.10(−0.04)	1.55(0.03)	5.30(−0.07)	−0.89(0.06)	318
l001	0.59(−0.05)	0.37(0.07)	−3.36(−0.05)	1.31(0.06)	11.92(−0.16)	−2.02(0.11)	368
l002	−0.39(−0.26)	−6.13(0.25)	1.46(−0.24)	2.14(0.19)	−1.41(−0.15)	−7.93(0.14)	170
l003	−2.73(−0.21)	−4.75(0.20)	0.62(−0.18)	3.54(0.17)	−3.46(−0.10)	−7.96(0.10)	243
l004	−1.86(−0.28)	−10.18(0.26)	−0.34(−0.23)	0.11(0.19)	−3.71(−0.21)	−8.44(0.19)	70
l005	1.18(−0.29)	−0.28(0.28)	−3.99(−0.19)	−3.54(0.19)	4.39(−0.21)	3.49(0.19)	78
l006	0.83(−0.05)	0.60(0.06)	−1.17(−0.05)	−1.36(0.06)	5.88(−0.05)	5.48(0.05)	109
l007	1.97(−0.17)	−0.39(0.16)	−4.50(−0.09)	−4.50(0.00)	6.00(−0.12)	3.87(0.11)	93
l008	1.58(−0.14)	0.68(0.16)	4.58(−0.12)	1.43(0.15)	−2.39(−0.13)	−0.37(0.15)	59
l009	1.74(−0.10)	−1.52(0.09)	6.15(−0.09)	1.00(0.09)	−4.82(−0.08)	−2.29(0.08)	55
l010	0.28(−0.08)	−0.17(0.08)	3.70(−0.08)	1.98(0.09)	−4.18(−0.08)	−3.78(0.07)	77
l011	−1.05(−0.04)	−1.56(0.04)	−0.94(−0.03)	−0.04(0.02)	−1.18(−0.07)	−4.22(0.08)	122
l012	−2.31(−0.10)	−2.31(0.10)	−3.80(−0.08)	−0.70(0.09)	1.49(−0.09)	−1.83(0.08)	102
l013	−0.75(−0.05)	0.07(0.05)	−1.49(−0.05)	−0.59(0.05)	0.66(−0.05)	0.86(0.06)	198
l014	−0.28(−0.20)	−1.86(0.20)	6.05(−0.15)	−1.72(0.16)	−5.88(−0.15)	−0.25(0.15)	137
l015	−2.19(−0.26)	−5.01(0.26)	5.79(−0.17)	−2.64(0.19)	−7.93(−0.20)	−2.19(0.20)	164
l016	−0.90(−0.45)	−6.30(0.45)	5.79(−0.26)	−2.31(0.28)	−4.28(−0.25)	−2.92(0.20)	63
l017	−0.45(−0.32)	−4.95(0.36)	−1.29(−0.22)	−3.88(0.26)	2.42(−0.26)	1.18(0.27)	62

Table 3.4 (cont'd)

Field Name	$\Delta\ell$(HG-v2)	Δb(HG-v2)	$\Delta\ell$(v1-v2)	Δb(v1-v2)	$\Delta\ell$(HG-v1)	Δb(HG-v1)	N(v1 sources)
l018	0.17(−0.23)	−0.84(0.21)	−1.07(−0.17)	−1.97(0.17)	1.24(−0.15)	0.56(0.14)	55
l019	−7.93(−0.28)	0.17(0.25)	0.89(−0.11)	−2.69(0.10)	−7.42(−0.25)	2.92(0.23)	179
l020	2.43(−0.07)	−2.01(0.08)	0.07(−0.07)	−2.60(0.06)	2.50(−0.06)	0.70(0.06)	110
l021	2.64(−0.21)	−1.18(0.21)	1.86(−0.17)	−1.74(0.16)	0.68(−0.14)	0.68(0.14)	103
l022	1.74(−0.21)	−2.76(0.21)	−0.65(−0.16)	0.48(0.14)	3.57(−0.20)	−3.12(0.20)	87
l023	2.69(−0.12)	−3.75(0.11)	−0.20(−0.09)	−0.31(0.08)	3.08(−0.10)	−3.42(0.10)	213
l024	2.70(−0.09)	−2.70(0.09)	−0.44(−0.09)	−0.27(0.08)	2.32(−0.10)	−2.40(0.10)	250
l025	1.62(−0.08)	−1.95(0.08)	0.08(−0.07)	1.15(0.07)	1.65(−0.06)	−3.25(0.07)	183
l026	1.66(−0.15)	−0.42(0.16)	0.06(−0.12)	0.62(0.13)	1.72(−0.10)	−1.21(0.11)	151
l027	1.46(−0.15)	−0.34(0.14)	−0.48(−0.12)	0.87(0.12)	2.28(−0.10)	−1.04(0.10)	119
l028	2.56(−0.07)	1.21(0.08)	6.22(−0.07)	8.35(0.07)	−3.63(−0.11)	−7.17(0.12)	188
l029	−0.96(−0.11)	−0.73(0.11)	4.58(−0.09)	6.38(0.09)	−5.27(−0.09)	−7.27(0.09)	177
l030	0.06(−0.11)	−0.28(0.12)	2.05(−0.09)	3.23(0.11)	−3.21(−0.07)	−6.58(0.06)	276
l031	−1.10(−0.06)	−0.42(0.05)	−1.69(−0.03)	−1.46(0.02)	0.44(−0.07)	3.19(0.07)	354
l032	−0.24(−0.08)	−0.60(0.09)	1.18(−0.08)	−2.42(0.08)	−2.33(−0.09)	1.88(0.08)	189
l033	2.07(−0.05)	−2.21(0.05)	6.10(−0.06)	−5.71(0.06)	−4.04(−0.06)	3.56(0.06)	210
l034	−2.32(−0.09)	0.04(0.08)	−0.46(−0.05)	−0.10(0.05)	−1.55(−0.11)	−5.88(0.10)	203
l035	−1.88(−0.12)	−2.05(0.12)	0.31(−0.11)	−0.59(0.10)	−2.08(−0.13)	−1.41(0.12)	247
l036	−1.63(−0.14)	−0.96(0.15)	0.82(−0.12)	3.01(0.11)	−2.62(−0.14)	−4.19(0.14)	126
l037	−1.07(−0.32)	−2.87(0.29)	−2.31(−0.25)	0.51(0.24)	0.73(−0.23)	−2.31(0.21)	83
l038	−1.60(−0.15)	−3.18(0.17)	−0.79(−0.12)	0.34(0.14)	−0.59(−0.11)	−3.40(0.12)	69
l039	0.62(−0.26)	−3.43(0.24)	−0.23(−0.16)	1.12(0.14)	1.10(−0.19)	−4.30(0.17)	69
l040	1.74(−0.23)	−3.43(0.24)	1.86(−0.18)	2.98(0.17)	1.38(−0.17)	−5.20(0.16)	40
l041	0.23(−0.29)	−2.48(0.29)	1.07(−0.24)	5.23(0.20)	−0.96(−0.23)	−7.70(0.23)	44
l042	−1.01(−0.48)	−2.81(0.45)	0.11(−0.26)	5.06(0.23)	−2.02(−0.34)	−7.42(0.29)	36
l043	0.08(−0.10)	−1.15(0.09)	2.07(−0.08)	−2.52(0.09)	−1.74(−0.07)	0.84(0.05)	17
l044	−1.63(−0.29)	−4.11(0.27)	4.78(−0.26)	−8.16(0.20)	−4.44(−0.17)	4.11(0.15)	27

3.5.6 ATLASGAL offset

Contreras et al. (2013) performed a comparison of the Bolocam and ATLASGAL catalogs, identifying a systematic offset between the catalogs of $\Delta\ell = -4.7''$, $\Delta b = 1.2''$. Because the offset is measured between catalog points, the meaning of this measured offset is not immediately clear. In the BGPS maps in the ATLASGAL-BGPS overlap region, there were 12 individual sub-regions ($3^\circ \times 1^\circ$, with $1^\circ \times 1^\circ$ regions in the CMZ) that could have independendent pointing. Because we did not have direct access to the ATLASGAL maps or catalog, we compared the Bolocam v1.0 and v2.0 catalogs to each other determine whether the pointing changes in v2.0 might account for the observed ATLASGAL offset, assuming that the v2.0 pointing is more accurate than the v1.0 pointing.

We performed an inter-catalog match between v1.0 and v2.0, considering sources between the two catalogs to be a match if the distance between the centroid positions of the two sources is $< 40''$ (this distance is more conservative than that used in Section 3.8.2). We then compared the pointing offset as measured by the mean offset between the catalogs to the offset measured via cross-correlation analysis of the maps on a per-square-degree basis. The catalog and image offsets agree well, with no clear systematic offsets between the two estimators. The scatter in the catalog-based measurements is much greater, which is expected since the source positions are subject to spatial scale recovery differences between the versions and because the sources include less signal than the complete maps.

There is no clear net offset between either version of the BGPS and the Herschel Hi-Gal survey, or between the two versions of the BGPS. However, the scatter in the pointing offsets between v1.0 and Herschel is substantially greater than the v2.0-Herschel offsets. The offset measured in Contreras et al. (2013) is likely a result of particularly large offsets in a few fields with more identified sources. As shown in Table 3.5, the mean offset, **weighted by number of sources**, is greater for the ATLASGAL overlap region than overall. We reproduce a number similar to the ATLASGAL-measured longitude offset of $\Delta\ell = -4.7''$ (our source-count-weighted $\Delta\ell = -3.7''$),

Table 3.4 (cont'd)

Field Name	$\Delta\ell$(HG-v2)	Δb(HG-v2)	$\Delta\ell$(v1-v2)	Δb(v1-v2)	$\Delta\ell$(HG-v1)	Δb(HG-v1)	N(v1 sources)
l045	−1.52(−0.16)	−3.43(0.15)	4.42(−0.14)	−7.73(0.12)	−5.36(−0.10)	4.32(0.09)	30
l046	−0.90(−0.27)	−2.70(0.27)	−1.24(−0.26)	−5.29(0.21)	1.69(−0.25)	3.71(0.25)	53
l047	0.68(−0.85)	−3.38(0.63)	0.34(−0.38)	−3.71(0.27)	3.26(−0.56)	4.39(0.41)	11
l048	−0.45(−1.35)	−4.05(1.31)	8.16(−0.27)	−3.32(0.30)	−6.08(−0.76)	−0.23(0.76)	6
l049	−2.15(−0.08)	−1.00(0.08)	−0.35(−0.05)	−0.75(0.06)	−3.35(−0.09)	0.08(0.05)	113
l050	0.56(−0.18)	−0.79(0.19)	1.77(−0.14)	−0.14(0.12)	−0.73(−0.06)	−12.66(0.30)	31
l051	−1.91(−0.73)	−1.69(0.82)	4.95(−0.23)	0.45(0.32)	−3.15(−0.36)	−1.35(0.45)	9
l052	−2.70(−2.16)	−0.90(2.25)	−3.71(−0.54)	3.26(0.21)	3.38(−1.51)	−5.18(1.35)	0
l053	−3.04(−0.39)	−1.91(0.38)	−1.01(−0.28)	2.59(0.19)	−0.39(−0.30)	−5.68(0.28)	26
l054	−3.26(−0.60)	−1.01(0.61)	1.35(−0.27)	1.35(0.18)	−2.36(−0.45)	−3.26(0.43)	26
l055	−4.05(−1.26)	−1.35(1.26)	−0.23(−0.34)	1.58(0.23)	−3.15(−0.81)	−3.15(0.76)	4
l056	−4.72(−1.28)	−1.12(1.28)	4.39(−0.44)	−0.79(0.24)	−1.24(−0.53)	−0.11(0.53)	10
l057	−3.15(−1.76)	0.45(1.71)	2.81(−0.50)	0.11(0.21)	1.35(−1.08)	−1.35(0.99)	1
l058	−1.35(−1.30)	−1.35(1.22)	−6.86(−0.48)	0.79(0.25)	2.02(−0.99)	−2.02(0.79)	4
l059	0.45(−1.08)	−3.15(0.99)	−4.28(−0.23)	1.12(0.68)	−6.75(−1.71)	−4.95(1.26)	2
l060	3.43(−0.29)	5.34(0.29)	−7.09(−0.14)	4.61(0.17)	10.30(−0.24)	1.29(0.23)	17
l061	−6.92(−0.29)	−1.52(0.23)	5.12(−0.16)	3.54(0.16)	−11.89(−0.23)	−3.85(0.19)	4
l062	−1.80(−1.62)	−1.80(1.80)	4.72(−0.18)	5.18(0.25)	−5.85(−1.71)	−4.05(1.62)	1
l063	−0.68(−0.95)	−2.02(0.88)	2.64(−0.18)	4.67(0.27)	−6.41(−0.83)	−7.09(0.81)	5
l064	2.25(−2.43)	−2.25(2.07)	−24.98(−0.43)	−2.92(0.83)	15.52(−1.26)	−2.48(1.15)	1
l065	−1.35(−3.60)	2.25(3.82)	−24.08(−0.63)	−4.28(0.99)	9.90(−1.80)	−2.70(1.62)	1

The offsets reported are in units of arcseconds, and the values in parentheses represent the 1-σ error bars.

Table 3.5. Cross-Correlation Offset Means and Standard Deviations

	$\Delta\ell$(HG-v2)	Δb(HG-v2)	$\Delta\ell$(v1-v2)	Δb(v1-v2)	$\Delta\ell$(HG-v1)	Δb(HG-v1)
Mean	0.23	−1.8	0.16	−0.37	−0.0047	−1.7
Standard Deviation	2.2	2.5	5.3	3.9	4.9	3.7
Weighted Mean	−0.47	−0.89	0.26	−1.1	−0.089	−0.87
Weighted Standard Deviation	1.7	1.8	3.1	3.5	4	3.6
N(src) Weighted Mean	−0.24	−1.1	0.26	0.58	−1.3	−1.9
N(src) Weighted Standard Deviation	2.3	2.1	3.5	3.2	5.7	3.6
N(src) Weighted Mean $\ell < 21$	−0.24	−1	1.5	0.84	−3.7	−1.9
N(src) Weighted Standard Deviation $\ell < 21$	2.9	2.8	4.1	3.2	7.3	3.4

The offsets reported are in units of arcseconds, and the values in parentheses represent the 1-σ error bars.

despite a much larger standard deviation and despite no significant offset being measured directly in the images. These measurements imply that the pointing offset measured by Contreras et al. (2013) was localized to a few fields **and** that the offset is corrected in the v2.0 data.

3.6 The Angular Transfer Function of the BGPS

3.6.1 Simulations with synthetic sky and atmosphere

In order to determine the angular response of the Bolocam array and BGPS pipeline in realistic observing conditions, we performed simulations of a plausible synthetic astrophysical sky with synthetic atmospheric signal added to the bolometer timestream.

To generate the simulated atmosphere, we fit a piecewise power law to a power spectrum of a raw observed timestream (Figure 3.5). The power spectrum varies in amplitude depending on weather conditions and observation length, but the shape is generally well-represented by $1/f$ (pink) noise $P_\nu \propto \nu^{-1.5}$ for $\nu < 2$ Hz and white noise $P_\nu \sim const$ for $\nu \geq 2$ Hz where ν is the frequency. We show a fitted timestream power spectrum in Figure 3.5. The deviations from $1/f$ and white noise have little affect on the reduction process.

The Fourier transform of the atmosphere timestream is generated by applying noise to the fitted power spectrum. The power at each frequency is multiplied by a random number sampled from a Gaussian distribution[3] with width 1.2, determined to be a reasonable match to the data, and mean 1.0. The resulting Fourier-transformed timestream $d(t)$ is $FT(d(t)) = (r_{\nu 1} P_f)^{1/2} + i(r_{\nu 2} P_f)^{1/2}$, where r_1 and r_2 are the normally distributed random variables and P_f is the fitted power-law power spectrum. The atmosphere timestream is then created by inverse Fourier transforming this signal.

Gaussian noise is added to the atmospheric timestream of each bolometer independently, which renders the correlation between timestreams imperfect. This decorrelation is important for the PCA cleaning, which would remove all of the atmosphere with just one nulled component if the correlation was exact. The noise level set in the individual timestreams determines the noise

[3] We experimented with different noise distributions that reasonably matched the data, including a lognormal distribution, and found that the angular transfer function was highly insensitive to the noise applied to the atmosphere time series power spectrum.

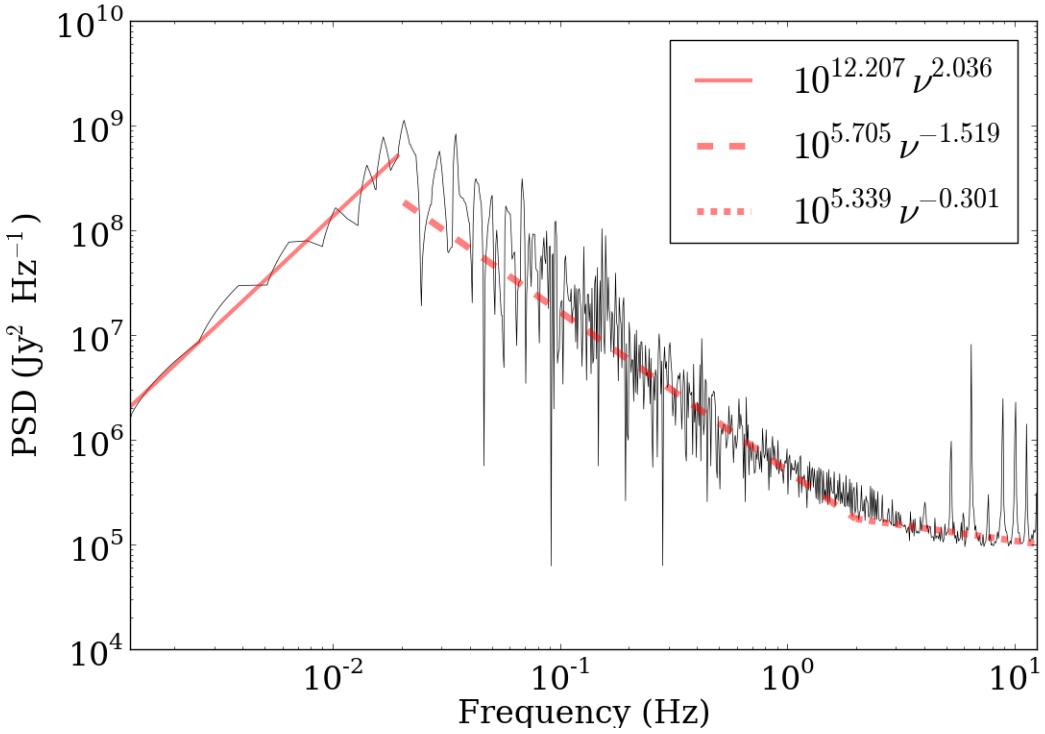

Figure 3.5 Fit to the raw downsampled power spectrum of a $\sim$ 30 minute observation. Three independent power laws are fit to the data, with a fixed break at 0.02 Hz (below which the AC-coupled bolometer bias and readout electronics remove signal) and a fitted break at higher frequency, near 2 Hz, where the power spectrum flattens towards white noise. The beam FWHM is at about 4 Hz using the standard scan rate of $120''$ s^{-1}.

level in the output map.

3.6.1.1 Simulated Map Parameters

We simulated the astrophysical sky by randomly sampling signal from an azimuthally symmetric 2D power-law distribution in Fourier space. The power distribution as a function of angular frequency is given by

$$P(1/r) \propto (1/r)^{-\alpha_{ps}} \tag{3.1}$$

where r is the angular size-scale and α_{ps} is the power-law spectral index for power spectra. We modeled this signal using power spectrum power-law indices ranging from -3 to +0.5; in the HiGal $\ell = 30^{\circ}$ Science Demonstration Phase (SDP) field, the power-law index measured from the 500 μm map is $\alpha_{ps} \sim 2$ (see Section 3.6.3). The data were smoothed with a model of the instrument PSF to simulate the telescope's aperture and illumination pattern. For each power-law index, three realizations of the map using different random seeds were created. The signal map was then sampled into timestreams with the Bolocam array using a standard pair of perpendicular boustrophedonic scan patterns. Examples of one of these realizations with identical random numbers and different power laws are shown in Figure 3.6.

3.6.2 The Angular Transfer Function

We used a subset of these power-law simulations to measure the amount of recovered signal at each angular (spatial) scale. For each power-law in the range $1 < \alpha_{ps} < 2$, which best match the Herschel 500 μm power-spectra, we used three different realizations of the map to measure the angular transfer function, defined as $STF(f) = F_{out}(f)/F_{in}(f)$ where f is the angular frequency, F_{out} is the azimuthally averaged power-spectrum of the pipeline-processed map, and F_{in} is the azimuthally averaged power-spectrum of the simulated input map.

The angular transfer function shows only weak dependence on the ratio of astrophysical to atmospheric power, and is approximately constant at $\sim 95\%$ recovery over the range of angular scales between the beam size and $\sim 2'$. The angular transfer function is shown in Figure 3.7. At

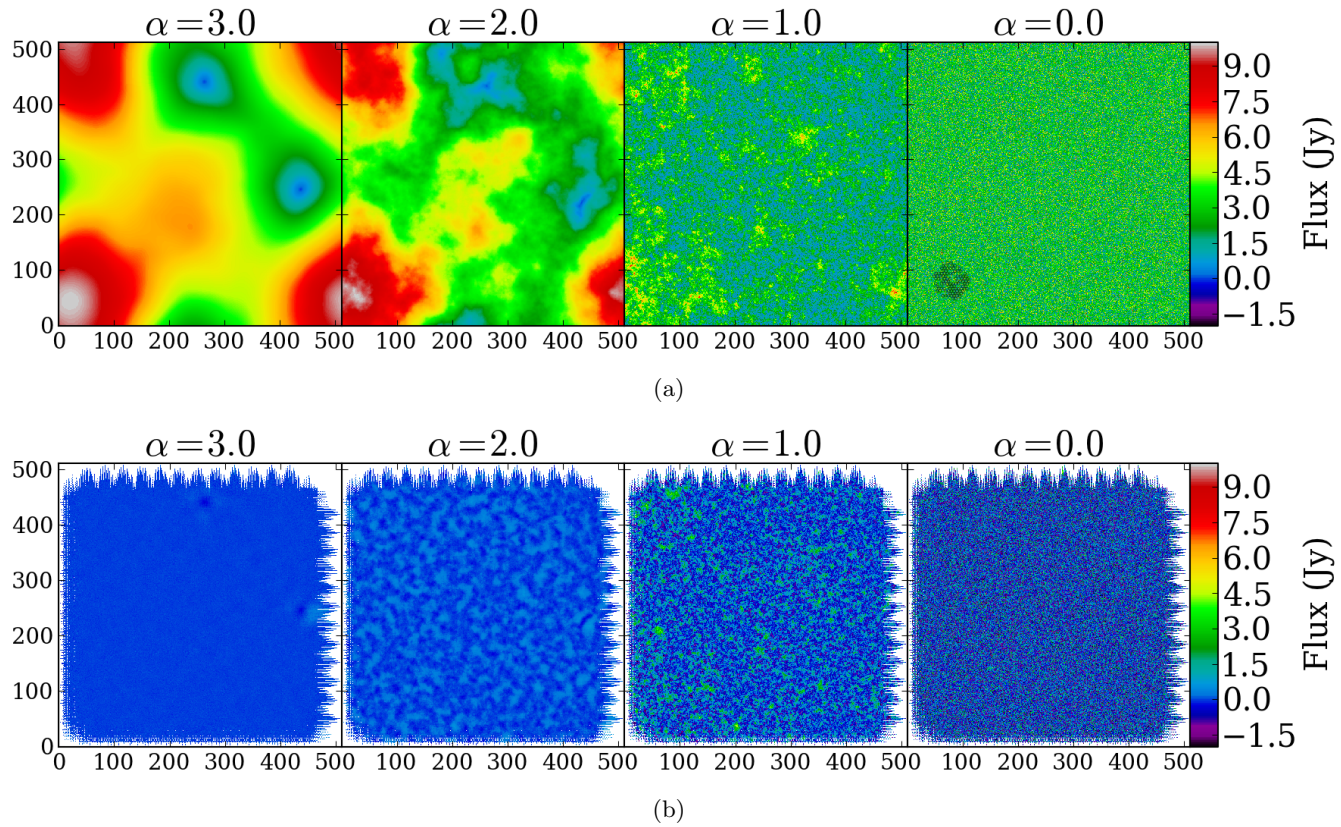

(a)

(b)

Figure 3.6 Examples of input (top) and output (bottom) maps for different input power-spectrum power law α_{ps} values. For very steep power laws, most of the power is on the largest scales. $\alpha_{ps} = 0$ is white noise. The axis scales are in pixels, where each pixel is 7.2″, so each field is approximately 1° on a side. The Bolocam footprint is plotted with a circle of diameter 33″ representing each beam in its appropriate relative location. It is shown in the right panel of the top figure as an indication of the largest possible recovered angular scales; it is about 1/8th the width of the map. The input images are normalized to have the same **peak** flux density. The pipeline recovers no emission from the simulation with $\alpha_{ps} = 3$, but this value of α_{ps} is not representative of the real astrophysical sky - Herschel sees structure with $\alpha_{ps} \lesssim 2$, and the BGPS detected a great deal of astrophysical signal (see Section 3.6.3 and Figure 3.8).

larger angular scales, in the range $2'-8'$, the recovery is generally low. Our simulations included the full range of observed astrophysical to atmospheric flux density ratios, from $\sim 10^{-2}$ for the Central Molecular Zone (CMZ) down to $\sim 10^{-4}$ for sparsely populated regions in the $\ell \sim 70^{\circ}$ region.

Chapin et al. (2013) perform a similar analysis for the SCUBA-2 pipeline. Our transfer function (Figure 3.7) cuts off at a scale $\sim 1/6$ the SCUBA-2 scale. While the angular extent of the Bolocam footprint is only slightly smaller than SCUBA-2's, some feature of the instrument or pipeline allows SCUBA-2 to recover larger angular scales. We speculate that the much larger number of bolometers in the SCUBA-2 array allows the atmosphere to be more reliably separated from astrophysical and internal electrical signals (bias and readout noise), so the SCUBA-2 pipeline is able to run with an atmosphere subtraction algorithm less aggressive than the 13-PCA approach we adopted.

3.6.3 Comparison to other data sets: Aperture Photometry

Given an understanding of the spatial transfer function, it is possible to compare the BGPS to other surveys, e.g. Hi-Gal, ATLASGAL, and the JCMT Galactic Plane Survey (JPS), for temperature and β measurements.

Because the systematic uncertainties in temperature/β derivation from dust SEDs are severe (e.g. Shetty et al., 2009b,a; Kelly et al., 2012), we recommend a conservative approach when comparing BGPS data with other data sets. For compact sources, aperture extraction with background subtraction in both the BGPS and other data set should be effective. Section 3.8.1 discusses aperture extraction in the presence of typical power-law distributed backgrounds.

3.6.4 Comparison to other data sets: Fourier-space treatment

In order to compare extended structures, which includes any sources larger than the beam, a different approach is required. The safest approach is to "unsharp mask" (high-pass-filter) both the BGPS and the other data set with a Gaussian kernel with FWHM $\lesssim 120''$ ($\sigma \lesssim 51''$). The filtering will limit the spatial dynamic range, but will provide accurate results over the angular

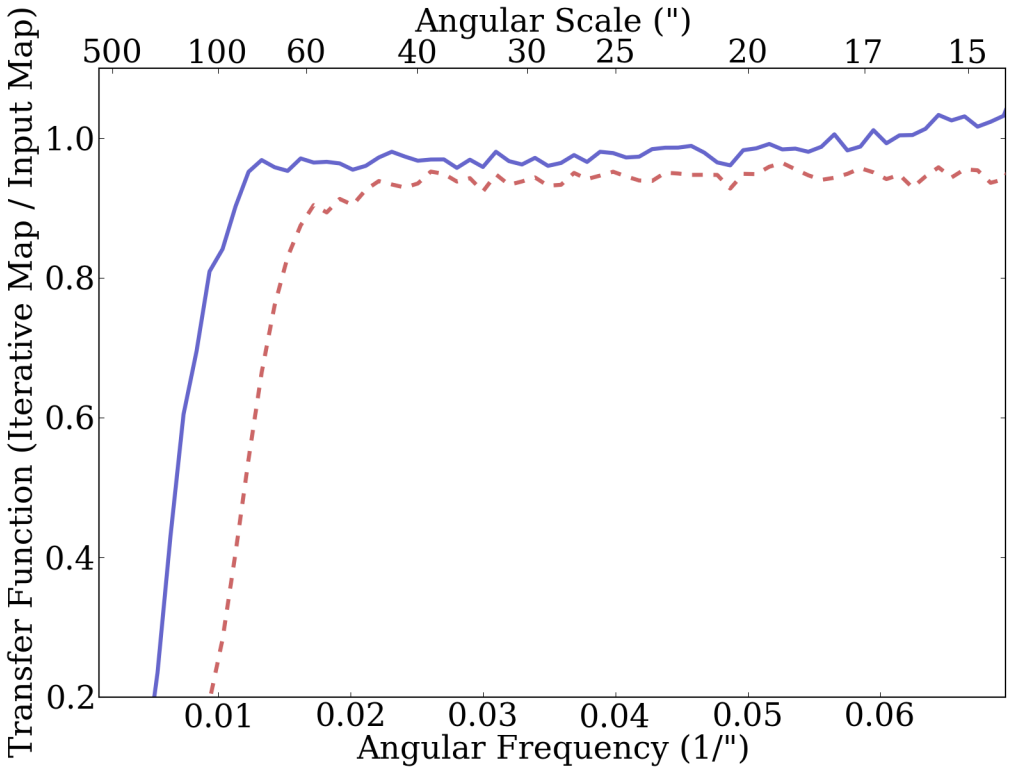

Figure 3.7 The angular transfer function over the range of angular scales where the BGPS data are reliable after 20 iterations (blue) and without iterative mapping (red dashed). At higher angular frequency (smaller angular scale), the beam smooths out any signal. At lower angular frequency, the atmospheric subtraction removes signal. The benefits of iterative mapping in recovered flux density on all scales, but particularly the improvement in large-scale recovery, are evident. The simulations used for this measurement had a power-law sky structure with $\alpha_{ps} = 2$.

scales sampled.

Direct comparison of power spectra over the reproduced range is also possible. A demonstration of this approach is given in Figure 3.8, which shows the structure-rich $\ell = 30^\circ$ field. The BGPS power spectrum has a shape very similar to that of HiGal. The spectral index is a commonly used measure of the ratio between flux densities at two different wavelengths in the radio,

$$\frac{F_2}{F_1} = \left(\frac{\lambda_2}{\lambda_1}\right)^{-\alpha_\nu} = \left(\frac{\nu_2}{\nu_1}\right)^{\alpha_\nu} \tag{3.2}$$

The spectral index between the BGPS at 1.1 mm and Herschel at 500 μm is $\alpha_\nu \approx 3.7$ over the range $33'' < dx < 300''$. On the Rayleigh-Jeans tail, $\alpha_\nu = \beta + 2$, so this spectral index is consistent with typical dust emissivity index β measurements in the range $1.5 < \beta < 2$.

3.7 Examination of BGPS and HiGal power-spectra

3.7.1 Power Spectral Density comparison

In Section 3.6.3, we showed the power spectral density of the Bolocam and Herschel Hi-Gal observations of the $\ell = 30^\circ$ field. Over the range in which the Bolocam and Herschel data are both sensitive, the data are consistent with a 500 μm - 1100 μm spectral index $\alpha_\nu \sim 3.7$, or $\beta \gtrsim 1.7$ depending on the temperature. This measurement hints that structures over a range of spatial scales (0.5-6 pc in the $\ell = 30^\circ$ region, assuming a distance ~ 3.5 kpc) have similar dust emissivity properties.

Changes in the spectral index as a function of angular scale are evident when comparing to shorter wavelengths (250 and 350 μm; Figure 3.9). This variation indicates that either temperature or emissivity is scale-dependent.

3.7.2 Dust β and Temperature

The observed spectral indices provide some constraints on dust temperature and β. However, we caution that the spectral index measurements we present average over lines of sight that may include many different temperatures and dust properties.

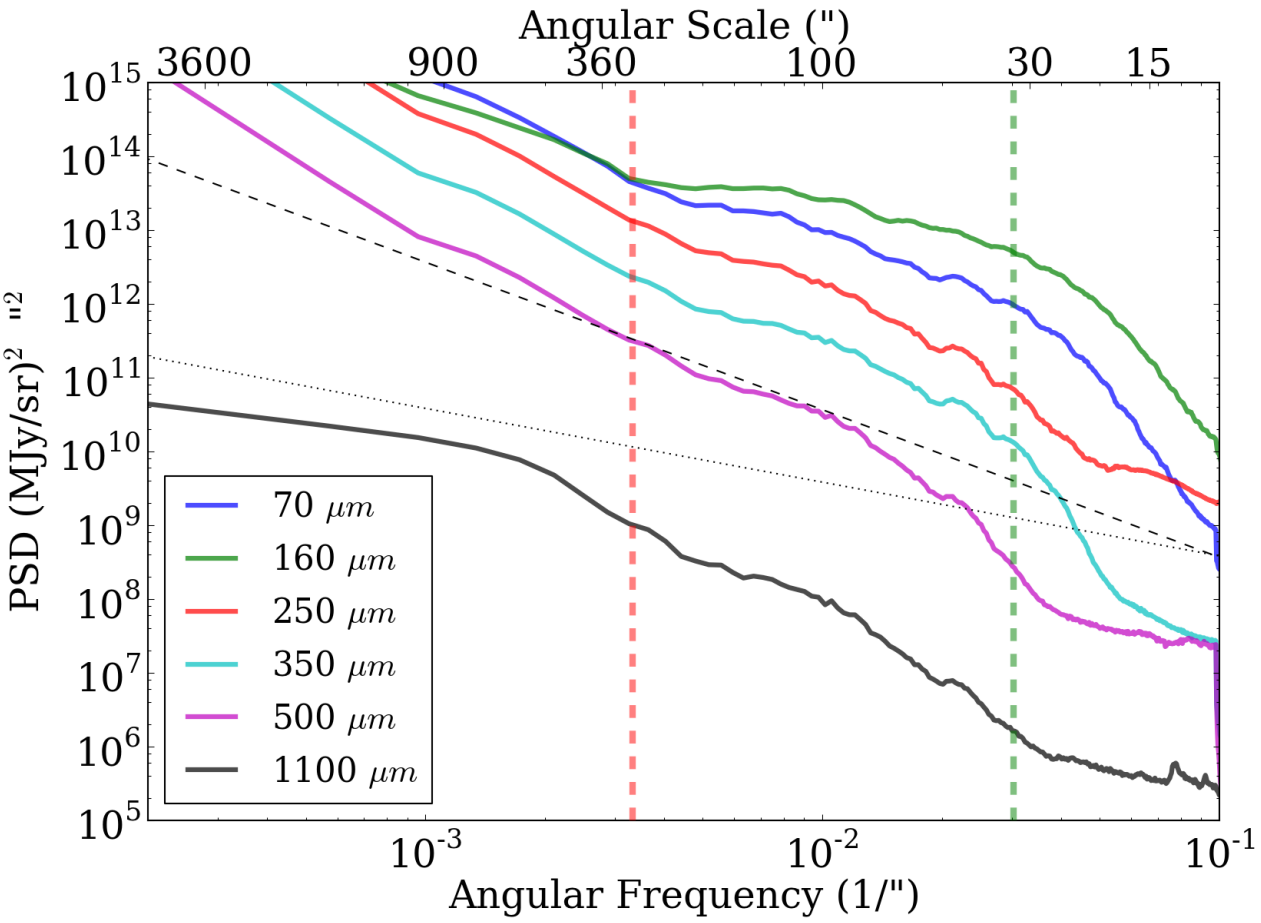

Figure 3.8 A comparison of the power spectra of the $\ell = 30°$ HiGal SDP fields with the BGPS power spectrum covering the same area. The area included is 1 square degree. The dashed and dotted black lines indicate power laws with $\alpha_{ps} = 2$ and $\alpha_{ps} = 1$ respectively, with arbitrary normalizations, as a guide for comparison. The vertical dashed red and green lines indicate the large angular scale 50% recovery point of the BGPS and the BGPS beam FWHM respectively. The ratio of 500 μm to 1100 μm in this example has a spectral index $\alpha_\nu \sim 3.7$. Note that the 500 μm power begins falling off more steeply at $\sim 40''$ because the Herschel FWHM beam size is $35.2''$ at 500 μm, slightly larger than Bolocam's (at 250 and 350 μm, the Herschel beam is $17.6''$ and $23.9''$, respectively).

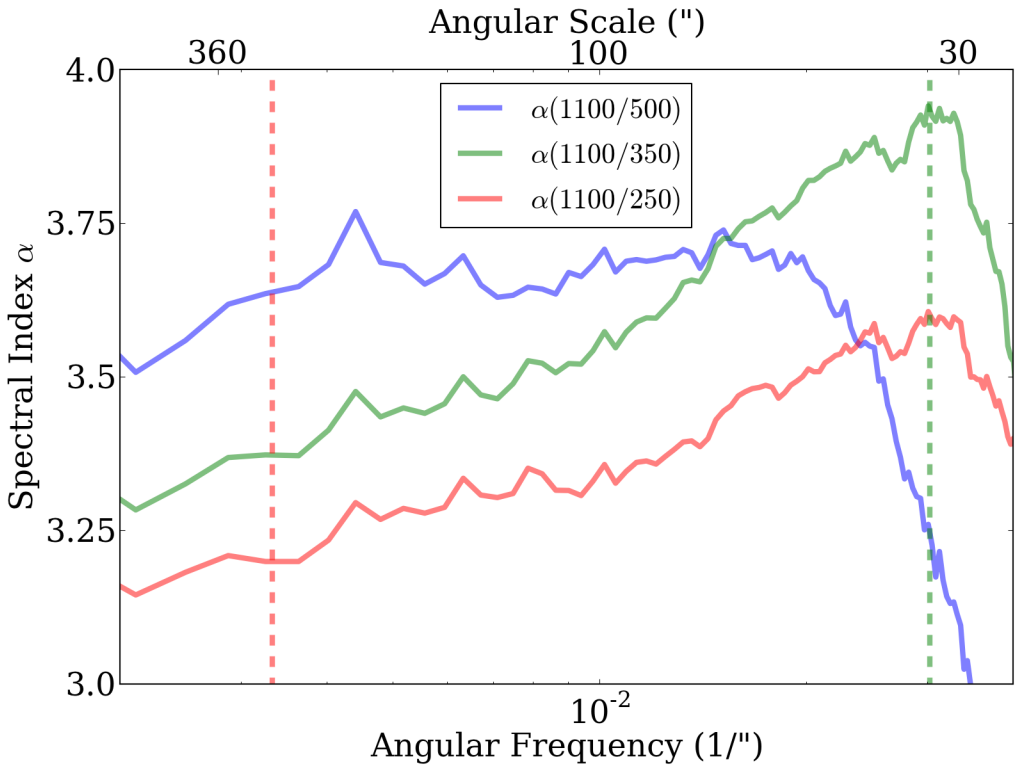

Figure 3.9 The 'spectral index' α_{nu} between the BGPS and the three Herschel-SPIRE bands as a function of angular scale. This figure shows the power spectrum ratio for the $\ell = 30°$ 1-square degree field. The vertical dashed lines are the same as in Figure 3.8: they show the largest angular scale the BGPS is sensitive to (red) and the beam FWHM at 33″ (green).

The dust spectral index is sensitive to both the temperature, which controls the location of the blackbody peak, and the dust opacity power-law index β, which controls the Rayleigh-Jeans slope. Depending on the properties of the dust, it is in some cases possible to constrain one parameter or the other. For high temperatures, T$\gtrsim$ 30 K, the Herschel SPIRE and BGPS wavelengths are firmly on the Rayleigh-Jeans (RJ) tail, and therefore can be used to constrain the slope of the RJ tail, i.e. the β index. For lower temperatures, with λ_{max} near one of the SPIRE wavelengths, the spectral indices constrain T but provide only weak constraints on β (though β measurements could be obtained by future comparison with 850 μm measurements from ATLASGAL or SCUBA-2).

To measure temperature and opacity properties, we identify the allowed T$-\beta$ parameter space for the measured spectral indices in two regimes: small angular scale ($40'' < dx < 100''$, selected to be larger than the 500 μm beam at $36''$) and large angular scale ($100'' < dx < 300''$). These two regimes are notably different in Figure 3.9, showing the short-wavelength spectral indices rising towards smaller angular scales while $\alpha_{500\mu\mathrm{m}}$ remains flat down to the Herschel beam size.

In Figure 3.10, we show the parameter space allowed by the full range of the spectral index measurements in the two angular scale regimes for $\ell = 30^\circ$. Small angular scales only have a lower-limit on temperature $T \gtrsim 20$ K and a reasonably narrow constraint on beta $1.8 \lesssim \beta \lesssim 2.3$. Large angular scales, however, have a temperature $15 < T < 25$ K and beta $2.1 \lesssim \beta \lesssim 2.6$. If the variation in observed α_ν is caused primarily by differing temperatures at different angular scales, which is very likely, the smallest structures exhibit the highest temperatures in the $\ell = 30^\circ$ region, implying that, at least in this region, local heating dominates large-scale heating of the dust.

3.7.3 Other Regions

We measured the power spectral density of both the Herschel Hi-Gal images and the BGPS images on a per-square-degree basis in the manner described in Section 3.7.1 and 3.7.

For some regions, in particular the Galactic Center, there is no allowed portion of T$-\beta$ parameter space covered by all three spectral indices. In the specific case of the Galactic Center, the prevalent synchrotron and free-free emission likely contaminate the spectral indices.

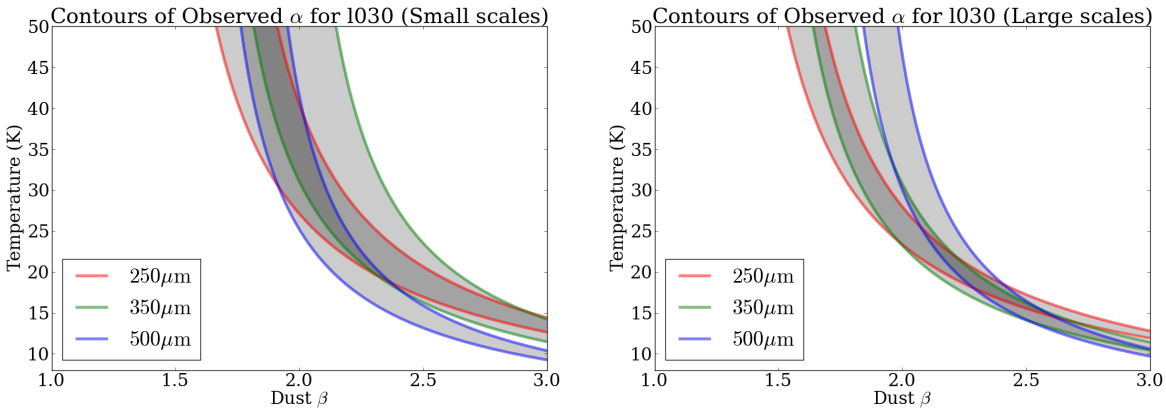

Figure 3.10 Contours of the 'spectral index' α_ν between the BGPS and the three Herschel-SPIRE bands on scales 40-100″ (left) and 100-300″ (right) for the $\ell = 30$ 1-square degree field. The grey zones show the full range of the measured spectral indices from plots like Figure 3.9. The darker grey areas show regions where one or more of the spectral indices overlap.

For $\ell \gtrsim 45^\circ$, the constraints on β tend toward upper limits at both large and small scale as the spectral indices get shallower. While there are exceptions for some 1-square-degree fields, for the area $\ell \gtrsim 45^\circ$ β is constrained to be $\beta \lesssim 2$ for large scales and $\beta \lesssim 1.8$ for small scales. In the inner galaxy, $\ell < 45$, more typically $2 \lesssim \beta$ on large scales, and β is more often larger on small scales.

These values are consistent with larger **spatial** scales having steeper β, since the same **angular** scale probes a larger **spatial** scale at $\ell < 45$ because the distance to the bulk of the emission is greater in the inner galaxy on average. However, the different properties at lower ℓ may be a consequence of averaging over a longer dusty line-of-sight.

3.8 Source Extraction

Rosolowsky et al. (2010) presented the Bolocat catalog of sources extracted from the v1.0 data with a watershed decomposition algorithm. We have used the same algorithm to create a catalog from the v2.0 catalog. We have also performed comparisons between the v1.0 and v2.0 data based on the extracted sources. The new catalog was derived using the same Bolocat parameters as in v1.0. This catalog includes regions that were not part of the v1.0 survey area, but we restrict our comparison between v1.0 and v2.0 to the area covered by both surveys.

3.8.1 Aperture Extraction

One major change from the v1.0 catalog is that the fluxes in the v2.0 catalog are reported with background subtracted. The backgrounds are calculated from the mode of the pixels in the range $[2R, 4R]$, where R represents the aperture radius ($20''$, $40''$, or $60''$). The mode is computed using the IDL astrolib routine `skymod.pro`, which returns the mean of the selected data if the mean $\bar{\mu}$ is less than the median $\mu_{1/2}$ (indicating low "contamination" from source flux) or $3\mu_{1/2} - 2\bar{\mu}$ otherwise, then performs iterative rejection of bad pixels (Landsman, 1995; Stetson, 1987).

We performed aperture extraction on simulated data sets to determine what size apertures are appropriate when comparing to other data sets. In Figure 3.11, we show the results of aperture

extraction with and without background subtraction on a simulated power-law generated image with $\alpha_{ps} = 2$ before and after pipeline processing. The map has had point sources added to it randomly distributed throughout the field with flux densities randomly sampled from the range $[0.1, 1]$ Jy, and the power-law extended flux has an amplitude ≈ 1.8 Jy. Sources are extracted from the pipeline-processed map using Bolocat, then the same source locations and masks are used to extract flux measurements from the input map. Figure 3.12 shows the input, pipeline-processed, and point-source-only maps along with the Bolocat apertures to give the reader a visual reference for an $\alpha_{ps} = 2$ background with point sources. The scatter between the flux density measurements derived from the input simulated sky map and the iteratively produced map is small when background subtraction is used (the blue points), but large and unpredictable otherwise (the red points).

The agreement between the flux densities extracted from the iterative map and the input synthetic map is excellent for $40''$ diameter background-subtracted apertures. For these apertures, the RMS of the difference between the iterative map and the input map fluxes is $\sigma = 0.03$ Jy when background subtraction is used, indicating the utility and necessity of this approach. The agreement is similarly good for $80''$ apertures ($\sigma = 0.10$ Jy), but the $120''$ apertures exhibit a source- and background-brightness dependent bias, so we recommend against apertures that large when comparing to other data sets.

There are caveats to this analysis. If the "background" power-law map has a peak flux density $\gtrsim 10\times$ the peak point-source flux density, the point sources will not be recovered: the cataloging algorithm will pick out peaks in the power law flux distribution. These cannot be analyzed with simple aperture extraction for an $\alpha_{ps} = 2$ flux density distribution. However, for shallower power-law distributions, i.e. $\alpha_{ps} \lesssim 1$, aperture extraction effectively recovered accurate flux-densities in the processed maps - shallow power-law distributions more strongly resemble point-source-filled maps.

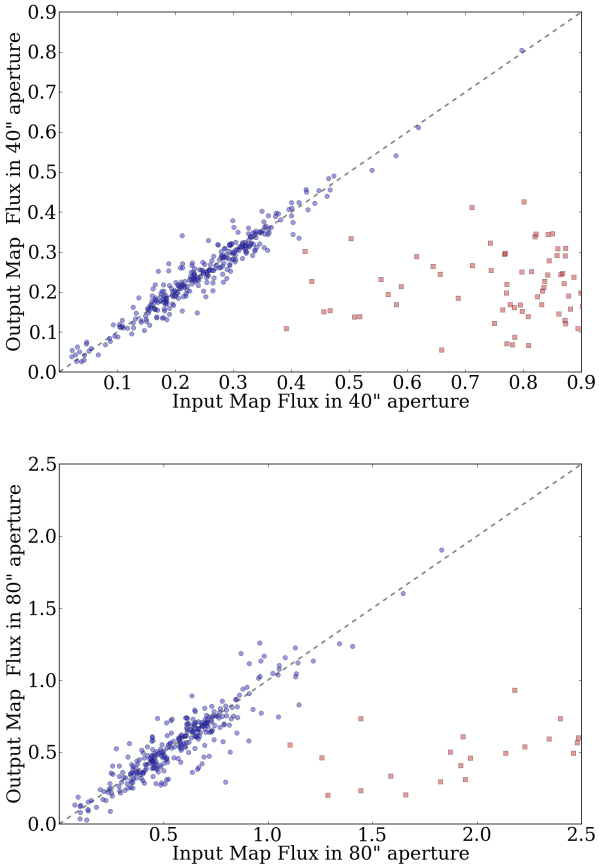

Figure 3.11 The aperture-extracted flux densities in a simulated map. Sources are identified from the pipeline-processed map, then flux densities are extracted from both the unprocessed input map and the pipeline-processed map. The X-axis shows the flux density of the source in the input map with (blue circles) and without (red squares) the flux density in a background annulus subtracted. Many of the red sources are not displayed as they are far to the right side of the plot, indicating poor agreement between the input and processed maps. The Y-axis shows the flux density extracted in the same aperture from the output pipeline-processed map. The black dashed line is the 1-1 line. The left plot shows 40″ and the right plot 80″ diameter apertures. Section 3.8 describes the background subtraction process; the v2.0 catalog reports background-subtracted flux density measurements.

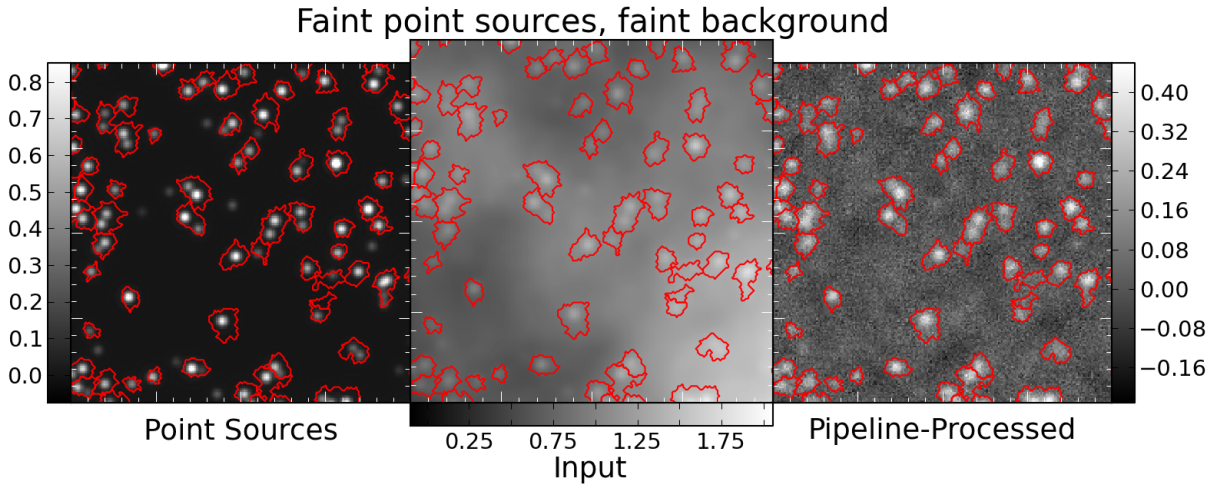

Figure 3.12 Images from a simulation of a power-law distributed background with $\alpha_{ps} = 2$ and point sources with peak flux densities in the range $[0.1, 1]$ Jy/beam. The left panel shows the pipeline-processed map, which was used to define the Bolocat masks shown as red contours. The colorbars show the flux density in units of Jy/beam. The power-law flux density distribution is evident as the structure between point sources in the left image; it is only weakly recovered by the pipeline because most of the power is on large angular scales and therefore filtered out.

3.8.2 Catalog Matching between v1.0 and v2.0

We matched the v1.0 and v2.0 catalogs based on source proximity. For each source in v1.0, we identified the nearest neighbor from v2.0, and found that 5741 v2.0 sources are the nearest neighbor for a v1.0 source out of 8004 v2.0 sources in the v1.0-v2.0 overlap region. Similarly, we identified the nearest neighbor in v1.0 for each v2.0 source, finding 5745 v1.0 sources are the nearest neighbor for a v2.0 source out of 8358 v1.0 sources. There are 5538 v1.0-v2.0 source pairs for which each member of the pair has the other as its nearest-neighbor. These sources are clearly reliable and stable source identifications and constitute about 70% of the v2.0 sample.

Most of the unmatched sources have low flux density (Figure 3.13), but some were significantly higher - these generally represent sources that were split or merged going from v1.0 to v2.0. A few examples of how mismatches can happen are shown in Figures 3.14 and 3.15. The low-flux-density sources were most commonly unmatched in regions where the noise in v1.0 and v2.0 disagreed significantly. The high-flux-density mismatches tend to be different decompositions of bright sources and are preferentially found near very bright objects, e.g. in the Galactic center region.

3.8.3 Source flux density, size, shape, and location distributions

We reproduce parts of Rosolowsky et al. (2010) Figures 17 and 19 as our own Figures 3.16 and 3.17. These figures show the distributions of extracted source properties (flux density, size, and aspect ratio) for the v1.0 and v2.0 data. The source flux density distributions above the completeness cutoff are consistent between v1.0 and v2.0, both exhibiting power-law flux density distributions

$$\frac{dN}{dS_\nu} \propto S_\nu^{-\alpha_{src}} \tag{3.3}$$

with values in the range $\alpha_{src} = 2.3 - 2.5$ for sources with $S_\nu \gtrsim 0.5$ Jy. In the left panel of Figure 3.16, we have included the v2.0 aperture-extracted data both with and without annular background subtraction. The v1.0 catalog had no background subtraction performed because the backgrounds were thought to be negligible, but the v2.0 catalog has had background subtraction performed so

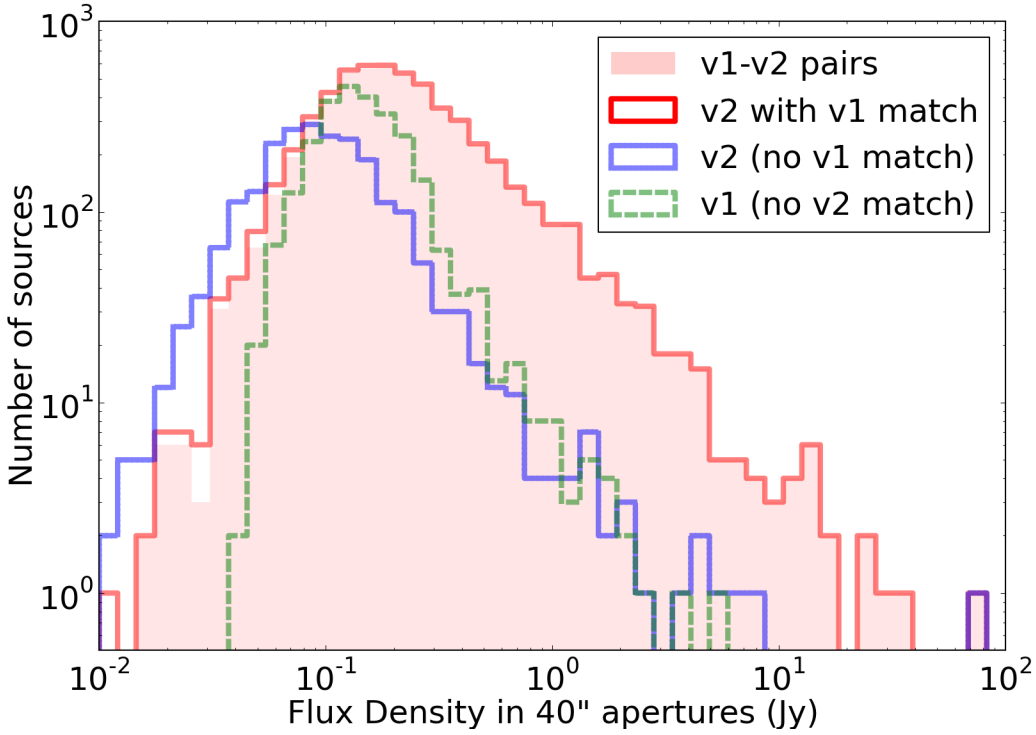

Figure 3.13 Histograms showing the sources matched between the v1.0 and v2.0 catalogs. Most of the v2.0 sources (5741 of 8004 v2.0 sources in the v1.0-v2.0 overlap region) have matches from v1.0, but there is a substantial population with no match. The unmatched sources tend to have lower flux densities. The shaded area shows 1-1 matches, while the solid red line shows one-way (unreciprocated) matches.

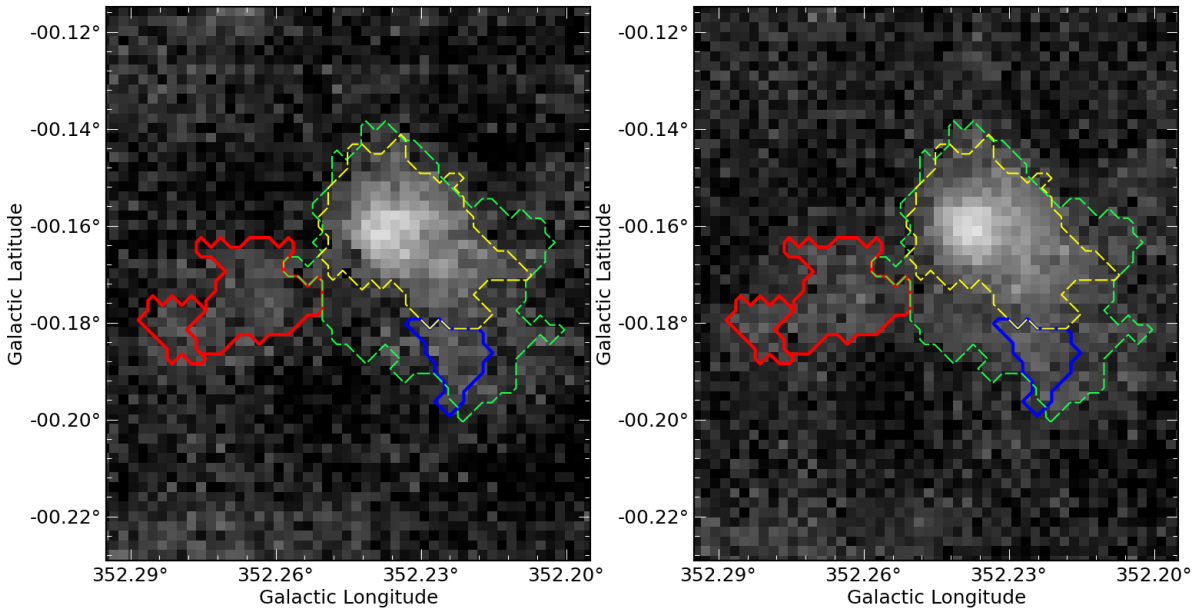

Figure 3.14 Contours of the extracted sources overlaid on grayscale images of a region in v1.0 (left) and v2.0 (right). The v1.0 data are scaled up by the 1.5× calibration correction. The red contours show new v2.0 sources with no v1.0 match, while the blue contours show v1.0 sources with no v2.0 match. The green and yellow contours show v2.0 and v1.0 sources with a one-to-one match, respectively. In this example, the v2.0 source is significantly larger than the v1.0 source and merges with a shoulder that was classified as a separate source in v1.0. Additional v2.0 sources are detected because of increased signal-to-noise in the red-contoured regions.

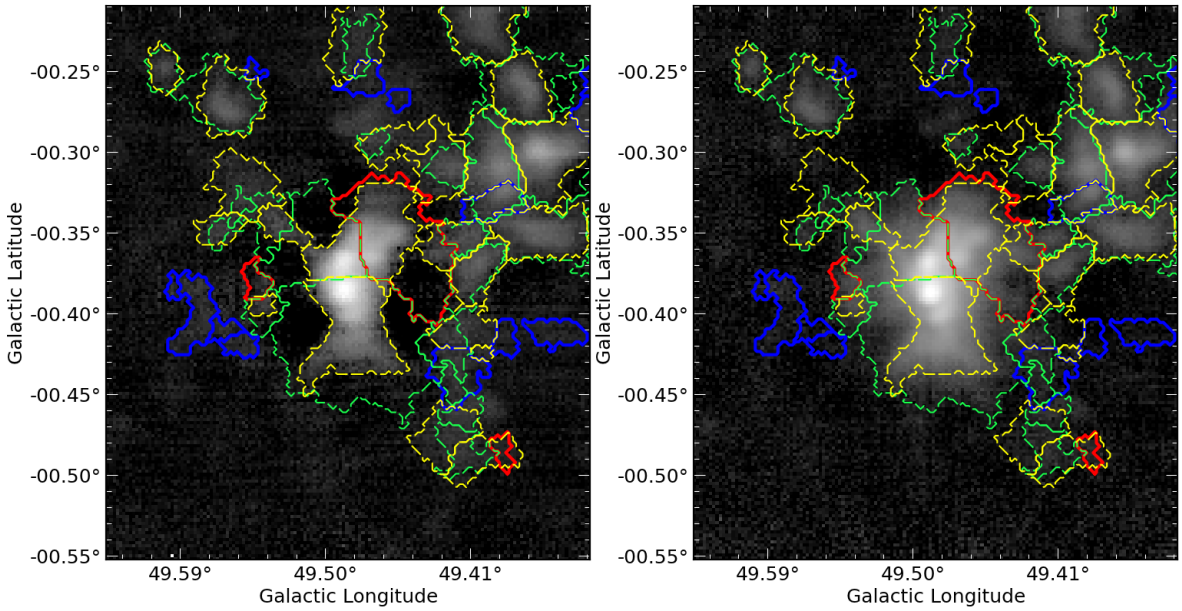

Figure 3.15 Same as Figure 3.14, but for the W51 complex. The area displayed is larger in order to encompass the entire source structure. The v2.0 sources are larger than the corresponding v1.0 sources because the negative bowl structures have been filled in. The red contours show regions where v2.0 sources were detected, but because of crowding no nearest-neighbor pair was identified in v1.0: there are more v2.0 sources than v1.0 sources. In this region, the brightest v2.0 sources are larger and brighter, but there are fewer fainter sources than in v1.0.

that the flux densities reported more accurately represent the sky. The v2.0 data include more large sources.

The longitude and latitude source flux density distribution plots, Figure 15 of Rosolowsky et al. (2010), are reproduced in Figure 3.18. The properties are generally well-matched, although even with the 1.5× correction factor to the v1.0 data, there is more flux density per square degree in v2.0 sources. The gain in flux density recovery is both because of an increased flux density recovery on large angular scales and because of improved noise estimation, which results in a greater number of pixels being included in sources (see Section 3.8.2 for more details and Figures 3.14 and 3.15 for examples).

A two-dimensional histogram providing a broad overview of the survey contents is shown in Figure 3.19. The ratio of source counts per half square degree is included in panel 3. This figure illustrates that the two catalog versions are broadly consistent, and the regions in which they differ significantly tend to have fewer sources. The most extreme ratios of v2.0 to v1.0 source counts tend to occur along field edges both because of preferentially low source counts and because the v2.0 images have slightly greater extents in latitude than the v1.0.

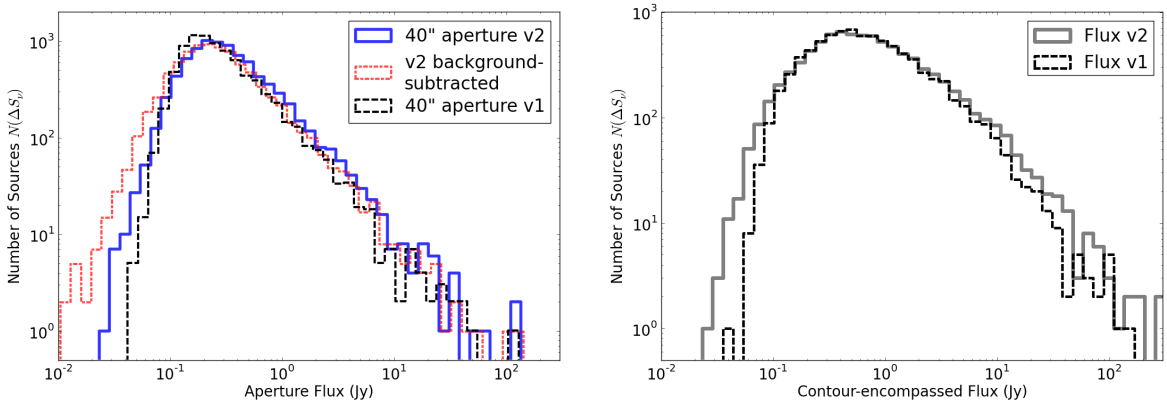

Figure 3.16 Comparisons of v1.0 and v2.0 flux density histograms. (*left*) Flux density distribution within 40″ diameter apertures. The 40″ apertures show the v2.0 data both with and without annular background subtraction; the v1.0 data are not background-subtracted. The histogram lines are slightly offset in order to minimize overlap. (*right*) Flux density distribution in contour-defined apertures. No background subtraction is performed for the contour-based flux densities in either version.

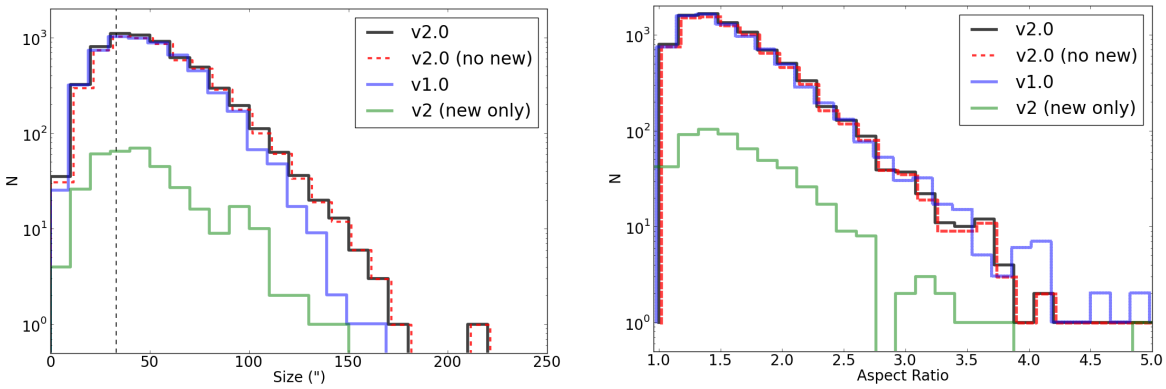

Figure 3.17 Distributions of deconvolved angular sizes (left) and aspect ratios (right) of sources in the BGPS catalog. The vertical dashed line in the left figure is plotted at the FWHM of the beam. The BGPS v2.0 includes newly observed regions not in the v1.0 survey, so separate histograms excluding the new (red dashed) and excluding the old (green solid) regions are shown. In both plots, the histograms are slightly offset to reduce line overlap.

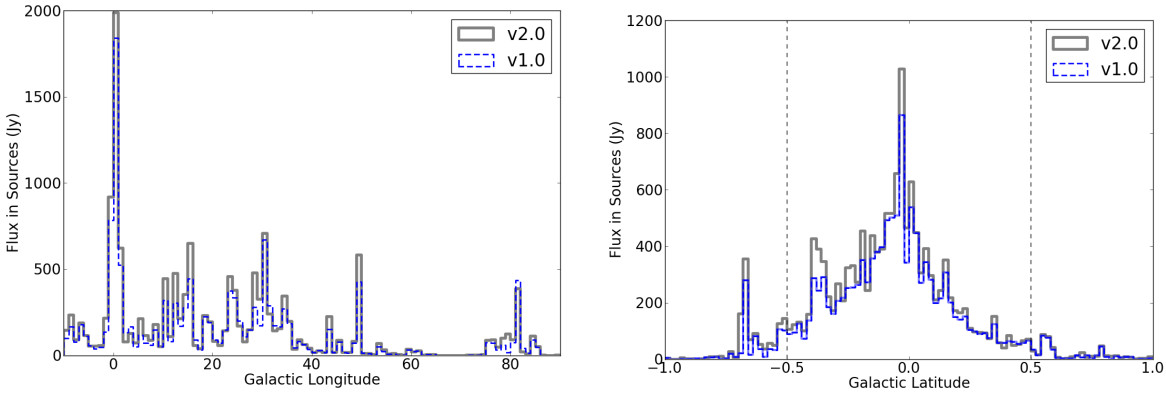

Figure 3.18 Distribution of total flux density in catalog sources as a function of longitude (*left*) and latitude (*right*) in the Galactic plane. The distributions contain sources extracted in the $-10^\circ < \ell < 90^\circ$ region. (*right*) Vertical dashed lines indicate the extent of complete coverage in the latitude direction ($\pm 0.5^\circ$). The large excess in v2.0 compared to v1.0 at $b \sim -0.4$ is due to the W51 complex, in which the flux density recovered in v2.0 was 1.5× greater than in v1.0, largely because of reduced negative bowls around the brightest two sources (see Figure 3.15).

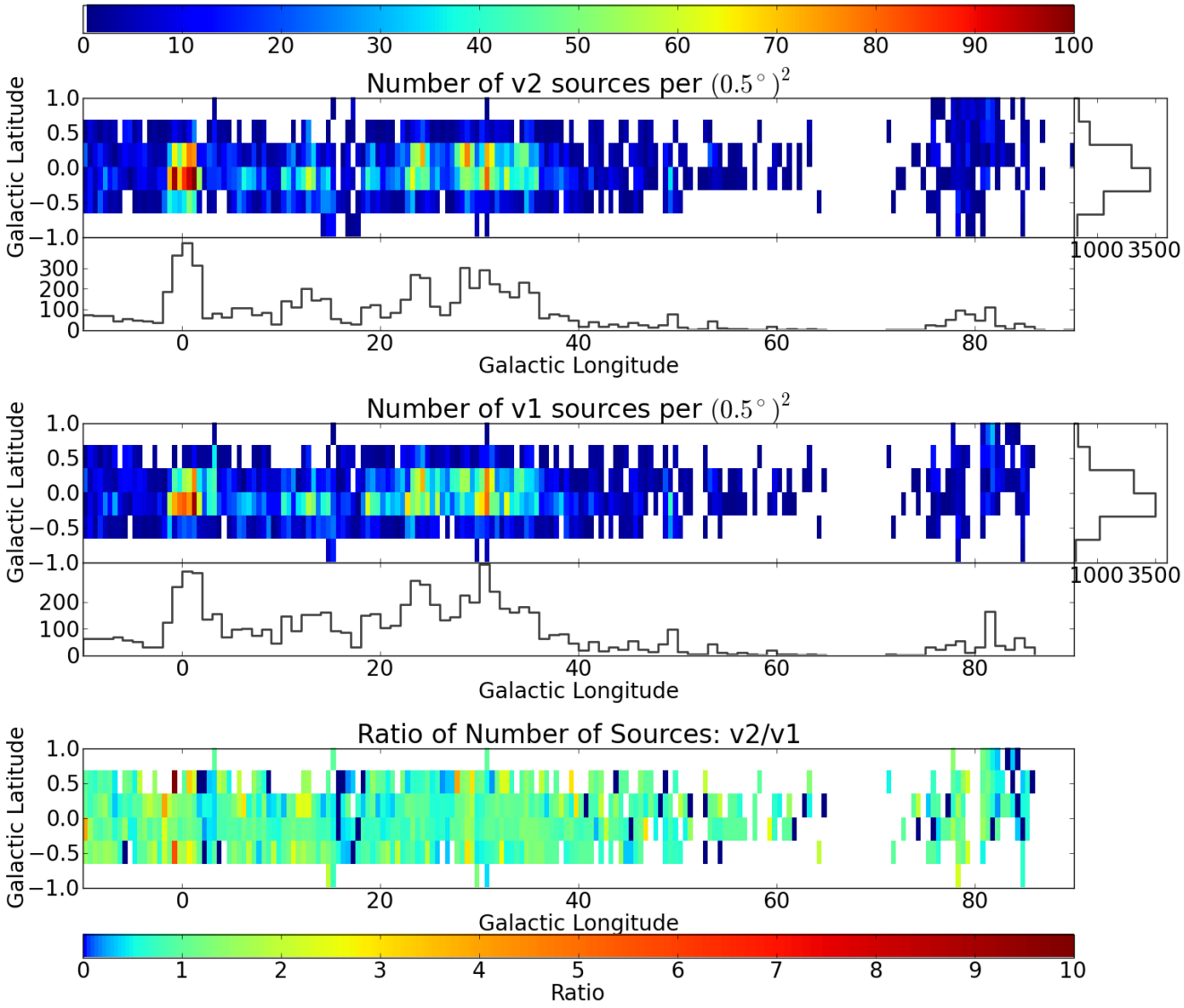

Figure 3.19 The two-dimensional distribution of source counts in both v1.0 and v2.0. The colors in the first two panels illustrate the number of sources per half-degree-squared bin as indicated by the top colorbar. The bottom colorbar labels the ratio of the count of v2.0 to v1.0 sources. The histograms are coarse versions of Figure 3.16 and show the projection of the 2D histograms along each axis. A preference toward negative-latitude sources is evident at $\ell < 60°$, corresponding to our view of the Galaxy from slightly above the plane.

3.9 Conclusions

We presented Version 2 of the Bolocam Galactic Plane Survey, which is a significant improvement over v1.0 in pointing and flux calibration accuracy. The v2.0 data show an improvement in large angular scale recovery. The v2.0 release includes new observations of regions in the outer galaxy.

- We have characterized the angular transfer function of the Bolocam pipeline. Flux recovery is $> 95\%$ for scales between $33'' < dx < 100''$. The angular transfer function shows a sharp drop in recovered power above $\gtrsim 100''$ scales.

- We compared the pointing of the BGPS to that in Hi-Gal, and found that the surveys are consistent to within the measurement error $\sigma \approx 3.5''$.

- We measured the power spectral density in some regions and compared it to that in Hi-Gal, concluding that the power spectra are consistent with the normally used dust emissivity values in the range $\beta \sim 1.5 - 2$. The largest-scale structures appear to be the coolest.

- A new version of the catalog has been released. The improved quality of the v2.0 images has some effects on the BGPS catalog but the basic statistical properties of the catalog have not significantly changed. Because of changing noise properties within the images, only 70% of the individual sources in v2.0 have an obvious v1.0 counterpart and vice versa. The remaining 30% of sources do not have obvious counterparts because of two effects:

  (1) At low significance, changing noise levels recover different features at marginal significance. It is likely that low significance sources in v1.0 and v2.0 are **both** real features but have been rejected in the other catalog because of the relatively conservative limits placed on catalog membership.

  (2) At high significance, the catalog algorithm is dividing up complex structure using the underlying watershed algorithm. In this case, the precise boundaries between objects

are sensitive to the shape of the emission. All of the high significance features appear in both catalogs, but the objects to which a piece of bright emission are assigned can vary.

Despite these changes in the catalogs, the overall statistical properties of the population show little variation except that the largest sources appear brighter and larger owing to better recovery of the large scale flux density.

Chapter 4

Bound HII regions and Young Massive Protoclusters

4.1 Preface

During a visit from Eli Bressert, we discussed methods of identifying the precursors to young massive clusters. A central idea was that the primary unbinding energy comes from ionized gas, so that if a region could remain bound against the pressure provided by ionized gas, it would proceed to high star formation efficiency. This notion resulted in two papers: the theory paper (Bressert et al., 2012b) and the observational paper (Ginsburg et al., 2012). The observational paper, which summarizes the population of proto-YMCs discovered in the BGPS, is reproduced here.

Since this paper is a Letter, a great deal of the work that went in to this chapter is hidden in a few short phrases. In particular, the search for distances to the candidate source occupied an enormous amount of time and will be the limiting factor in future searches for candidate proto-clusters.

Since its publication, parts of the proposed follow-up work were carried out by another group. At the end of this chapter, I incorporate their new data to enhance our results and re-measure the Cluster Formation Rate $1 < CFR < 3$ Myr^{-1} $(1-\sigma)$ more accurately.

4.1.1 Abstract

We search the $\lambda = 1.1$ mm Bolocam Galactic Plane Survey for clumps containing sufficient mass to form $\sim 10^4$ $M_\odot$ star clusters. 18 candidate massive proto-clusters are identified in the first Galactic quadrant outside of the central kiloparsec. This sample is complete to clumps with mass

$M_{\rm clump} > 10^4\ M_\odot$ and radius $r \lesssim 2.5$ pc. The overall Galactic massive cluster formation rate is $CFR(M_{\rm cluster} > 10^4) \lesssim 5\ {\rm Myr}^{-1}$, which is in agreement with the rates inferred from Galactic open clusters and M31 massive clusters. We find that all massive proto-clusters in the first quadrant are actively forming massive stars and place an upper limit of $\tau_{starless} < 0.5$ Myr on the lifetime of the starless phase of massive cluster formation. If massive clusters go through a starless phase with all of their mass in a single clump, the lifetime of this phase is very short.

4.2 Introduction

The Milky Way contains about 150 Globular clusters (GCs) with masses of 10^4 to over 10^6 $M_\odot$ and tens of thousands of open clusters containing from 100 to over 10^4 stars. However, young massive clusters containing $\gtrsim 10^4\ M_\odot$ of stars are rare, with only a handful known (Portegies Zwart et al., 2010). While no GCs have formed in the Milky Way within the last 5 Gyr, open clusters that survive many crossing times continue to form. A few of these clusters have stellar masses greater than 10^4 $M_\odot$ and therefore qualify as young massive clusters (YMCs; Portegies Zwart et al., 2010). YMCs must either form from clumps having masses greater than and sizes comparable to the final cluster or be formed from a larger, more diffuse reservoir, in which case massive protocluster clumps may be rare or nonexistent (Kennicutt & Evans, 2012).

Massive proto-clusters (MPCs) are massive clusters ($M_{\rm cluster} > 10^4\ M_\odot$) in the process of forming from a dense gas cloud. In Bressert et al. (2012b), we examine the theoretical properties of MPCs: MPCs are assumed to form from massive, cold starless clumps analagous to pre-stellar cores (Williams et al., 2000). In this paper, we refer to two classes of objects: starless MPCs, which have very low luminosity and do not contain OB stars, and MPCs, which are gas-rich but have already formed OB stars. The only currently known starless MPC is G0.253+0.016, which lies within the dense central molecular zone and is subject to greater environmental stresses than similar objects in the Galactic plane (Longmore et al., 2012).

Because massive clusters contain many massive stars, at some point during their evolution ionization pressure will prevail over protostellar outflows as the dominant feedback mechanism.

Other sources of feedback are less than ionization pressure up until the first supernova explosion (Bressert et al., 2012b). These proto-clusters must have masses $M_{clump} > M_*/SFE$ [1] , or about $3 \times 10^4\ M_\odot$ for an assumed SFE=30% (an upper limit on the star formation efficiency), confined in a radius $r \lesssim 2.5$ pc, in order to remain bound against ionization feedback. These properties motivate our search for proto-clusters in the Bolocam Galactic Plane Survey (BGPS; Aguirre et al., 2011, `http://irsa.ipac.caltech.edu/data/BOLOCAM_GPS/`).

The distinction between relatively short-lived 'open clusters' and long-lived ($t \gtrsim 1$ Gyr) bound clusters occurs at about $10^4\ M_\odot$ (Portegies Zwart et al., 2010). Clusters with $M_{cluster} < 1 \times 10^4 M_\odot$ will be destroyed by interactions with giant molecular clouds over the course of a few hundred million years after they have dispersed their gas (Kruijssen et al., 2011b), while clusters with $M_{cluster} \gtrsim 10^4 M_\odot$ may survive $\gtrsim 1$ Gyr. Closer to the Galactic center, within approximately a kiloparsec, all clusters will be destroyed on shorter timescales by strong tidal forces or interactions with molecular clouds.

In the Galaxy, there are few known massive clusters. Portegies Zwart et al. (2010) catalogs a few of them, of which NGC 3603, Trumpler 14, and Westerlund 1 and 2 are the likely descendants of the objects we investigate. These clusters have $r_{eff} \lesssim 1$ pc, $M \sim 10^4\ M_\odot$, and ages $t \lesssim 4$ Myr. We present a census of their ancestral analogs.

4.3 Observations and Analysis

4.3.1 The Bolocam Galactic Plane Survey

The BGPS is a 1.1 mm survey of the first quadrant of the Galactic plane in the range $-0.5 < b < 0.5$ with resolution $\sim 33''$ sensitive to a maximum spatial scale of $\sim 120''$ (Aguirre et al., 2011; Ginsburg et al., 2013a). The BGPS 'Bolocat' v1.0 catalog includes sources identified by a watershed decomposition algorithm and flux measurements within apertures of radius $20''$, $40''$, and $60''$ (Rosolowsky et al., 2010).

We searched the BGPS for candidate MPCs in the 1st quadrant ($6 < \ell < 90$; 5991 sources).

[1] We define a star formation efficiency $SFE = M_{*,final}/M_{gas,initial}$.

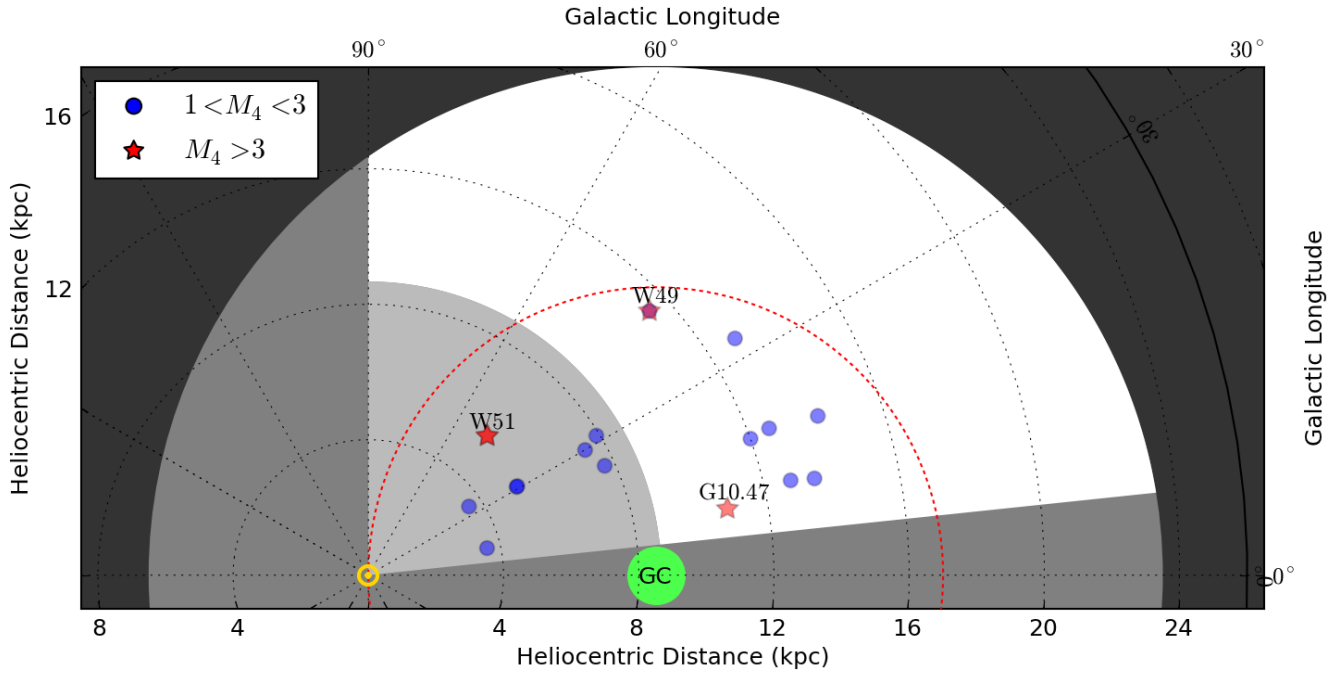

Figure 4.1 Plot of the massive proto-cluster (MPC) candidates overlaid on the Galactic plane. The green circle represents the galactic center, and the yellow $\odot$ is the Sun. A 15 kpc radius disc centered on the Galactic Center indicates the approximate extent of Galactic star formation. The white region indicates the coverage of the Bolocam Galactic Plane survey and our source selection limits based on distance and longitude. The inner cutoff (light grey) is the nearby incompleteness limit set by the Bolocam spatial filtering; the catalog includes sources but is incomplete in this region. The red dashed circle traces the solar circle. Blue filled circles represent initial candidates that passed the mass-cutoff criterion $M(20K) > 10^4\ M_\odot$; red stars are those with $M(20K) > 3 \times 10^4 M_\odot$. In the legend, M_4 means mass in units of $10^4 M_\odot$.

The inner 6 degrees of the Galaxy are excluded because physical conditions are significantly different from those in the rest of the galaxy (Yusef-Zadeh et al., 2009) and the BGPS is confusion-limited in that region.

4.3.2 Source Selection & Completeness

We identify a flux-limited sample by setting our search criteria to include all sources with $\mathrm{M_{clump}} > 10^4\ M_\odot$ in a $20''$ radius out to 26 kpc, or a physical radius of 2.5 pc at that distance. The radius cutoff is motivated by completeness and physical considerations: the cutoff of 26 kpc includes the entire star forming disk in our targeted longitudes, and $r = 2.5$ pc corresponds to the radius at which a $3 \times 10^4\ M_\odot$ mass has an escape speed $v_{esc} = 10$ km s^{-1}, i.e. ionized gas will be bound. The maximum radius and minimum mass imply a minimum mean density $\bar{n} = 6 \times 10^3$ cm^{-3}, which implies a maximum free-fall time $t_{ff} < 0.65$ Myr.

Using the Bolocat v1.0 catalog, we first set a flux limit on the sample by assuming the maximum distance of $d = 26$ kpc and imposing a mass cutoff of $\mathrm{M_{clump}} \geq 10^4\ M_\odot$ inside a $20''$ (2.5 pc) radius aperture. Following equation 19 in Aguirre et al. (2011):

$$\mathrm{M_{gas}} \approx 14.3 \left(e^{13.0/T_d} - 1\right) \left(\frac{S_\nu}{1\ \mathrm{Jy}}\right) \left(\frac{D}{1\ \mathrm{kpc}}\right)^2 M_\odot \tag{4.1}$$

and assuming $T_{dust} = 20$K, the implied flux cutoff is 1.13 Jy [2] , above which 456 'flux-cutoff' candidates were selected in the Bolocat v1.0 catalog. Cutoffs of 4.3 Jy for the $40''$ and 10.2 Jy for the $60''$ Bolocat v1.0 apertures were used to select more nearby candidates inside the same physical radius, but no sources were selected based on these larger apertures.

The BGPS is insensitive to scales larger than $120''$ (Ginsburg et al., 2013a)[3] . As a result, the survey is incomplete below a distance

$$D_{min} = 8.7 \left(\frac{r_{cluster}}{2.5\mathrm{pc}}\right) \mathrm{kpc}$$

[2] As per Rosolowsky et al. (2010), Aguirre et al. (2011), and Ginsburg et al. (2013a), a factor of 1.5 calibration correction and 1.46 aperture correction are required for the $20''$ radius aperture fluxes reported in the catalog. These factors have been applied to the data.

[3] Ginsburg et al. (2013a) presents v2.0 of the BGPS

from the Sun. Within this radius, alternate methods must be sought to determine the total mass within $r_{cluster} < 2.5$ pc. Although the sample is incomplete for $D < 8.7$ kpc, sources that have sufficient mass despite the $120''$ spatial filtering are included.

Distances to BGPS-selected candidates were determined primarily via literature search. Where distances were unavailable, we used velocity measurements from Schlingman et al. (2011) and assumed the far distance for source selection. We then resolved the kinematic distance ambiguity towards these sources by searching for associated near-infrared stellar extinction features from the UKIDSS GPS (Lucas et al., 2008). Most literature distances were determined using a rotation curve model and some method of kinematic distance ambiguity resolution. Because the literature used different rotation curve models, there is a $\sim 10\%$ systematic error in distance resulting in a $\sim 20\%$ systematic error in mass. We used the larger $40''$ radius apertures to determine the flux for sources at $D < 13.0$ kpc and $60''$ radius apertures for sources at $D < 8.7$ kpc (corresponding to $r < 2.5$ pc).

The masses were computed assuming a temperature $T_{dust} = 20$K, opacity $\kappa_{271.1GHz} = 0.0114$ cm^{2}g^{-1}, and gas-to-dust ratio of 100 (Aguirre et al., 2011) [4] . The mass estimate drops by a factor of 2.38 if the temperature assumed is doubled to $T_{dust} = 40$K.

Ginsburg et al. (2011b) notes that significant free-free contamination, as high as 80%, is possible for some 1.1 mm sources, so the selected candidates may prove to be more moderate-mass and evolved proto-clusters. We used the NRAO VLA Archive Survey (NVAS; Crossley et al., 2008) to estimate the free-free contamination for the sample. For most sources, the free-free contamination inferred from the VLA observations is small ($< 20\%$), but for a subset the contamination was $\sim 20 - 35\%$ assuming that the free-free emission is optically thin. Corrected masses using the measured free-free contamination and higher dust temperatures are listed in Table 4.1; these are reasonable lower limits on the total mass of these regions. All of the contamination estimates are technically lower limits both because of the assumption that the free-free emission is optically thin

[4] $T_{dust} = 20$K is more appropriate for a typical pre-star-forming clump than an evolved HII-region hosting one (Dunham et al., 2010, e.g.). However, because we are interested in cold progenitors as well as actively forming clusters, the selection is based on $T_{dust} = 20$K, which is more inclusive.

and because the VLA filters out large-scale flux. However, in most cases, the emission is likely to be dominated by optically thin emission (evolved HII regions tend to be optically thin and bright, while compact HII regions are optically thick but relatively faint; Keto, 2002) and for most sources VLA C or D-array observations were used, and at 3.6 and 6 cm the largest angular scale recovered is 180-300 $''$, greater than the largest angular scale in the BGPS.

Applying a cutoff of $\mathrm{M_{clump}} > 10^4\ M_\odot$ left 18 protocluster candidates out of the original 456. The more stringent cut $\mathrm{M_{clump}} > 10^4/SFE \approx 3 \times 10^4\ M_\odot$ leaves only 3 MPCs .

The final candidate list contains only sources with $M(20K) > 10^4 M_\odot$ (the completeness limit; see Table 4.1). The table lists their physical properties, their literature distance, their mass (assuming $T_{dust} = 20$ and $40K$ and a free-free subtracted lower-limit) , and their inferred escape speed ($v_{esc} = \sqrt{2GM(20K)/r}$) assuming a radius equal to the aperture size at that distance. The table also includes measurements of the IRAS luminosity in the 60 and 100 μm bands within the source aperture.

4.3.3 Source Separation

These 18 candidates include some overlapping sources. There are two clumps in W51 separated by about 1.5 pc and 4.5 km s^{-1} along the line of sight that are each independently massive enough to be classified as MPCs, but are only discussed as a single entity because they are likely to merge if their three-dimensional separation is similar to their projected distance. The candidates in W49 are more widely separated, about 4.4 pc and 7 km s^{-1} along the line of sight, but could still merge.

Additionally, 9 of the 18 are within 8.7 kpc, so the mass estimates are lower limits. These are promising candidates for follow-up, but cannot be considered complete for population studies. If our radius restriction is dropped to 1.5 pc, the minimum complete distance drops to 5.2 kpc and the three lowest-mass sources in Table 4.1 no longer qualify, but otherwise the source list remains unchanged. Our analysis is therefore robust to the selection criteria used.

4.4 Results

4.4.1 Cluster formation rate

The massive clumps in Table 4.1 can be used to constrain the Galactic formation rate of massive clusters (MCs) above 10^4 $M_\odot$ if we assume that the number of observed proto-clusters is a representative sample. The region surveyed covers a fraction of the surface area of the Galaxy $f_{observed} = A_{survey}/A_{Galaxy} \approx 30\%$ assuming the star forming disk has a radius of 15 kpc[5] . The cumulative cluster formation rate above a cluster mass M_{cl} is given by

$$CFR(>\mathrm{M}_{cl}) = \frac{N_{MPC}}{\tau_{SF} f_{observed}}$$

where $\tau_{SF} \approx 2$ Myr is the assumed cluster formation timescale [6] . With the measured $N_{MPC}(\mathrm{M_{cluster}} > 10^4 M_\odot) = 3$ proto-clusters, we infer a Galactic formation rate

$$CFR \lesssim 5 \left(\frac{\tau_{SF}}{2 \text{ Myr}}\right)^{-1} \text{ Myr}^{-1}$$

This cluster formation rate is statistically weak, with Poisson error of about 3.5 Myr^{-1} and can be improved with more complete surveys (e.g., Hi-Gal, Molinari et al., 2010). This formation rate is an upper limit because all of the estimated masses are upper limits as discussed in Section 4.3.2.

4.4.2 Comparison to Clusters in Andromeda

We use cluster observations in M31 from Vansevičius et al. (2009) to infer the massive cluster formation rate in M31. They observe 2 clusters with $\mathrm{M_{cluster}} > 10^4 M_\odot$ and ages < 10 Myr in 15% of the M31 star-forming disk. The implied cluster formation rate in Andromeda is $\dot{N_{cl}} = N_{cl}/0.15/(10 \text{ Myr}) \approx 1.3 \text{ Myr}^{-1}$. Given M31's total star formation rate $\sim 5\times$ lower than the Galactic rate (Andromeda $\dot{M} = 0.4$, Milky Way $\dot{M} = 2\ M_\odot\ \mathrm{Myr}^{-1}$; Barmby et al., 2006; Chomiuk & Povich, 2011), the predicted Galactic cluster formation rate is $\dot{N_{cl}}(MW) = 5\ \dot{N_{cl}}(M31) = 6.5$

[5] The observed fraction of the galaxy changes to 21% if we only include the area within the solar circle as discussed in §5.8.

[6] τ_{SF}, the time from the start of star formation until gas expulsion, is a poorly understood quantity, but is reasonably constrained to be $\gtrsim 1$ Myr from the age spread in the Orion Nebula cluster (Hillenbrand, 1997) and $\lesssim 10$ Myr because the most massive stars will go supernova by that time.

Myr^{-1} (assuming the CFR scales linearly with the SFR; Bastian, 2008). The scaled-up Andromeda cluster formation rate matches the observed Galactic cluster formation rate. The samples are small, but as a sanity check, the agreement is comforting.

4.4.3 Star Formation Activity

In the sample of potential proto-clusters, all have formed massive stars based on a literature search and IRAS measurements. A few of the low mass sources, G012.209-00.104, G012.627-00.016, G019.474+00.171, and G031.414+00.307 have relatively low IRAS luminosities ($L_{IRAS} = L_{100} + L_{60} < 10^5 L_\odot$) and little free-free emission. However, **all** are detected in the radio as H II regions (some ultracompact) and have luminosities indicating early-B type powering stars.

Non-detection of 'starless' proto-cluster clumps implies an upper limit on the starless lifetime. For an assumed $\tau_{sf} \sim 2$ Myr, the 1σ upper limit on the starless proto-MC clump is $\tau_{starless} < (\sqrt{N_{cl}}/N_{cl})\tau_{sf} = 0.5$ Myr assuming Poisson statistics and using all 18 sources. This limit is consistent with massive star formation on the clump free-fall timescale ($\tau_{ff} \leq 0.65$ Myr). It implies that massive stars form rapidly when these large masses are condensed into cluster-scale regions and hints that massive stars are among the first to form in massive clusters.

4.5 Discussion

Assuming a lower limit 30% SFE and $\mathrm{T}_{dust} = 20$K, 3 candidates in Table 4.1 will become massive clusters like NGC 3603: G010.472+00.026, W51, and W49 (G043.169+00.01). Even if $\mathrm{T}_{dust} = 40$K, W49 is still likely to form a $\sim 10^4\ M_\odot$ MC, although G10.47 would be too small. W51, which is within the spatial-filtering incompleteness zone, passes the cutoff and is likely to form a pair of massive clusters. However, if the dust in W51 is warm and the free-free contamination is considered, the total mass in each of the W51 clumps is below the $3{\times}10^4\ M_\odot$ cutoff.

The BGPS covers about 30% of the Galactic star-forming disk in the range 1 kpc $< R_{gal} <$ 15 kpc. We can extrapolate our 3 detections to predict that there are $\leq$10 ($\pm$6) proto-clusters in the Galaxy outside of the Galactic center. The agreement between the SFR-based prediction from M31

and our observations implies that we have selected genuine massive proto-clusters (MPCs).

These most massive sources have escape speeds greater than the sound speed in ionized gas, indicating that they can continue to accrete gas even after the formation of massive stars. Assuming they are embedded in larger-scale gas reservoirs, we are measuring lower bounds on the 'final' clump plus cluster mass.

All of the young massive proto-clusters candidates observed are within the solar circle despite our survey covering more area outside of the solar circle. The outer radius limit for massive cluster formation is consistent with the observed metallicity shift noted at the same radius by Lépine et al. (2011). They identify the solar circle as the corotation radius of pattern speed and orbits within the Galaxy (within this radius, stars orbit faster than the spiral pattern). The fact that this radius also represents a cutoff between the inner, massive-cluster-forming disk and the outer, massive-cluster-free disk hints that gas crossing spiral arms may be the triggering mechanism for massive cluster formation. However, given the small numbers, the detected clusters are consistent with a gaussian + exponential disk distribution following that described by Wolfire et al. (2003).

Future work should include a census for MPCs within $D \lesssim 5$ kpc using the Herschel Hi-Gal survey (Molinari et al., 2010) and in the Southern plane with ATLASGAL (Schuller et al., 2009). Some surveys have already identified proto-clusters in these regions (e.g. Faúndez et al., 2004; Battersby et al., 2011), but they are not complete. A complete survey of distances will be essential for continuum surveys to be used.

There are two modes of massive cluster formation consistent with our observations that can be observationally distinguished. Either a compact starless massive proto-cluster phase does occur and is short, or the mass to be included in the cluster is accumulated from larger volumes over longer timescales. Extending our proto-cluster survey to the Southern sky, e.g. using the ATLASGAL and Hi-Gal surveys, will either discover starless MPCs or strengthen the arguments that there is no starless MPC phase. If instead massive clusters form by large scale ($r > 2.5$ pc) accretion, substantial reservoirs of gas should surround these most massive regions and be flowing into them. Signatures of this accretion process should be visible: MPCs should contain molecular filamentary

structures feeding into their centers (e.g. Correnti et al., 2012; Hennemann et al., 2012; Liu et al., 2012). Alternatively, lower mass clumps may merge to form massive clusters (Fujii et al., 2012), in which case clusters of clumps - which should be detectable in extant galactic plane surveys - are the likely precursors to massive clusters. Finally, massive clusters may form from the global collapse of structures on scales larger than we have probed, which could also produce clusters of clumps.

4.6 Conclusions

Using the BGPS, we have performed the first flux-limited census of massive proto-cluster candidates. We found 18 candidates that will be part of the next generation of open clusters and 3 that could form massive clusters similar to NGC 3603 ($\mathrm{M_{cluster}} > 10^4\ M_\odot$). We have measured a Galactic massive cluster formation rate $CFR(\mathrm{M_{cluster}} > 10^4) \lesssim 5\ \mathrm{Myr}^{-1}$ assuming that clusters are equally likely to form everywhere within the range 1 kpc $< R_{gal} <$ 15 kpc. The observed MPC counts are consistent with observed cluster counts in Andromeda scaled up by SFR_{M31}/SFR_{MW} assuming a formation timescale of 2 Myr.

Despite this survey being the first sensitive to pre-star-forming MPC clumps, none were detected. This lack of detected pre-star-forming MPCs suggests a timescale upper limit of about $\tau_{starless} < 0.5$ Myr for the pre-massive-star phase of massive cluster formation, and hints that massive clusters may never form highly condensed clumps ($\bar{n} \gtrsim 10^4\ \mathrm{cm}^{-3}$) prior to forming massive stars. It leaves open the possibility that massive clusters form from large-scale ($\gtrsim 10$ pc) accretion onto smaller clumps over a prolonged ($\tau > 2$ Myr) star formation timescale.

Observations are needed to distinguish competing models for MC formation: Birth from isolated massive proto-cluster clumps, either compact and rapid or diffuse and slow, or from smaller clumps that never have a mass as large as the final cluster mass. This sample of the 18 most massive proto-cluster clumps in the first quadrant (where they can be observed by both the VLA and ALMA) presents an ideal starting point for these observations.

Table 4.1 Massive Protocluster Candidates detected in the Bolocam Galactic Plane Survey with $M > 10^4 M_\odot$

Name	Common Name	Distance kpc	M(20K) $1000 M_\odot$	M(40K) $1000 M_\odot$	[a]M(min) $1000 M_\odot$	Radius pc	$\bar{n}(H_2)$ $10^4 \mathrm{cm}^{-3}$	v_{esc} km s^{-1}	[b]f_{ff}	L(IRAS) $10^5 L_\odot$
G010.472+00.026	G10.47	10.8[7]	38	16	16	2.1	1.4	12.7	0.01	5.0
G012.209-00.104	-	13.5[7]	14	6	5	1.3	2.3	9.9	0.05	0.61
G012.627-00.016	-	12.8[9]	10	4	3	2.5	0.2	5.9	0.05	0.59
G012.809-00.200	W33	3.6[7]	12	5	3	1.0	3.8	10.2	0.32	3.0
G019.474+00.171	-	14.1[12]	11	4	4	1.4	1.6	8.6	0.02	0.26
G019.609-00.233	G19.6	12.0[7]	26	11	7	2.3	0.7	10.0	0.31	6.4
G020.082-00.135	IR18253	12.6[10]	13	5	4	2.4	0.3	6.8	0.14	2.8
G024.791+00.083	G24.78	7.7[11]	14	6	5	2.2	0.4	7.4	0.11	1.5
G029.955-00.018	-	7.4[3]	10	4	2	2.2	0.3	6.4	0.34	5.3
G030.704-00.067	W43b	5.1[6]	11	4	4	1.5	1.1	8.0	0.11	1.0
G030.820-00.055	W43a	5.1[10]	11	4	4	1.5	1.2	8.1	0.13	1.9
G031.414+00.307	G31.41	7.9[2]	18	7	7	2.3	0.5	8.3	0.05	0.8
G032.798+00.193	G32.80	12.9[1]	22	9	7	2.5	0.5	8.9	0.27	6.9
G034.258+00.154	G34	3.6[4]	13	5	4	1.0	4	10.5	0.12	2.7
G043.164-00.031	W49	11.4[5]	24	10	6	2.2	0.7	9.7	0.38	9.9
G043.169+00.009	W49	11.4[5]	120	52	39	2.2	4	22.2	0.25	16.0
G049.489-00.370	W51IRS2	5.4[8]	48	20	14	1.6	4.3	16.2	0.27	4.5
G049.489-00.386	W51MAIN	5.4[8]	52	22	15	1.6	4.7	17.0	0.29	4.7

1: Araya et al. (2002), 2: Churchwell et al. (1990), 3: Fish et al. (2003), 4: Ginsburg et al. (2011b), 5: Gwinn et al. (1992), 7: Pandian et al. (2008), 8: Sato et al. (2010), 9: Sewilo et al. (2004), 10: Urquhart et al. (2012), 11: Vig et al. (2008), 12: Xu et al. (2003). 6: The distances to G030.704 was determined using the near kinematic distance from the velocity of the HHT-observed HCO+ line (Schlingman et al., 2011). [a]: The minimum likely mass, $M_{min} = (1 - f_{ff}) M(40K)$. [b]: The fraction of flux from free-free emission (as opposed to dust emission) at $\lambda = 1.1$ mm

4.7 Follow-up work

In order to get a complete census of massive proto-clusters in the Galactic plane, it is necessary to examine the southern plane as well. Urquhart et al. (2013) began this examination using ATLASGAL data and identified 6 new candidates in the southern sky. In principle, the detectin of more sources in the South indicates either some incompleteness in the BGPS or a genuinely higher cluster formation rate in the southern sky (which, with such small numbers, is easily consistent with uniform sampling from a disk distribution).

However, we note that two of the candidates in Urquhart et al. (2013) are assigned the wrong kinematic distance - they are placed at the far distance when strong evidence exists putting them instead at the near.

We report measurements of the distance to three sources reported as young massive cluster candidates in Urquhart et al. (2013). Two of these sources were also observed in the Bolocam Galactic Plane Survey, but exluded as YMPC candidates by Ginsburg et al. (2012) because of different distance assumptions based on the Bressert et al. (2012a) criteria.

4.8 AGAL351.774-00.537

This source was identified in the BGPS as G351.775-00.538. It is clearly associated with a thick infrared dark cloud (Figure 4.2) and shows strong evidence of extincting stars, indicating that it must be on the near side of the Galactic center. No cloud should show such strong extinction features if located at a distance $D > 17$ kpc.

This source is also located substantially below $b = 0$, hinting that it is likely very nearby, within a few kpc, since our perspective from ~ 25 pc above the Galactic plane makes any nearby objects in the Galactic plane appear below it (see Goodman et al. (2013) for a particularly compelling illustration of this effect for clouds at $D \sim 3.5$ kpc).

Its favored distance in the literature is 0.7 - 2.2 kpc Leurini et al. (2009). The cloud is moving at $v_{LSR} \approx 0$ km s^{-1}, which requires it to be very near ($D < 4$ kpc) or very far ($D > 15$ kpc) if it

follows a normal rotation curve.

4.9 AGAL352.622-01.077

While this source is not detected in the BGPS, its location substantially below $b = 0$ hints that it is likely nearby. It is also associated with an IRDC.

4.10 AGAL350.111+0.089

This source would have been included in the Ginsburg et al. (2012) catalog of YMPCs had it been at $\ell > 6$; assuming its distance is at least 7 kpc, it should be massive enough to host a YMPC. However, depending on its distance, it may not be compact enough to satisfy the Bressert et al. (2012a) criterion. This object is not associated with an IRDC or strong extinction feature and therefore is likely to be beyond ~ 8 kpc. For the purpose of further analysis, we regard this source as a proto-massive-cluster.

4.11 Implications

The Galactic population of proto-massive clusters therefore consists of 7 sources outside the CMZ (in which both "the brick", G0.253, and Sgr B2 must be considered proto-massive clusters by the Bressert et al. (2012a) definition).

In order to understand what the observed population tells us about the formation rate of YMCs, we construct a model of their formation rate and starless and observable lifetimes. We use a markov chain monte carlo approach to model the population of young massive clusters within our galaxy.

We model the galaxy as a disc with uniform probability of forming a cluster from some inner cutoff radius ~ 1 kpc, below which our observations do not detect protoclusters, out to an outer cutoff radius constrained to be at least 8.5 kpc, the approximate galactocentric radius of W49.

The YMCs are assumed to be drawn from a power-law distribution in mass, with the power-law index allowed to vary between 1.5 and 5. A lower cutoff to this distribution of 10^4 $M_\odot$ is

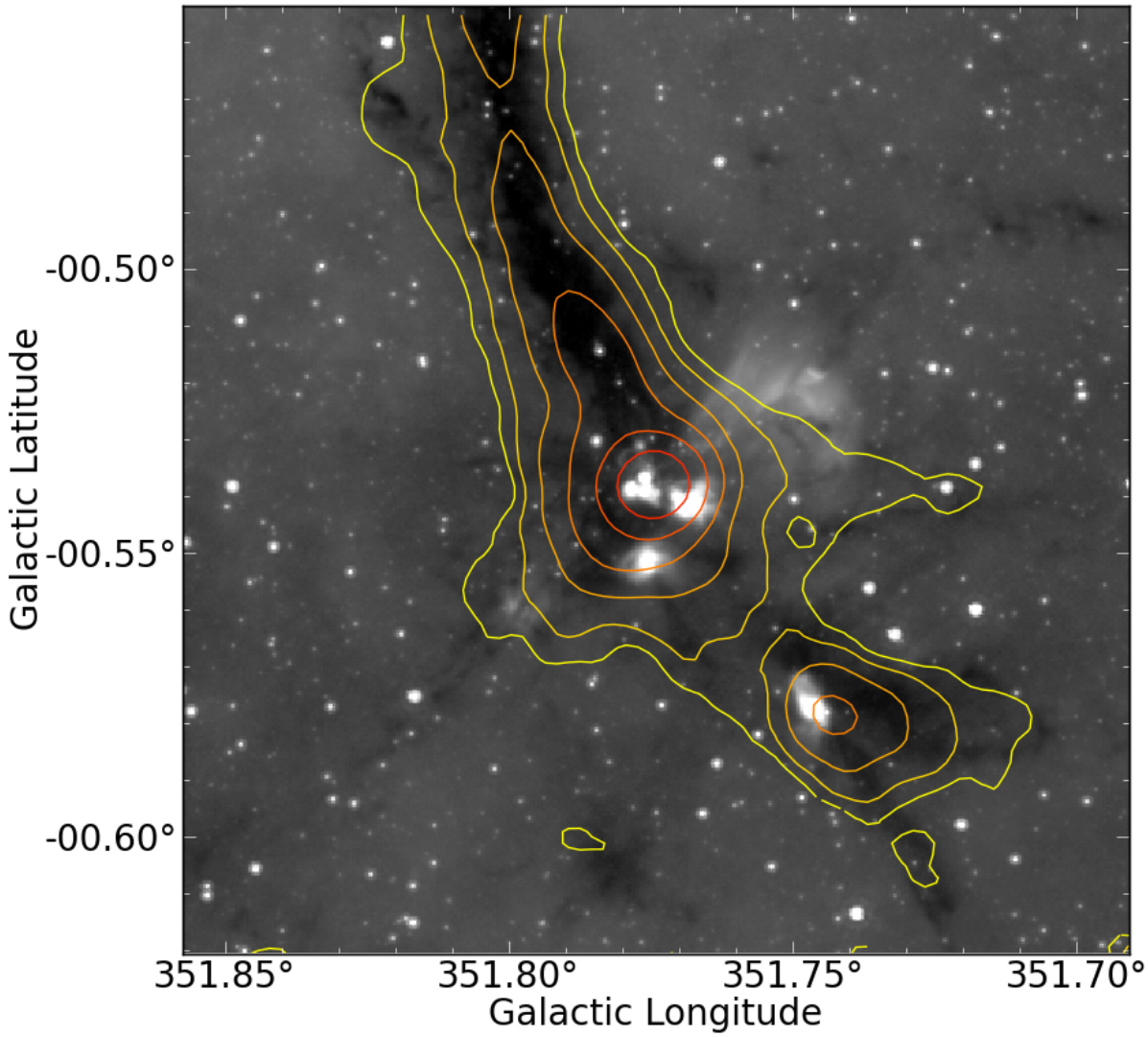

Figure 4.2 The G351.77-0.537 object shown at 8 μm from the Spitzer GLIMPSE survey. The contours show BGPS 1.1 mm flux densities at levels $0.15, 0.35, 0.90, 2.2, 5.5, 13.4, 32.0$ Jy/beam (approximately logarithmically separated). The morphological match between the 8 μm absorption and the 1.1 mm emission is obvious. Such dark clouds cannot be observed at D¿8 kpc, indicating this cloud must be at the near distance. At $D \lesssim 4$ kpc, its mass is less than 10^4 $M_\odot$ (using the Urquhart et al. (2013) mass measurement and distnace), so it is not a massive proto-cluster.

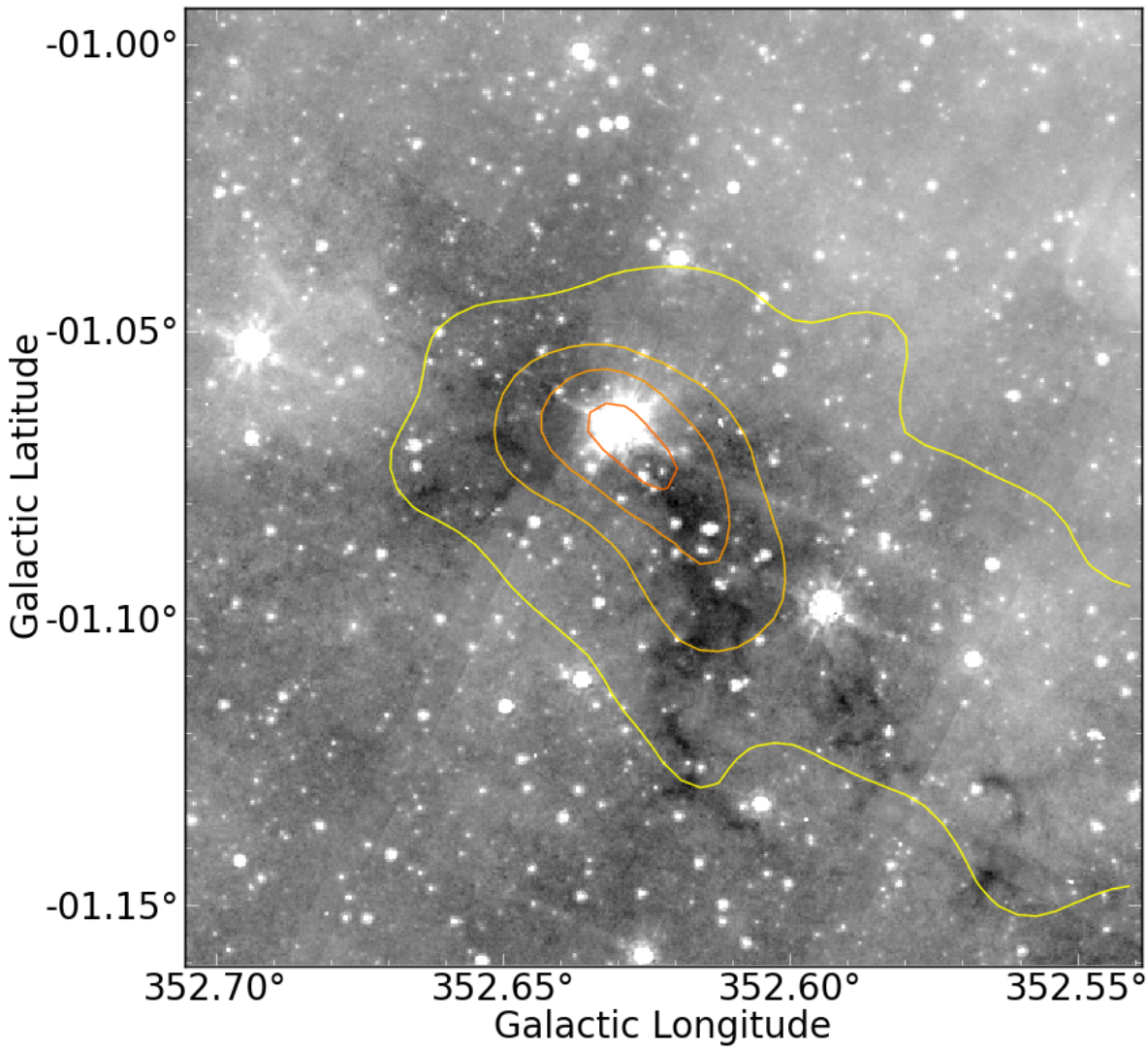

Figure 4.3 G352.62-01.077 shown at 8 μm from the Spitzer GLIMPSE survey. The contours show BGPS 1.1 mm flux densities at levels $0.15, 0.35, 0.90, 2.2, 5.5, 13.4$ Jy/beam (approximately logarithmically separated).

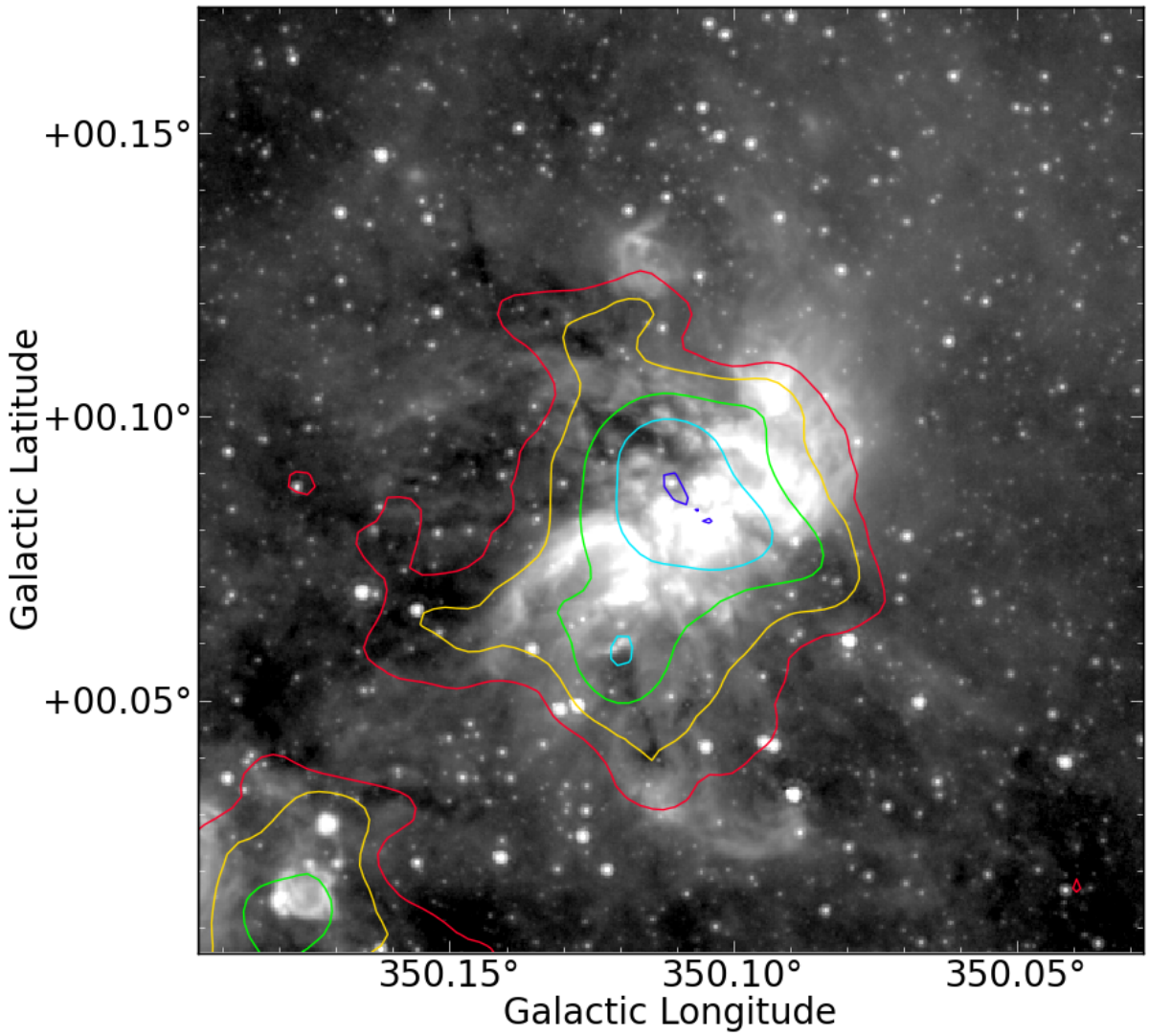

Figure 4.4 G350.111+0.089 shown at 8 μm from the Spitzer GLIMPSE survey. The contours show Herschel Hi-Gal 500 μm surface brightnesses at levels $200, 500, 1000, 2000$ MJy/sr.

imposed to match our observational selection, though it is allowed to vary between 5×10^3 and 5×10^4 to account for observational uncertainty.

The formation rate is modeled as the number of YMCs formed per kpc^2 per Myr. It is evaluated at the minimum allowed mass, then the power-law mass distribution is integrated to yield the formation rate per kpc^2 of clusters with $M \geq M_{min}$.

Finally we model the "formation timescale" and "observable timescale." The formation timescale τ_{form} is the time from "initial collapse" to the formation of the first O-star (more specifically, the time from "initial collapse" until $L = 10^5 L_\odot$). The "observable timescale" τ_{obs} is the time from "initial collapse" until the gas is evacuated, rendering the YMC undetectable at mm wavelengths but probably detectable in the optical/IR if it is appropriately located. Both are limited to a maximum timescale of 10 Myr, after which it is presumed that, if the system is legitimately a YMC, many supernovae must have occurred, which is not true of any of our sample. They are also limited to a minimum timescale of 0.

All of the above variables are given uniformly distributed priors.

The probability of the observed object being starless is given by a Bernoulli distribution with $p(0) = \tau_{form}/\tau_{obs} < 1$.

As of this Thesis, we assume that all of the Urquhart et al. (2013) sources are star-forming, but if any are starless, this analysis will change significantly.

Most of the variables noted above are poorly constrained by our data set, but we note two interesting constraints. We are able to place an upper limit on the ratio $\tau_{form}/\tau_{obs} < 0.14$, which is consistent with the constraint reported in Ginsburg et al. (2012) above, and assuming $\tau_{obs} \sim 2$ Myr, implies a limit $\tau_{starless} < 0.3$ Myr. This constraint is more robustly determined and is only applied to clumps with $M > 3\times10^4\ M_\odot$ (the Ginsburg et al. (2012) limit was derived by examining all sources with $M > 10^4\ M_\odot$, but that limit is not available for the whole plane).

The power-law $\alpha_{cluster}$ value is moderately steeper than $\alpha_{cluster} = 2$, though with low significance, hinting that the cutoff in the Schechter mass distribution is likely within our observed range $3 \times 10^4 M_\odot < M_* < 1 \times 10^5 M_\odot$, where M_* is the 'characteristic mass' in the distribution.

Finally, the overall formation rate of young massive clusters in the Galaxy is well-constrained, with a median formation rate of 1.7 clusters per Myr and a 95% confidence interval between 0.66 and 7.9 per Myr, consistent with the conclusion in Ginsburg et al. (2012) but stronger.

The marginalized single-variable distributions are shown in Figure 4.5 and 4.6.

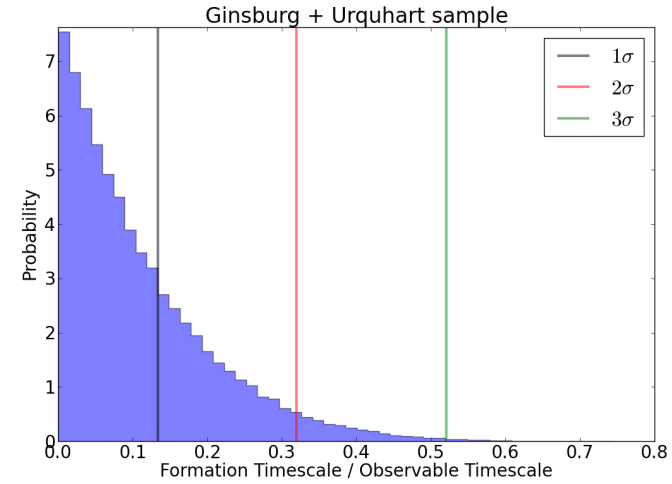

(a)

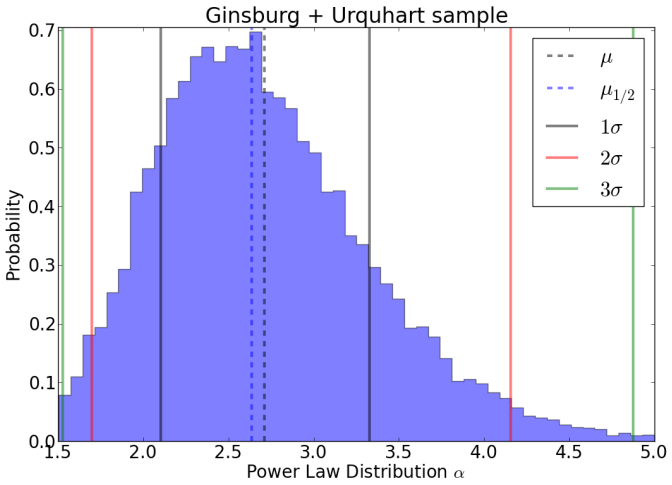

(b)

Figure 4.5 (left) The probability distribution function (PDF) of the ratio of τ_{form}/τ_{obs} recovered from a markov-chain monte carlo examination of the combined sample of PMCs. The vertical bars show the 68%, 95%, and 99.7% upper limits. (right) The PDF of the power-law $\alpha_{cluster}$ for the sample. The vertical bars show the 68%, 95%, and 99.7% confidence intervals.

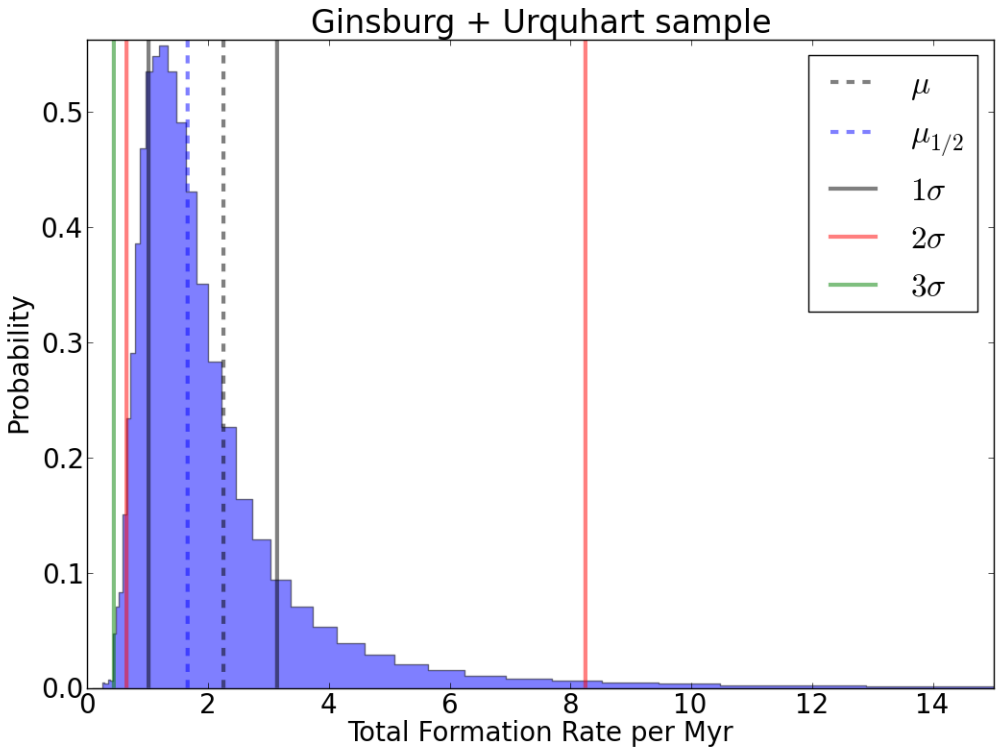

Figure 4.6 The PDF of the overall cluster formation rate integrated over the Galaxy. The 95% confidence interval goes from 0.7 to 8 clusters per Myr

Chapter 5

H_2CO observations of BGPS sources previously observed with Arecibo

5.1 Preface

Jeremy Darling introduced me to the notion of using H_2CO as a gas densitometer in place of wildly inaccurate 'critical-density' based measurements. I asked whether this had been done in the Galaxy, and the answer was: generally, no. So we started with a simple pilot project: ask for GBT time to observe some previously observed H_2CO sources. The project was awarded 4 hours of time that led to hundreds of hours of analysis. This paper performs a level of analysis typically reserved for extragalactic observations on a small sample of Galactic UCHII regions.

The most surprising, and perhaps most interesting, result of this paper was the discovery of relatively high H_2CO $2_{11}-2_{12}$ to $1_{10}-1_{11}$ ratios in 'blindly' selected GMCs, i.e. line-of-sight GMCs not associated with star formation. Within these clouds, we discovered high density material that is difficult to reconcile with standard pictures of turbulence in GMCs. While this topic is treated in detail here, the evidence is difficult to understand and follow-up work comparing to different lines (i.e., CO) is necessary to cleanly demonstrate the observed effect.

It turns out the property of turbulence I have measured here has been discussed under other terminology. Hennebelle & Falgarone (2012) describe the boundaries between GMCs in the cold neutral medium and the surrounding warm neutral medium. In their description, GMCs consist of low volume-filling-factor cold clumps interspersed within a warm ($\sim 10^4$ K) medium. Williams et al. (1995) measure the inter-clump medium density as $n \sim 4\mathrm{cm}^{-3}$. I discuss the clump densities in this chapter and the next.

5.2 Abstract

We present a pilot survey of 21 lines of sight towards ultracompact H II (UCH II) regions and three towards continuum-free lines of sight in the formaldehyde (H_2CO) $1_{10} - 1_{11}$ (6 cm) and $2_{11} - 2_{12}$ (2 cm) transitions, using the H_2CO centimeter lines as a molecular gas densitometer. Using Arecibo and Green Bank beam-matched observations, we measure the density of 51 detected H_2CO line pairs and present upper limits on density for an additional 24 detected $1_{10}-1_{11}$ lines. We analyze the systematic uncertainties in the H_2CO densitometer, achieving H_2 density measurements with accuracies $\sim 0.1 - 0.3$ dex. The densities measured are not correlated with distance, implying that it is possible to make accurate density measurements throughout the galaxy without a distance bias. We confirm that ultracompact HII regions are associated with, and possibly embedded in, gas at densities $n(H_2) \gtrsim 10^5$ cm^{-3}. The densities measured in line-of-sight molecular clouds suggest that they consist of low volume filling factor ($f \sim 10^{-2}$) gas at high ($n(H_2) > 10^4$ cm^{-3}) density, which is inconsistent with purely supersonic turbulence and requires high-density clumping greater than typically observed in gravo-turbulent simulations. We observe complex line morphologies that indicate density variations with velocity around UCH II regions, and we classify a subset of the UCH II molecular envelopes as collapsing or expanding. We compare these measurements to Bolocam Galactic Plane Survey 1.1 mm observations, and note that most UCH II regions have 1.1 mm emission consisting of significant (5-70%) free-free emission and are therefore not necessarily dominated by optically thin dust emission as is often assumed when computing clump masses. A comparison of our data with the Mangum et al. (2008) starburst sample shows that the area filling factor of dense ($n(H_2) \sim 10^5$ cm^{-3}) molecular gas in typical starburst galaxies is $\lesssim 0.01$, but in extreme starburst galaxies like Arp 220, is ~ 0.1, suggesting that Arp 220 is physically similar to an oversized UCH II region.

5.3 Introduction

Massive stars are known to form preferentially in clustered environments (de Wit et al., 2005). They therefore likely form from "clumps," collections of gas and dust more dense and compact than Giant Molecular Clouds (GMCs) but larger and more diffuse than typical low-mass protostellar cores. "Clumps" have been observed with masses ranging from $10 - 10^6 M_\odot$ (but more typically $10^2 - 10^3 M_\odot$) and with beam-averaged densities in the range $10^3 \lesssim n(\mathrm{H_2}) \lesssim 10^5$ cm^{-3} and sizes ~ 1 pc (e.g., Rosolowsky et al., 2010; Dunham et al., 2010). While giant molecular clouds in the Galaxy have been surveyed (e.g., Jackson et al., 2006), the process by which these clouds condense into clumps and cores and the mechanisms by which they are dispersed are not understood.

It is still not known what sets the final mass of massive stars, but it is thought that they must ignite while still accreting (McKee & Ostriker, 2007b). Hot O and B stars emitting strongly in the ultraviolet will ionize their surroundings, creating density-bounded H II regions. They progress from hypercompact through ultracompact and compact and finally diffuse H II region phases, during which they either dissociate or blow out their surrounding medium (Churchwell, 2002; Keto, 2007). The brightest sources in the Galactic plane in both the free-free continuum in the cm-wavelength regime and the dust continuum in the sub-mm to mm-wavelength regime generally host UCH II regions.

While the gas within UCH II regions is hot and ionized, the surrounding gas is initially molecular. At the interface between the molecular cloud and the ionization front, a photon-dominated or photodissociation region appears (Roshi et al., 2005). Churchwell et al. (2010) observed $\mathrm{HCO^+}$ towards a sample of UCH II regions and noted both infall and outflow motions in molecular tracers towards these objects. It should be possible to determine whether the UCH II regions still have collapsing envelopes (infall signatures) or only disks (outflow signatures) and thereby determine relative evolutionary states of the regions.

Two centimeter transitions of formaldehyde, o-$\mathrm{H_2CO}$ $1_{10} - 1_{11}$ (6 cm) and $2_{11} - 2_{12}$ (2 cm)[1]

, have been used to measure the density of molecular clouds in massive-star-forming regions (e.g., Dickel et al., 1986; Dickel & Goss, 1987), high-latitude Galactic clouds (e.g., Turner et al., 1989), the Galactic Center (e.g., Zylka et al., 1992) starburst galaxies (e.g., Mangum et al., 2008), and molecular clouds in a gravitational lens (e.g., Zeiger & Darling, 2010). Studies similar to our own have been performed by Wadiak et al. (1988) and Henkel et al. (1983), in which bright continuum sources were observed in the same transitions with (approximately) beam-matched telescopes at $\sim 2'$ resolution. Our study delves deeper into the spectral line profiles and systematic uncertainties of H_2CO densitometry and is performed at higher spatial resolution than past work.

This paper presents a pilot study as a proof-of-concept for a much larger ongoing survey[2] towards 400 lines of sight and the methodology applicable to the larger survey.

In section 5.4 we present the new observations and describe other data sets used in our analysis. Section 5.5 describes the modeling procedure used to derive density from the H_2CO line observations. Section 5.6 presents detailed discussion of the modeling and derivation of physical parameters and their uncertainties. Section 5.7 describes the derived and measured values. Section 5.8 discusses the larger implications of our results. We conclude with a brief summary of important results.

5.4 Observations and Data

5.4.1 Source Selection

The observed lines-of-sight included 21 sources selected from the Araya et al. (2002) UCH II sample and 3 from the Araya et al. (2004) "massive-star forming candidate" sample. The sources were selected primarily on the basis of having been previously observed with Arecibo[3] in the $1_{10} - 1_{11}$ transition of H_2CO with the intent of demonstrating the densitometry method within the Galaxy rather than making systematic observations of any source class. Nonetheless, the Araya

[1] All references to H_2CO in this paper, except where otherwise noted, are to the ortho o-H_2CO population, as no para p-H_2CO lines were observed

[2] GBT project code GBT10B-019

[3] The Arecibo Observatory is part of the National Astronomy and Ionosphere Center, which is operated by Cornell University under a cooperative agreement with the National Science Foundation.

et al. (2002) sample includes the majority of the bright UCH II regions accessible to Arecibo. Additionally, there are many detected GMCs along the line of sight to these UCH II regions.

The Araya et al. (2004) observations included 15 pointings towards infrared dark cloud (IRDC) candidates and High-Mass Protostellar Object (HMPO) candidates. The sources we selected from this sample include two sources classified as IRDCs based on MSX data and one HMPO candidate. The selection of these sources was arbitrary; we were only able to observe 24 lines-of-sight in our 4 hour observation block. The remaining sources will be discussed in a later paper. The observed lines of sight are listed in Table 5.1.

Table 5.1. Measured H_2CO $1_{10} - 1_{11}$ line properties

Source Name[a]	l °	b °	6cm Continuum (Jy)	Peak (Jy)	Center (km s^{-1})	FWHM (km s^{-1})	RMS (Jy)	Channel Width (km s^{-1})
G32.80+0.19 0	0.1904	32.7968	2.18 (0.01)	-0.393 (0.008)	15.39 (0.05)	6.57 (0.06)	0.0049	1.1374
G32.80+0.19 1	0.1904	32.7968	2.18 (0.01)	-0.092 (0.008)	11.45 (0.26)	10.25 (0.65)	0.0049	1.1374
G32.80+0.19 2	0.1904	32.7968	2.18 (0.01)	-0.063 (0.008)	80.63 (0.13)	2.49 (0.36)	0.0049	1.1374
G32.80+0.19 3	0.1904	32.7968	2.18 (0.01)	-0.254 (0.008)	84.61 (0.02)	1.37 (0.06)	0.0049	1.1374
G32.80+0.19 4	0.1904	32.7968	2.18 (0.01)	-0.090 (0.008)	88.66 (0.09)	3.21 (0.31)	0.0049	1.1374
G33.13-0.09 0	-0.0949	33.1297	0.49 (0.00)	-0.192 (0.007)	75.92 (0.05)	3.80 (0.12)	0.0045	1.1374
G33.13-0.09 1	-0.0949	33.1297	0.49 (0.00)	-0.023 (0.007)	81.62 (0.35)	2.49 (0.88)	0.0045	1.1374
G33.13-0.09 2	-0.0949	33.1297	0.49 (0.00)	-0.040 (0.007)	101.50 (0.40)	11.30 (0.80)	0.0045	1.1374
G33.13-0.09 3	-0.0949	33.1297	0.49 (0.00)	-0.039 (0.007)	10.39 (0.08)	2.04 (0.24)	0.0045	1.1374
G33.92+0.11 0	0.1112	33.914	0.83 (0.00)	-0.081 (0.008)	107.28 (0.18)	6.62 (0.34)	0.005	1.1374
G33.92+0.11 1	0.1112	33.914	0.83 (0.00)	-0.079 (0.008)	106.03 (0.06)	2.41 (0.23)	0.005	1.1374
G33.92+0.11 2	0.1112	33.914	0.83 (0.00)	-0.160 (0.030)	57.30 (0.40)	10.60 (0.80)	0.005	1.1374
G34.26+0.15 0	0.1538	34.2572	5.57 (0.01)	-1.828 (0.015)	60.24 (0.01)	3.80 (0.03)	0.0063	1.1374
G34.26+0.15 1	0.1538	34.2572	5.57 (0.01)	-0.160 (0.015)	26.69 (0.08)	1.04 (0.22)	0.0063	1.1374
G34.26+0.15 2	0.1538	34.2572	5.57 (0.01)	-0.099 (0.015)	11.25 (0.19)	2.01 (0.40)	0.0063	1.1374
G34.26+0.15 3	0.1538	34.2572	5.57 (0.01)	-0.126 (0.015)	51.70 (2.00)	4.20 (1.00)	0.0063	1.1374
G34.26+0.15 4	0.1538	34.2572	5.57 (0.01)	-0.047 (0.015)	48.20 (2.00)	1.80 (1.00)	0.0063	1.1374
G35.20-1.74 0	-1.7409	35.1997	5.17 (0.00)	-1.018 (0.008)	43.37 (0.01)	3.67 (0.02)	0.0051	1.1374
G35.20-1.74 1	-1.7409	35.1997	5.17 (0.00)	-0.147 (0.008)	36.67 (0.10)	1.49 (0.27)	0.0051	1.1374
G35.20-1.74 2	-1.7409	35.1997	5.17 (0.00)	-0.324 (0.008)	14.08 (0.01)	0.93 (0.03)	0.0051	1.1374
G35.20-1.74 3	-1.7409	35.1997	5.17 (0.00)	-0.039 (0.008)	50.59 (0.53)	4.92 (1.31)	0.0051	1.1374
G35.57-0.03 0	-0.0306	35.5779	0.47 (0.00)	-0.064 (0.009)	52.10 (0.10)	4.60 (0.30)	0.0053	1.1374
G35.57-0.03 1	-0.0306	35.5779	0.47 (0.00)	-0.021 (0.009)	45.60 (0.30)	1.90 (0.60)	0.0053	1.1374
G35.57-0.03 2	-0.0306	35.5779	0.47 (0.00)	-0.019 (0.009)	57.60 (0.50)	2.90 (0.97)	0.0053	1.1374
G35.57-0.03 3	-0.0306	35.5779	0.47 (0.00)	-0.031 (0.009)	12.80 (0.20)	1.84 (0.41)	0.0053	1.1374

Table 5.1 (cont'd)

Source Name[a]	l °	b °	6cm Continuum (Jy)	Peak (Jy)	Center (km s^{-1})	FWHM (km s^{-1})	RMS (Jy)	Channel Width (km s^{-1})
G35.57-0.03 4	-0.0306	35.5779	0.47 (0.00)	-0.031 (0.008)	29.04 (0.11)	0.82 (0.25)	0.0053	1.1374
G35.58+0.07 0	0.0657	35.5801	0.53 (0.01)	-0.146 (0.004)	49.37 (0.21)	5.33 (0.34)	0.0048	1.1374
G35.58+0.07 1	0.0657	35.5801	0.53 (0.01)	-0.049 (0.013)	53.13 (0.25)	2.98 (0.64)	0.0048	1.1374
G35.58+0.07 2	0.0657	35.5801	0.53 (0.01)	-0.025 (0.004)	58.12 (0.29)	3.63 (0.74)	0.0048	1.1374
G35.58+0.07 3	0.0657	35.5801	0.53 (0.01)	-0.034 (0.004)	13.24 (0.17)	2.80 (0.39)	0.0048	1.1374
G37.87-0.40 0	-0.3993	37.873	4.40 (0.01)	-0.531 (0.006)	60.23 (0.11)	8.73 (0.35)	0.0069	1.1374
G37.87-0.40 1	-0.3993	37.873	4.40 (0.01)	-0.124 (0.014)	53.27 (0.19)	4.03 (0.46)	0.0069	1.1374
G37.87-0.40 2	-0.3993	37.873	4.40 (0.01)	-0.356 (0.019)	65.13 (0.04)	2.74 (0.15)	0.0069	1.1374
G37.87-0.40 3	-0.3993	37.873	4.40 (0.01)	-0.324 (0.045)	72.18 (0.04)	1.35 (0.14)	0.0069	1.1374
G37.87-0.40 4	-0.3993	37.873	4.40 (0.01)	-0.424 (0.013)	73.97 (0.13)	3.01 (0.22)	0.0069	1.1374
G37.87-0.40 5	-0.3993	37.873	4.40 (0.01)	-0.185 (0.012)	79.98 (0.06)	1.80 (0.14)	0.0069	1.1374
G37.87-0.40 6	-0.3993	37.873	4.40 (0.01)	-0.114 (0.015)	91.96 (0.08)	1.21 (0.18)	0.0069	1.1374
G37.87-0.40 7	-0.3993	37.873	4.40 (0.01)	-0.175 (0.012)	14.32 (0.14)	2.94 (0.20)	0.0069	1.1374
G37.87-0.40 8	-0.3993	37.873	4.40 (0.01)	-0.072 (0.022)	13.16 (0.10)	0.87 (0.32)	0.0069	1.1374
G37.87-0.40 9	-0.3993	37.873	4.40 (0.01)	-0.137 (0.012)	20.54 (0.06)	1.37 (0.14)	0.0069	1.1374
G43.89-0.78 0	-0.7838	43.8892	0.66 (0.00)	-0.181 (0.004)	54.86 (0.02)	2.19 (0.06)	0.0032	1.1374
G43.89-0.78 1	-0.7838	43.8892	0.66 (0.00)	-0.020 (0.002)	50.55 (0.59)	15.90 (1.20)	0.0032	1.1374
G45.07+0.13 0	0.1323	45.0711	0.47 (0.00)	-0.056 (0.006)	57.49 (0.10)	4.24 (0.23)	0.0035	1.1374
G45.07+0.13 1	0.1323	45.0711	0.47 (0.00)	-0.036 (0.006)	65.44 (0.15)	4.09 (0.34)	0.0035	1.1374
G45.12+0.13 0	0.1326	45.1223	4.28 (0.01)	-0.188 (0.006)	55.70 (0.12)	3.32 (0.24)	0.0065	1.1374
G45.12+0.13 1	0.1326	45.1223	4.28 (0.01)	-0.154 (0.009)	59.40 (0.13)	3.11 (0.33)	0.0065	1.1374
G45.12+0.13 2	0.1326	45.1223	4.28 (0.01)	-0.200 (0.010)	24.86 (0.03)	1.68 (0.08)	0.0065	1.1374
G45.12+0.13 3	0.1326	45.1223	4.28 (0.01)	-0.027 (0.004)	65.53 (0.82)	7.23 (2.03)	0.0065	1.1374
G45.45+0.06 0	0.0593	45.4548	4.77 (0.01)	-1.347 (0.018)	59.58 (0.02)	3.18 (0.05)	0.0063	1.1374
G45.45+0.06 1	0.0593	45.4548	4.77 (0.01)	-0.123 (0.040)	55.34 (0.38)	3.15 (0.38)	0.0063	1.1374

Table 5.1 (cont'd)

Source Name[a]	l °	b °	6cm Continuum (Jy)	Peak (Jy)	Center (km s^{-1})	FWHM (km s^{-1})	RMS (Jy)	Channel Wid (km s^{-1})
G45.45+0.06 2	0.0593	45.4548	4.77 (0.01)	-0.056 (0.005)	25.02 (0.12)	2.82 (0.28)	0.0063	1.1374
G45.47+0.05 0	0.0455	45.4655	0.75 (0.00)	-0.274 (0.003)	60.62 (0.03)	6.59 (0.07)	0.0039	1.1374
G45.47+0.05 1	0.0455	45.4655	0.75 (0.00)	-0.017 (0.004)	25.55 (0.23)	2.18 (0.55)	0.0039	1.1374
G48.61+0.02 0	0.0229	48.6055	1.01 (0.00)	-0.067 (0.003)	18.08 (0.09)	4.97 (0.22)	0.0035	1.1374
G48.61+0.02 1	0.0229	48.6055	1.01 (0.00)	-0.024 (0.005)	6.08 (0.13)	1.20 (0.31)	0.0035	1.1374
G48.61+0.02 2	0.0229	48.6055	1.01 (0.00)	-0.018 (0.003)	53.73 (0.33)	4.72 (0.79)	0.0035	1.1374
G50.32+0.68 0	0.6761	50.3153	0.24 (0.00)	-0.011 (0.003)	26.28 (0.40)	3.32 (0.94)	0.0031	1.1374
G60.88-0.13 0	-0.1285	60.8826	0.66 (0.01)	-0.093 (0.009)	22.60 (0.15)	3.24 (0.35)	0.0096	1.1374
G61.48+0.09 0	0.0893	61.4769	6.16 (0.01)	-0.531 (0.009)	21.45 (0.02)	2.81 (0.06)	0.0084	1.1374
G69.54-0.98 0	-0.9759	69.5398	0.28 (0.01)	-0.280 (0.006)	10.65 (0.05)	4.55 (0.11)	0.0076	1.1374
G70.29+1.60 0	1.6006	70.2927	4.37 (0.13)	-0.372 (0.008)	-21.74 (0.07)	3.92 (0.15)	0.0108	1.1374
G70.29+1.60 1	1.6006	70.2927	4.37 (0.13)	-0.050 (0.007)	-27.17 (0.58)	4.86 (1.33)	0.0108	1.1374
G70.33+1.59 0	1.589	70.3296	2.21 (0.01)	-1.201 (0.007)	-21.24 (0.01)	3.65 (0.03)	0.0115	1.1374
IRAS 20051+3435 0	0.2088	32.4662	0.00 (0.01)	-0.019 (0.001)	10.77 (0.07)	3.60 (0.18)	0.00071	2.2747
G41.74+0.10 0	0.0975	41.7415	0.34 (0.00)	-0.062 (0.004)	14.60 (0.09)	2.56 (0.26)	0.0033	1.1374
G41.74+0.10 1	0.0975	41.7415	0.34 (0.00)	-0.020 (0.004)	10.99 (0.29)	2.52 (0.71)	0.0033	1.1374
G41.74+0.10 2	0.0975	41.7415	0.34 (0.00)	-0.066 (0.004)	34.25 (0.05)	1.63 (0.13)	0.0033	1.1374
G41.74+0.10 3	0.0975	41.7415	0.34 (0.00)	-0.022 (0.005)	56.61 (0.13)	1.15 (0.32)	0.0033	1.1374
G41.74+0.10 4	0.0975	41.7415	0.34 (0.00)	-0.043 (0.005)	17.57 (0.07)	1.13 (0.18)	0.0033	1.1374
IRDC 1923+13 0	-0.4972	48.9325	0.40 (0.00)	-0.011 (0.001)	50.20 (0.08)	1.83 (0.19)	0.0008	0.7582
IRDC 1923+13 1	-0.4972	48.9325	0.40 (0.00)	-0.009 (0.001)	57.56 (0.09)	2.57 (0.22)	0.0008	0.7582
IRDC 1923+13 2	-0.4972	48.9325	0.40 (0.00)	-0.005 (0.001)	47.32 (0.20)	2.11 (0.51)	0.0008	0.7582
IRDC 1916+11 0	-0.2923	45.666	0.00 (0.01)	-0.005 (0.001)	25.94 (0.17)	2.53 (0.41)	0.00083	0.7582
IRDC 1916+11 1	-0.2923	45.666	0.00 (0.01)	-0.013 (0.001)	55.91 (0.13)	6.21 (0.34)	0.00083	0.7582
IRDC 1916+11 2	-0.2923	45.666	0.00 (0.01)	-0.003 (0.001)	48.85 (0.48)	3.58 (1.13)	0.00083	0.7582

Table 5.1 (cont'd)

Source Name[a]	l °	b °	6cm Continuum (Jy)	Peak (Jy)	Center (km s^{-1})	FWHM (km s^{-1})	RMS (Jy)	Channel Width (km s^{-1})

[a]Sources are labeled by the line-of-sight followed by the number of the component identified, indexed from zero. The components do not follow a particular order, but are uniquely identifiable by their velocity, width, and amplitude.

Table 5.2. Measured H_2CO $2_{11} - 2_{12}$ line properties

Source Name	2cm Continuum (Jy)	Peak[a] (Jy)	Center (km s^{-1})	FWHM (km s^{-1})	RMS[b] (Jy)
G32.80+0.19 0	3.68 (0.02)	-0.519 (0.032)	15.65 (0.03)	5.72 (0.08)	0.0038
G32.80+0.19 1	3.68 (0.02)	-0.076 (0.019)	11.90 (1.18)	8.17 (0.98)	0.0038
G32.80+0.19 2	3.68 (0.02)	-0.016 (0.001)	80.47 (0.14)	4.35 (0.36)	0.0038
G32.80+0.19 3	3.68 (0.02)	-0.065 (0.002)	84.96 (0.02)	1.29 (0.05)	0.0038
G32.80+0.19 4	3.68 (0.02)	-0.026 (0.001)	88.83 (0.06)	2.31 (0.14)	0.0038
G33.13-0.09 0	0.47 (0.02)	-0.224 (0.003)	76.17 (0.02)	3.31 (0.05)	0.003
G33.13-0.09 1	0.47 (0.02)	0.000 (0.000)	0.00 (0.00)	0.00 (0.00)	0.003
G33.13-0.09 2	0.47 (0.02)	0.000 (0.000)	0.00 (0.00)	0.00 (0.00)	0.003
G33.13-0.09 3	0.47 (0.02)	0.000 (0.000)	0.00 (0.00)	0.00 (0.00)	0.003
G33.92+0.11 0	0.87 (0.02)	-0.086 (0.003)	106.43 (0.03)	2.17 (0.09)	0.0032
G33.92+0.11 1	0.87 (0.02)	-0.069 (0.002)	108.83 (0.11)	6.82 (0.16)	0.0032
G33.92+0.11 2	0.87 (0.02)	0.000 (0.000)	0.00 (0.00)	0.00 (0.00)	0.0032
G34.26+0.15 0	5.89 (0.02)	-1.356 (0.006)	60.99 (0.01)	3.96 (0.02)	0.0051
G34.26+0.15 1	5.89 (0.02)	-0.046 (0.003)	27.11 (0.04)	1.03 (0.09)	0.0051
G34.26+0.15 2	5.89 (0.02)	-0.018 (0.002)	11.23 (0.16)	3.19 (0.38)	0.0051
G34.26+0.15 3	5.89 (0.02)	-0.025 (0.004)	52.82 (0.58)	6.34 (1.53)	0.0051
G34.26+0.15 4	5.89 (0.02)	-0.018 (0.007)	47.05 (0.47)	2.47 (1.15)	0.0051
G35.20-1.74 0	5.98 (0.03)	-0.482 (0.004)	43.38 (0.02)	3.71 (0.04)	0.0055
G35.20-1.74 1	5.98 (0.03)	-0.028 (0.005)	37.91 (0.32)	3.46 (0.76)	0.0055
G35.20-1.74 2	5.98 (0.03)	-0.056 (0.003)	14.18 (0.02)	1.00 (0.05)	0.0055
G35.20-1.74 3	5.98 (0.03)	0.000 (0.000)	0.00 (0.00)	0.00 (0.00)	0.0055
G35.57-0.03 0	0.32 (0.15)	-0.075 (0.003)	52.14 (0.09)	4.39 (0.21)	0.0046
G35.57-0.03 1	0.32 (0.15)	-0.015 (0.006)	47.39 (0.25)	1.31 (0.60)	0.0046
G35.57-0.03 2	0.32 (0.15)	0.000 (0.000)	0.00 (0.00)	0.00 (0.00)	0.0046
G35.57-0.03 3	0.32 (0.15)	0.000 (0.000)	0.00 (0.00)	0.00 (0.00)	0.0046

Table 5.2 (cont'd)

Source Name	2cm Continuum (Jy)	Peak[a] (Jy)	Center (km s^{-1})	FWHM (km s^{-1})	RMS[b] (Jy)
G35.57-0.03 4	0.32 (0.15)	-0.024 (0.008)	29.25 (0.11)	0.43 (0.15)	0.0046
G35.58+0.07 0	0.23 (0.09)	-0.106 (0.002)	49.21 (0.06)	5.00 (0.14)	0.0031
G35.58+0.07 1	0.23 (0.09)	0.000 (0.004)	0.00 (0.00)	0.00 (0.00)	0.0031
G35.58+0.07 2	0.23 (0.09)	0.000 (0.004)	0.00 (0.00)	0.00 (0.00)	0.0031
G35.58+0.07 3	0.23 (0.09)	0.000 (0.004)	0.00 (0.00)	0.00 (0.00)	0.0031
G37.87-0.40 0	3.73 (0.02)	-0.221 (0.003)	59.99 (0.12)	8.53 (0.14)	0.0048
G37.87-0.40 1	3.73 (0.02)	-0.045 (0.007)	54.55 (0.25)	5.99 (0.34)	0.0048
G37.87-0.40 2	3.73 (0.02)	-0.036 (0.007)	65.06 (0.11)	2.57 (0.45)	0.0048
G37.87-0.40 3	3.73 (0.02)	-0.053 (0.003)	72.44 (0.05)	1.37 (0.08)	0.0048
G37.87-0.40 4	3.73 (0.02)	-0.047 (0.002)	74.25 (0.07)	2.07 (0.18)	0.0048
G37.87-0.40 5	3.73 (0.02)	-0.016 (0.001)	80.04 (0.03)	1.28 (0.07)	0.0048
G37.87-0.40 6	3.73 (0.02)	-0.010 (0.002)	91.99 (0.12)	1.60 (0.28)	0.0048
G37.87-0.40 7	3.73 (0.02)	-0.026 (0.002)	14.89 (0.12)	1.40 (0.20)	0.0048
G37.87-0.40 8	3.73 (0.02)	-0.017 (0.002)	13.29 (0.19)	1.52 (0.34)	0.0048
G37.87-0.40 9	3.73 (0.02)	-0.017 (0.001)	20.52 (0.10)	3.09 (0.23)	0.0048
G43.89-0.78 0	0.53 (0.02)	-0.059 (0.004)	54.61 (0.08)	2.85 (0.23)	0.003
G43.89-0.78 1	0.53 (0.02)	-0.015 (0.002)	49.59 (0.94)	14.49 (1.69)	0.003
G45.07+0.13 0	0.79 (0.07)	-0.073 (0.003)	57.18 (0.08)	3.45 (0.18)	0.0029
G45.07+0.13 1	0.79 (0.07)	-0.011 (0.003)	65.67 (0.42)	3.46 (0.98)	0.0029
G45.12+0.13 0	5.20 (0.20)	-0.086 (0.002)	56.21 (0.11)	5.22 (0.21)	0.0044
G45.12+0.13 1	5.20 (0.20)	-0.059 (0.005)	59.70 (0.06)	2.42 (0.16)	0.0044
G45.12+0.13 2	5.20 (0.20)	-0.047 (0.002)	25.14 (0.04)	1.55 (0.09)	0.0044
G45.12+0.13 3	5.20 (0.20)	-0.021 (0.001)	64.68 (0.39)	8.15 (0.87)	0.0044
G45.45+0.06 0	3.16 (0.02)	-0.260 (0.003)	59.58 (0.01)	2.06 (0.03)	0.0043
G45.45+0.06 1	3.16 (0.02)	-0.042 (0.002)	57.90 (0.14)	9.40 (0.31)	0.0043

Table 5.2 (cont'd)

Source Name	2cm Continuum (Jy)	Peak[a] (Jy)	Center (km s^{-1})	FWHM (km s^{-1})	RMS[b] (Jy)
G45.45+0.06 2	3.16 (0.02)	0.000 (0.000)	0.00 (0.00)	0.00 (0.00)	0.0043
G45.47+0.05 0	0.38 (0.02)	-0.124 (0.003)	61.67 (0.07)	5.85 (0.17)	0.0049
G45.47+0.05 1	0.38 (0.02)	-0.000 (0.007)	0.00 (0.00)	0.00 (0.00)	0.0049
G48.61+0.02 0	0.41 (0.02)	-0.022 (0.003)	18.50 (0.25)	4.39 (0.59)	0.0033
G48.61+0.02 1	0.41 (0.02)	-0.000 (0.000)	0.00 (0.00)	0.00 (0.00)	0.0033
G48.61+0.02 2	0.41 (0.02)	-0.005 (0.002)	52.50 (1.25)	7.47 (2.94)	0.0033
G50.32+0.68 0	0.16 (0.02)	-0.011 (0.003)	26.21 (0.44)	3.10 (1.03)	0.0036
G60.88-0.13 0	0.29 (0.02)	-0.016 (0.003)	21.63 (0.21)	2.47 (0.50)	0.003
G61.48+0.09 0	3.42 (0.02)	-0.300 (0.004)	21.40 (0.02)	2.39 (0.04)	0.0037
G69.54-0.98 0	0.23 (0.02)	-0.220 (0.002)	9.97 (0.03)	5.81 (0.08)	0.0031
G70.29+1.60 0	6.21 (0.02)	-0.159 (0.003)	-23.52 (0.06)	5.36 (0.13)	0.0046
G70.29+1.60 1	6.21 (0.02)	-0.000 (0.000)	-0.00 (0.00)	0.00 (0.00)	0.0046
G70.33+1.59 0	2.68 (0.02)	-1.081 (0.005)	-21.17 (0.01)	2.95 (0.01)	0.0038
IRAS 20051+3435 0	0.00 (0.02)	-0.016 (0.003)	11.51 (0.37)	4.14 (0.88)	0.0032
G41.74+0.10 0	0.28 (0.02)	-0.014 (0.002)	14.36 (0.34)	3.80 (0.80)	0.0032
G41.74+0.10 1	0.28 (0.02)	0.000 (0.004)	0.00 (0.00)	0.00 (0.00)	0.0032
G41.74+0.10 2	0.28 (0.02)	0.000 (0.004)	0.00 (0.00)	0.00 (0.00)	0.0032
G41.74+0.10 3	0.28 (0.02)	0.000 (0.004)	0.00 (0.00)	0.00 (0.00)	0.0032
G41.74+0.10 4	0.28 (0.02)	0.000 (0.004)	0.00 (0.00)	0.00 (0.00)	0.0032
IRDC 1923+13 0	0.00 (0.02)	0.000 (0.000)	0.00 (0.00)	0.00 (0.00)	0.0032
IRDC 1923+13 1	0.00 (0.02)	0.000 (0.000)	0.00 (0.00)	0.00 (0.00)	0.0032
IRDC 1923+13 2	0.00 (0.02)	0.000 (0.000)	0.00 (0.00)	0.00 (0.00)	0.0032
IRDC 1916+11 0	0.00 (0.02)	0.000 (0.000)	0.00 (0.00)	0.00 (0.00)	0.0048
IRDC 1916+11 1	0.00 (0.02)	0.000 (0.000)	0.00 (0.00)	0.00 (0.00)	0.0048
IRDC 1916+11 2	0.00 (0.02)	0.000 (0.000)	0.00 (0.00)	0.00 (0.00)	0.0048

Table 5.2 (cont'd)

Source Name	2cm Continuum (Jy)	Peak[a] (Jy)	Center (km s^{-1})	FWHM (km s^{-1})	RMS[b] (Jy)

[a] The Upper Limit Flag is 1 when the measurement indicated is a $3-\sigma$ upper limit on the $2_{11}-2_{12}$ line depth when there is a corresponding $1_{10}-1_{11}$ line detection.

[b]RMS in 1.011 km s^{-1} channels.

Table 5.3. Distance, BGPS 1.1 mm, and other properties

Source Name	Distance (kpc)	Galactocentric Distance (kpc)	KDA[a] Resolution	$S_{1.1mm}$ (Jy)	Source Type	H_2CO Spectrum Type	Scenario[b]
G32.80+0.19 0	12.9	7.4	far	6.94	UCHII	red gradient	2+3
G32.80+0.19 1	13.1	7.6	far	6.94	UCHII	envelope	2+3
G32.80+0.19 2	9.4	5.1	far	6.94	GMC	-	2+3
G32.80+0.19 3	9.2	5.0	far	6.94	GMC	-	2+3
G32.80+0.19 4	9.0	4.9	far	6.94	GMC	-	2+3
G33.13-0.09 0	9.6	5.2	far	2.26	UCHII	red gradient	2
G33.13-0.09 1	9.3	5.1	far	2.26	GMC	envelope	2
G33.13-0.09 2	7.1	4.7	tangent	2.26	GMC	-	2
G33.13-0.09 3	0.9	7.6	near	2.26	GMC	-	2
G33.92+0.11 0	7.0	4.6	tangent	3.86	UCHII	red gradient	2
G33.92+0.11 1	7.0	4.6	tangent	3.86	UCHII	envelope	2
G33.92+0.11 2	3.6	5.8	near	3.86	GMC	-	2
G34.26+0.15 0	3.6	5.7	near	35.69	UCHII	red gradient	2
G34.26+0.15 1	1.9	6.9	near	35.69	GMC	-	2
G34.26+0.15 2	1.0	7.6	near	35.69	GMC	-	2
G34.26+0.15 3	3.6	6.0	near	35.69	GMC	envelope	2
G34.26+0.15 4	3.6	6.1	near	35.69	GMC	-	2
G35.20-1.74 0	2.8	6.3	near	-	UCHII	single	4
G35.20-1.74 1	2.5	6.5	near	-	GMC	-	4
G35.20-1.74 2	1.1	7.5	near	-	GMC	-	4
G35.20-1.74 3	3.2	6.1	near	-	GMC	-	4
G35.57-0.03 0	10.3	6.0	far	2.57	UCHII	single	2+3
G35.57-0.03 1	10.7	6.2	far	2.57	GMC	-	2+3
G35.57-0.03 2	3.6	5.9	near	2.57	GMC	-	2+3

Table 5.3 (cont'd)

Source Name	Distance (kpc)	Galactocentric Distance (kpc)	KDA[a] Resolution	$S_{1.1mm}$ (Jy)	Source Type	H_2CO Spectrum Type	Scenario[b]
G35.57-0.03 3	1.1	7.6	near	2.57	GMC	-	2+3
G35.57-0.03 4	2.0	6.8	near	2.57	GMC	-	2+3
G35.58+0.07 0	10.5	6.1	far	1.44	UCHII	blue gradient	2
G35.58+0.07 1	10.3	6.0	far	1.44	UCHII	-	2
G35.58+0.07 2	3.6	5.8	near	1.44	GMC	-	2
G35.58+0.07 3	1.1	7.5	near	1.44	GMC	-	2
G37.87-0.40 0	9.4	5.9	far	4.14	UCHII	blue gradient	1
G37.87-0.40 1	9.8	6.1	far	4.14	UCHII	blue gradient	1
G37.87-0.40 2	9.2	5.7	far	4.14	UCHII	blue gradient	1
G37.87-0.40 3	8.7	5.6	far	4.14	GMC	-	1
G37.87-0.40 4	8.6	5.5	far	4.14	GMC	-	1
G37.87-0.40 5	8.1	5.4	far	4.14	GMC	-	1
G37.87-0.40 6	6.6	5.1	tangent	4.14	GMC	-	1
G37.87-0.40 7	1.2	7.5	near	4.14	GMC	-	1
G37.87-0.40 8	1.1	7.6	near	4.14	GMC	-	1
G37.87-0.40 9	1.5	7.2	near	4.14	GMC	-	1
G43.89-0.78 0	8.3	6.2	far	-	UCHII	blue gradient	3
G43.89-0.78 1	8.6	6.3	far	-	GMC	envelope	3
G45.07+0.13 0	7.6	6.2	far	4.26	UCHII	single	2
G45.07+0.13 1	6.5	6.0	far	4.26	GMC	-	2
G45.12+0.13 0	7.4	6.2	far	6.78	UCHII	other	1
G45.12+0.13 1	7.4	6.1	far	6.78	UCHII	envelope	1
G45.12+0.13 2	1.9	7.2	near	6.78	GMC	-	1
G45.12+0.13 3	7.4	6.0	far	6.78	GMC	envelope	1

Table 5.3 (cont'd)

Source Name	Distance (kpc)	Galactocentric Distance (kpc)	KDA[a] Resolution	$S_{1.1mm}$ (Jy)	Source Type	H_2CO Spectrum Type	Scenario[b]
G45.45+0.06 0	7.2	6.1	far	3.71	UCHII	blue gradient	2
G45.45+0.06 1	7.6	6.2	far	3.71	GMC	envelope	2
G45.45+0.06 2	1.9	7.2	near	3.71	GMC	-	2
G45.47+0.05 0	7.1	6.1	far	3.34	UCHII	red gradient	1+2+3
G45.47+0.05 1	1.9	7.2	near	3.34	GMC	-	1+2+3
G48.61+0.02 0	9.6	7.5	far	2.20	UCHII	red gradient	2+3
G48.61+0.02 1	0.7	8.0	near	2.20	GMC	-	2+3
G48.61+0.02 2	6.5	6.4	far	2.20	GMC	-	2+3
G50.32+0.68 0	2.1	7.2	near	-	UCHII	-	1
G60.88-0.13 0	2.8	7.4	near	4.90	UCHII	limit	2
G61.48+0.09 0	5.2	7.5	far	7.86	UCHII	single	4
G69.54-0.98 0	2.57	7.9	tangent	-	UCHII	thick	4+5
G70.29+1.60 0	7.3	9.1	far	-	UCHII	blue gradient	2
G70.29+1.60 1	7.8	9.3	far	-	GMC	envelope	2
G70.33+1.59 0	7.3	9.1	far	-	UCHII	single	1+2
IRAS 20051+3435 0	2.6	7.6	tangent	-	GMC	limit	-1
G41.74+0.10 0	11.3	7.6	far	0.56	UCHII	limit	-1
G41.74+0.10 1	11.6	7.7	far	0.56	UCHII	-	-1
G41.74+0.10 2	2.4	6.8	near	0.56	GMC	-	-1
G41.74+0.10 3	3.8	6.1	near	0.56	GMC	-	-1
G41.74+0.10 4	11.2	7.4	far	0.56	UCHII	-	-1
IRDC 1923+13 0	4.2	6.5	near	-	GMC	limit	-1
IRDC 1923+13 1	5.5	6.3	tangent	-	GMC	-	-1
IRDC 1923+13 2	3.8	6.6	near	-	GMC	-	-1

Table 5.3 (cont'd)

Source Name	Distance (kpc)	Galactocentric Distance (kpc)	KDA[a] Resolution	$S_{1.1mm}$ (Jy)	Source Type	H_2CO Spectrum Type	Scenario[b]
IRDC 1916+11 0	2.0	7.2	near	-	GMC	limit	-1
IRDC 1916+11 1	4.2	6.2	near	-	GMC	-	-1
IRDC 1916+11 2	3.6	6.4	near	-	GMC	-	-1

[a]The Kinematic Distance Ambiguity described in Section 5.7.3.

[b]Scenario or scenarios most likely to be consistent with the observed spectrum, as described in Section 5.8.3. In some cases, the spectrum was consistent with multiple scenarios or some blend of multiple scenarios. In others, the source could not be classified, in which case it is marked with -1 in this column.

Table 5.4. Inferred H_2CO line properties

Source Name	τ_{1-1}	τ_{1-1} (FFC)	τ_{2-2}	τ_{2-2} (FFC)	2-2 Upper Limit Flag	2cm Area[a] $''^2$	6cm Area [a] $''^2$
G32.80+0.19 0	0.18 (0.055)	0.2 (0.059)	0.12 (0.024)	0.15 (0.031)	0	88.0	226.2
G32.80+0.19 1	0.04 (0.013)	0.043 (0.013)	0.016 (0.0051)	0.021 (0.0065)	0	88.0	226.2
G32.80+0.19 2	0.027 (0.0089)	0.029 (0.0095)	0.0033 (0.00069)	0.0042 (0.00088)	0	88.0	226.2
G32.80+0.19 3	0.11 (0.035)	0.12 (0.037)	0.014 (0.0028)	0.018 (0.0035)	0	88.0	226.2
G32.80+0.19 4	0.039 (0.012)	0.042 (0.013)	0.0055 (0.0011)	0.0071 (0.0014)	0	88.0	226.2
G33.13-0.09 0	0.34 (0.1)	0.49 (0.15)	0.16 (0.032)	0.63 (0.12)	0	33.5	33.5
G33.13-0.09 1	0.035 (0.015)	0.047 (0.02)	0 (0.0059)	0 (0.0031)	1	33.5	33.5
G33.13-0.09 2	0.062 (0.022)	0.084 (0.029)	0 (0.0059)	0 (0.0031)	1	33.5	33.5
G33.13-0.09 3	0.061 (0.021)	0.082 (0.028)	0 (0.0059)	0 (0.0031)	1	33.5	33.5
G33.92+0.11 0	0.084 (0.027)	0.1 (0.031)	0.045 (0.0091)	0.094 (0.018)	0	214.0	214.0
G33.92+0.11 1	0.082 (0.026)	0.098 (0.031)	0.036 (0.0072)	0.075 (0.014)	0	214.0	214.0
G33.92+0.11 2	0.17 (0.062)	0.21 (0.074)	0 (0.0049)	0 (0.0031)	1	214.0	214.0
G34.26+0.15 0	0.38 (0.12)	0.4 (0.12)	0.22 (0.043)	0.26 (0.052)	0	10.9	10.9
G34.26+0.15 1	0.028 (0.0089)	0.029 (0.0092)	0.0067 (0.0014)	0.0079 (0.0017)	0	10.9	10.9
G34.26+0.15 2	0.017 (0.0059)	0.018 (0.006)	0.0026 (0.00059)	0.0031 (0.0007)	0	10.9	10.9
G34.26+0.15 3	0.022 (0.0072)	0.023 (0.0074)	0.0036 (0.00092)	0.0043 (0.0011)	0	10.9	10.9
G34.26+0.15 4	0.0082 (0.0036)	0.0085 (0.0037)	0.0026 (0.0011)	0.003 (0.0013)	0	10.9	10.9
G35.20-1.74 0	0.21 (0.063)	0.22 (0.066)	0.071 (0.014)	0.084 (0.017)	0	39.5	39.5
G35.20-1.74 1	0.028 (0.0085)	0.029 (0.0088)	0.0039 (0.0011)	0.0046 (0.0013)	0	39.5	39.5
G35.20-1.74 2	0.063 (0.019)	0.065 (0.019)	0.008 (0.0017)	0.0095 (0.0019)	0	39.5	39.5
G35.20-1.74 3	0.0073 (0.0027)	0.0075 (0.0028)	0 (0.0023)	0 (0.0031)	1	39.5	39.5
G35.57-0.03 0	0.11 (0.035)	0.15 (0.049)	0.056 (0.011)	0.26 (0.054)	0	6.7	6.7
G35.57-0.03 1	0.034 (0.018)	0.046 (0.024)	0.011 (0.0047)	0.047 (0.02)	0	6.7	6.7
G35.57-0.03 2	0.03 (0.017)	0.042 (0.023)	0 (0.0099)	0 (0.019)	1	6.7	6.7
G35.57-0.03 3	0.05 (0.021)	0.069 (0.029)	0 (0.0099)	0 (0.019)	1	6.7	6.7

Table 5.4 (cont'd)

Source Name	τ_{1-1}	τ_{1-1} (FFC)	τ_{2-2}	τ_{2-2} (FFC)	2-2 Upper Limit Flag	2cm Area[a] $''^2$	6cm Area [a] $''^2$	F
G35.57-0.03 4	0.051 (0.02)	0.069 (0.028)	0.017 (0.0065)	0.077 (0.029)	0	6.7	6.7	
G35.58+0.07 0	0.24 (0.071)	0.32 (0.097)	0.085 (0.017)	0.61 (0.12)	0	2.1	2.1	
G35.58+0.07 1	0.072 (0.029)	0.096 (0.038)	0 (0.0072)	0 (0.019)	1	2.1	2.1	
G35.58+0.07 2	0.037 (0.012)	0.049 (0.016)	0 (0.0072)	0 (0.019)	1	2.1	2.1	
G35.58+0.07 3	0.05 (0.016)	0.066 (0.021)	0 (0.0072)	0 (0.01)	1	2.1	2.1	
G37.87-0.40 0	0.12 (0.037)	0.13 (0.038)	0.047 (0.0095)	0.061 (0.012)	0	27.5	170.9	
G37.87-0.40 1	0.028 (0.0089)	0.029 (0.0092)	0.0095 (0.0024)	0.012 (0.0031)	0	27.5	170.9	
G37.87-0.40 2	0.081 (0.025)	0.084 (0.026)	0.0075 (0.0021)	0.0096 (0.0027)	0	27.5	170.9	
G37.87-0.40 3	0.074 (0.024)	0.076 (0.025)	0.011 (0.0023)	0.014 (0.003)	0	27.5	170.9	
G37.87-0.40 4	0.097 (0.029)	0.1 (0.03)	0.0098 (0.002)	0.013 (0.0026)	0	27.5	170.9	
G37.87-0.40 5	0.041 (0.013)	0.043 (0.013)	0.0033 (0.00068)	0.0043 (0.00087)	0	27.5	170.9	
G37.87-0.40 6	0.025 (0.0083)	0.026 (0.0086)	0.0021 (0.00052)	0.0026 (0.00066)	0	27.5	170.9	
G37.87-0.40 7	0.039 (0.012)	0.04 (0.012)	0.0054 (0.0012)	0.0069 (0.0015)	0	27.5	170.9	
G37.87-0.40 8	0.016 (0.0069)	0.016 (0.0071)	0.0035 (0.00081)	0.0046 (0.001)	0	27.5	170.9	
G37.87-0.40 9	0.03 (0.0095)	0.031 (0.0098)	0.0035 (0.00073)	0.0045 (0.00094)	0	27.5	170.9	
G43.89-0.78 0	0.25 (0.074)	0.32 (0.096)	0.037 (0.0078)	0.12 (0.024)	0	13.5	13.5	
G43.89-0.78 1	0.025 (0.0077)	0.031 (0.0097)	0.0097 (0.0022)	0.029 (0.0067)	0	13.5	13.5	
G45.07+0.13 0	0.092 (0.029)	0.13 (0.04)	0.04 (0.0081)	0.096 (0.02)	0	2.5	2.5	
G45.07+0.13 1	0.058 (0.02)	0.08 (0.027)	0.0061 (0.0019)	0.014 (0.0045)	0	2.5	2.5	
G45.12+0.13 0	0.043 (0.013)	0.045 (0.013)	0.014 (0.0028)	0.017 (0.0033)	0	15.4	516.6	
G45.12+0.13 1	0.035 (0.011)	0.036 (0.011)	0.0095 (0.002)	0.011 (0.0025)	0	15.4	516.6	
G45.12+0.13 2	0.046 (0.014)	0.048 (0.014)	0.0075 (0.0015)	0.009 (0.0019)	0	15.4	516.6	
G45.12+0.13 3	0.006 (0.002)	0.0062 (0.0021)	0.0033 (0.00068)	0.004 (0.00082)	0	15.4	516.6	
G45.45+0.06 0	0.32 (0.096)	0.32 (0.095)	0.063 (0.013)	0.069 (0.012)	0	1963.0	1963.0	
G45.45+0.06 1	0.025 (0.011)	0.026 (0.011)	0.01 (0.0021)	0.011 (0.0019)	0	1963.0	1963.0	

Table 5.4 (cont'd)

Source Name	τ_{1-1}	τ_{1-1} (FFC)	τ_{2-2}	τ_{2-2} (FFC)	2-2 Upper Limit Flag	2cm Area[a] $''^2$	6cm Area [a] $''^2$
G45.45+0.06 2	0.011 (0.0036)	0.012 (0.0035)	0 (0.0031)	0 (0.01)	1	1963.0	1963.0
G45.47+0.05 0	0.35 (0.11)	0.45 (0.14)	0.089 (0.018)	0.39 (0.079)	0	3.0	3.0
G45.47+0.05 1	0.018 (0.0068)	0.023 (0.0084)	0 (0.01)	0 (0.01)	1	3.0	3.0
G48.61+0.02 0	0.058 (0.018)	0.068 (0.021)	0.015 (0.0034)	0.053 (0.012)	0	25.5	25.5
G48.61+0.02 1	0.02 (0.0075)	0.023 (0.0088)	0 (0.0067)	0 (0.0026)	1	25.5	25.5
G48.61+0.02 2	0.016 (0.0052)	0.018 (0.0061)	0.0033 (0.0013)	0.012 (0.0046)	0	25.5	25.5
G50.32+0.68 0	0.027 (0.01)	0.045 (0.017)	0.0089 (0.0031)	0.058 (0.019)	0	108.0	108.0
G60.88-0.13 0	0.12 (0.037)	0.14 (0.043)	0.011 (0.0031)	0.031 (0.0071)	0	615.0	615.0
G61.48+0.09 0	0.088 (0.026)	0.09 (0.027)	0.069 (0.014)	0.088 (0.017)	0	355.0	355.0
G69.54-0.98 0	0.98 (0.29)	5.7 (1.7)	0.18 (0.037)	2.9 (0.57)	0	0.5	0.5
G70.29+1.60 0	0.086 (0.026)	0.089 (0.027)	0.022 (0.0044)	0.026 (0.0052)	0	52.8	52.8
G70.29+1.60 1	0.011 (0.0037)	0.012 (0.0038)	0 (0.0019)	0 (0.0026)	1	52.8	52.8
G70.33+1.59 0	0.7 (0.21)	0.78 (0.24)	0.34 (0.068)	0.52 (0.1)	0	16.4	16.4
IRAS 20051+3435 0	0.12 (0.036)	0.13 (0.014)	0.015 (0.0041)	0.016 (0.0034)	0	2747.75	2747.75
G41.74+0.10 0	0.13 (0.04)	0.2 (0.06)	0.01 (0.0027)	0.045 (0.012)	0	75.2	75.2
G41.74+0.10 1	0.04 (0.014)	0.06 (0.021)	0 (0.0071)	0 (0.0026)	1	75.2	75.2
G41.74+0.10 2	0.14 (0.043)	0.21 (0.065)	0 (0.0071)	0 (0.0026)	1	75.2	75.2
G41.74+0.10 3	0.045 (0.017)	0.067 (0.025)	0 (0.0071)	0 (0.0026)	1	75.2	75.2
G41.74+0.10 4	0.089 (0.029)	0.13 (0.043)	0 (0.0071)	0 (0.0028)	1	75.2	75.2
IRDC 1923+13 0	0.02 (0.0062)	0.02 (0.0047)	0 (0.009)	0 (0.0028)	1	2747.75	2747.75
IRDC 1923+13 1	0.016 (0.0051)	0.017 (0.0038)	0 (0.009)	0 (0.0028)	1	2747.75	2747.75
IRDC 1923+13 2	0.0081 (0.0028)	0.0083 (0.0023)	0 (0.009)	0 (0.0028)	1	2747.75	2747.75
IRDC 1916+11 0	0.033 (0.011)	0.036 (0.0062)	0 (0.014)	0 (0.042)	1	2747.75	2747.75
IRDC 1916+11 1	0.082 (0.025)	0.089 (0.0095)	0 (0.014)	0 (0.042)	1	2747.75	2747.75
IRDC 1916+11 2	0.017 (0.0064)	0.018 (0.0046)	0 (0.014)	0 (0.042)	1	2747.75	2747.75

Table 5.4 (cont'd)

Source Name	τ_{1-1}	τ_{1-1} (FFC)	τ_{2-2}	τ_{2-2} (FFC)	2-2 Upper Limit Flag	2cm Area[a] $''^2$	6cm Area [a] $''^2$	FFC Error

[a]The beam area is $2747.75''^2$, which is used when the CMB is the only background continuum illumination

Table 5.5. Derived physical properties from H_2CO

Source Name	$N(H_2CO)$[a] (cm^{-2})	$N(H_2CO)$ (FFC)[b] (cm^{-2})	$n(H_2)$ [a] (cm^{-3})	$n(H_2)$ (FFC)[b] (cm^{-3})	X_{H_2CO}[a]	X_{H_2CO} (FFC)[b]	Flag[c]
G32.80+0.19 0	$12.79^{+0.11}_{-0.16}$	$\mathbf{12.94^{+0.16}_{-0.24}}$	$5.10^{+0.25}_{-0.26}$	$\mathbf{5.21^{+0.27}_{-0.29}}$	$-10.79^{+0.15}_{-0.20}$	$\mathbf{-10.75^{+0.15}_{-0.18}}$	2
G32.80+0.19 1	$12.05^{+0.12}_{-0.11}$	$\mathbf{12.14^{+0.13}_{-0.13}}$	$4.96^{+0.22}_{-0.28}$	$\mathbf{5.05^{+0.21}_{-0.28}}$	$-11.39^{+0.20}_{-0.23}$	$\mathbf{-11.39^{+0.17}_{-0.20}}$	2
G32.80+0.19 2	$11.66^{+0.10}_{-0.10}$	$\mathbf{11.71^{+0.10}_{-0.10}}$	$4.16^{+0.39}_{-0.38}$	$\mathbf{4.33^{+0.31}_{-0.32}}$	$-10.97^{+0.44}_{-0.46}$	$\mathbf{-11.10^{+0.37}_{-0.37}}$	2
G32.80+0.19 3	$12.18^{+0.10}_{-0.09}$	$\mathbf{12.23^{+0.09}_{-0.09}}$	$4.07^{+0.38}_{-0.39}$	$\mathbf{4.23^{+0.32}_{-0.32}}$	$-10.37^{+0.44}_{-0.45}$	$\mathbf{-10.48^{+0.36}_{-0.38}}$	2
G32.80+0.19 4	$11.82^{+0.10}_{-0.09}$	$\mathbf{11.87^{+0.10}_{-0.09}}$	$4.30^{+0.31}_{-0.32}$	$\mathbf{4.44^{+0.26}_{-0.29}}$	$-10.97^{+0.37}_{-0.37}$	$\mathbf{-11.05^{+0.31}_{-0.32}}$	2
G33.13-0.09 0	> 12.80	$> \mathbf{13.56}$	> 4.54	$> \mathbf{5.10}$	> -10.62	$> \mathbf{-11.70}$	8
G33.13-0.09 1	< 11.96	$< \mathbf{11.90}$	< 4.50	$< \mathbf{3.91}$	< -8.44	$< \mathbf{-8.45}$	6
G33.13-0.09 2	$< \mathbf{12.20}$	< 0.00	$< \mathbf{4.29}$	< 0.00	$< \mathbf{-8.29}$	< 0.00	5
G33.13-0.09 3	$< \mathbf{12.20}$	< 0.00	$< \mathbf{4.32}$	< 0.00	$< \mathbf{-8.29}$	< 0.00	5
G33.92+0.11 0	> 12.35	$> \mathbf{12.64}$	> 4.86	$> \mathbf{5.16}$	> -11.29	$> \mathbf{-12.30}$	8
G33.92+0.11 1	$12.34^{+0.07}_{-0.08}$	$\mathbf{12.65^{+0.11}_{-0.17}}$	$4.97^{+0.22}_{-0.23}$	$\mathbf{5.26^{+0.22}_{-0.24}}$	$-11.11^{+0.19}_{-0.22}$	$\mathbf{-11.09^{+0.13}_{-0.16}}$	2
G33.92+0.11 2	-	-	-	-	-	-	9
G34.26+0.15 0	$13.01^{+0.10}_{-0.17}$	$\mathbf{13.13^{+0.15}_{-0.23}}$	$4.91^{+0.28}_{-0.29}$	$\mathbf{5.01^{+0.31}_{-0.32}}$	$-10.38^{+0.18}_{-0.23}$	$\mathbf{-10.36^{+0.17}_{-0.23}}$	2
G34.26+0.15 1	$11.79^{+0.09}_{-0.08}$	$\mathbf{11.83^{+0.09}_{-0.08}}$	$4.67^{+0.23}_{-0.25}$	$\mathbf{4.75^{+0.21}_{-0.24}}$	$-11.36^{+0.26}_{-0.27}$	$\mathbf{-11.40^{+0.23}_{-0.25}}$	2
G34.26+0.15 2	$11.53^{+0.10}_{-0.10}$	$\mathbf{11.56^{+0.10}_{-0.10}}$	$4.38^{+0.30}_{-0.33}$	$\mathbf{4.48^{+0.28}_{-0.30}}$	$-11.33^{+0.36}_{-0.37}$	$\mathbf{-11.40^{+0.32}_{-0.34}}$	2
G34.26+0.15 3	$11.63^{+0.11}_{-0.10}$	$\mathbf{11.66^{+0.10}_{-0.10}}$	$4.43^{+0.29}_{-0.32}$	$\mathbf{4.53^{+0.26}_{-0.30}}$	$-11.28^{+0.34}_{-0.35}$	$\mathbf{-11.34^{+0.31}_{-0.32}}$	2
G34.26+0.15 4	$11.40^{+0.17}_{-0.14}$	$\mathbf{11.45^{+0.17}_{-0.16}}$	$4.87^{+0.31}_{-0.43}$	$\mathbf{4.94^{+0.30}_{-0.42}}$	$-11.95^{+0.30}_{-0.35}$	$\mathbf{-11.98^{+0.27}_{-0.34}}$	2
G35.20-1.74 0	$12.60^{+0.08}_{-0.07}$	$\mathbf{12.65^{+0.08}_{-0.07}}$	$4.72^{+0.25}_{-0.25}$	$\mathbf{4.79^{+0.25}_{-0.26}}$	$-10.61^{+0.23}_{-0.27}$	$\mathbf{-10.62^{+0.22}_{-0.26}}$	2
G35.20-1.74 1	$11.69^{+0.11}_{-0.10}$	$\mathbf{11.72^{+0.11}_{-0.10}}$	$4.30^{+0.33}_{-0.37}$	$\mathbf{4.41^{+0.30}_{-0.33}}$	$-11.09^{+0.39}_{-0.39}$	$\mathbf{-11.16^{+0.34}_{-0.36}}$	2
G35.20-1.74 2	$11.97^{+0.09}_{-0.09}$	$\mathbf{12.00^{+0.09}_{-0.09}}$	$4.20^{+0.34}_{-0.35}$	$\mathbf{4.31^{+0.30}_{-0.30}}$	$-10.70^{+0.39}_{-0.41}$	$\mathbf{-10.79^{+0.34}_{-0.36}}$	2
G35.20-1.74 3	< 11.41	$< \mathbf{11.44}$	< 4.89	$< \mathbf{5.02}$	< -9.24	$< \mathbf{-9.30}$	6
G35.57-0.03 0	> 12.42	$> \mathbf{13.38}$	> 4.82	$> \mathbf{5.61}$	> -11.20	$> \mathbf{-12.02}$	8
G35.57-0.03 1	> 11.72	$> \mathbf{12.25}$	> 4.51	$> \mathbf{5.13}$	> -11.80	$> \mathbf{-12.72}$	8
G35.57-0.03 2	< 11.98	$< \mathbf{12.12}$	< 4.96	$< \mathbf{5.12}$	< -8.71	$< \mathbf{-8.72}$	6
G35.57-0.03 3	< 12.09	$< \mathbf{12.23}$	< 4.60	$< \mathbf{4.78}$	< -8.38	$< \mathbf{-8.37}$	6

Table 5.5 (cont'd)

Source Name	N(H_2CO)[a] (cm^{-2})	N(H_2CO) (FFC)[b] (cm^{-2})	n(H_2) [a] (cm^{-3})	n(H_2) (FFC)[b] (cm^{-3})	X_{H_2CO}[a]	X_{H_2CO} (FFC)[b]	Flag[c]
G35.57-0.03 4	> 11.93	$> \mathbf{12.47}$	> 4.58	$> \mathbf{5.20}$	> -11.55	$> \mathbf{-12.48}$	8
G35.58+0.07 0	> 12.58	$> \mathbf{14.06}$	> 4.50	$> \mathbf{5.48}$	> -10.79	$> \mathbf{-11.71}$	8
G35.58+0.07 1	< 12.19	$< \mathbf{12.32}$	< 4.08	$< \mathbf{4.55}$	< -8.07	$< \mathbf{-8.14}$	6
G35.58+0.07 2	< 11.96	$< \mathbf{12.10}$	< 4.57	$< \mathbf{4.95}$	< -8.53	$< \mathbf{-8.63}$	6
G35.58+0.07 3	< 12.06	$< \mathbf{12.17}$	< 4.35	$< \mathbf{4.38}$	< -8.32	$< \mathbf{-8.24}$	6
G37.87-0.40 0	$12.44^{+0.07}_{-0.07}$	$\mathbf{12.53^{+0.07}_{-0.09}}$	$4.86^{+0.22}_{-0.23}$	$\mathbf{4.98^{+0.21}_{-0.24}}$	$-10.90^{+0.20}_{-0.24}$	$\mathbf{-10.92^{+0.18}_{-0.21}}$	2
G37.87-0.40 1	$11.87^{+0.10}_{-0.09}$	$\mathbf{11.95^{+0.10}_{-0.09}}$	$4.89^{+0.22}_{-0.26}$	$\mathbf{5.00^{+0.21}_{-0.24}}$	$-11.50^{+0.21}_{-0.24}$	$\mathbf{-11.53^{+0.18}_{-0.22}}$	2
G37.87-0.40 2	$12.10^{+0.18}_{-0.26}$	$\mathbf{12.09^{+0.14}_{-0.28}}$	$3.16^{+1.15}_{-1.20}$	$\mathbf{3.79^{+1.78}_{-0.71}}$	$-9.54^{+1.32}_{-1.41}$	$\mathbf{-10.18^{+0.77}_{-2.06}}$	4
G37.87-0.40 3	$12.05^{+0.10}_{-0.10}$	$\mathbf{12.10^{+0.10}_{-0.09}}$	$4.33^{+0.32}_{-0.33}$	$\mathbf{4.49^{+0.28}_{-0.29}}$	$-10.76^{+0.37}_{-0.39}$	$\mathbf{-10.87^{+0.31}_{-0.34}}$	2
G37.87-0.40 4	$12.17^{+0.17}_{-0.25}$	$\mathbf{12.14^{+0.10}_{-0.09}}$	$3.36^{+1.35}_{-0.98}$	$\mathbf{4.13^{+0.35}_{-0.36}}$	$-9.67^{+1.12}_{-1.60}$	$\mathbf{-10.46^{+0.41}_{-0.42}}$	2
G37.87-0.40 5	$11.85^{+0.18}_{-0.21}$	$\mathbf{11.88^{+0.18}_{-0.25}}$	$3.05^{+1.04}_{-1.17}$	$\mathbf{3.34^{+1.33}_{-1.03}}$	$-9.68^{+1.32}_{-1.25}$	$\mathbf{-9.94^{+1.17}_{-1.58}}$	4
G37.87-0.40 6	$11.67^{+0.19}_{-0.23}$	$\mathbf{11.70^{+0.19}_{-0.26}}$	$3.08^{+1.07}_{-1.21}$	$\mathbf{3.33^{+1.32}_{-1.13}}$	$-9.89^{+1.36}_{-1.30}$	$\mathbf{-10.11^{+1.26}_{-1.58}}$	4
G37.87-0.40 7	$11.81^{+0.10}_{-0.09}$	$\mathbf{11.86^{+0.10}_{-0.09}}$	$4.28^{+0.31}_{-0.33}$	$\mathbf{4.45^{+0.27}_{-0.29}}$	$-10.95^{+0.37}_{-0.38}$	$\mathbf{-11.07^{+0.32}_{-0.32}}$	2
G37.87-0.40 8	$11.56^{+0.11}_{-0.11}$	$\mathbf{11.63^{+0.11}_{-0.10}}$	$4.67^{+0.30}_{-0.33}$	$\mathbf{4.80^{+0.29}_{-0.31}}$	$-11.59^{+0.34}_{-0.38}$	$\mathbf{-11.65^{+0.30}_{-0.34}}$	2
G37.87-0.40 9	$11.72^{+0.13}_{-0.29}$	$\mathbf{11.74^{+0.10}_{-0.09}}$	$3.98^{+1.97}_{-0.52}$	$\mathbf{4.32^{+0.31}_{-0.32}}$	$-10.74^{+0.60}_{-2.26}$	$\mathbf{-11.06^{+0.36}_{-0.37}}$	2
G43.89-0.78 0	$12.49^{+0.10}_{-0.09}$	$\mathbf{12.76^{+0.08}_{-0.07}}$	$4.18^{+0.34}_{-0.33}$	$\mathbf{4.68^{+0.28}_{-0.28}}$	$-10.17^{+0.37}_{-0.40}$	$\mathbf{-10.40^{+0.24}_{-0.30}}$	2
G43.89-0.78 1	$\mathbf{11.87^{+0.09}_{-0.08}}$	$12.80^{+0.61}_{-1.00}$	$\mathbf{4.95^{+0.20}_{-0.23}}$	$6.16^{+0.96}_{-1.84}$	$\mathbf{-11.56^{+0.19}_{-0.22}}$	$-11.84^{+0.88}_{-0.42}$	1
G45.07+0.13 0	$12.38^{+0.08}_{-0.08}$	$\mathbf{12.75^{+0.13}_{-0.20}}$	$4.96^{+0.22}_{-0.24}$	$\mathbf{5.25^{+0.25}_{-0.27}}$	$-11.06^{+0.19}_{-0.22}$	$\mathbf{-10.97^{+0.15}_{-0.18}}$	2
G45.07+0.13 1	-	-	-	-	-	-	9
G45.12+0.13 0	$12.02^{+0.08}_{-0.07}$	$\mathbf{12.07^{+0.08}_{-0.07}}$	$4.83^{+0.21}_{-0.21}$	$\mathbf{4.92^{+0.19}_{-0.21}}$	$-11.30^{+0.20}_{-0.23}$	$\mathbf{-11.32^{+0.19}_{-0.21}}$	2
G45.12+0.13 1	$11.90^{+0.09}_{-0.08}$	$\mathbf{11.95^{+0.08}_{-0.08}}$	$4.74^{+0.22}_{-0.23}$	$\mathbf{4.83^{+0.21}_{-0.23}}$	$-11.32^{+0.23}_{-0.25}$	$\mathbf{-11.36^{+0.21}_{-0.23}}$	2
G45.12+0.13 2	$11.90^{+0.10}_{-0.08}$	$\mathbf{11.93^{+0.09}_{-0.09}}$	$4.41^{+0.26}_{-0.28}$	$\mathbf{4.52^{+0.24}_{-0.26}}$	$-11.00^{+0.32}_{-0.32}$	$\mathbf{-11.06^{+0.29}_{-0.30}}$	2
G45.12+0.13 3	$11.48^{+0.08}_{-0.09}$	$\mathbf{11.55^{+0.08}_{-0.12}}$	$5.15^{+0.19}_{-0.21}$	$\mathbf{5.23^{+0.19}_{-0.22}}$	$-12.15^{+0.16}_{-0.18}$	$\mathbf{-12.16^{+0.14}_{-0.17}}$	2
G45.45+0.06 0	$12.62^{+0.08}_{-0.08}$	$\mathbf{12.64^{+0.07}_{-0.08}}$	$4.33^{+0.29}_{-0.31}$	$\mathbf{4.37^{+0.28}_{-0.28}}$	$-10.19^{+0.33}_{-0.35}$	$\mathbf{-10.21^{+0.30}_{-0.33}}$	2
G45.45+0.06 1	$11.89^{+0.08}_{-0.08}$	$\mathbf{11.92^{+0.07}_{-0.07}}$	$5.00^{+0.26}_{-0.28}$	$\mathbf{5.04^{+0.26}_{-0.27}}$	$-11.59^{+0.25}_{-0.29}$	$\mathbf{-11.60^{+0.23}_{-0.28}}$	2

Table 5.5 (cont'd)

Source Name	$N(H_2CO)$[a] (cm^{-2})	$N(H_2CO)$ (FFC)[b] (cm^{-2})	$n(H_2)$ [a] (cm^{-3})	$n(H_2)$ (FFC)[b] (cm^{-3})	X_{H_2CO}[a]	X_{H_2CO} (FFC)[b]	Flag[c]
G45.45+0.06 2	< 11.55	$< \mathbf{11.66}$	< 4.77	$< \mathbf{5.39}$	< -9.04	$< \mathbf{-9.43}$	6
G45.47+0.05 0	$12.71^{+0.09}_{-0.07}$	$\mathbf{13.48^{+0.32}_{-0.50}}$	$4.46^{+0.28}_{-0.28}$	$\mathbf{5.21^{+0.40}_{-0.34}}$	$-10.23^{+0.28}_{-0.31}$	$\mathbf{-10.21^{+0.21}_{-0.19}}$	2
G45.47+0.05 1	$< \mathbf{11.91}$	< 11.92	$< \mathbf{5.34}$	< 5.23	$< \mathbf{-8.65}$	< -8.57	5
G48.61+0.02 0	$12.06^{+0.09}_{-0.09}$	$\mathbf{12.53^{+0.13}_{-0.17}}$	$4.68^{+0.23}_{-0.25}$	$\mathbf{5.29^{+0.22}_{-0.24}}$	$-11.10^{+0.25}_{-0.26}$	$\mathbf{-11.25^{+0.13}_{-0.16}}$	2
G48.61+0.02 1	$< \mathbf{11.88}$	< 11.91	$< \mathbf{5.09}$	< 4.47	$< \mathbf{-8.61}$	< -8.58	5
G48.61+0.02 2	$11.54^{+0.14}_{-0.13}$	$\mathbf{11.94^{+0.18}_{-0.23}}$	$4.60^{+0.28}_{-0.39}$	$\mathbf{5.22^{+0.23}_{-0.36}}$	$-11.54^{+0.33}_{-0.33}$	$\mathbf{-11.76^{+0.14}_{-0.19}}$	2
G50.32+0.68 0	> 11.71	$> \mathbf{12.41}$	> 4.61	$> \mathbf{5.31}$	> -11.77	$> \mathbf{-12.63}$	8
G60.88-0.13 0	$12.24^{+0.18}_{-0.25}$	$\mathbf{12.35^{+0.09}_{-0.09}}$	$3.20^{+1.19}_{-1.16}$	$\mathbf{4.51^{+0.27}_{-0.28}}$	$-9.44^{+1.29}_{-1.43}$	$\mathbf{-10.64^{+0.28}_{-0.31}}$	2
G61.48+0.09 0	> 12.51	$> \mathbf{12.62}$	> 5.07	$> \mathbf{5.19}$	> -11.27	$> \mathbf{-12.33}$	8
G69.54-0.98 0	-	-	-	-	-	-	11
G70.29+1.60 0	$12.21^{+0.09}_{-0.08}$	$\mathbf{12.25^{+0.08}_{-0.08}}$	$4.67^{+0.23}_{-0.23}$	$\mathbf{4.74^{+0.23}_{-0.24}}$	$-10.94^{+0.24}_{-0.26}$	$\mathbf{-10.97^{+0.23}_{-0.26}}$	2
G70.29+1.60 1	< 11.53	$< \mathbf{11.55}$	< 4.50	$< \mathbf{4.67}$	< -8.92	$< \mathbf{-8.98}$	6
G70.33+1.59 0	$13.16^{+0.09}_{-0.14}$	$\mathbf{13.41^{+0.19}_{-0.35}}$	$4.64^{+0.34}_{-0.32}$	$\mathbf{4.83^{+0.39}_{-0.37}}$	$-9.96^{+0.22}_{-0.31}$	$\mathbf{-9.90^{+0.21}_{-0.26}}$	2
IRAS 20051+3435 0	$\mathbf{12.20^{+0.11}_{-0.10}}$	$12.23^{+0.04}_{-0.05}$	$\mathbf{4.12^{+0.39}_{-0.41}}$	$4.11^{+0.21}_{-0.23}$	$\mathbf{-10.40^{+0.45}_{-0.46}}$	$-10.35^{+0.22}_{-0.22}$	3
G41.74+0.10 0	$12.25^{+0.17}_{-0.23}$	$\mathbf{12.48^{+0.10}_{-0.09}}$	$2.99^{+0.99}_{-1.18}$	$\mathbf{4.50^{+0.28}_{-0.31}}$	$-9.23^{+1.31}_{-1.22}$	$\mathbf{-10.50^{+0.29}_{-0.32}}$	2
G41.74+0.10 1	$< \mathbf{12.12}$	< 0.00	$< \mathbf{4.72}$	< 0.00	$< \mathbf{-8.37}$	< 0.00	5
G41.74+0.10 2	$< \mathbf{12.18}$	< 0.00	$< \mathbf{3.21}$	< 0.00	$< \mathbf{-8.91}$	< 0.00	5
G41.74+0.10 3	$< \mathbf{12.17}$	< 0.00	$< \mathbf{4.70}$	< 0.00	$< \mathbf{-8.32}$	< 0.00	5
G41.74+0.10 4	$< \mathbf{12.27}$	< 0.00	$< \mathbf{4.11}$	< 0.00	$< \mathbf{-8.22}$	< 0.00	5
IRDC 1923+13 0	$< \mathbf{11.86}$	< 11.84	$< \mathbf{5.19}$	< 4.47	$< \mathbf{-8.63}$	< -8.65	5
IRDC 1923+13 1	$< \mathbf{11.86}$	< 11.77	$< \mathbf{5.30}$	< 4.58	$< \mathbf{-8.70}$	< -8.72	5
IRDC 1923+13 2	$< \mathbf{13.29}$	< 11.53	$< \mathbf{8.00}$	< 5.00	$< \mathbf{-8.95}$	< -8.96	5
IRDC 1916+11 0	$< \mathbf{12.05}$	< 12.57	$< \mathbf{5.16}$	< 5.62	$< \mathbf{-8.44}$	< -8.46	5
IRDC 1916+11 1	$< \mathbf{12.36}$	< 12.40	$< \mathbf{4.61}$	< 5.03	$< \mathbf{-8.13}$	< -8.16	5
IRDC 1916+11 2	$< \mathbf{12.09}$	< 13.77	$< \mathbf{5.55}$	< 8.00	$< \mathbf{-8.68}$	< -8.68	5

Table 5.5 (cont'd)

Source Name	$N(H_2CO)$[a] (cm^{-2})	$N(H_2CO)$ (FFC)[b] (cm^{-2})	$n(H_2)$ [a] (cm^{-3})	$n(H_2)$ (FFC)[b] (cm^{-3})	X_{H_2CO}[a]	X_{H_2CO} (FFC)[b]	Flag[c]

[a]The values used in this paper are shown in boldface. Uncorrected values are listed in this column. The filling-factor corrected values are shown for comparison in the next column even though they were not used for analysis.

[b]The values used in this paper are shown in boldface. Filling-factor corrected values are listed in this column. The uncorrected values are shown for comparison in the previous column even though they not used for analysis.

[c]Flags:

(1) No filling factor correction (no FFC) is the most reliable.

(2) Filling factor correction (FFC) is the most reliable

(3) There is an ambiguity between low density / high abundance and low abundance / high density (no FFC)

(4) There is an ambiguity between low density / high abundance and low abundance / high density (FFC)

(5) Upper Limit (No FFC)

(6) Upper Limit (FFC)

(7) Lower Limit (No FFC)

(8) Lower Limit (FFC)

(9) Unreliable estimate because of continuum / filling factor uncertainty.

(10) No limit (S/N)

(11) Optically Thick

5.4.2 Green Bank Telescope

We observed the H_2CO $2_{11}-2_{12}$ line at 2 cm (14.488789 GHz) with the Green Bank Telescope (GBT)[4] dual-beam Ku-band receiver as part of project GBT09C-049. The GBT dual-beam Ku-band receiver was used for 4 hours on January 18th, 2010 in beam-switched nodding mode. System temperatures ranged from 27 to 38 K in the H_2CO band centered on the $2_{11}-2_{12}$ line. A bandwidth of 12.5 MHz (258.8 km s^{-1}) and channel width of 3.052 kHz (0.063 km s^{-1}) were used with 9-level sampling, with receiver temperature $\approx$ 21K. Three additional tunings were acquired simultaneously, centered between the H and He 75α, 76α, and 77α radio recombination lines (RRLs) with the same channel widths and bandwidths as above at 14.1315, 14.6930, and 15.2846 GHz. Each source was observed for 150 seconds in each receiver for a total on-source integration time of 300 seconds. Each observation in the pair was independently inspected to search for emission/absorption in the off position, which was 5.5′ away in azimuth. When absorption was detected in one of the off positions, that on/off pair was discarded if one of the detected lines was affected, but otherwise was noted and ignored. Pointing and focus observations on the calibrator source 1822-0938 were taken at the start of and two hours into the observations.

The gain was assumed to be 1.91 K/Jy based on previous calibration observations on point sources in Ku-band; our flux density measurements will therefore be overestimates for extended sources. The aperture efficiency was $\eta_A = 0.671$, and the main beam efficiency $\eta_{MB} = 1.32\eta_A = 0.886$, so our main-beam corrected measurements could overestimate extended source flux densities by at most 13% (ignoring atmospheric absorption). The data were calibrated using the normal GETNOD procedure in GBTIDL [5], which assumes an atmospheric opacity at zenith $\tau = 0.014$ at 14.488 GHz.

We assume primary beam $\theta_{FWHM} = 51.1''$ per the GBT observers manual. We assume a conservative 10% error in the beam area $\Omega = 7.8 \times 10^{-8}$ sr, which governs the flux density received

[4] The National Radio Astronomy Observatory operates the GBT and VLA and is a facility of the National Science Foundation operated under cooperative agreement by Associated Universities, Inc.

[5] GBTIDL (http://gbtidl.nrao.edu/) is the data reduction package produced by NRAO and written in the IDL language for the reduction of GBT data. The National Radio Astronomy Observatory is a facility of the National Science Foundation operated under cooperative agreement by Associated Universities, Inc.

from the CMB over the observed area. Beam size error should be dominated by small errors in focus. By utilizing the 305 m Arecibo telescope at 6 cm and the 100 m GBT at 2 cm, we acquired beam-matched (FWHM$\sim 50''$) observations of the H_2CO $1_{10} - 1_{11}$ and $2_{11} - 2_{12}$ lines.

5.4.2.1 GBT Data Reduction

In the 24 lines of sight, 75 independent components were identified from the $1_{10} - 1_{11}$ spectra. These were fit with gaussians using GBTIDL's FITGAUSS routine. Out of these 75 components, 51 had corresponding $2_{11} - 2_{12}$ detections. The fitted gaussian spectral lines are listed by line of sight in Table 5.1. The gaussian fits may not be representative of the true spectral line profile; complex spectral line profiles are discussed in Section 5.8.2.

The 2 cm continua were measured by fitting a first-order baseline in each reduced nodded pair excluding the line and the bandpass edges. Figure 5.1 shows the flat baselines achieved in the observations, though the RRL spectrum shows an example of the artifacts seen at the edges of the bandpass. The continuum error listed in the table is the RMS of only the data included in the baseline fit after the baseline was subtracted from the spectrum; the systematic error from flux calibration uncertainty is 20% and dominant.

5.4.3 Arecibo

The Arecibo 4.829660 GHz H_2CO $1_{10} - 1_{11}$ observations used in this project were previously presented in Araya et al. (2002) and Araya et al. (2004) and were kindly provided in reduced form by E. Araya. All observations were performed using standard on/off position switching and 5 minute integration times in both the on and off positions, resulting in off positions 1.25 degrees away from the pointing center. We assume a 30% error in the continuum (based on measured gains in the range 2.0-2.5 as reported in Araya et al., 2002) and an effective diameter of 227m ($\theta_{FWHM} = 56''$, $\Omega = 9.0 \times 10^{-8}$ sr) with 10% uncertainty[6] .

The Arecibo spectral lines were re-fit for this paper by converting the Arecibo data from

[6] http://www.naic.edu/$\sim$phil/sysperf/misc/hpbw_vs_lambda_2004.html

CLASS[7] to GBTIDL's SDFITS format[8] and using GBTIDL's FITGAUSS routine. The 6 cm continua were taken directly from Araya et al. (2002) Table 3.

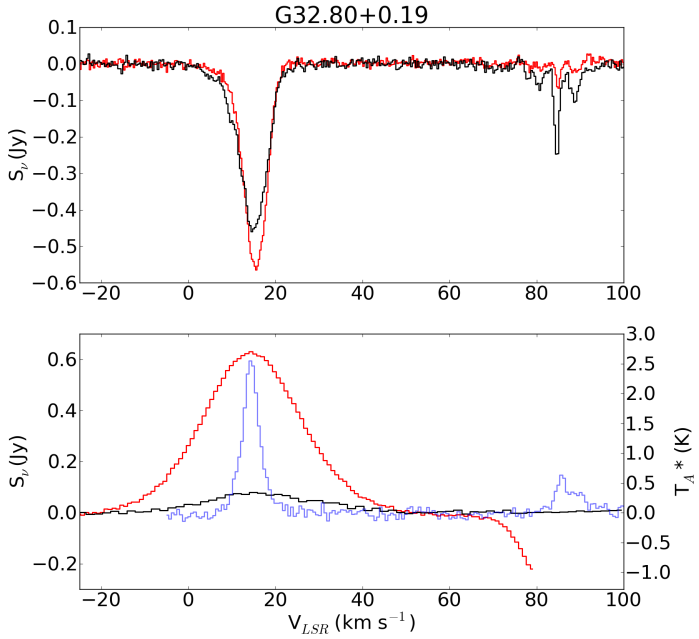

Figure 5.1 *Top:* The GBT $2_{11} - 2_{12}$ (red) and Arecibo $1_{10} - 1_{11}$ (black) spectra of G32.80+0.19. *Bottom:* The GBT H75α (red) and Arecibo H110α (black) spectra with the GRS ^{13}CO spectrum (light blue) overlaid. The left axis is for the RRLs and the right axis is for the ^{13}CO. The C and He RRLs are not displayed.

5.4.4 Other Archival Data

5.4.4.1 Very Large Array

We acquired VLA archival images from the Multi-Array Galactic Plane Imaging Survey (MAGPIS) 6 cm Epoch 3 data set (Helfand et al., 2006) and the NRAO VLA Archive Survey (NVAS)[9] . MAGPIS has a resolution of $\sim 4''$ and sensitivity $\sigma \sim 2.5$mJy/bm. The NVAS has variable resolution and sensitivity since it is based on VLA archival data. The VLA data was used to estimate source sizes and interferometer-to-single-dish flux ratios.

[7] CLASS is part of the GILDAS software developed by IRAM.

[8] Code for the CLASS-GBTIDL conversion is available from `http://code.google.com/p/casaradio/wiki/class\_to\_gbt`

[9] The NVAS is run by Lourant Sjouwerman at the NRAO. It has not yet been published.

5.4.4.2 Bolocam 1.1 mm

We extract 1.1 mm dust continuum fluxes from the Bolocam Galactic Plane Survey (BGPS) v1.0 release summing over a 25″ radius aperture after subtracting the median in a 50-200″ annulus to remove background contributions. The aperture size is selected to match the 1.1 mm data to the 2 and 6 cm data. We assume a uniform 50% systematic error in BGPS fluxes from combined uncertainties in the calibration and background subtraction. Aguirre et al. (2011) contains a complete discussion of the uncertainties in the BGPS. We apply the Aguirre et al. (2011) recommended flux correction of 1.5 and aperture correction for a 25″ aperture of 1.21. Additionally, data from the Bolocam catalog (Rosolowsky et al., 2010) was used with the flux correction and an aperture correction of 1.46 for 20″ apertures.

5.4.4.3 Boston University / Five College Radio Observatory Galactic Ring Survey

The BU FCRAO GRS (Jackson et al., 2006) is a survey of the Galactic plane in the ^{13}CO 1-0 line with $\sim$ 46″ resolution. We extracted spectra in 25″ radius apertures from the publicly available data for comparison with the H_2CO spectra.

5.4.4.4 GLIMPSE

The Galactic Legacy Infrared Mid-Plane Survey Extraordinaire (Benjamin et al., 2003, GLIMPSE) maps were used to examine the morphology of the objects in our survey in order to determine whether an IRDC was present.

5.5 Models and Error Estimation

A grid of large velocity gradient (LVG) models was run using both the RADEX (van der Tak et al., 2007a) code and a proprietary code by Henkel et al. (1980) with a gradient of 1 km s^{-1}pc^{-1}. The models from the two codes were consistent to within $\sim$ 10% in predicted optical depth and T_{ex}. Both utilized collision rates from Green (1991) extracted from the LAMDA database[10]

[10] `http://www.strw.leidenuniv.nl/$\sim$moldata/`

and multiplied by the recommended factor of 1.6 to account for collisions with H_2 being more efficient than He. The expected accuracy is $\sim 30\%$. Zeiger & Darling (2010) demonstrated that the errors in collision rates lead to systematic errors $\lesssim 50\%$ (0.3 dex) in the measured quantities ($N(H_2CO)$, $n(H_2)$). When measuring density and column, we used the RADEX models because of their extensively tested code and documentation. All of the models used a kinetic temperature of 40 K and covered a range of 500 densities $\times$ 500 columns logarithmically sampled over $10^1 < n(H_2) < 10^7$ cm^{-3} and $10^{11} < N(\text{o-}H_2CO) < 10^{16}$ cm^{-2}. The assumption $T_K = 40$ K is reasonable in UCH II regions, which should be warmer than IRDCs and other cold molecular clouds. Dust temperatures measured towards UCH II regions are around 40 K (Rivera-Ingraham et al., 2010). In the foreground clouds, this assumption is less well supported, but as long as the temperatures are higher than ~ 20 K, the models change little with temperature (Figure 5.2).

Because of a collisional selection effect, above its critical density ($n_{cr}(H_2CO\ 1_{10} - 1_{11}) \approx 8$ cm^{-3}, $n_{cr}(H_2CO\ 2_{11} - 2_{12}) \approx 76$ cm^{-3}, Mangum et al., 2008) H_2CO preferentially overpopulates lower states of the K-doublet (ΔJ =0, $\Delta K_a = 0$, $\Delta K_c = \pm 1$, Henkel et al., 1980). These spectral lines are cooled to excitation temperatures lower than the CMB and can therefore be seen in absorption against it. The $1_{10} - 1_{11}/2_{11} - 2_{12}$ absorption line ratio is sensitive to the density of H_2 at densities $\gtrsim 10^{3.5}$ cm^{-3}, allowing measurements of the density to within $\sim$0.3 dex with little sensitivity to gas kinetic temperature (Mangum et al., 2008). When density is 'measured' with critical density based tracers such as CO, CS, HCN, or HCO^+, the estimate can be off by as much as 2 orders of magnitude because of radiative trapping effects. Similarly, measurements of density assuming spherical symmetry can be very far from the local values.

The collision rates of H_2CO with H_2 have been re-derived with a claimed accuracy of 10% by Troscompt et al. (2009b). Troscompt et al. (2009a) showed that collisions with para-H_2 are more efficient at cooling H_2CO into absorption against the CMB than He or ortho-H_2 and that H_2CO absorption is therefore sensitive to the Ortho/Para ratio of H_2. These improved rates are not used in this paper since they are only computed over a more limited range of temperatures, but may be used in future works.

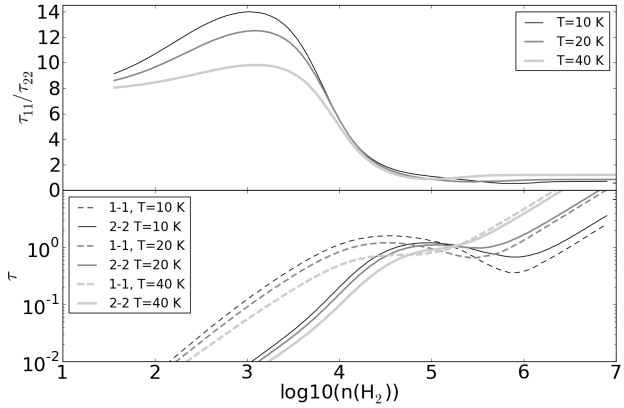

Figure 5.2 The predicted optical depth ratio (*top*) and optical depth (*bottom*) vs. volume density assuming a fixed abundance $X_{\text{o-H}_2\text{CO}} = 10^{-9}$ per km s^{-1}pc^{-1} shows that the dependence of the derived density on temperature is weak. At lower abundances, these curves shift to the right, providing sensitivity to moderately higher densities. Our 5-σ detection limit is generally around $\tau \sim 0.01$.

5.5.1 Turbulence

Molecular gas is often observed to have spectral line widths consistent with supersonic turbulence (Kainulainen et al., 2009) and therefore a lognormal density distribution (Kritsuk et al., 2007). Our LVG models assume constant density per velocity bin, so the resulting models should be smoothed by the probability distribution function (PDF) of the density. For clouds with a narrow density distribution (logarithmic standard deviation of the density $\sigma_s \equiv \sigma_{ln(\rho)/ln(\bar{\rho})} \lesssim 0.5$)[11] , the effect of smoothing is smaller than other systematic errors, but for more turbulent clouds the density PDF width can exceed an order of magnitude (e.g., Federrath et al., 2010a) and will substantially change the derived density. Because the Mach numbers of the turbulence in the observed clouds are unconstrained, we cannot correct for this added uncertainty. The change in measured density is $|\Delta \log(\rho)| < 0.25$ for $\sigma_s \leq 0.5$, with a slight bias towards higher densities at lower optical depth ratio $\tau_{1_{10}-1_{11}}/\tau_{2_{11}-2_{12}}$ (Figure 5.3). However, for $\sigma_s = 1.5$, the bias exceeds an order of magnitude at some densities.

Additionally, we consider the effects of "gravoturbulence", in which a high-density tail inconsistent with a lognormal distribution is observed. Kainulainen et al. (2009) report column density distributions derived from 2MASS extinction measurements that can be used as a proxy for the density distribution for a wide variety of clouds. Non-star-forming clouds retain a lognormal distribution and are consistent with the analysis presented above. However, evolved star-forming regions develop a high-column density tail. For evolved (actively star-forming) regions like Ophiucus, Orion, and Perseus, the high-column density tail is substantial, and H_2CO density measurements will be highly biased towards the highest density gas. More quiescent regions like the Pipe and Coalsack nebulae are consistent with a lognormal column distribution to a degree that the high-column density tail would not affect H_2CO density measurements significantly.

To demonstrate the effects of turbulent distributions, we calculate the optical depth ratio as a function of the mean density for three turbulent widths in Figure 5.3. We compare the density that

[11] We use ρ to indicate number density in this section in order to be consistent with the cited literature. Because the widths are relative to a mean density, the scaling between mass and number density is unimportant.

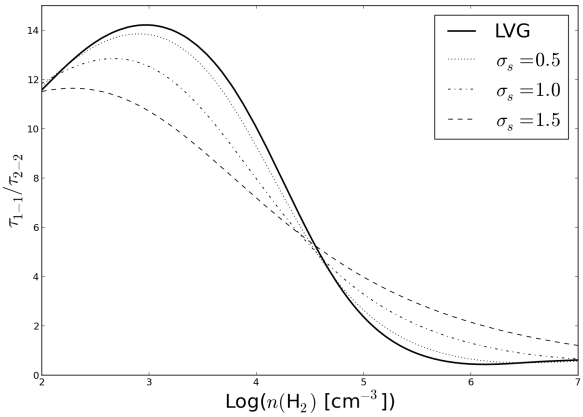

Figure 5.3 The optical depth ratio as a function of density for turbulent density distributions with widths specified in the legend. The optical depth ratio varies more slowly with density than in the pure LVG model (the solid line is the same as the black 10 K line in Figure 5.2a).

would be inferred from the spectral line ratio assuming no turbulence (just LVG) to the 'correct' density including turbulent effects in Figure 5.4. We have also compared the LVG and turbulent densities to "gravoturbulent" density distributions, in which a power law tail of high-density gas begins at about 10^{-2} times the peak density (e.g., Klessen, 2000; Cho & Kim, 2011), but because the density distributions in these simulations are relatively narrow, the effects of the high-density tail on the measured density are negligible except for the most turbulent cases.

Figure 5.3 is meant to demonstrate the effects of turbulence, but it is **not** used to derive densities, since the true density distribution in observed clouds is unknown. However, future measurements of the density distribution can be used to apply the 'correction' shown in Figure 5.4.

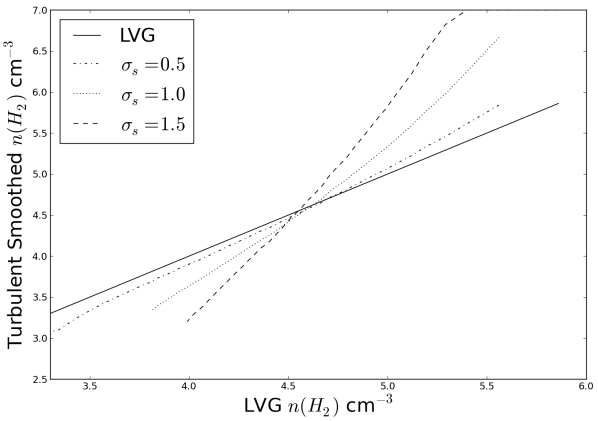

Figure 5.4 The mean density from a lognormal density distribution plotted against the density derived assuming a single density per region (i.e., the directly LVG-derived density). At low densities, the wider turbulent distributions are heavily biased towards "observing" higher densities than the true mean density. The distributions cut off at the low end where the optical depth ratio becomes a double-valued function of density; at these low densities, no detections are expected at our survey's sensitivity. The cutoff at the high end is where the optical depth ratio becomes constant.

5.6 Analysis

5.6.1 Measuring Line Optical Depth

In order to measure physical properties of an absorbing source, measurements must be obtained of the optical depths of both the $1_{10} - 1_{11}$ and $2_{11} - 2_{12}$ lines. These measurements are presented in Tables 5.1 and 5.1. Once an optical depth with errors is determined, the spectral line

depths can be matched to large velocity gradient (LVG) models to determine column and spatial density. The spectral line optical depth depends both on the nadir flux density of the absorption line and the strength of the illuminating background continuum source. If the background is the CMB, the 'filling factor' of the molecular cloud is simply its size relative to the beam size. If there is a continuum source in addition to the CMB, the size of the continuum source and the intervening molecular cloud both affect the absorption depth. Throughout this paper, we use the term 'filling factor' to refer to the fraction of the beam area filled by the absorbing molecular cloud and 'covering factor' to refer to the fraction of the background continuum source that is covered by the intervening molecular material.

The VLA archival images were used to estimate the size of the illuminating background source. When images at both wavelengths were available, we separately determined the 2 cm and 6 cm source sizes. The source size determination is imprecise because we select a single source size for non-uniform surface brightness profiles, and in many cases the VLA observation did not recover the full flux density seen in single-dish measurements. Araya et al. (2002) estimated the interferometer- to- single-dish flux ratio at 6 cm in this sample and found that the interferometer observations recovered anywhere from 3% to 100% of the single-dish flux. We repeat these measurements at 2 cm and find that the typical recovery fraction is higher, $\sim$ 40% to 100%, although sources for which only VLA upper limits could be measured have recovery fractions $< 1\%$.

The optical depth measurements were "filling factor corrected" by assuming the CMB only contributed flux density over the same area as the H II region (i.e., the foreground cloud covers the exact same patch of sky as the UCH II region). When the H II region is small (e.g., 10% of the beam area or less), the contribution of the CMB to the continuum is negligible, but in cases of more diffuse H II regions, the CMB contribution is significant, particularly at 2 cm. The inferred optical depths and source areas are presented in Table 5.4. Both "filling factor corrected" and uncorrected densities are presented in Table 5.5. The effect of the filling factor correction (FFC) on density measurements is shown in Figure 5.5. In a few cases, no volume density-column density parameter space in the models (Section 5.5) was consistent with the spectral line ratio after filling

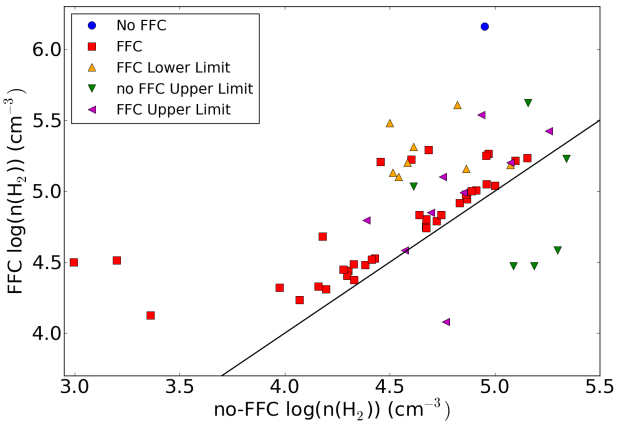

Figure 5.5 The filling factor corrected (FFC) density vs. the derived density with no filling factor correction. While there are some cases where the correction results in an order of magnitude or more increase in the density, most points show a small correction. The black line is the one-one line. Red squares show where the filling factor corrected point was used, while blue circles show where the uncorrected point was used. Magenta left-pointing triangles are limits where the filling factor correction was used, green downward triangles are limits where the uncorrected points were used, and orange upward triangles are lower limits where the filling-factor correction was used.

factor correction: in these cases, the filling factor correction was not used. Similarly, no filling factor correction was applied to sources without detected continuum. These exceptions are noted in Table 5.5 in the "Flag" column.

The above definitions are summarized briefly in the following equations:

$$\begin{aligned} S_{\nu,obs} &= S_{\nu,cont}(1 - CFe^{-\tau_\nu}) - S_{\nu,CMB}(FFe^{-\tau_\nu}) \\ FF &= \Omega_{cloud}/\Omega_{beam} \\ CF &= \Omega_{cloud}/\Omega_{continuum} \end{aligned}$$

in which CF is the "covering factor", FF is the "filling factor", and there is no positive contribution from the CMB because it is assumed to be removed by position-switching.

The systematic uncertainties in the continuum and the filling factor result in similar errors in the optical depth measurement, and together dominate the total error budget for our measurements. A 30% error in the $1_{10} - 1_{11}$ and 20% error in the $2_{11} - 2_{12}$ continuum levels were assumed because of flux calibration uncertainty characteristic of the instruments. An additional 10% error in the beam area, which sets the maximum coupling to the CMB (assuming a beam-filling source), was included to account for focus error. A 20% statistical error in the cloud filling factor was assumed for the majority of the survey, but it was decreased to 10% when the ratio of continuum to CMB flux was > 0.5 and the source size was small, indicating that the VLA-measured source is indeed the dominant continuum component in the beam. The statistical error does not account for systematic errors in the geometric assumptions. Note that changes to the filling factor should have a minimal effect on the derived density unless the source sizes at 2 cm and 6 cm differ substantially, while changes in the filling factor will always have a large effect on the derived column density (Figure 5.6).

Measurements of volume and column density were taken by averaging over the regions of LVG model parameter space consistent with both spectral line optical depth measurements to within 1σ. The "1σ" (68% confidence; errors are non-gaussian) error bars on the derived parameters (N, n, X)

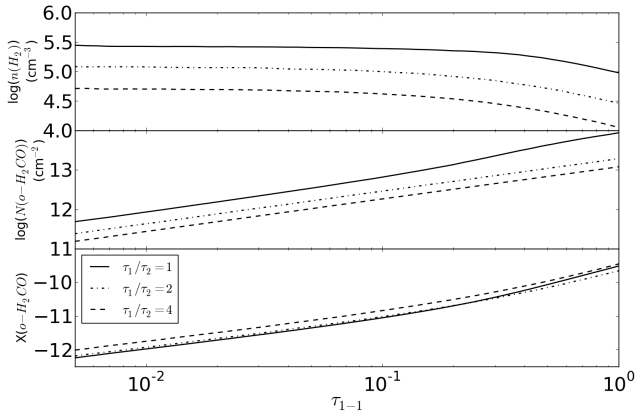

Figure 5.6 The dependence of derived parameters on the filling factor, assuming an optical depth ratio $\tau_{1_{10}-1_{11}}/\tau_{2_{11}-2_{12}}$ =1 (solid), 2 (dash-dot), or 4 (dashed). The X-axis is the "real" optical depth, $\tau_{1-1}(real) = \tau_{1-1}(observed)/FF$. Assuming the same filling factor correction is applied to both the $1_{10} - 1_{11}$ and $2_{11} - 2_{12}$ lines, filling factor correction will only move the measurements along the X-axis of these plots. A decrease in the filling factor requires an increase in the true optical depth to maintain a constant apparent $\tau(observed)$, which in turn drives up the derived abundance and column density while leaving the volume density unchanged (except at high optical depths, $\tau \gtrsim 0.2$).

were taken to be the extrema of these regions. An example of this fitting process is shown in Figure 5.7. A second example demonstrating a lower-limit on the density (instead of a direct measurement) is shown in Figure 5.8. This method is not as robust as χ^2 fitting, but because there are no free fit parameters, a statistically meaningful χ^2_ν cannot be computed.

In some cases, the ratio of the spectral line optical depths was consistent with low density ($n \lesssim 100$ cm^{-3}) and high abundances ($X(\text{o-H}_2\text{CO}) > 10^{-8}$ per km s^{-1}pc^{-1}), but these were ruled out based on the prior assumption that extremely high H_2CO abundances should not be observed at very low densities, since it is formed at higher densities and destroyed by hard UV at low columns (see discussion in Troscompt et al., 2009a).

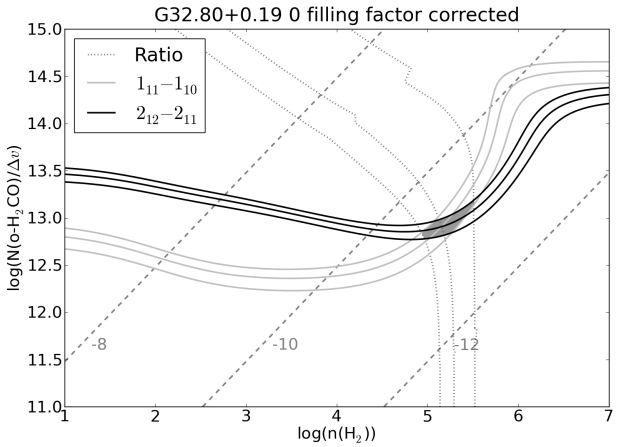

Figure 5.7 An example of the column density - density parameter space available given measured $1_{10} - 1_{11}$ and $2_{11} - 2_{12}$ optical depths. The dashed lines show abundances $\log_{10}(X(\text{o-H}_2\text{CO}))$ per km s^{-1}pc^{-1}. The contours show the regions allowed by the measurements of optical depth ($1_{10} - 1_{11}$: black, $2_{11} - 2_{12}$: grey, ratio: dotted); the middle curve is the measured value, while the pair of curves around it are $\pm 1\sigma$ including systematic error. The shaded region shows the allowed parameter space from which the physical parameters are derived.

5.6.2 Systematic Errors: Absorption Geometry

There are potential systematic errors associated with geometric assumptions, i.e. the filling factor. There are four geometric configurations possible; these are outlined in Table 5.6. The "small source" geometry (3 and 4) is technically impossible given that the CMB is always present in these observations, but it is equivalent to the scenario in which the small illuminating compact source

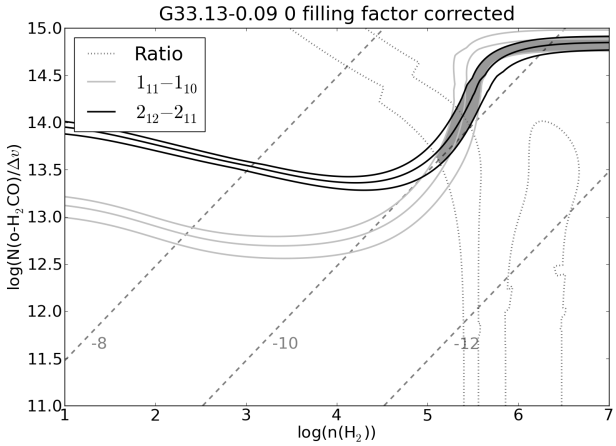

Figure 5.8 Same description as Figure 5.7 but for the strongest component in G33.13-0.09. It was only possible to measure lower limits on the volume and column density for this line; it is therefore assigned flag 8 in Table 5.5.

Table 5.6. H_2CO Geometric Systematic Errors

Real Geometry	Assumed filling factor = 1	Assumed filling factor < 1
1. Beam-filling source, beam-filling absorber	[a]τ_M = [b]τ_R	$\tau_M > \tau_R$
2. Beam-filling source, small absorber	$\tau_M < \tau_R$	$\tau_M = \tau_R$
3. Small source, beam-filling absorber	$\tau_M = \tau_R$	$\tau_M >= \tau_R$
4. Small source, smaller absorber	$\tau_M < \tau_R$	$\tau_M = \tau_R$

[a]τ_M = measured optical depth

[b]τ_R = real optical depth

(UCH II) is much brighter than the CMB in the beam. The second column shows the effects of applying the 'true' filling factor correction for errors 2 and 4. For error type 3, the optical depth will only be overestimated if the absorber is "corrected" to be smaller than the background source (i.e., if a correction is applied when none should have been).

Figure 5.6 shows the effects of incorrect geometric assumptions. Type 1 and 3 errors - i.e. filling factor overcorrections - will result in measurements of column and abundance that are **greater** than the real values, while type 2 and 4 errors will result in column and abundance measurements that are **lower** than the real values.

Additionally, it is possible that an observation will include a beam-filling, low-density source that will contribute negligibly in $2_{11} - 2_{12}$ line absorption but substantially in $1_{10} - 1_{11}$ absorption over most of the beam area. This type of error will result in an underestimate of the volume density.

Since these errors are failures of assumptions, they cannot be quantified, but Figure 5.5 shows the effects of correcting for these errors to the extent possible with the available data.

5.6.3 RRLs

Radio recombination lines are used to measure the velocity of the UCH II regions. The recombination lines 75-77α were independently fitted with gaussians because the signal-to-noise in each spectrum with a detection was high. Out of our 24 spectra, there were 21 H detections,

13 He detections, and 12 C detections; Table 5.7 shows the fitted parameters using the 76α lines (75α and 77α were also measured but are not reported for brevity). For some of the analysis in later sections, we additionally use the deeper and more careful RRL study by Roshi et al. (2005), who observed 17 of our sample in the 89-92α lines. We attempted to measure carbon RRLs in the Araya et al. (2002) spectra, who only measured hydrogen RRLs. We detected one carbon line in G61.48 and tentatively ($\sim 2\sigma$) detected another three in G32.80, G34.26, and G45.45; we report the low-significance detections in these sources because of corresponding detections of C75-77α.

We compare the central velocities of the H and C α lines to the velocities of the H_2CO absorption lines on a case-by-case basis in supplementary Figures not included in this Thesis. The spectral line profiles are used to fit the observations into the models discussed in detail in Sections 5.8.2 and 5.8.3.

Table 5.7. Measured RRL 76 properties

Source Name	H			He			C		
	Peak H76α[a] (Jy)	Center H76α (km s^{-1})	FWHM H76α (km s^{-1})	Peak He76α (Jy)	Center He76α (km s^{-1})	FWHM He76α (km s^{-1})	Peak C76α (Jy)	Center C76α (km s^{-1})	FWHM C76α (km s^{-1})
G32.80+0.19	0.622	15.69	12.09	0.066	16.49	9.25	0.015	15.40	8.27
	(0.001)	(0.03)	(0.03)	(0.002)	(0.36)	(0.38)	(0.002)	(1.45)	(1.64)
G33.13-0.09	0.067	73.49	14.10	-	-	-	-	-	-
	(0.001)	(0.17)	(0.17)						
G33.92+0.11	0.157	101.86	12.16	0.013	99.07	13.60	-	-	-
	(0.001)	(0.07)	(0.07)	(0.001)	(0.87)	(0.87)			
G34.26+0.15	0.367	54.68	10.43	0.034	51.98	6.54	0.026	59.54	5.66
	(0.004)	(0.06)	(0.09)	(0.002)	(0.46)	(0.49)	(0.002)	(0.55)	(0.56)
	0.251	37.46	22.76	-	-	-	-	-	-
	(0.003)	(0.29)	(0.12)						
G35.20-1.74	1.016	47.94	10.70	0.105	48.26	8.27	0.045	44.18	4.05
	(0.002)	(0.02)	(0.02)	(0.002)	(0.21)	(0.21)	(0.003)	(0.33)	(0.33)
G35.57-0.03	0.036	52.38	13.71	-	-	-	-	-	-
	(0.001)	(0.41)	(0.41)						
G35.58+0.07	0.044	46.68	10.55	0.007	43.15	6.30	-	-	-
	(0.001)	(0.20)	(0.20)	(0.001)	(0.94)	(0.94)			
G37.87-0.40	0.446	59.99	15.47	0.042	60.16	11.88	0.018	59.27	7.93
	(0.001)	(0.08)	(0.07)	(0.001)	(0.55)	(0.55)	(0.001)	(0.98)	(0.89)
	0.049	26.21	10.49	-	-	-	-	-	-
	(0.002)	(0.52)	(0.42)						
G41.74+0.10	0.038	11.46	13.89	-	-	-	-	-	-
	(0.001)	(0.29)	(0.29)						

Table 5.7 (cont'd)

Source Name	H			He			C		
	Peak H76α[a] (Jy)	Center H76α (km s^{-1})	FWHM H76α (km s^{-1})	Peak He76α (Jy)	Center He76α (km s^{-1})	FWHM He76α (km s^{-1})	Peak C76α (Jy)	Center C76α (km s^{-1})	FWHM C76α (km s^{-1})
G43.89-0.78	0.103	54.98	10.83	0.010	54.18	7.72	0.007	54.08	0.82
	(0.001)	(0.08)	(0.08)	(0.001)	(0.68)	(0.68)	(0.002)	(0.34)	(0.30)
G45.07+0.13	0.041	58.22	10.05	-	-	-	-	-	-
	(0.004)	(0.41)	(0.64)						
	0.043	41.57	20.01	-	-	-	-	-	-
	(0.003)	(1.53)	(0.59)						
G45.12+0.13	0.461	58.70	17.42	0.039	59.85	10.70	0.023	59.58	12.37
	(0.002)	(0.08)	(0.08)	(0.005)	(2.50)	(1.62)	(0.003)	(4.92)	(3.76)
G45.45+0.06	0.493	55.38	11.80	0.050	56.41	8.02	0.014	63.40	10.42
	(0.001)	(0.03)	(0.03)	(0.004)	(0.93)	(0.56)	(0.002)	(4.57)	(3.05)
G45.47+0.05	0.040	64.01	14.51	-	-	-	-	-	-
	(0.001)	(0.41)	(0.41)						
G48.61+0.02	0.076	16.77	10.53	0.007	16.33	7.73	0.006	19.08	4.71
	(0.001)	(0.14)	(0.14)	(0.001)	(1.30)	(1.39)	(0.001)	(1.26)	(1.29)
G50.32+0.68	0.034	26.94	10.27	-	-	-	-	-	-
	(0.001)	(0.27)	(0.27)						
G60.88-0.13	0.067	18.30	9.08	-	-	-	0.023	21.77	2.54
	(0.001)	(0.12)	(0.12)				(0.002)	(0.19)	(0.19)
G69.54-0.98	0.017	3.69	16.24	-	-	-	-	-	-
	(0.001)	(0.64)	(0.64)						
G70.33+1.59	0.343	-19.18	12.59	0.032	-20.14	10.12	0.025	-21.67	3.28
	(0.001)	(0.05)	(0.05)	(0.001)	(0.44)	(0.46)	(0.002)	(0.33)	(0.33)

Table 5.7 (cont'd)

Source Name	H			He			C		
	Peak H76α[a] (Jy)	Center H76α (km s^{-1})	FWHM H76α (km s^{-1})	Peak He76α (Jy)	Center He76α (km s^{-1})	FWHM He76α (km s^{-1})	Peak C76α (Jy)	Center C76α (km s^{-1})	FWHM C76α (km s^{-1})
G70.29+1.60	0.545	-26.97	17.82	0.042	-26.32	14.53	0.032	-24.78	4.71
	(0.001)	(0.12)	(0.09)	(0.001)	(0.64)	(0.68)	(0.002)	(0.36)	(0.42)
	0.066	-64.41	13.12	-	-	-	-	-	-
	(0.002)	(0.70)	(0.50)						
G61.48+0.09	0.566	25.96	11.16	0.046	28.80	7.86	0.059	21.27	2.48
	(0.001)	(0.02)	(0.02)	(0.001)	(0.24)	(0.24)	(0.002)	(0.11)	(0.11)

[a]Some H lines were fit with two gaussian components, in which case the second fit component is on the second line below. Errors (1σ) are indicated by the numbers in parentheses on the line below the measurement.

Table 5.8. Inferred properties

	UCH II			Other Lines (GMC)			
Parameter	Median[a]	Mean [a]	RMS [a]	Median [b]	Mean [b]	RMS [b]	KS PTE
log(H_2 Density) (cm^{-3})	4.95	4.91	0.27	4.49	4.61	0.32	0.022
log(o-H_2CO Column) (cm^{-2})	12.59	12.59	0.44	11.86	11.83	0.20	6×10^{-6}
X(o-H_2CO)	-10.84	-10.80	0.46	-11.16	-11.26	0.45	0.028

[a]Spectral line components associated with UCH II regions

[b]Other spectral lines (associated with line-of-sight molecular clouds)

5.7 Results

5.7.1 Derived Properties

The average properties of the spectral line components associated with the UCH II regions and the other spectral lines representing molecular clouds are shown in Table 5.8. The table includes the mean and median only of spectral lines with both $1_{10}-1_{11}$ and $2_{11}-2_{12}$ detections that yielded measurements of density; upper and lower limits are not included. The full results are presented in Table 5.5.

There is statistical evidence that the deepest spectral line components have higher H_2CO column and/or abundance than the other (GMC) components (Table 5.8). It is unlikely that this difference could be caused by underestimates of the optical depths in the GMC components (type 2 and 4 errors, see Table 5.6) because the filling factor correction should tend to cancel out these errors. However, it is possible that, in those cases where the H II emission and the CMB emission in the beam are the same order of magnitude, type 1 errors have occurred: the H II region absorber is much larger than the H II region and a significant fraction of the spectral line depth comes from absorption against the CMB; this error should have little effect on the derived density (see Figure 5.6) but may lead to overestimates of the derived column density.

Each identified Gaussian component was associated with an UCH II region if it was within

5 km s^{-1} of the RRL peak, since RRLs are assumed to be generated in the UCH II regions. Any spectral lines blended with the UCH II H_2CO lines were also associated with the UCH II region. Other velocity components, including those without corresponding RRL detections, were assumed to be from GMCs along the line of sight or part of the larger cloud not directly associated with the UCH II region; 29 components were associated with UCH II regions and 46 were associated with unrelated line-of-sight GMCs (Table 5.3).

The density difference between the two populations is significant by a Kolmogorov-Smirnov (KS) test with $\sim 2\%$ probability of being drawn from the same distribution (the 'probability to exceed' or PTE in Table 5.8). This result is in contradiction to the results of Wadiak et al. (1988), who found no significant density difference between "warm clouds" and "cold clouds" selected and observed in the same manner (though with larger beams). The difference is likely because the larger beam sizes in their study and a failure to include the continuum contribution of the CMB (which is more substantial in a larger beam, especially at 2 cm), resulting in a type 3 error and an underestimate of density for their "warm clouds" in particular.

The measured H_2 densities do not display any trend with heliocentric distance over the range 2-14 kpc, contrasing with mm-continuum surveys of star forming regions that tend to measure lower densities at greater distances (Reid et al., 2010). The lack of correlation in Figure 5.9 demonstrates the strength of the H_2CO densitometry method: the properties of star-forming gas can be explored throughout the galaxy with distance bias largely removed. Similarly, no trend with Galactocentric distance was readily apparent.

Densities were measured within a range 10^4 cm^{-3} $\lesssim n(H_2) \lesssim 10^6$ cm^{-3} due to sensitivity cutoffs at low densities and thermalization of the spectral line ratio (ratio $\rightarrow 1$) at high densities (see Section 5.8.5 for a discussion of the limitations of the densitometer). On the high density end, a lower limit on the density remains interesting, as densities $n(H_2) \gtrsim 10^6$ cm^{-3} are close to those of low-mass protostellar cores and are a strong indication of runaway gravitational collapse, since such high densities are rarely observed in non-star-forming regions. On the low density end, it should be possible to detect the $2_{11} - 2_{12}$ transition with sensitivity improvements $\sim 2 - 10\times$, a

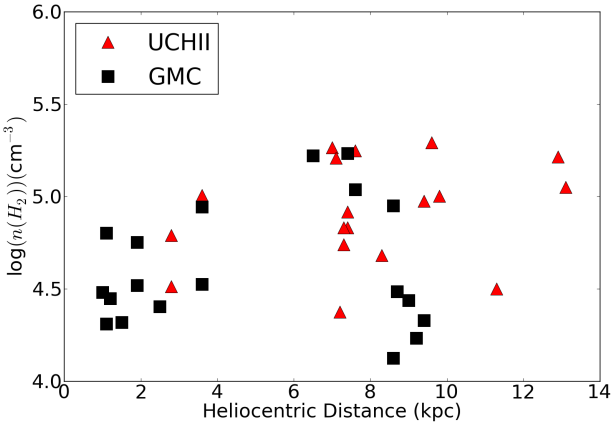

Figure 5.9 Derived density plotted against kinematic distance. No trend is obvious, demonstrating that the H_2CO densitometer is not biased by source distance. Black squares represent GMCs along the line of sight; red triangles represent UCH II regions.

consideration that will govern the allocated time-on-source for future $2_{11} - 2_{12}$ observations.

5.7.2 Free-free Contribution to 1.1 mm Flux Density Measurements

It is expected that all young star-forming regions should be dust-rich and therefore bright at 1.1 mm. We therefore compare the BGPS 1.1 mm, GBT 2 cm, and Arecibo 6 cm continuum measurements for sources covered by the BGPS in Figure 5.10. For a flat-spectrum ($\alpha \approx -0.1$, $\tau_{ff} << 1$; Wilson et al., 2009) free-free continuum source, the 2 cm flux density should be 1.34× the 1.1 mm flux density. For an optically thick source, $S_{1.1mm} = 330\ S_{2cm}$.

The objects targeted in our survey include 9 of the 13 brightest ($S_{1.1mm,40''} > 1.5$ Jy) sources in the range $32 < \ell < 48$, and 11 of 26 with $S_{1.1mm,40''} > 1.0$ Jy. We use flux density measurements from the $40''$ apertures in the BGPS catalog because they are most appropriate for determining peak brightness of point-like sources (Rosolowsky et al., 2010). Out of the sample within the BGPS survey area, 6 of 15 sources have free-free fractions of at least 30%, but potentially much higher if the free-free emission is not optically thin. Since the sample was selected from well-known UCH II regions, these (rather incomplete) statistics are a warning that most of the brightest 1.1 mm emission sources in the BGPS are likely to be active UCH II regions and therefore may include a significant contribution from free-free emission to their measured flux densities (Figure 5.11). The same warning applies to other mm-wavelength galactic plane surveys, though the contamination should be less severe at shorter wavelengths.

In order to evaluate the impact of this conclusion on the BGPS, we examine the flux distribution of 6 cm continuum sources from the MAGPIS survey compared to the BPGS in the same area, $5 < \ell < 42$ and $|b| < 0.42$, which is the full range of the MAGPIS survey excluding the galactic center, where the BGPS catalog follows a different flux distribution (Bally et al., 2010).

In Figure 5.12, we plot histograms of the MAGPIS 6 cm flux density and the BGPS $40''$ aperture flux density along with the best-fit power-law distribution line [12] . Since the 6 cm power-

[12] The power law was fit using the python translation of the Clauset et al. (2009) power-law fitter provided at `http://code.google.com/p/agpy/wiki/PowerLaw`. The fitter computes the maximum likelihood value of the power-law α and the cutoff of the distribution, below which a power law is no longer valid either because of incompleteness

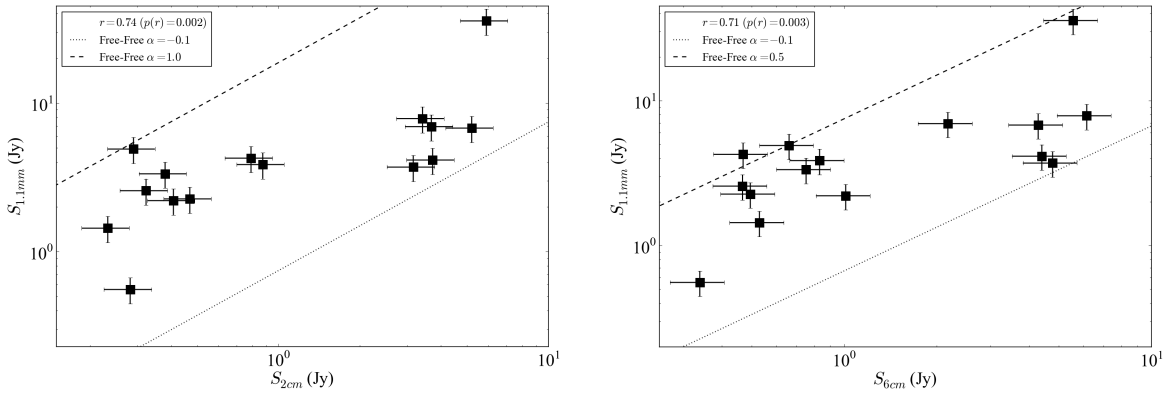

Figure 5.10 Bolocam 1.1 millimeter flux density versus the cm continuum flux density at 2 cm (left) and 6 cm (right). The BGPS 1.1 mm flux density is moderately correlated with both cm continuum measurements; the legend shows the regression parameter. The expectation for optically-thin free-free emission ($\alpha = -0.1$, dotted) and for intermediate spectral index emission ($\alpha > 0$, dashed) are shown to illustrate that some sources have significant free-free contributions at 1.1 mm (the optically thick case is not shown for either 2 or 6 cm because it does not fit on the plot). The legend shows the predicted flux densities for a given spectral index α, the regression parameter r, and its likelihood p. The brighter sources are likely to be less optically thick in the free-free continuum than the faint sources.

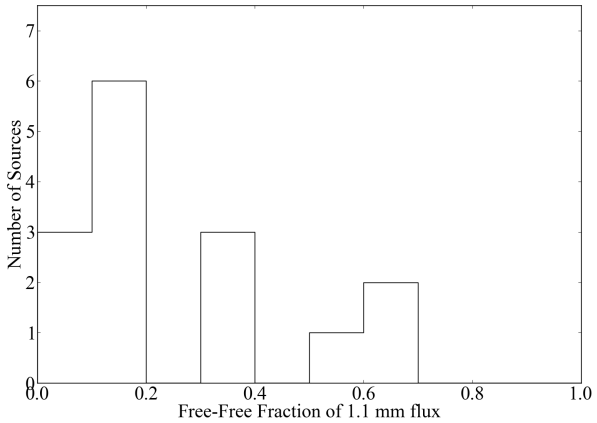

Figure 5.11 The distribution of free-free contributions to the 1.1 mm flux density assuming the UCH II region is optically thin at 2 cm, $f_{ff} = (S_{2cm}/1.34)/S_{1.1mm}$. While 9 sources are either dust-dominated or optically thick at 2 cm, 6 sources have free-free contributrions of 30% or greater. The other sources in the sample were missing 1.1 mm flux density measurements because they are outside the BGPS survey area.

law distribution is shallower than the 1.1 mm distribution, the 6 cm sources can dominate at high flux densities, although the power-law fit for the 6 cm sources significantly overpredicts the highest-flux bins and therefore the power-law is not an acceptable fit above $S_{6cm} > 1$ Jy [13] . The dashed line in Figure 5.12 shows the best-fit power-law distribution of the MAGPIS flux densities scaled down by 0.67, which is the expected decrement for an optically thin free-free source from 6 cm to 1.1 mm (spectral index $\alpha = -0.1$).

Figure 5.12b shows the ratio of the BGPS to the MAGPIS best-fit power-law distribution, indicating that the free-free contamination fraction is only large ($\sim 10\%$) at values much greater than the valid range of the 6 cm power law fit, which overpredicts the number of sources at $S_{6cm} \approx 1$ Jy. However, if any of these sources are **not** optically thin at 6 cm, this fraction could be much larger. Additionally, these numbers only describe the sources in which **all** of the 1.1 mm flux is free-free emission; the implication remains that a large number of 1.1 mm sources have a substantial (if not dominant) free-free contribution.

Finally, we emphasize that unless a large fraction of 6 cm sources are optically thick in free-free continuum, the lower flux-density BGPS dust-continuum sample should be negligibly contaminated by free-free emission sources, but the brightest BGPS sources may have a significant free-free contribution.

5.7.3 Distances

We measure a kinematic distance to each source using the Reid et al. (2009) rotation curve. We resolved the Kinematic Distance Ambiguity (KDA) towards each line of sight using a variety of methods described below. The method in Sewilo et al. (2004) allows a resolution in favor of the far distance for UCH II regions with an intervening molecular absorption line at more positive velocities in the first Galactic quadrant. Associations with infrared dark clouds (IRDCs) can resolve the KDA

or a change in the underlying distribution.

[13] We have tested the consistency of the two data sets with a low-cutoff power-law distribution by the Monte-Carlo process described in Clauset et al. (2009). The BGPS $40''$ aperture flux densities are consistent with a power-law distribution at the $p = 0.64$ level, while the MAGPIS 6 cm fluxes are inconsistent, with $p < 0.001$ (where p measures the probability that the data are drawn from a low-cutoff power-law distribution)

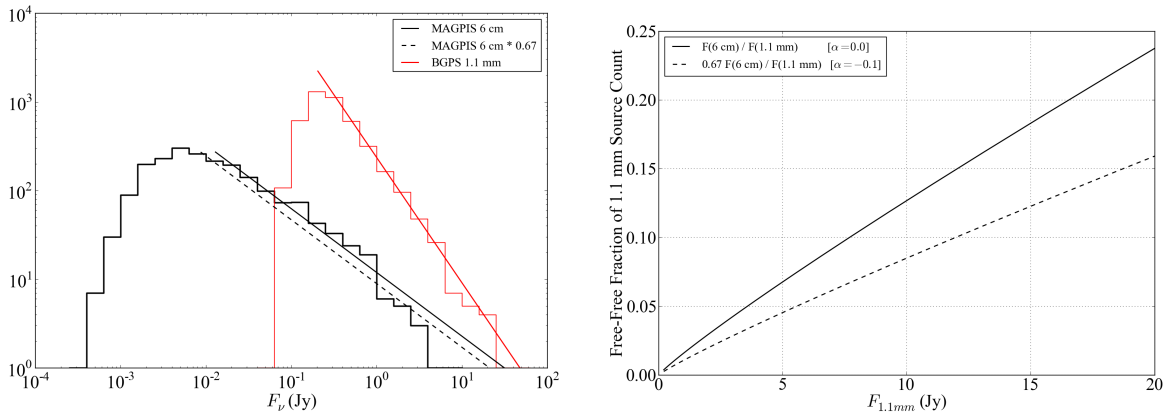

Figure 5.12 *Left:* Histograms of BGPS 1.1 mm 40″ aperture flux densities (red) and the MAGPIS 6 cm flux densities (black), and their respective best-fit power-law distributions ($\alpha(1.1mm) = 2.41 \pm 0.03$, $\alpha(6cm) = 1.72 \pm 0.03$). The dashed black line shows the MAGPIS best-fit power-law scaled down to the expected flux density at 1.1 mm assuming all sources are optically thin. Both distributions appear to be reasonably well-fit by power-laws above a cutoff (presumably set by completeness), although the power-law significantly over-predicts the number of sources with $S_{6cm} > 1$Jy. The histograms are binned by 0.1 dex, and while the best-fit α and x_{min} values are independent of the binning scheme, the normalization is not. *Right:* The ratio of the number of MAGPIS 6 cm sources to BGPS 1.1 mm sources as a function of flux density for the best-fit power laws. Only 10 1.1 mm sources are detected above 5 Jy (in 40″ apertures), so even the brightest detected 1.1 mm sources are not purely free-free, but they probably have a substantial free-free component.

in favor of the near distance. We compare our KDA resolutions to Anderson et al. (2009), with whom we agree on all common sources except for G33.13-0.09, which we place at the far distance based on the Sewilo et al. (2004) method. The derived distances are listed in Table 5.3.

5.7.3.1 Size Estimates

We estimate the source size using two methods. First, we use the VLA measurements of UCH II region sizes. As stated in Section 5.6.1, the VLA size measurements are very uncertain and are simplifications of an evidently complicated geometry. We estimate a spherical radius $r = \sqrt{area/\pi}$. Second, we assume the gas traced by H_2CO and the BGPS 1.1 mm images are the same and get a 'size scale' $r = 2N_{mm}(H_2)/n(H_2)$ where $n(H_2)$ is derived from the H_2CO line ratio.

The sizes derived from the two methods are plotted against each other in Figure 5.13. The sizes estimated from the two different methods are not well correlated and disagree by around an order of magnitude in most sources. The disagreement could be because of poor VLA-based size estimates, substantial 1.1 mm emission from low-density gas, or incorrect dust temperature or opacity estimates. While additional line-of-sight GMCs could in principle contribute to the N/n size estimate, the disagreement for sources even without associated GMCs prevents this hypothesis from fully explaining the disagreement. Therefore, any quantities derived from the size - i.e. mass, which depends on r^3 - are even less constrained. We therefore do not derive any quantities dependent on the intrinsic source size.

5.8 Discussion

5.8.1 Comparison to extragalactic observations

We compare our measured column and volume densities to a selection of starburst galaxies from Mangum et al. (2008) in Figure 5.14. All of the extragalactic observations have much lower column densities per km s^{-1} than we measure in the main lines of most UCH II regions, but similar volume densities. This discrepancy can be easily explained by a difference in the area filling factor

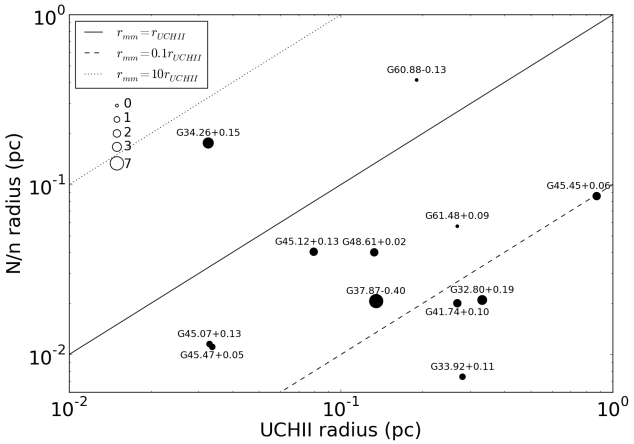

Figure 5.13 A plot of the two derived sizes discussed in Section 5.7.3.1. The two size estimates are at best very weakly correlated. Because of the substantial disagreement between the two methods, we choose not to explore any parameters with a strong dependence on the size. The plotted point size indicates the number of associated line-of-sight GMCs, which in principle could lead to an overestimate of the N/n size because of additional mass included in the 1.1 mm continuum measurement.

of molecular clouds in observations of galaxies and UCH II regions. In a galaxy, the total area filling factor of molecular clouds per km s^{-1} (which is similar but not identical to the volume filling factor) is likely to be < 1, even in extreme starbursts; although the galaxy may appear to be uniformly filled with molecular gas in projection, at any given velocity it is likely to have significant gaps of ionized or neutral atomic gas. In contrast, an UCH II region should be completely embedded in a molecular cloud that is much larger than the free-free emitting continuum region, so the covering factor of molecular gas should be ~ 1.

It is therefore interesting to note that Arp 220, possibly the most extreme nearby example of a starburst galaxy, has nearly the same column per channel as the low end of the UCH II regions, suggesting that it is analagous to a scaled-up UCH II region to within a factor of a few; the measured density in Arp 220 is consistent with only the highest-density UCH II regions. M82, on the other hand, has a bright continuum background analagous to an UCH II region, but a correspondingly low filling factor, implying that it consists of many compact but bright sources with a total filling factor 0.001-0.1. Alternatively, the density and column measurements are consistent with M82 being dominated by quiescent GMCs, but that is unlikely given the starburst nature of the galaxy.

The gravitational lens source B0218+357 is a different scenario. Its low density is consistent with that of a non-star-forming GMC, while its column per km s^{-1} is comparable to the Galactic sample. This source is therefore likely to be a sightline through a 'normal' quiescent molecular cloud in its host galaxy, similar to the narrow beam of an UCH II region through the Galactic disk. Zeiger & Darling (2010) note that there is a range of covering factors cited in the literature, which can affect the measured density and column, but should not affect the conclusion that the B0128+357 cloud's density is not consistent with that of massive-star forming regions. The low-density gas is detected partly because the Zeiger & Darling (2010) data are 3.5× more sensitive than ours with a background continuum source of similar brightness.

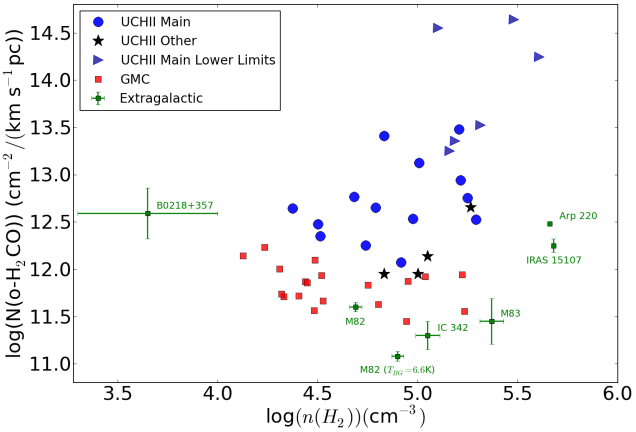

Figure 5.14 Comparison of the UCH II sample (blue circles are measurements, blue triangles are lower limits on volume density with poorly constrained column densities), the GMC sample (red squares), secondary lines associated with UCH II regions (black stars) and the extragalactic sample of Mangum et al. (2008) (green squares). The errorbars on the Galactic data points are excluded for clarity. The observed galaxies have similar densities to the Galactic UCH II sample, but significantly lower column densities, suggesting that the molecular gas in these galaxies has a filling factor $<< 1$. The lack of direct density measurements of UCHII regions at high densities is due to the presence of a dominant background source; in Arp 220 a direct measurement of density was possible because H_2CO was seen in emission.

5.8.2 Line Profiles

Despite the many systematics discussed above that can affect H_2CO absorption measurements with a compact illumination source, it is possible to directly compare the properties of gas along a given line of sight without most of these hindering factors. Since most of our spectra have kinematically resolved spectral line profiles, it is possible to make many density measurements at different velocities towards each source. An example of this type of analysis is shown in Figure 5.15. An example demonstrating the need for this type of analysis is shown in Figure 5.16, in which two lines well-fit by gaussian profiles nonetheless display a density gradient because the line centers are significantly offset; the figure also demonstrates that the offset cannot be accounted for by any instrumental effects.

Of our sample, 18 of the 24 observed lines-of-sight had high enough signal-to-noise spectra (S/N$\gtrsim$ 5 in at least four adjacent 0.4 km s^{-1} channels in both lines) to measure the density in many velocity bins. Of these, 12 have different peak velocities in the $1_{10} - 1_{11}$ and $2_{11} - 2_{12}$ lines, indicating density gradients in the molecular gas with velocity. Figure 5.15b is an example density-velocity plot.

We have classified each high S/N spectrum as *gradient*, *envelope*, or *single* based on spectral line morphology. The *gradient* classification was used for gaussian or nearly gaussian lines in which the $1_{10}-1_{11}$ and $2_{11}-2_{12}$ line centers were offset, indicating a gradient in the density with velocity; the color listed in the table indicates the direction of **increasing** density. The *envelope* classification was used for flat profiles on the wings of deeper gaussian lines. The *single* classification was used for lines where the $1_{10}-1_{11}$ and $2_{11}-2_{12}$ velocities matched. Low S/N spectra were not classified. Classifications are given in Table 5.3.

Of the 12 sources with density gradients, 6 show an increased density towards the red and 5 towards the blue. One source, G45.12+0.13, shows a slight increase towards the red over a broad (8 km s^{-1}) velocity range, but a sharp increase towards the blue over only 1 km s^{-1} and is therefore classified as *other*.

Figures not included in this thesis show the 'main line' (associated with the UCH II region) profile and the associated density, column, and abundance velocity profiles. The density, column, and abundance measured for each main line via the gaussian fit technique are shown overplotted on the profiles with blue squares. In all cases, the gaussian fit measurement of density is consistent with the individual channels nearby and the gaussian fit measurements of column and abundance are consistent with the peak column and abundance. The consistency of adjacent velocity bins confirms the validity of associating gaussian components in observations of whole galaxies (e.g., Mangum et al., 2008) or kpc-scale regions, since on these scales the $1_{10} - 1_{11}$ and $2_{11} - 2_{12}$ lines should be blended by kinematics to have the same shape.

5.8.3 Comparison of RRLs and H_2CO lines

We compare the density spectra with the fitted RRL centroids and attempt to interpret these spectra in the context of various simple models of H II region interaction with molecular clouds. The simple models described below may actually be short-lived but recurring stages in the normal life cycle of a collapsing clump that is forming massive ($M \gtrsim 10 M_{\odot}$) stars (Peters et al., 2010).

We consider five simple models of embedded UCH II regions. For each scenario, we include a brief description of the model and an analysis of the observational consequences in terms of C and H RRL velocities and velocity-density structure. We assume that the carbon RRLs are only detected if seen in the foreground of a bright source. This assumption is based on predictions that C RRLs will be amplified by an order of magnitude even in the presence of a weak background (Natta et al., 1994). It is backed by a strong correlation between the continuum and the C RRL intensity (Roshi et al., 2005). We also assume that lower-frequency RRLs will have a stronger stimulated emission component than higher-frequency RRLs (Lockman & Brown, 1978). All H_2CO absorption is assumed to be against the UCH II region in this section. The scenario that describes a given spectrum is listed in the figure caption for each spectrum and in Table 5.3.

- SCENARIO 1: STATIC

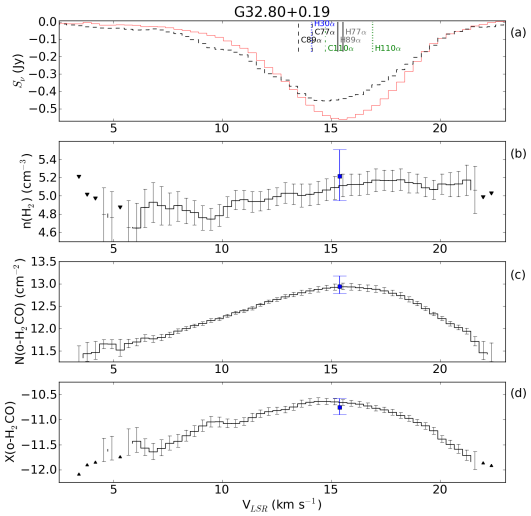

Figure 5.15 Plot of the derived parameters per velocity bin for the main line of G32.80+0.19; the full spectrum is shown in Figure 5.1. The density peak around 16 km s^{-1} is slightly redshifted of the H and C RRL velocity centers, although the C RRLs are blueshifted of the H RRLs, indicating that the PDR has been accelerated towards us along the line of sight. The blueshifted emission tail is suggestive of an outflow. This source cannot therefore be easily classified under any of the scenarios in Section 5.8.3, but is consistent with components of scenarios 2 and 3. *a.* The spectra of G32.80+0.19. The GBT $2_{11}-2_{12}$ spectrum (red solid) has been smoothed to a resolution of 0.38 km s^{-1} to match the Arecibo (black dashed) spectral resolution. Labeled vertical bars indicate the measured velocity centers of H and C RRLs from this work, Roshi et al. (2005), and Churchwell et al. (2010). *b.* The measured densities in each spectral bin. The Y-scale is in $\log_{10}$ units. Error bars include a 10% systematic uncertainty in the continuum and therefore errors in adjacent channels are not independent. Limits are indicated by triangles. Bins with no information above the 1-σ noise cutoff are left blank. The increase of density towards higher velocities led us to classify this source as a *red gradient* in Table 5.3. *c.* The measured column densities per spectral bin. Because these column densities are derived from a large velocity gradient code, they are in per km s^{-1}pc^{-1} units. *d.* The measured abundances per spectral bin. The column and abundance are somewhat degenerate, but it is possible in some cases to place tight constraints on the total o-H_2CO column while only placing upper limits on abundance and density. The abundance must also be interpreted per km s^{-1}pc^{-1}. In plots *b* through *d*, the blue square with error bars represents the measured value from Table 5.5 using gaussian fits to the lines.

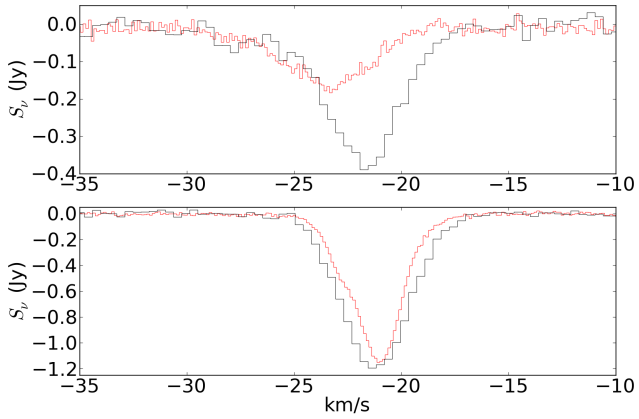

Figure 5.16 Comparison of G70.29+1.60 (top) and G70.33+1.59 (bottom) spectra as observed by Arecibo (black) and GBT (red/grey). Note that in G70.29+1.60, the $2_{11}-2_{12}$ line is shifted towards the blue of the $1_{10}-1_{11}$ line, while in G70.33+1.59 the line centers match well.

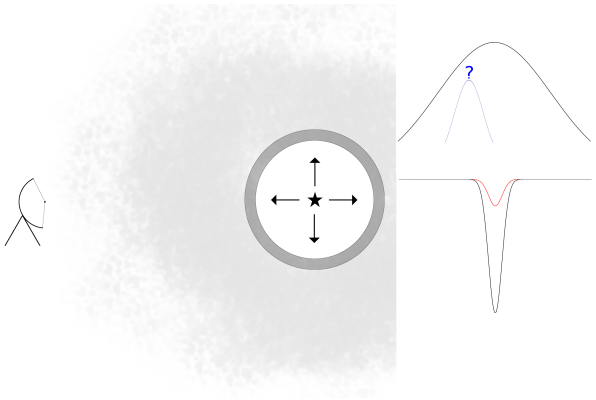

Figure 5.17 Scenario 1: An UCH II region forms and begins expanding spherically in a uniform density gas cloud. A cartoon of the geometry seen by the observer is shown on the left side of the figure, with arrows indicating expansion and darkness of the gray shading indicating relative density. The white region around the central star is the ionized UCH II region. On the right side, a cartoon of the relative velocity and width of the RRLs and H_2CO lines is shown. The relative heights of the H_2CO lines is representative of the observed density; black is $1_{10}-1_{11}$ and red is $2_{11}-2_{12}$. The narrow emission line with a ? above it indicates a possible blueshifted carbon RRL; its height has no physical meaning. In this scenario, the hydrogen recombination and H_2CO lines should occur at the same velocity, and the H_2CO lines should show relatively low-density (high $1_{10}-1_{11}/2_{11}-2_{12}$ ratio) and modest spectral line widths. A blueshifted carbon RRL may form, but is not guaranteed.

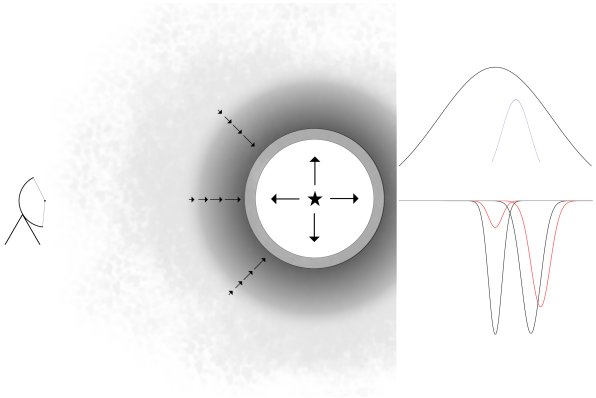

Figure 5.18 Scenario 2: An UCH II region forms from a gravitationally unstable cloud undergoing inside-out collapse. See Figure 5.17 for a complete description of the figure. The highest density should correspond to the highest-velocity infall, so the $2_{11} - 2_{12}$ line peak should be redshifted of the $1_{10} - 1_{11}$ line peak. The hydrogen recombination line may align with a low-density cloud but should be blueshifted of the infalling gas. The carbon RRL should be redshifted from the hydrogen RRL and blueshifted from the H_2CO line.

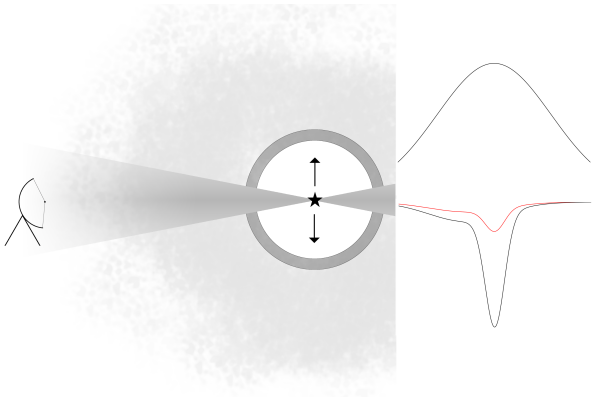

Figure 5.19 Scenario 3: An UCH II region expanding in a uniform medium ejects a bipolar outflow. Presumably the bipolar outflow comes from a disk-accreting source. See Figure 5.17 for a complete description of the figure. The outflow (indicated by the cones emitting from the central source) should have lower column density but could have high or low volume density. It will be observed as high-velocity blueshifted absorption in a line wing. Carbon recombination line emitting regions may be destroyed by the outflowing material. As in the simple scenario 1, the hydrogen recombination line should be at the same velocity as the molecular cloud.

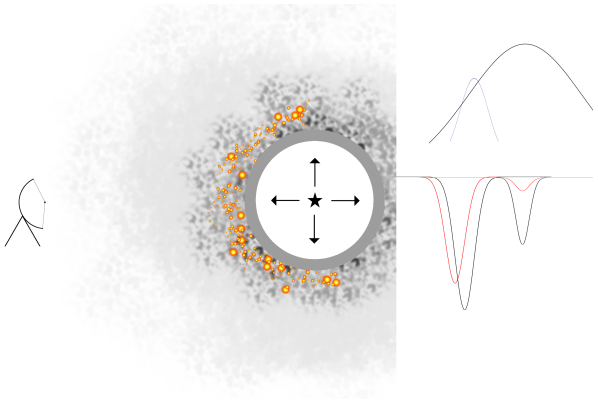

Figure 5.20 Scenario 4: An UCH II region expanding in a uniform medium sweeps up and accelerates material that undergoes triggered star formation. Because the highest-density material is the swept up material, it should be the most blueshifted. See Figure 5.17 for a complete description of the figure. The orange and yellow circles are meant to indicate triggered star formation.

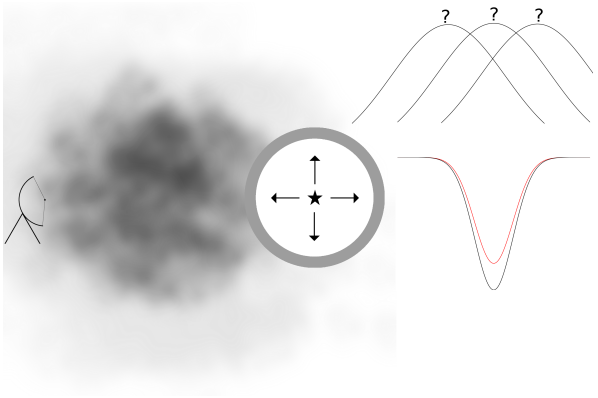

Figure 5.21 Scenario 5: An UCH II region is seen behind a high-density, turbulent gas cloud. The turbulence drives large spectral line widths, while the high density makes the $1_{10} - 1_{11}$ and $2_{11} - 2_{12}$ line depths very close. The RRL velocity could in principle be at any velocity relative to the foreground turbulent cloud. See Figure 5.17 for a complete description of the figure. In this case, the ?'s indicate an uncertain velocity for the hydrogen RRLs; a carbon RRL is not expected because the H II region is not necessarily interacting with the molecular gas.

In a uniform medium with no bulk motions (i.e., no collapse), a massive star ignites and generates an expanding H II region. Figure 5.17.

(1) Lower frequency RRLs are blueshifted from higher-frequency RRLs because of an increased stimulated emission component (Lockman & Brown, 1978)

(2) A carbon RRL should be seen at the same velocity as or blueshifted from the hydrogen RRL line center.

(3) Molecular gas closest to the H II region should have the highest density because of compression by the expanding H II region. It will be at a similar velocity or blueshifted from the H RRLs.

- SCENARIO 2: COLLAPSE

  A massive star ignites while spherically accreting from a molecular cloud undergoing bulk (inside-out) collapse. Figure 5.18.

  (1) The H_2CO-measured density should peak at the velocities most redshifted relative to the hydrogen RRLs. Inside-out collapse dictates that the highest densities should be infalling at the highest speeds.

  (2) The C RRL velocity should be between the H_2CO and H RRL velocity since the PDR will be decelerated by radiation and gas pressure from the H II region

  (3) Since the accreting star should be at approximately the rest velocity of the cloud, there should be little to no gas blueshifted from the RRL velocity

- SCENARIO 3: OUTFLOW

  An accreting massive star generates a massive outflow with a significant component along the line of sight. Figure 5.19.

  (1) Substantial low-column, low-abundance per km s^{-1} gas should be observed at velocities blue of the RRL velocities. Densities can range from low to high. Covering factors

may be low.

(2) No carbon RRL is expected from the outflow, though if the flow is accelerated by ionization pressure a C RRL should be observed blueshifted of the H RRL velocity.

- SCENARIO 4: SWEEPING

  An expanding H II region pushes on a low-density envelope, possibly triggering a new stage of star formation as in the "collect and collapse" scenario. This scenario is similar to #1 but with either a higher-density envelope or with more gas swept up (i.e., #4 may represent a more evolved region). Figure 5.20.

  (1) The hydrogen RRLs should be red of the dense gas and the carbon RRLs. The expanding H II region should accelerate the dense gas blue along the line of sight.

  (2) A low-density envelope should persist at the same velocity as the H II region

- SCENARIO 5: FOREGROUND CLUMP

  A high density, highly turbulent or high mass and rotating clump of gas is in front of the UCH II region or surrounds it. This physical situation may exist in all of the above and provides alternate explanations for any spectral line wings. Figure 5.21.

  (1) Moderate density gas from a molecular cloud will result in high column but moderate density at the center velocity

  (2) Wide wings of high density gas will exist both blue and redshifted of the highest-column point

5.8.4 The Filling Factor of Molecular Clouds

We have measured the density in 19 line-of-sight molecular clouds in addition to the 18 measurements of densities around UCH II regions (we only include measurements, not limits, in these counts). The measured density from the H_2CO line ratio can be compared to other measures of density, e.g. the mean molecular cloud density measured by Roman-Duval et al. (2010a) from

the BU-FCRAO GRS. It is clear from Figure 5.22 that the average density in GMCs is typically $\sim 2-3$ orders of magnitude lower than densities measured in our sample of line-of-sight GMCs.

Roman-Duval et al. (2010a) point out that the mean densities they measure are significantly below the critical density of ^{13}CO, $n_{cr} = 2.7 \times 10^3$ cm^{-3}, indicating that they do not resolve the high-density clumps that make up the GMCs. Our data indicate that a typical GMC consists of $n \sim 3 \times 10^4$ cm^{-3} gas (the median of our GMC subsample excluding upper limits), substantially higher than the critical density of ^{13}CO. Taking the ratio of the median density in the Roman-Duval et al. (2010a) catalog to that in our sample, we derive a volume filling factor of 5×10^{-3} of dense gas in molecular clouds.

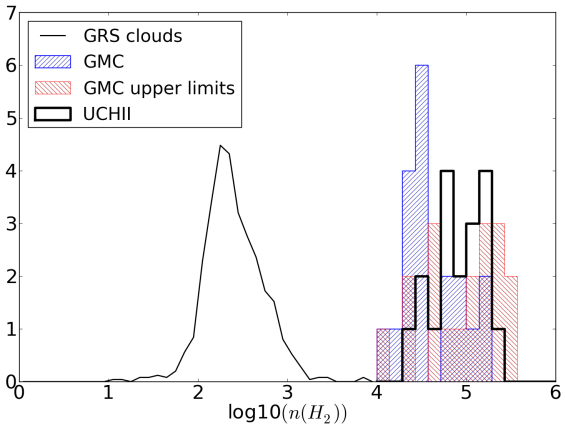

Figure 5.22 Histograms of the GMC and UCH II subsamples from our data plotted along with the GMC-averaged densities from the ^{13}CO Roman-Duval et al. (2010a) GRS measurements arbitrarily scaled to fit on this plot. The measured densities in UCH II regions are significantly (by a KS test) higher than densities in GMCs. The H_2CO-measured densities in GMCs are 2-4 orders of magnitude higher than volume-averaged densities of GMCs from the GRS, suggesting that GMCs consist of very low volume-filling factor ($\sim 5 \times 10^{-3}$) high-density ($n(H_2) \sim 3 \times 10^4$ cm^{-3}) clumps. In Section 5.8.4, we argue that the observed difference is most likely not a selection effect imposed by the different gas tracers. The GMC upper limits shown are $3-\sigma$ upper limits, and all are consistent with the measured GMC densities.

We measured an additional 20 upper limits towards GMCs, all of which are consistent with high densities ($n(H_2) > 10^4$ cm^{-3}), but could represent a sample of lower density ($n(H_2) \sim 10^3$ cm^{-3}) gas, in which case our 'measurement' of the cloud volume filling factor is biased to be too low. In order to test for this bias, we need to acquire more sensitive observations of the upper-limit systems. However, we continue analysis below based on the assumption that the cloud filling factor

measurement is realistic, i.e. assuming that the density upper limit measurements have densities consistent with the other observed GMCs.

Can a medium with supersonic turbulence produce the same density measurements without having to invoke high-density clumping? Below about $n(H_2) \approx 10^5$ cm^{-3}, measurements of density in a turbulent medium are biased towards higher densities, i.e. the densities we report may be overestimates for GMCs since they have a median density $n(H_2) = 10^{4.49}$ cm^{-3}. For turbulent density PDFs with logarithmic widths $\sigma_{ln(\rho)/ln(\bar{\rho})} \lesssim 1.5$, the overestimate is no more than 0.4 dex, and therefore can only bring the filling factor up by a factor < 3. As discussed in Section 5.5.1 and Figure 5.4, a high-density tail could create a larger discrepancy ($\sim$ 0.5 dex). However, at the measured densities, these are extreme upper limits on the 'turbulent correction', and therefore (gravo)turbulence alone cannot account for the measured densities.

What clumping properties are required to reproduce the observed density? As long as the clumps are all optically thin in the H_2CO absorption lines, the spectral line optical depths and ratio are independent of clumping. However, a large number of low-density ($n(H_2) \approx 10^{3.5}$ cm^{-3}) clumps optically thick in the $1_{10} - 1_{11}$ line and thin in the $2_{11} - 2_{12}$ line would appear to have a higher density. This phenomenon could only occur at densities $\lesssim 10^{4.5}$ cm^{-3}, where the $1_{10}-1_{11}$ absorption line is much stronger than the $2_{11}-2_{12}$ line, and column densities 10^{14}cm$^{-2} \gtrsim N$(o-H_2CO) $\gtrsim 10^{13.5}$ cm^{-2} per clump (at higher columns, both lines are optically thick; at lower columns, both lines are optically thin). Assuming a typical H_2CO abundance (ortho+para) $X_{H_2CO} = 10^{-9}$, the required spherical clump radius would be $\sim$ 0.3 pc, which would be Jeans-unstable at the assumed density and temperature (40 K) and is therefore unlikely to persist for long time periods [14] . We therefore regard a collection of optically thick clumps in the H_2CO $1_{10} - 1_{11}$ line to be unlikely; clumps optically thick in both lines are even less likely following the same line of reasoning.

The combination of the observed large spatial scales (and therefore low volume-averaged density) of GMCs and the high densities measured along essentially arbitrary sightlines through

[14] However, the lifetime of such clumps in a turbulent medium in which small-scall turbulence supports the clumps against collapse is unconstrained.

these GMCs suggests that GMCs are not consistent with a purely turbulent medium with a lognormal density distribution. The observations also require a more substantial high-density tail than typically seen in gravoturbulent simulations, i.e. they require a clumpier medium.

Alternatively, it is possible that H_2CO is chemically enriched in high-density pockets within a turbulent medium, which would imply that H_2CO observations probe different gas than CO. No such mechanism has been proposed on theoretical grounds, and the timescales for enhancement would have to be very short (intermittent density enhancement occurs on timescales much shorter than the dynamical timescale; Kritsuk et al., 2007), so we regard this possibility as unlikely but include it for completeness.

Another alternative is that the ^{13}CO systematically underestimates the mass or overestimates the volume of the cloud, resulting in an underestimate of the cloud density. Sub-thermal excitation of ^{13}CO in the low-density parts of the cloud can lead to an underestimate of the mass (Roman-Duval et al., 2010a, Section 9.3). Since the cloud sizes were derived using an assumed spherical symmetry, but molecular gas is typically observed in filamentary structures, the densities in Roman-Duval et al. (2010a) are likely to be lower limits on the mean density in the molecular gas. While both of these factors bring the H_2CO and ^{13}CO densities into closer agreement, it is difficult to quantify these effects.

5.8.5 Strengths and Weaknesses of the H_2CO K-doublet Densitometer

The dynamic range of a spectral line as a tracer of a physical quantity is an important consideration when designing an experiment. We have demonstrated only a modest dynamic range in density measurements using the $1_{10}-1_{11}$ and $2_{11}-2_{12}$ lines in absorption against bright background sources: above $n(H_2) \approx 10^{5.6}$ cm^{-3}, we are only able to set lower limits on the density because the spectral line ratio asymptotes to 1 , and below $n(H_2) \approx 10^4$ cm^{-3}, the $2_{11} - 2_{12}$ line optical depth drops to very low levels (Figure 5.2).

The lower limits on density at $n(H_2) \gtrsim 10^{5.6}$ cm^{-3} can only be modestly improved upon by using higher K-doublet transitions (e.g. $3_{12} - 3_{13}$) when observing H_2CO in absorption against

bright continuum sources. However, when observing anomolous absorption against the CMB, an additional density diagnostic is the transition from absorption to emission at higher densities, which expands the sensitivity of the $1_{10} - 1_{11}/2_{11} - 2_{12}$ pair to $n(H_2) \approx 10^{6.5}$ cm^{-3}.

The low-density end can only be probed by more sensitive observations of the $2_{11} - 2_{12}$ line. Because the H_2CO line depths become negligible below $n(H_2) \approx 10^3$ cm^{-3}, the densitometer is not a useful probe below these densities. However, at such low densities, even within a molecular cloud, it is questionable whether any molecular probes are reliable, as even CO will be underabundant in these environments (e.g., Glover et al., 2010).

As noted in Mangum et al. (2008) and Zeiger & Darling (2010), the K-doublet densitometer has the advantage that line detection only depends on the brightness of the background source and the gas density. It can therefore be used nearly independent of distance when observing clouds against the CMB or bright illuminating background sources. The Zeiger & Darling (2010) measurements are more sensitive than any presented in our study because of longer integration times and the selection of a bright illuminating background source despite their target being at a distance z=0.68. Following this line of reasoning, any bright synchrotron or free-free source can be used to sensitively probe the density of a line-of-sight molecular cloud in the Galaxy. The observation will have angular resolution limited only by the size of the background source as long as it is much brighter than the CMB in the beam.

5.9 Conclusions

We have presented a pilot study to measure molecular gas densities in clouds along 24 lines of sight in the H_2CO $1_{10} - 1_{11}$ and $2_{11} - 2_{12}$ transitions primarily toward UCH II regions . We have shown that the H_2CO densitometer is robust within reasonable ranges of turbulent density distributions, most cloud geometries, and different cloud clumping properties. We have presented the methodology and discussed the errors intrinsic to the H_2CO densitometer.

Gas volume densities were measured toward 14 of the 24 sources using the best-fit gaussian profiles; density limits were measured for the remaning 10. In 18 sources, it was possible to estimate

the density in each 0.4 km s^{-1}-wide channel centered on the main line. Of these, 12 showed some sign of a density gradient with velocity, 5 appeared to have a single-valued density (i.e. only a single spectral line component well-fit by a gaussian), and one, G69.54-0.98, had a spectral line optical depth that was beyond our ability to model.

Velocity-density gradients have been used to fit 18 sources with simple models of UCH II regions embedded in molecular clouds. We have found some examples consistent with inside-out collapse onto the UCH II region, UCH II region expansion, and bulk outflow. H_2CO absorption provides a unique probe of the physical conditions around UCH II regions because it is only seen in absorption against the continuum background (for sources much brighter than the CMB), giving different constraints than mm and sub-mm spectral lines that are seen both in front of and behind the UCH II region.

The measurements of serendipitously detected line-of-sight GMCs revealed densities ~ 200 times higher than volume-average densities measured using ^{13}CO. The high density measured suggests that GMCs consist of many sparsely distributed high-density clumps and have density distributions inconsistent with the lognormal distribution predicted by supersonic turbulent models. The implied density distribution is also more skewed to high densities than predicted by typical gravoturbulent simulations. Alternatively, the ^{13}CO-based mean densities may be lower than the mean densities within the molecular gas either because they underestimate the mass or overestimate the volume of GMCs.

The density measurements show that UCH IIs are associated with high-density ($n(H_2) > 10^{4.5}$ cm^{-3}) gas, and UCH IIs are associated with higher column and volume densities than other line-of-sight molecular clouds, in contradiction with previous results (Wadiak et al., 1988).

The 6 cm, 2 cm, and 1.1 mm flux density measurements are strongly correlated and in most objects in our sample the 1.1 mm flux density has a substantial ($> 30\%$) contribution free-free continuum emission. This result implies that the brightest sources detected in the BGPS have significant free-free emission. A comparison to the 6 cm MAGPIS survey suggests that the sample of 1.1 mm sources below about 3 Jy is not significantly contaminated by pure free-free emission

sources.

Comparison of the density measurements in our sample to the starburst sample of Mangum et al. (2008) suggest that the molecular gas volume filling factor in most of these galaxies is small (~ 0.01), but in Arp 220 it is quite high ($\gtrsim 0.1$). The physical properties measured by H_2CO in Arp 220 are similar to those in UCH II regions. Although velocity-density gradients are observed in our sample, we argue that kinematic spectral line blending should uphold the assumption of a single spectral line profile in galaxies as robust for radiative transfer purposes.

Chapter 6

H_2CO observations of BGPS sources not previously observed with Arecibo

6.1 Preface

Given our success with the simple 4-hour GBT observation of ~ 20 sources, it was decided that a large-scale survey of BGPS sources accessible to Arecibo and the GBT would be productive. We therefore selected 400 pointings in the Arecibo-accessible declination range, 137 of which are in the outer galaxy ($172 < \ell < 207$) and the others in the inner galaxy ($31 < \ell < 65$).

The selected sources included **all** 1.1 mm peaks in the outer galaxy regions of the BGPS, including the newly observed regions from the v2.0 survey.

As of the thesis defense, all of the data for the large survey has been reduced, but the analysis and interpretation is ongoing. We report here only initial results from the outer galaxy component of the large survey and selected analysis from the inner galaxy survey.

Further follow-up projects based on these observations, in particular VLA observations of the W51 star forming complex, have been approved and are queued for observation.

6.2 Introduction

There are a few predictions common to all models of star formation. Gas initially in a cold (T< 20K) Giant Molecular Cloud will fragment to some degree (which varies significantly depending on the theoretical model adopted), and these fragments collapse into cores and eventually stars. During the collapse process, the gas density within a fragment necessarily increases with time up until stellar densities are reached (although there are intermediate hydrostatic phases during which

this evolution halts). Therefore, the gas density should be a reasonable proxy for the evolutionary state of a gas clump.

The fraction of gas at a given density divided by the free-fall time at that density is put forward as a test of the Core Accretion model of massive star formation by Krumholz & Tan (2007). A higher density yields a shorter free-fall time, but Krumholz claims that the SFR/t_{ff} is constant up to densities $\sim 10^{12}\mathrm{cm}^{-3}$. It is therefore important to understand what fraction of the gas is actually at the 'mean' density which is often reported based on column-density observations of the gas mass and density and simple geometric arguments. Direct observations of density with the H_2CO densitometer provide a more powerful test of the density-based theories.

The turbulent fragmentation model of Padoan & Nordlund (2002) and Padoan et al. (2007a) is a plausible explanation for core mass functions within molecular clouds. They demonstrate that the shape of the mass function depends on the mach number and presence of magnetic fields in turbulent gas. However, the simulations underlying turbulent fragmentation theory lack self-gravity and feedback, and thus they do not consitute a complete theory of star formation. Measurements of the density distribution in turbulent gas can provide an independent test of whether turbulence sets the initial conditions for star formation within molecular clouds.

As discussed in Ginsburg et al. (2011a), the beam-matched H_2CO densitometry performed using the Green Bank Telescope (GBT) and Arecibo Observatory in conjunction is one of the most powerful means of measuring local gas density within the Galaxy. In any molecular cloud, the centimeter lines can be observed in absorption against the CMB. In those clouds containing H II regions, the lines will instead be observed in absorption against brighter free-free continuum emission. In this latter situation, the H_2CO lines therefore trace only foreground gas, rather than integrating over the whole cloud, providing a unique opportunity to measure the velocity structure of gas without foreground/background ambiguity. Other lines can be seen in absorption against bright backgrounds, but most are in the sub-millimeter regime and require high local gas temperatures and densities: they do not trace GMC gas as H_2CO does.

Mangum et al. (2008) and Mangum et al. (2013) used the H_2CO densitometer to measure

density in external galaxies, observing high mean densities in all of the targeted starburst galaxies. The narrow observed range raises a concern about bias intrinsic to the densitometer, which also raised questions in Ginsburg et al. (2011a). In this paper, we demonstrate that lower-density regions are also detectable using H_2CO densitometry, though they are "fainter" (really, less absorptive).

6.3 Observations and Data

6.3.1 Source Selection

We selected 137 sources in the Outer Galaxy within the range $172.8 < \ell < 207.6$, $-2.6 < b < 4.6$ from the Expanded Bolocam Galactic Plane Survey (Aguirre et al., 2011; Ginsburg et al., 2013b). Sources were selected in this range in order to ensure that they could be observed by the Arecibo Radio Observatory.

Because no automated catalog had been generated when these observations were being planned, source selection was performed 'by eye' in most fields by centering on the local 1.1 mm maximum. Since the GBT and Arecibo beams are $\sim 50''$ at the observed frequencies, it was not essential to be perfectly centered on a source. Additionally, some lines of sight were selected from non-point-like features such as 'tails' pointing away from 'cores' - as a result, we do not sample 137 independent clumps and clouds, but may sample some multiple times. This is intentional, as we are searching for density variations in these objects.

Within the expanded BGPS survey, our sample selection is flux-limited. However, the expanded BGPS was not a blind survey - it targeted ^{12}CO and IRAS 100 μm bright regions. Since H_2CO should not exist where ^{12}CO does not, we most likely are sampling the largest and most active star forming regions along the Perseus arm within our targeted longitude range.

6.3.2 Green Bank Telescope

We observed the H_2CO $2_{11}-2_{12}$ line at 2 cm (14.488789 GHz) with the Green Bank Telescope (GBT)[1] dual-beam Ku-band receiver as part of project GBT10B-019. The GBT dual-beam Ku-band receiver was used in beam-switched nodding mode.

System temperatures ranged from 25 to 40 K in the H_2CO band centered on the $2_{11} - 2_{12}$ line. A bandwidth of 50.0 MHz (1035 km s^{-1}) and channel width of 12.2 kHz (0.25 km s^{-1}) were used with 9-level sampling. Three additional tunings were acquired simultaneously, centered at 13.03606, 14.12861, and 14.80500 GHz targeting the NaCl 1-0 and SO 1(2)-1(1), H77α, and H_2CN 2(11)-2(12) lines, respectively.

Each source was observed for 150 seconds in each receiver for a total on-source integration time of 300 seconds. Each observation in the pair was independently inspected to search for emission or absorption in the off position, which was 5.5′ away in azimuth. When absorption was detected in one of the off positions, that on/off pair was discarded if one of the detected lines was affected, but otherwise was noted and ignored.

The gain was assumed to be 1.91 K/Jy based on previous calibration observations on point sources in Ku-band (see discussion in Mangum et al., 2013). For this paper, we focus on measurements in brightness temperature units, but for mapping experiments - particularly when combining with VLA data - the gain is important. The aperture efficiency was $\eta_A = 0.671$, and the main beam efficiency $\eta_{MB} = 1.32\eta_A = 0.886$.

The data were calibrated using the normal GETNOD procedure in GBTIDL[2] . Atmospheric opacity was computed for each observing session by fitting $T_{obs} = T_{rec} + T_X A$ to the whole session's observations, where A is the airmass $A = sin^{-1}(l)$, and T_{rec} is the receiver temperature. T_X is the slope and is related to the atmospheric temperature, optical depth, and airmass by $T_X = T_{atm}(1 - e^{-\tau_z A})$. Using measurements of the atmospheric temperature T_{atm} from Ron Maddalena's

[1] The National Radio Astronomy Observatory operates the GBT and VLA and is a facility of the National Science Foundation operated under cooperative agreement by Associated Universities, Inc.

[2] GBTIDL (`http://gbtidl.nrao.edu/`) is the data reduction package produced by NRAO and written in the IDL language for the reduction of GBT data. The National Radio Astronomy Observatory is a facility of the National Science Foundation operated under cooperative agreement by Associated Universities, Inc.

temperature monitor[3] , we compute the zenith optical depth $\tau_z = -\ln(1 - T_X/T_{atm})/A$.

We assume primary beam $\theta_{FWHM} = 51.1''$ per the GBT observers manual. We assume a conservative 10% error in the beam area $\Omega = 7.8 \times 10^{-8}$ sr, which governs the flux density received from the CMB over the observed area. Beam size error should be dominated by small errors in focus.

During each observing session, 3C123 was observed as a continuum calibrator. For the inner galaxy sessions, which are not reported here, DR21 was observed as a spectral line calibrator - we report the calibration results as a confirmation of the overall stability of the observations. The continuum measurements over 7 sessions varied by 8% RMS for 3C123; we adopt this value as our continuum uncertainty. The peak optical depth of the $2_{11} - 2_{12}$ line seen in DR21 varied by only 1.3% RMS, indicating an excellent overall calibration for spectral line observations despite the higher uncertainty in the continuum level.

6.3.3 Arecibo

The Arecibo[4] 4.829660 GHz H_2CO $1_{10} - 1_{11}$ observations were performed using the Mock spectrometer. We performed 150s on/off observation pairs (150 s on source; unlike the GBT, Arecibo has a single-pixel receiver in the H_2CO band). The H_2CO line was observed in two spectrometer configurations simultaneously, one with 1.4 kHz (0.086 km s^{-1}) and one with 10.5 kHz (0.647 km s^{-1}) channels. The $H_2{}^{13}CO$ 1-0 line was also observed at 1.4 kHz resolution, while the entire band from 4.6 to 5.4 GHz was observed at 10.5 kHz resolution. The observed band contains a few molecules that have been detected in, e.g., OMC1, but we did not detect any other than H_2CO.

The atmospheric opacity is expected to be negligible at 5 GHz, so no atmospheric corrections were performed. The H_2CO $1_{10} - 1_{11}$ line lies in a protected band, and no RFI was observed near our target line, though certain regions of the full band were severely affected.

[3] `http://www.gb.nrao.edu/~rmaddale/Weather/index.html`

[4] The Arecibo Observatory is part of the National Astronomy and Ionosphere Center, which was operated by Cornell University under a cooperative agreement with the National Science Foundation at the time of the observations.

Data reduction was performed using Phil Perrilat's `aoidl` package (`http://arecibo.naic.edu/~phil/`) in conjunction with some home-brewed wrapper scripts (`http://code.google.com/p/casaradio/source/browse/branches/aoidl/ginsburg/reduce_session.pro`).

We calibrated the data to T_{MB} for comparison with the GBT data. From a series of 5262 spider-scan calibration observations from January 1, 2006 to August 25, 2011, we report a measured $\eta_{MB} = 0.51 \pm 0.06$ over the range ZA=2-20. The best-fit η_{MB} had a modest dependence on zenith angle, ranging from 0.478 to 0.516. We used the η_{MB} determined from a 2nd order polynomial fit as a function of ZA centered on the mean ZA of each observation.

6.3.3.1 Data Reduction

We used the `GBTIDL` and `aoidl` data reduction packages for initial data reduction (on-off pair subtraction, calibration to T_{MB} scale), then exported the data to `FITS` format. We then used the PYSPECKIT package[5] to fit model profiles to the $1_{10} - 1_{11}$ and $2_{11} - 2_{12}$ lines. For an initial analysis, we fit gaussians to the $1_{10} - 1_{11}$ and $2_{11} - 2_{12}$ lines independently.

6.4 Results

Out of the 137 observed lines of sight, there were 125 $1_{10} - 1_{11}$ detections, of which 119 had corresponding $2_{11} - 2_{12}$ detections. Of these, 59 were flagged as well-fit by a single gaussian component in both lines.

Within the single-component sample, the $1_{10} - 1_{11}$ lines were systematically wider than the $2_{11} - 2_{12}$ lines. The width difference is small, ~ 0.2 km s^{-1}, but significant. Figure 6.1 shows the histograms of the widths, which are drawn from different distributions based on a KS test.

The first explanation we investigated is that the hyperfine components of the $1_{10} - 1_{11}$ line contribute significantly to the line width. In order to test this hypothesis, we fit a model H_2CO spectrum based on the measured line centers and theoretical relative strengths presented in Tucker et al. (1971, 1972) and compared to Gaussian fits. However, assuming the hyperfine components

[5] `http://pyspeckit.bitbucket.org`, Ginsburg & Mirocha (2011)

follow their theoretical statistical weights, a Gaussian fit is only ~ 0.04 km s^{-1} wider than a full hyperfine fit for our typical line widths (although for some lines, this difference is significant). It is therefore unlikely that the width difference is intrinsic to the H_2CO molecule.

Another possible explanation of this difference is that there is slightly more gas exhibiting $1_{10} - 1_{11}$ absorption than $2_{11} - 2_{12}$ absorption, and this gas is spread over a larger velocity range. Because the $1_{10} - 1_{11}$ line optical depth remains high and therefore detectable at lower densities than the $2_{11} - 2_{12}$ line, if there is a substantial moderate-density ($\log(n) \lesssim 3.5$ cm^{-3}) gas component with a higher line width, the $1_{10} - 1_{11}$ line should have a larger width. This additional gas along the line of sight has the net effect of increasing τ_{1-1} relative to τ_{2-2}, which in turn leads to a bias towards measuring **lower** densities. Quantifying this bias is not directly possible, but we can place limits on it. Since the minimum τ_{1-1}/τ_{2-2} is ≈ 1, anywhere the $2_{11} - 2_{12}$ line is detected, the $1_{10} - 1_{11}$ line must be **at least** as optically thick.

6.5 Line Modeling

After examining the systematic differences between the lines, and generally finding them to be small, we fit more involved models to the data. We used the RADEX code (van der Tak et al., 2007a) to generate a grid of absorption line properties as a function of volume and column density for a fixed temperature $T = 20$ K. The line properties are insensitive to temperature in the range $\sim 15 - 30$ K, which is the whole range observed in the Gem OB1 region by Dunham et al. (2010).

We used the PYSPECKIT package to simultaneously fit both the $1_{10} - 1_{11}$ and $2_{11} - 2_{12}$ lines, using volume density and column density per km s^{-1}pc^{-1} as the free parameters: the observable line temperature is set from the optical depth τ and T_{ex} from the RADEX models. This fitting process has the advantage of properly weighting the $1_{10} - 1_{11}$ and $2_{11} - 2_{12}$ lines by their statistical errors. It also has the advantage of revealing when our assumptions are incorrect by revealing disagreements in the $1_{10} - 1_{11}$ and $2_{11} - 2_{12}$ line shape directly - these disagreements can yield information about density-velocity profiles.

We continue our analysis based on the assumption that the two lines trace the same gas, as is

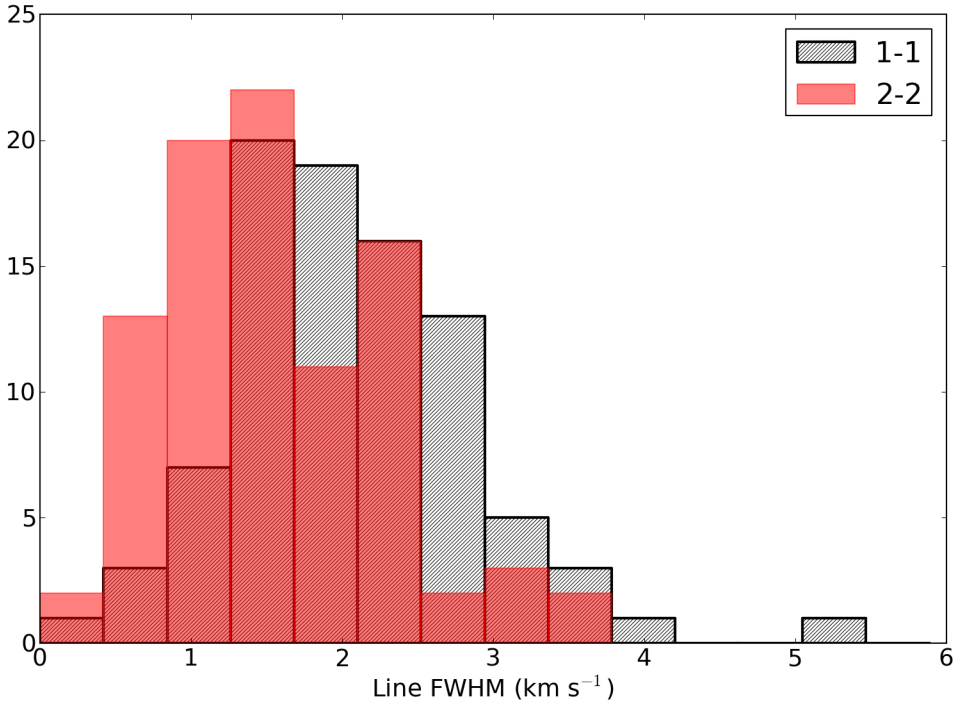

Figure 6.1 Histograms of the Gaussian-fitted widths for the Arecibo $1_{10} - 1_{11}$ line and GBT $2_{11} - 2_{12}$ line. By a two-sample Kolmogorov-Smirnov (KS) test, they are different distributions with $p(same) < 10^{-5}$. The $1_{10} - 1_{11}$ line is wider by 0.07 km s^{-1} on average (0.23 km s^{-1} difference between the medians).

frequently done in extragalactic studies in which line profiles are indistinguishable (Mangum et al., 2008; Mangum et al., 2013).

6.6 Emission Line Sources

Only a few H_2CO $1_{10} - 1_{11}$ emission sources have been discovered. Objects in which LVG analysis would predict emission have more often been seen to be depleted (Young et al., 2004). In our sample, no $1_{10} - 1_{11}$ emission sources were detected, while seven $2_{11} - 2_{12}$ emission sources were detected. The nondetections imply either that there are no high-density ($n > 10^{5.5}$), high-column-density sources in our sample, or that the $1_{10} - 1_{11}$ absorption masks the emission, or that depletion prevents the $1_{10} - 1_{11}$ line from being seen in emission in our whole sample.

The lack of $1_{10} - 1_{11}$ emission is somewhat surprising, even given the above considerations, since there are **entire galaxies** aglow in $1_{10} - 1_{11}$ emission. Mangum et al. (2013) showed that IR 15107+0724 and Arp 220 both have H_2CO $1_{10} - 1_{11}$ emission, but H_2CO $2_{11} - 2_{12}$ absorption. This lack may be because of both a temperature and column density difference between our sample and the LIRG emission-line galaxies. The Troscompt et al. (2009b) collision rates indicate that it is possible to have either line in emission with the other in absorption for $T < 50$ K and H_2 ortho/para < 1.5, but that at higher temperatures the parameter space available for $1_{10} - 1_{11}$ emission and $2_{11} - 2_{12}$ absorption shrinks. See Section 6.9 and Figure 6.8 for further discussion in the context of the ortho-to-para ratio.

Emission line sources have an added complication over simple absorption sources. Because their excitation temperature is unknown, we do not have enough information to independently extract T_{ex}, τ, and the size of the emission region. The ratio is no longer sensitive to density alone unless the filling factor is known; the filling factor and column density are completely degenerate.

The $2_{11} - 2_{12}$ emission line sources are:

(1) G173.69+2.86

(2) G173.72+2.69

(3) G188.95+0.88

(4) G188.95+0.89

(5) G188.95+0.89

(6) G192.59-0.04

(7) G192.60-0.05

6.7 SO $1_2 - 1_1$

The SO $1_2 - 1_1$ line at 13.04370 GHz was observed in parallel with the GBT H_2CO $2_{11} - 2_{12}$ observations. Of the 137 observed, 36 sources were detected in SO $1_2 - 1_1$. We fitted these lines with Gaussian profiles.

The widths of the H_2CO and SO $1_2 - 1_1$ lines are uncorrelated with Pearson R values $|r| < 0.1$ (though for the H_2CO $2_{11} - 2_{12}$ lines with single peaks, there is weak correlation, with $r = 0.26$; Figure 6.2). Similarly, comparing the whole samples of the $1_{10} - 1_{11}$ and $2_{11} - 2_{12}$ line peaks to the SO $1_2 - 1_1$ line peaks results in $|r| < 0.2$. However, when the single peaks are compared to the SO $1_2 - 1_1$ line peaks (Figure 6.3), there is an observed correlation, with Pearson $r_{1-1} = 0.54$ and $r_{2-2} = 0.57$ (in both cases, these values are significant at the 98% confidence level). These correlation measurements indicate that SO $1_2 - 1_1$ and H_2CO do not trace the same gas, but unsurprisingly, it remains likely that both are more readily detected when more molecular gas is present.

Additionally, we compared the SO $1_2 - 1_1$ line properties to the Bolocam measurements. The integral of the SO $1_2 - 1_1$ line is correlated with the Bolocam flux density with $r = 0.66$ with $p(r) < 10^{-6}$, i.e. very high significance. This indicates that SO $1_2 - 1_1$ is a decent tracer of column density, though apparently with large scatter (which prevents a determination of an SO "X-factor"). The scatter could be explained by temperature, opacity, or chemical variations within the sample. The critical density of the SO $1_2 - 1_1$ transition is $n_{cr} \approx 10^3 \mathrm{cm}^{-3}$ for T= 50 K (the

lowest temperature included in Green, 1994), so sub-thermal excitation may explain some but not all of the nondetections.

6.8 Abundance

The combination of the 1.1 mm BGPS with an extensive H_2CO survey allows us to make the best abundance determination of H_2CO to date. The abundance is approximately $X_{\text{o-}H_2CO} = 10^{-9}$, with a variation $\sigma \approx 0.4$. The correlation is weak and somewhat better represented by an offset power-law $X_{\text{o-}H_2CO} = 10^{0.75 \log N(H_2) - 3.6}$ than the simple linear relation, but the scatter remains significant around this relation, so there is not a statistically strong reason to adopt a different abundance relationship (Figure 6.7).

6.9 The Ortho-to-Para ratio of H_2

The refrigeration of the H_2CO lines is dominated by collisions with H_2 with a small contribution from He and other species. Troscompt et al. (2009b) demonstrated that Para-H_2 is significantly more efficient at refrigerating H_2CO then Ortho-H_2. The equilibrium gas-phase formation mechanism of H_2 results in a 3-to-1 ratio of ortho/para H_2. Collisions with other molecules (or alternate formation mechanisms, such as dust grain surface formation) may result in a lower ortho-to-para ratio (OPR).

We note a uniquely interesting feature of the $1_{10} - 1_{11}$ and $2_{11} - 2_{12}$ lines observed in our data. The density at which the $1_{10} - 1_{11}$ line crosses an excitation temperature $T_{ex} = 2.73$ is highly sensitive to the ortho-to-para ratio, while the $2_{11} - 2_{12}$ line is very insensitive to the ortho-to-para ratio. There are therefore regions in $n - N - OPR$ parameter space in which the $2_{11} - 2_{12}$ line will be seen in emission and the $1_{10} - 1_{11}$ line will be seen in absorption, and vice-versa. The $2_{11} - 2_{12}$ emission / $1_{10} - 1_{11}$ absorption case only occurs for $OPR < 3$, i.e. an OPR different from the equilibrium value, and occurs in more of parameter space at higher temperatures. By contrast, $1_{10} - 1_{11}$ emission and $2_{11} - 2_{12}$ absorption preferentially occurs at **low** temperatures, and is limited to either very low densities or columns for high temperature. The $1_{10} - 1_{11}$ emission / $2_{11} - 2_{12}$

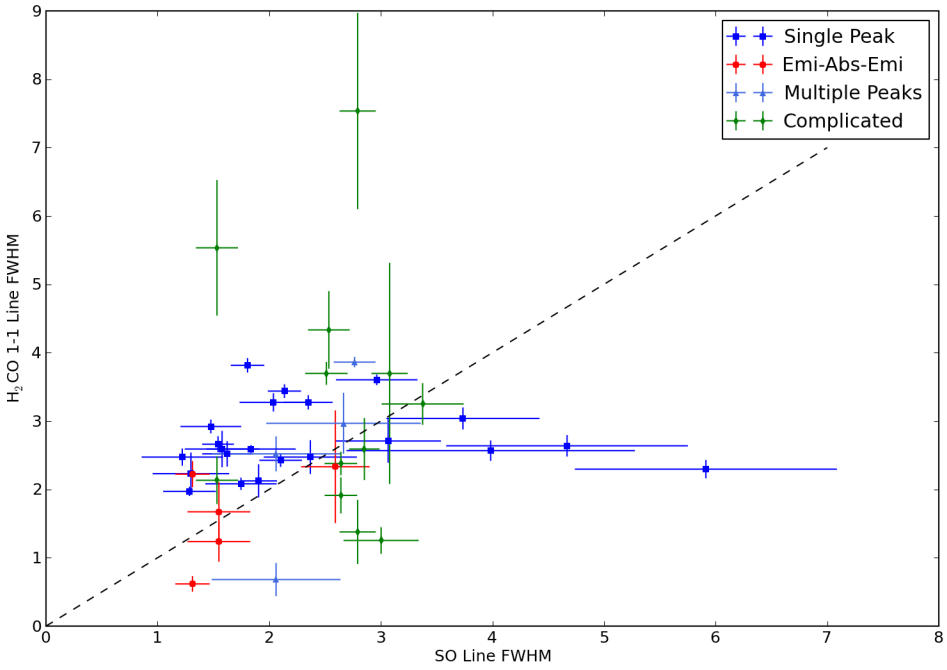

Figure 6.2 The H_2CO $1_{10}-1_{11}$ line widths plotted against the SO 1_2-1_1 line widths where SO 1_2-1_1 was detected. The Pearson correlation coefficient is $|r| < 0.1$ even when excluding outliers with FWHM in either line > 3.5 km s^{-1}, indicating that SO $1_2 - 1_1$ and H_2CO do not trace the same gas.

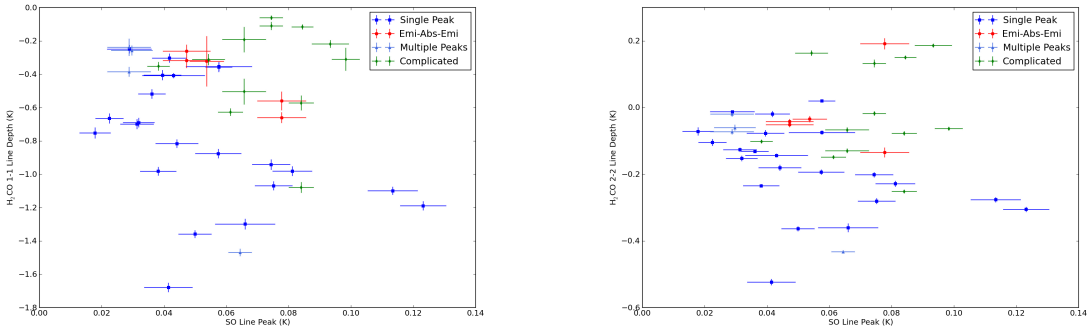

Figure 6.3 The H_2CO $1_{10}-1_{11}$ (left) and $2_{11}-2_{12}$ (right) line depths plotted against the SO 1_2-1_1 line peaks where SO $1_2 - 1_1$ was detected. Taken as a whole, the SO $1_2 - 1_1$ lines peaks are uncorrelated with the H_2CO line depths, but for single-peak H_2CO absorption, there is moderate correlation between the SO $1_2 - 1_1$ peak and the H_2CO absorption depth.

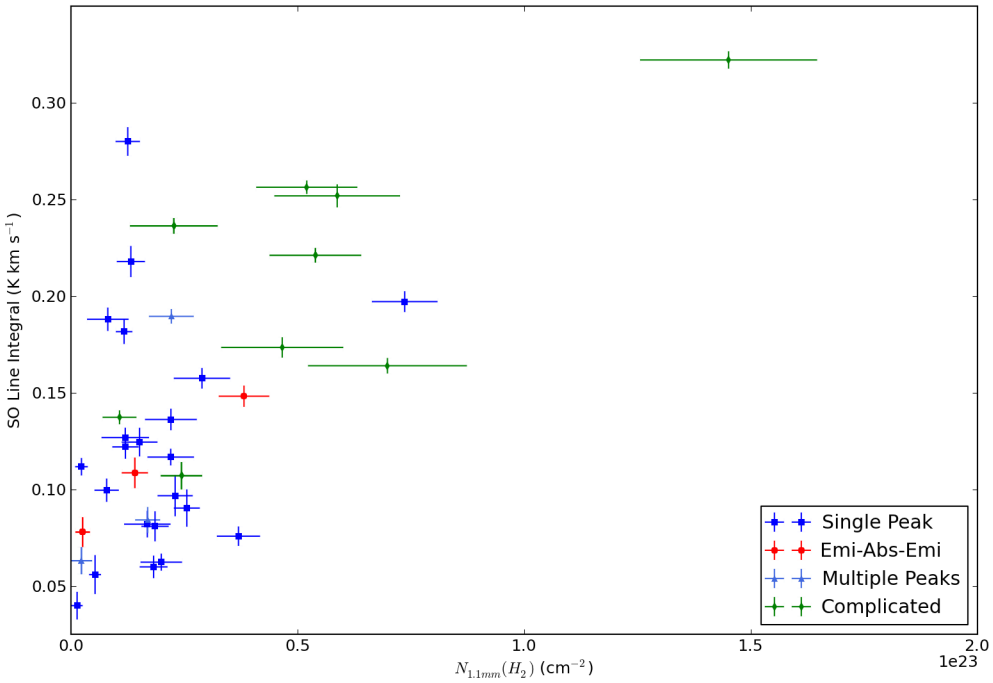

Figure 6.4 The SO $1_2 - 1_1$ line integrals plotted against the BGPS column densities (assuming $T_D = 20$K). The correlation indicates that SO $1_2 - 1_1$ weakly traces the total column density.

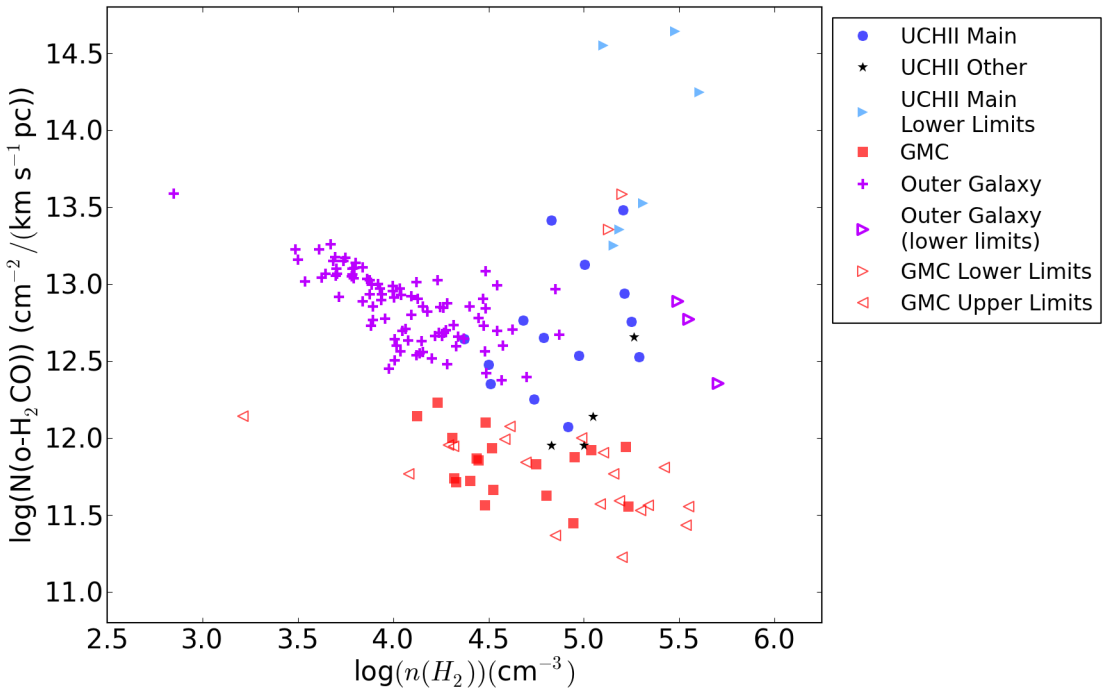

Figure 6.5 Volume Density vs. o-H_2CO Column Density for the pilot survey and outer galaxy samples.

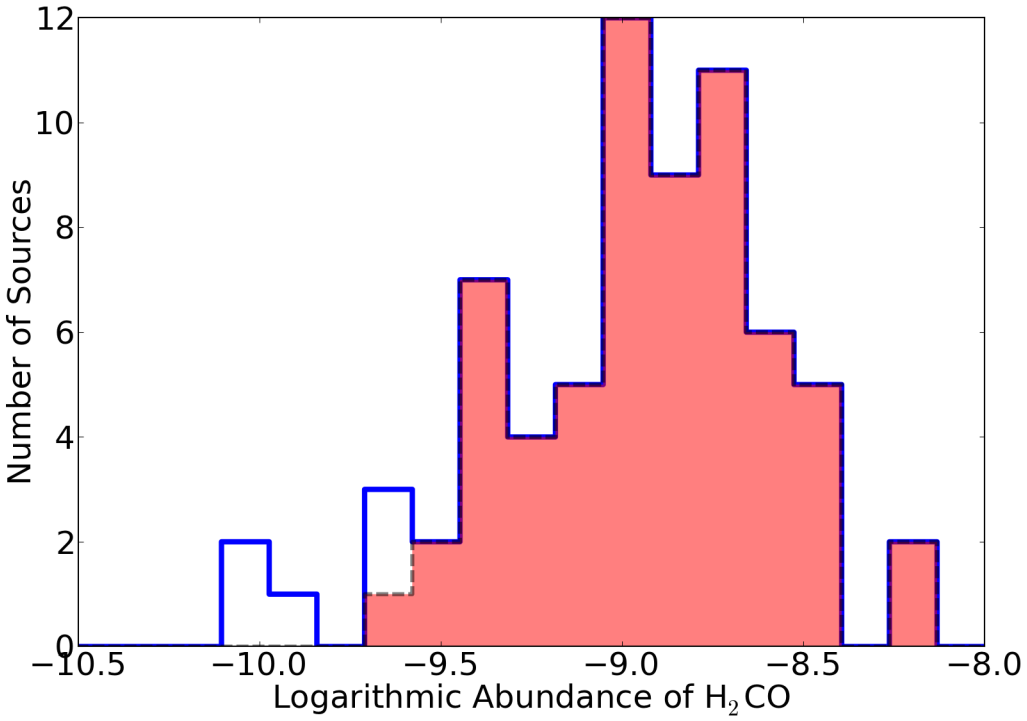

Figure 6.6 Histogram of the measured total abundance of o-H_2CO. The blue histogram shows all of the formaldehyde observations, while the red histogram shows only those consistent with the apparent gaussian distribution of abundances centered around $X_{\text{o-}H_2CO} \sim 10^{-9}$. Outliers were rejected using the `sklearn.covariance.MinCovDet` function.

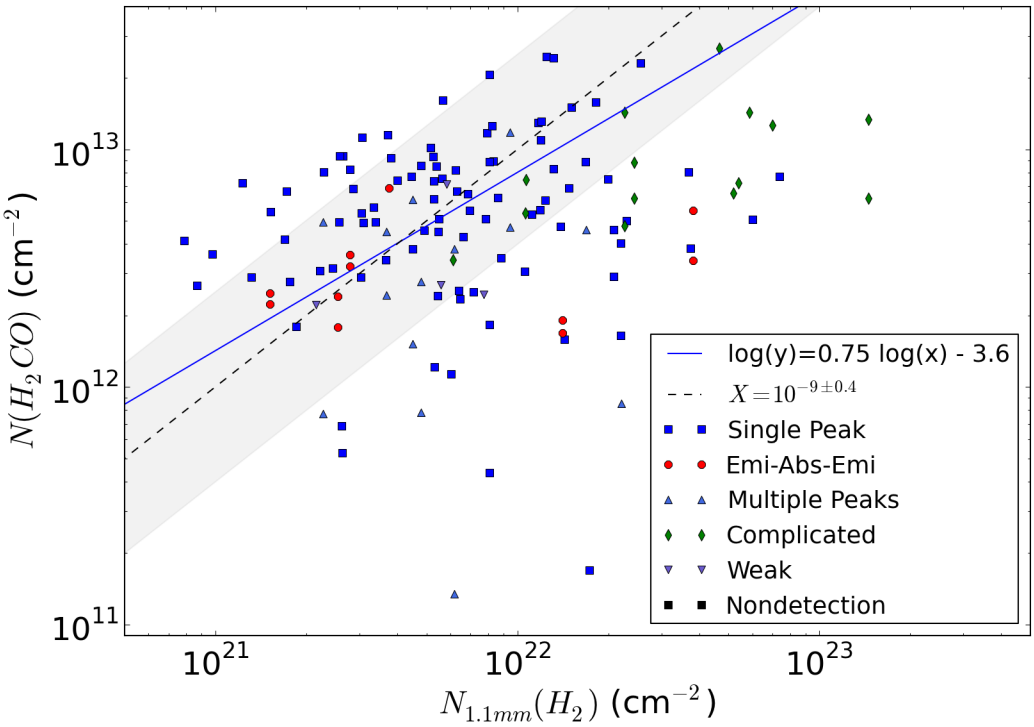

Figure 6.7 The total H_2CO column plotted against the total 1.1 mm column density. The data are reasonably correlated, but the best fit line has decreasing abundance with increasing column density. The best fits exclude outliers from the abundance distribution.

absorption case also prefers **high** ortho-to-para ratio. The parameter space available as a function of n, N, and OPR is shown in Figure 6.8.

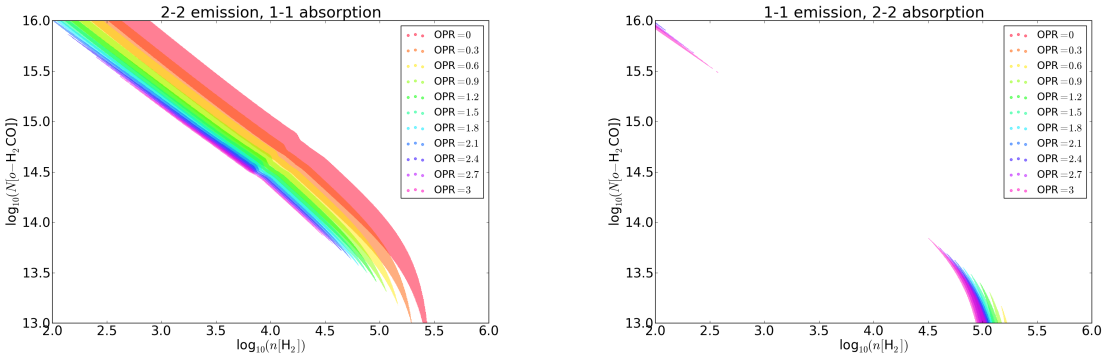

Figure 6.8 (left) Regions of parameter space in which the $2_{11}-2_{12}$ line will be seen in emission while the $1_{10}-1_{11}$ line is seen only in absorption for T= 50 K. For T= 20 K, the regions of parameter space that allow $2_{11}-2_{12}$ emission and $1_{10}-1_{11}$ absorption are smaller, but follow the same general trend. (right) Regions of parameter space where the $1_{10}-1_{11}$ line will be seen in emission and the $2_{11}-2_{12}$ line in absorption. Since we do not detect any examples of this case, but extragalactic observations have, we show the highest temperature case for which collision rates are available, T= 50 K. Note that the central region of this parameter space is empty: normal galactic clouds cannot have $1_{10}-1_{11}$ emission and $2_{11}-2_{12}$ absorption at T= 50 K.

Assuming both lines are tracing the same gas, these exact conditions are observed in multiple lines-of-sight, including G188.95+0.88, G188.95+0.89, G173.72+2.69, G173.69+2.86, G192.59-0.04. In these sources, we measure an upper limit on the ortho-to-para ratio $OPR \lesssim 1.5$.

6.10 Discussion

6.10.1 Column Density - Density Parameter Space

Figure 6.5 shows the column density of o-H_2CO per km s^{-1} pc, i.e. the column density per large velocity gradient bin, versus the derived H_2 number density. Compared to the pilot survey Ginsburg et al. (2011b), the observed sources cover a much larger range in density, but a narrower range in column. Because the pilot survey used H II regions as a backlight, two effects were possible that are not using the CMB as a backlight. First, it is possible to observe absorption against a very small background source, resulting in an effective beam much smaller than the (matched) Arecibo and GBT 50″ beams; this effect explains the sources with very high column. Second,

the backlighting sources provide much stronger signal against which absorption can be observed, resulting in a greater sensitivity and allowing us to detect low column density clouds along the line of sight.

The volume density population is significantly shifted from that observed in the pilot survey. UCH II regions are associated with gas with density $n \sim 10^{4.5} - 10^{5.5}\mathrm{cm}^{-3}$, but the Bolocam sources targeted in this portion of the large survey mostly have densities $10^{3.5}\mathrm{cm}^{-3} < n < 10^{4.5}\mathrm{cm}^{-3}$.

6.11 H_2CO Mapping

We were lucky enough to be awarded **double** the time we asked for on the GBT, allowing us to observe large areas in mapping mode. Naturally, we picked the brightest and best-known regions for mapping studies.

In the inner galaxy, we mapped out an area $\sim 50' \times 20'$ centered on the W51 massive star forming complex. This region is ideally suited to study from Arecibo, the GBT, and the VLA, since it is at declination +14 and is one of the brightest continuum sources in the Galactic plane. It also turns out to be the nearest proto-massive cluster at a VLBI-parallax-measured distance of 5.1 kpc (see Chapter 4 for a discussion of massive proto-clusters). The simple reduction of this data is nearly complete, but analysis has only begun.

In the outer galaxy, we targeted two regions: the Sh 255 complex in Gem OB1 and the Sh 233-IR/IRAS 05358 complex I studied for my Comps II project. We made small ($\sim 5' \times 5'$) maps of these objects in order to evaluate the density profiles and determine what systematic biases may have been present in our single-pointing observations. These outer galaxy sources are both at $D < 2$ kpc, so our resolution is $\lesssim 0.5$pc and we therefore have some marginal hope of discovering dense cores without diluting their signal too badly.

6.11.1 H_2CO maps of S233IR

For the S233IR region, we were able to create a density map, but found the surprising and counterintuitive result that the density was smallest at the peak of the BGPS 1.1 mm emission.

The "envelope" is at a nearly constant density $n \sim 10^{3.5}\mathrm{cm}^{-3}$, but the core is either at a low density (which is effectively ruled out on other considerations) or is significantly self-absorbed. It turns out that H_2CO $2_{11} - 2_{12}$ **emission** fills in the absorption.

Figure 6.9 shows the mapping results for the S233 IR region, where 'envelope' densities are measured to be $n \sim 10^{3.3} - 10^{3.7}\mathrm{cm}^{-3}$, but the 'core' density is more weakly constrained to be $10^{4.5}\mathrm{cm}^{-3} < n < 10^{5.5}\mathrm{cm}^{-3}$ based on the presence of H_2CO $2_{11} - 2_{12}$ emission and the absence of $1_{10} - 1_{11}$ emission. The lack of a direct measurement makes density profile measurement with the current observations impossible.

The moderate densities observed in the envelopes are nonetheless an order of magnitude higher than typical volume-averaged GMC densities (Roman-Duval et al., 2010a) as was previously noted for ordinary GMCs with H_2CO detections in Ginsburg et al. (2011b).

Perhaps most interesting is the contrast between the two BGPS sources shown in Figure 6.9. In Ginsburg et al. (2009), I examined primarily S233IR, but its neighboring region G173.58+2.45 is also a well-studied proto-cluster. Unlike S233IR, which has a B1/B2 10 $M_\odot$ star that is probably still accreting, G173.58 contains no massive stars and has an upper mass limit $M \lesssim 4M_\odot$ (Shepherd & Watson, 2002). The H_2CO observations reveal that the density in this clump is $\sim 10^{3.6}$ cm^{-3}, substantially less than the expected $n \sim 10^5$ cm^{-3} in the massive-star forming S233IR.

The BGPS data show this difference as well, but less strikingly. In the BGPS data, the inferred masses of S233IR and G173 are 840 and 190 $M_\odot$, respectively, though lower by a factor of ~ 2 in each when considering only their condensed $r \lesssim 0.4$ pc cores. Their densities differ by a smaller amount using the BGPS data and assuming spherical symmetry, with peak densities $n \sim 10^{4.1}$ in G173 and $n \sim 10^{4.8}$ in S233IR. The density difference reinforces the conclusion drawn from the H_2CO data, but also show that its density measuring power is greater, since the spherical symmetry assumption is known to be flawed.

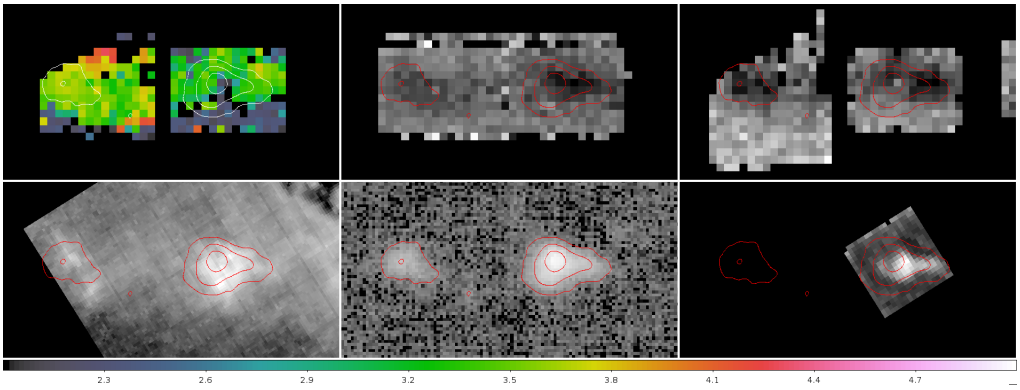

Figure 6.9 The S233IR / IRAS 05358+3543 region and its neighbor G173.58+2.45. *Top left:* The H_2CO density map covering densities $10^2 \mathrm{cm}^{-3} < n < 10^5 \mathrm{cm}^{-3}$ from grey to green. The grey areas show regions of low density ($n < 10^3$ cm^{-3}), while green show high-density regions ($n \gtrsim 10^{3.5}$ cm^{-3}). The 'hole' at the peak of the contours is likely very high density, $n > 10^5$ cm^{-3}. *Top center:* The H_2CO $1_{10} - 1_{11}$ absorption map. *Top right:* The H_2CO $2_{11} - 2_{12}$ absorption map. Note the lack of absorption at the contour peak: this is probably $2_{11} - 2_{12}$ emission filling in $2_{11} - 2_{12}$ absorption, indicating a high $n \gtrsim 10^5$ cm^{-3} density. *Bottom left:* CO 3-2 peak line brightness map. *Bottom center:* The BGPS v2.0 1.1 mm emission map, with contours at 0.2, 1.0, and 3.0 Jy. These contours are shown on all of the other maps for reference. *Bottom right:* SO $5_6 - 4_5$ map. This line has a very high critical density $n \sim 3.5 \times 10^6$ cm^{-3} and an upper level energy $T_U = 35$ K. Its morphology, with a hole at the peak of the dust emission, backs the claim that the density is highest in the area around the dust peak.

6.11.2 W51

The W51 survey was completed in September 2011. The data reduction process presented unique challenges: at C-band, the entire region surveyed contains continuum emission, so no truly suitable 'off' position was found within the survey data. Similarly, H_2CO is ubiquitous across the region, so it was necessary to 'mask out' the absorption lines when building an off position. This was done by interpolating across the line-containing region with a polynomial fit (Figure 6.10).

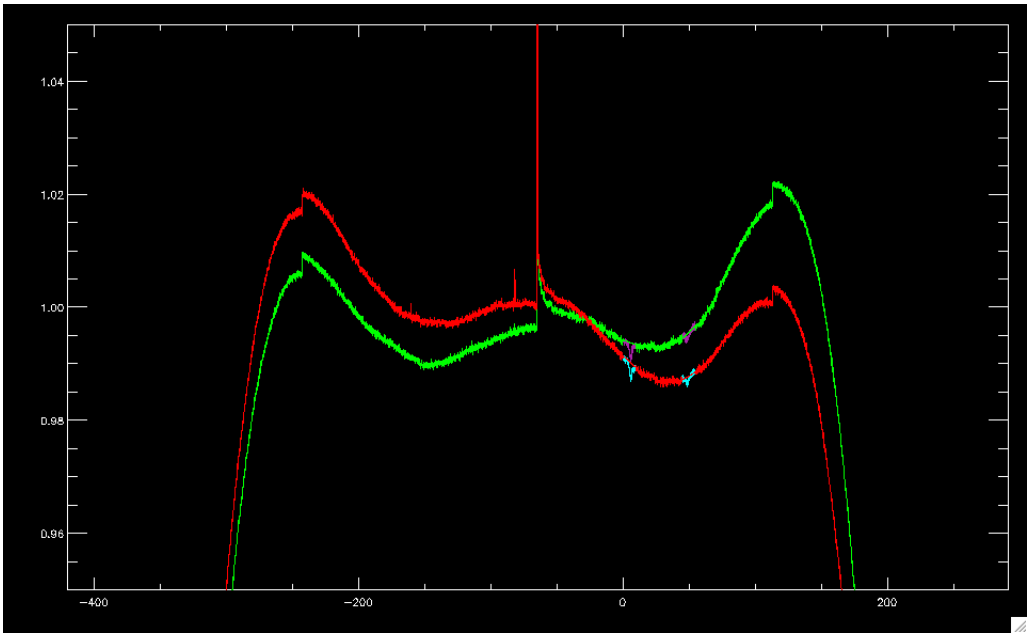

Figure 6.10 An example of the H_2CO line masking procedure for building an Off spectrum. The line-containing regions for each polarization are shown in cyan and purple, with the interpolated replacement in red and green.

The W51 data are converted into "optical depth" data cubes by dividing the integrated H_2CO absorption signature by the measured continuum level. These τ cubes are then fit with the RADEX models used for other H_2CO fitting. However, there are multiple velocity components in W51, so I used a two-component (unconstrained) fit for each pixel, which is frequently unstable but in the case of W51 looks to have produced reasonable results. Note that there was **no** H_2CO emission detected anywhere in the W51 region.

A first interesting note is that a local cloud at $v_{lsr} \sim 5$km s^{-1} is detected in H_2CO $1_{10} - 1_{11}$

across most of the cloud and not detected at $2_{11} - 2_{12}$, with $\tau_{1_{10}-1_{11}}/\tau_{2_{11}-2_{12}} \gtrsim 3$, implying a very low column $N_{\rm H_2CO} \sim 10^{11.5}$ or $N_{\rm H_2} \sim 10^{20.5}$. The cloud is seen in ^{13}CO as a very weak, diffuse feature, and in HI absorption as a very sharp, deep (self)-absorption feature.

I successfully made density maps of the W51 cloud, though because the velocity structure is quite complicated, it was necessary to fit two components to most of the map. Two-component fits are never particularly stable, so it was necessary to restrict the parameters being fitted, and even then the results aren't perfectly reliable. Despite those caveats, there are some reliable fits, particularly towards the 'core' of W51 Main / W51 IRS 2. There are two high-density components with $n \sim 10^5 - 10^{5.5}$ cm^{-3} at different velocities evident in Figure 6.11. The southern component, centered on W51 Main, has $v_{LSR} \sim 56 - 59$. The northern component, a strip going through IRS 2 and towards the west, peaks around $v_{LSR} \sim 68 - 69$ km s^{-1}. A 10 km s^{-1} difference between two extremely dense components, both which are necessarily in the foreground of the HII region, is shocking (probably, anyway, unless the sound speed is very high).

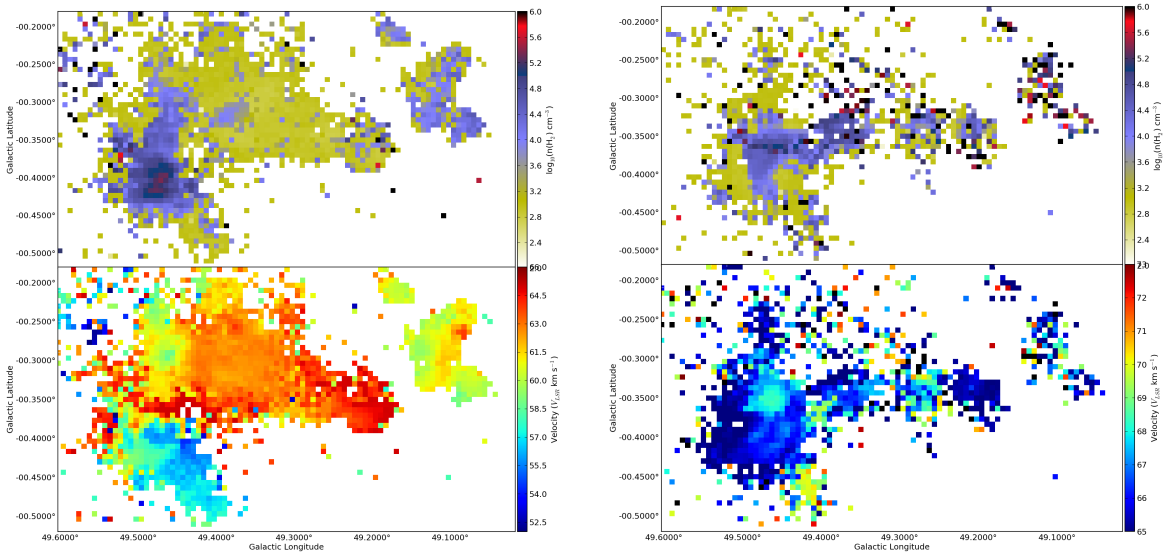

Figure 6.11 Density and velocity fits to the W51 Arecibo and GBT H_2CO data cubes. The yellow regions in the top panel correspond to $1_{10} - 1_{11}$ detections and $2_{11} - 2_{12}$ nondetections, indicating upper limits $n < 10^{3.8}$ (68% confidence) or $n < 10^{4.3}$ (99.7% confidence).

There is a large area where $1_{10} - 1_{11}$ was detected, but $2_{11} - 2_{12}$ was not. Our sensitivity allows us to place a modest upper limit on the gas density, with $3 - \sigma$ upper limits $\lesssim 10^{4.3}$ cm^{-3}

(but the most likely densities are $10^2 < n < 10^4$ cm^{-3}). Figure 6.12 shows a particular model for a spectrum that is especially unconstrained. The $1_{10} - 1_{11}/2_{11} - 2_{12}$ optical depth ratio in this object is $\sim 10 - 20$, indicating that the volume density must be low.

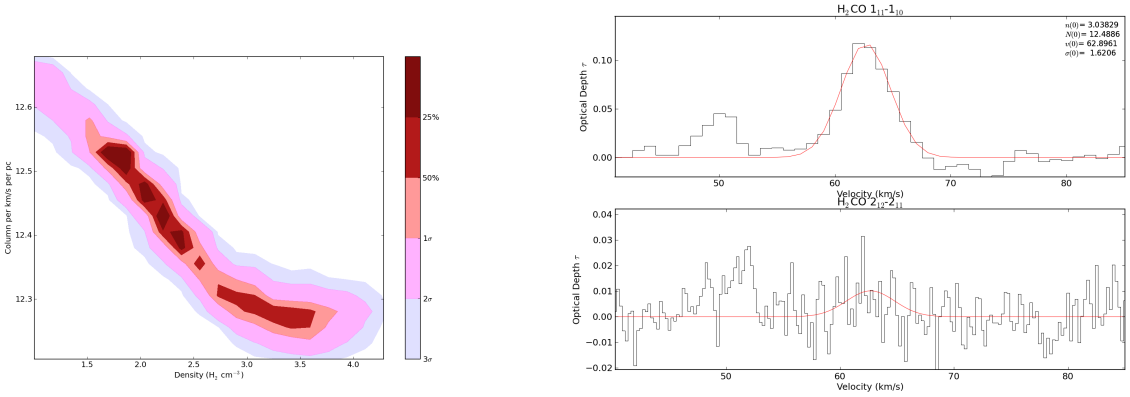

Figure 6.12 Plots demonstrating upper limit fits. The left plot shows the allowed parameter space from MCMC sampling of the data given the RADEX model. The right plot shows the 'best-fit' model to the optical depth spectra, which is clearly unconstrained by the relatively insensitive $2_{11} - 2_{12}$ spectrum. The sensitivity in the $1_{10} - 1_{11}$ line is better in large part because of brighter 6 cm background across the whole W51 region. Despite the lack of constraint on the volume density, there is a reasonably strong constraint on the column density.

The molecular gas is concentrated near, but not exactly on, the bright cm peaks. W51 IRS2 has a massive clump of gas at 65 km s^{-1}, and W51 e2 has a similar clump. However, e2 also seems to have a very dense ($n > 10^5$cm^{-3}) infalling clump. The spectra, along with multicomponent fits, are shown in Figure 6.13.

6.12 Introduction

Nearly all gas in the interstellar medium is supersonically turbulent. The properties of this turblence are essential for determining how star formation progresses. There are now predictive theories of star formation that include formulations of the Initial Mass Function (Hopkins, 2012b; Chabrier & Hennebelle, 2010; Hennebelle & Chabrier, 2011, 2013; Padoan et al., 2012; Padoan & Nordlund, 2011; Padoan et al., 2007b; Krumholz et al., 2005). The distribution of stellar masses depends critically on the properties of the turbulence. It is therefore essential to measure the properties of turbulence in the molecular clouds that produce these stars.

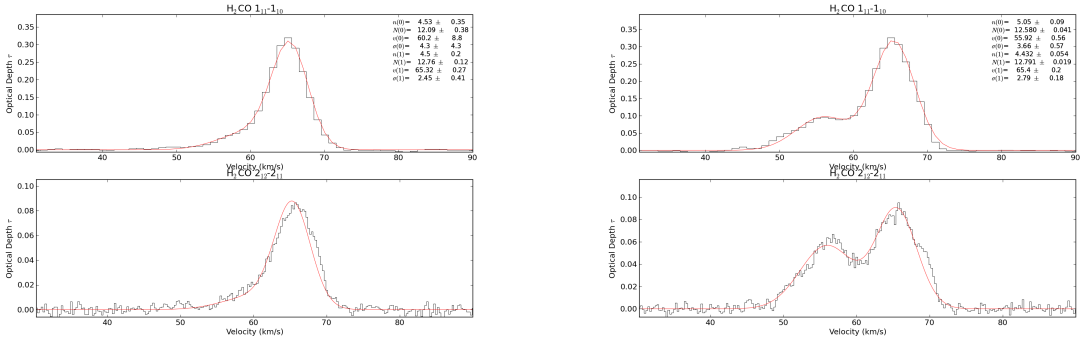

Figure 6.13 Plots of the optical depth spectra centered on W51 IRS2 (left) and W51 e2, an ultra-compact HII region (right). IRS2 shows high-density gas with a slight hint of infall, but otherwise a somewhat vanilla spectrum. W51e2 has a large, high-density red shoulder, indicating high-density gas at the most red velocity in the system. Because this is foreground gas, that high-density gas **must** be moving towards the UCH II region.

Recent works have used simulations to characterize the density distribution from different driving modes of turbulence (Federrath & Klessen, 2013; Federrath et al., 2011, 2010b, 2009, 2008; Kritsuk et al., 2011). These works determined that there is a relation between the mode of turbulent driving and the width of the turbulent distribution, with $\sigma_{\ln\rho} = \ln\left(1 + b^2\mathcal{M}^2\frac{\beta}{\beta+1}\right)$, where $\beta = 2(\mathcal{M}_A/\mathcal{M})^2 = 2(c_s/v_A)^2$. This equation can also be expressed in terms of the compressive mach number $\mathcal{M}_c = b\mathcal{M}$, with $b \approx 1/3$ corresponding to solenoidal forcing and $b = 1$ corresponding to purely compressive forcing (Federrath et al., 2010b; Konstandin et al., 2012; Molina et al., 2012).

All of the turbulence-based theories of star formation explicitly assume a lognormal form for the density probability distribution $P_V \ln\rho$ of the gas. However, recent simulations (Federrath & Klessen, 2013) and theoretical work (Hopkins, 2013) have shown that the assumption of a lognormal distribution is often very poor[6] , deviating by orders of magnitude at the extreme of the density distributions. Since these theories all involve an integral over the density probability distribution funcion (PDF), skew in the lognormal distribution can drastically affect the overall star formation rate and predicted initial mass function.

While simulations are powerful probes of wide ranges of parameter space, no simulation is capable of including all of the physical processes and spatial scales relevant to turbulence. Observations are required to provide additional constraints on properties of interstellar turbulence and guide simulators towards the most useful conditions and processes to include. Kainulainen et al. (2013) and Kainulainen & Tan (2012) provide some of the first observational constraints on the mode of turbulent driving, finding $b \approx 0.4$, i.e. that there is a mix of solenoidal and compressive modes.

Formaldehyde, H_2CO, is a unique probe of density in molecular clouds. Like CO, it is ubiquitous, with a nearly constant abundance wherever CO is found (Tang et al., 2013; Mangum & Wootten, 1993). The lowest rotational transitions of o-H_2CO at 2 and 6 cm can be observed in absorption against the cosmic microwave background or any bright continuum source (Ginsburg

[6] The simultaneous assumption of a lognormal mass-weighted and volume-weighted density distribution is also not self-consistent (Hopkins, 2013).

et al., 2011a; Darling & Zeiger, 2012). The ratio of these lines is strongly sensitive to the local density of H_2, but it is relatively insensitive to the local gas temperature (Wiesenfeld & Faure, 2013; Troscompt et al., 2009c). Unlike critical density tracers, the H_2CO line ratio has a direct dependence on the density that is independent of the column density.

However, the particular property of the H_2CO densitometer we explore here is its ability to trace the **mass-weighted** density of the gas. Typical density measurements from ^{13}CO or dust measure the total mass and assume a line-of-sight geometry, measuring a **volume-weighted** density, i.e. $\rho_V = M_{tot}/V_{tot}$. In contrast, the H_2CO densitometer is sensitive to the density that corresponds to the most mass, i.e. $\rho_M = \int M \rho dM / M_{tot}$. The volume- and mass- weighted densities will vary with different drivers of turbulence, so in clouds dominated by turbulence, if we have measurements of both, we can infer the driver.

In Ginsburg et al. (2011a), we noted that the H_2CO densitometer revealed volume densities much higher than expected given the cloud-average densities from ^{13}CO observations. The densities were higher even than typical turbulence will allow. However, this argument was made on the basis of a statistical argument; here we attempt to demonstrate that the clumps in GMCs are of very high density in individual clouds.

6.13 Observations

We report H_2CO observations performed at the Arecibo Radio Observatory[7] and the Green Bank Telescope[8] that will be described in more detail in (Ginsburg et al., 2011a), with additional data to be published in a future work. Arecibo and the GBT have FWHM$\approx 50''$ beams at the observed frequencies of 4.829 and 14.488 GHz, respectively. Observations were carried out in a position-switched mode with 3 and $5.5'$ offsets for the Arecibo and GBT observations respectively.

The Boston University / Five-College Radio Astronomy Observatory Galactic Ring Survey

[7] The Arecibo Observatory is part of the National Astronomy and Ionosphere Center, which is operated by Cornell University under a cooperative agreement with the National Science Foundation.

[8] The National Radio Astronomy Observatory operates the GBT and VLA and is a facility of the National Science Foundation operated under cooperative agreement by Associated Universities, Inc.

^{13}CO data was also used. The BU FCRAO GRS (Jackson et al., 2006) is a survey of the Galactic plane in the ^{13}CO 1-0 line with $\sim 46''$ resolution. We used reduced data cubes of the $\ell = 43$ region.

6.13.1 A non-star-forming molecular cloud

We examine the line of sight towards G43.17+0.01, also known as W49. In a large survey, we observed two lines of sight towards W49, the second at G43.16-0.03. Both are very bright continuum sources, and two GMCs are easily detected in both H_2CO absorption and ^{13}CO emission. Figure 6.14 shows the spectrum dominated by W49 itself, but with clear foreground absorption components. The continuum level subtracted from the spectra are 73 K at 6 cm and 11 K at 2 cm for the south component, and 194 K at 6 cm and 28 K at 2 cm for the north component.

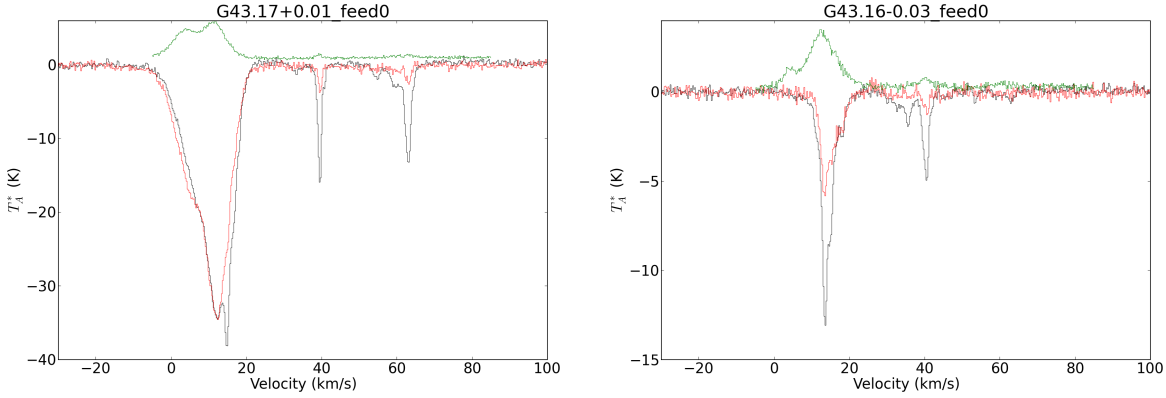

Figure 6.14 Spectra of the H_2CO $1_{10}-1_{11}$ (black), $2_{11}-2_{12}$ (red), and ^{13}CO 1-0 (green) lines towards G43.17+0.01 (left) and G43.16-0.03 (right). The H_2CO spectra are shown continuum-subtracted, and the ^{13}CO spectrum is offset by 1 K for clarity. The GBT $2_{11} - 2_{12}$ spectra are multiplied by a factor of 9 so the smaller lines can be seen.

We focus on the "foreground" line at ~ 40 km s^{-1}, since it is not associated with the extremely massive W49 region. The cloud, known as GRSMC 43.30-0.33 (Simon et al., 2001), was confirmed to have no associated star formation in that work. Additional H_2CO spectra of surrounding sources that are bright at 8-1100 μm and within the ^{13}CO contours of the cloud show that they are all at the velocity of W49 and therefore are not associated with these foreground clouds.

The H_2CO lines are is observed in the outskirts of the cloud, not at the peak of the ^{13}CO emission. The cloud spans $\sim 0.6°$, or ~ 30 pc at $D = 2.8$ kpc (Roman-Duval et al., 2009). It is

detected in $1_{10} - 1_{11}$ absorption at all 6 locations observed in H_2CO (Figure 6.15), but $2_{11} - 2_{12}$ is only detected in front of the W49 HII region because of the higher signal-to-noise at that location. The detected ^{13}CO and H_2CO lines are fairly narrow, with H_2CO FWHM $\sim$ 1.3-2.8 km s^{-1} and ^{13}CO widths from 1.8-5.9 km s^{-1}. The ^{13}CO lines are 50% wider than the H_2CO lines.

The highest ^{13}CO contours are observed as a modest infrared dark cloud in Spitzer 8 μm images, but no dust emission peaks are observed at 500 μm or 1.1 mm associated with the dark gas. This is an indication that any star formation, if present, is weak - no massive dense clumps are present within this cloud.

The cloud has mass $M_{CO} = 1.5 \times 10^4\ M_\odot$ in a radius $r = 15$ pc, so its mean density is $n(H_2) \approx 15$ cm^{-3} assuming spherical symmetry. If we instead assume a cubic volume, the mean density is $n(H_2) \sim 8$ cm^{-3}. For an oblate spheroid, with minor axis 0.1$\times$ the other axes, the mean density is $n \sim 150$cm^{-3}, which we regard as a conservative upper limit. Simon et al. (2001) report a mass $M_{CO} = 6 \times 10^4 M_\odot$ and $r = 13$ pc, yielding a density $n(H_2) = 100$ cm^{-3}, which is consistent with our estimates but somewhat higher than measured by Roman-Duval et al. (2010b) because of the improved optical depth corrections in the latter work.

6.14 Modeling H_2CO

In order to infer densities using the H_2CO densitometer, we use the low-temperature collision rates given by Troscompt et al. (2009c) with RADEX (van der Tak et al., 2007b) to build a grid of predicted line properties covering densities from $10 - 10^8$ H_2 cm^{-3}, temperatures from 5-50 K, column densities N(o-H_2CO) from $10^{11} - 10^{16}$ cm^{-2}, and ortho-to-para ratios from $10^{-3} - 3$.

The H_2CO densitometer measurements are shown in Figure 6.16. The figures show optical depth spectra, given by the equation

$$\tau = -\ln\left(\frac{S_\nu + 2.73}{\bar{C}_\nu + 2.73}\right) \tag{6.1}$$

where S_ν is the spectrum (with continuum included) and $\bar{C}_\nu$ is the measured continuum, both in Kelvins. The cosmic microwave background temperature is added to the continuum since H_2CO

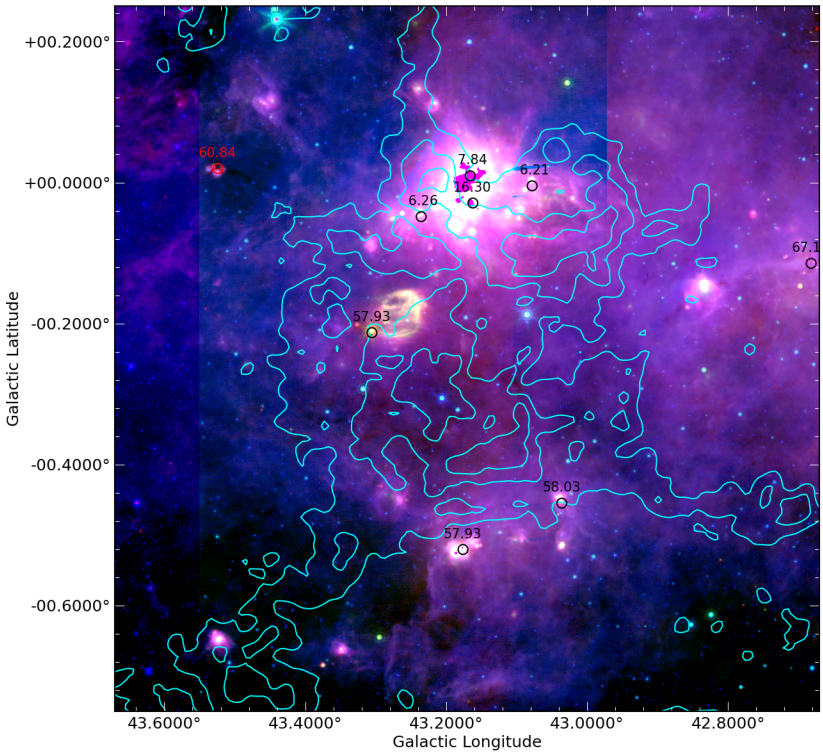

Figure 6.15 The G43 40 km s^{-1} cloud. The background image shows Herschel SPIRE 70 μm (red), Spitzer MIPS 24 μm (green), and Spitzer IRAC 8 μm (blue) in the background with the ^{13}CO integrated image from $v = 36$km s^{-1} to $v = 43$km s^{-1} at contour levels of 1, 2, and 3 K superposed in orange contours. The red and black circles show the locations of H_2CO pointings, and their labels indicate the LSR velocity of the strongest line in the spectrum. The W49 HII region is seen behind some of the faintest ^{13}CO emission that is readily associated with this cloud. The dark swath in the 8 and 24 μm emission going through the peak of the ^{13}CO emission in the lower half of the image is likely a low optical depth infrared dark cloud associated with this GMC.

can be seen in absorption against it, though towards W49 it is negligible.

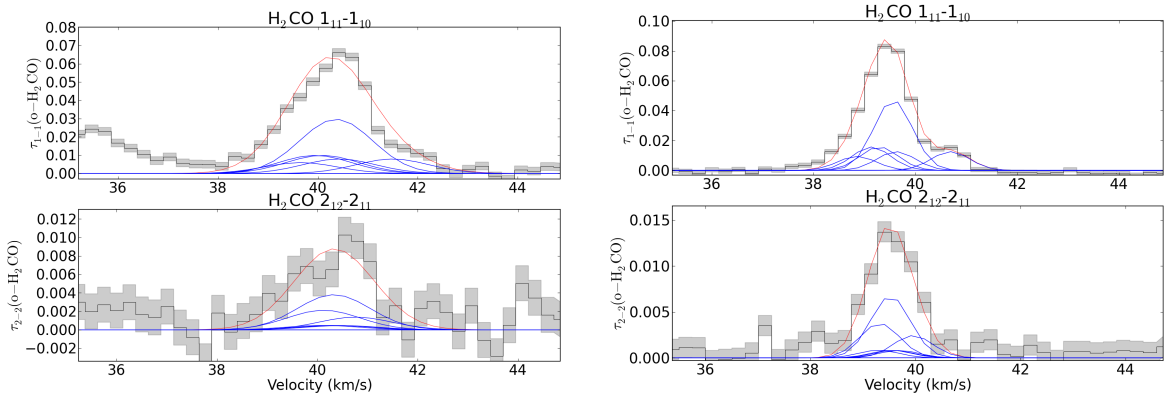

Figure 6.16 Optical depth spectra of the $1_{10} - 1_{11}$ and $2_{11} - 2_{12}$ lines towards the two W49 lines of sight, G43.16 (left) and G43.17 (right). The optical depth ratio falls in a regime where temperature has very little effect and there is no degeneracy between low and high densities.

We performed line fits to both lines simultaneously using a Markov-chain monte-carlo approach, assuming uniform priors across the modeled parameter space and independent gaussian errors on each spectral bin. The density measurements are very precise, with $n \approx 23,000^{+9300}_{-7700}$ cm^{-3} (95% confidence interval) and $n \approx 20,400^{+12000}_{-10000}$ cm^{-3} for G43.17+0.01 and G43.16-0.03 respectively. While this is a precise measurement of gas density, we now need to examine exactly what gas we have measured the density of.

Since the W49 line of sight is clearly on the outskirts of the cloud, not through its center, such a high density is unlikely to be an indication that this line of sight corresponds to a centrally condensed density peak (e.g., a core). The comparable density observed through two different lines of sight separated by ~ 2 pc also supports this idea.

6.15 Turbulence and H_2CO

Supersonic interstellar turbulence can be characterized by its driving mode, Mach number $\mathcal{M}$, and magnetic field strength. Assuming the distribution follows a lognormal distribution, defined as

$$P_V(s) = \frac{1}{\sqrt{2\pi\sigma_s^2}} \exp\left[-\frac{(s+\sigma_s^2/2)^2}{2\sigma_s^2}\right] \tag{6.2}$$

where the subscript V indicates that this is a volumetric density distribution function. The width of the turbulent density distribution is given by

$$\sigma_s^2 = \ln\left(1 + b^2\mathcal{M}^2\frac{\beta}{\beta+1}\right) \tag{6.3}$$

where $\beta = 2c_s^2/v_A^2 = 2\mathcal{M}_A^2/\mathcal{M}^2$ and b ranges from 1/3 (solenoidal, divergence-free forcing) to 1 (compressive, curl-free) forcing (Federrath et al., 2010b). The parameter s is the logarithmic overdensity, $s \equiv \ln(\rho/\rho_0)$.

The observed H_2CO ratio roughly depends on the **mass-weighted** probability distribution function (as opposed to the volume-weighted distribution function, which is typically reported in simulations). We first examine the implications assuming a lognormal distribution for the mass-weighted density.

We use LVG models of the H_2CO lines, which are computed assuming a fixed local density, as a starting point to model the observations of H_2CO in turbulence. Starting with a fixed **volume-averaged** density ρ_0, we compute the observed H_2CO optical depth in both the $1_{10} - 1_{11}$ and $2_{11} - 2_{12}$ line by averaging over the mass-weighted density distribution.

$$\tau(\rho_0) = \int_{-\infty}^{\infty} \frac{\tau_p(\rho)}{N_p} P_m(\ln\rho/\rho_0) d\ln\rho \tag{6.4}$$

$\tau_p(\rho)/N_p$ is the optical depth **per particle** at a given density, where N_p is the column density (per km $s^{-1}pc^{-1}$) from the LVG model. We assume a fixed abundance of o-H_2CO relative to H_2 (i.e., the H_2CO perfectly traces the H_2). Figure 6.17 shows the result of this integral for an abundance of o-H_2CO relative to H_2 $X(\text{o-}H_2CO) = 10^{-9}$, where the x-axis shows $\rho_0 = n(H_2)$ and the Y-axis shows the observable optical depth ratio of the two H_2CO centimeter lines.

6.15.1 Turbulence and GRSMC 43.30-0.33

We use the density measurements in GSRMC 43.30-0.33 to infer properties of that cloud's density distribution.

We measure the abundances of o-H_2CO relative to ^{13}CO, $X(\text{o-}H_2CO/^{13}CO) = 3.2\times10^{-4}$ and 9.8×10^{-4} for G43.16 and G43.17 respectively, or relative to H_2, 5.8×10^{-10} and 1.7×10^{-9}, which are

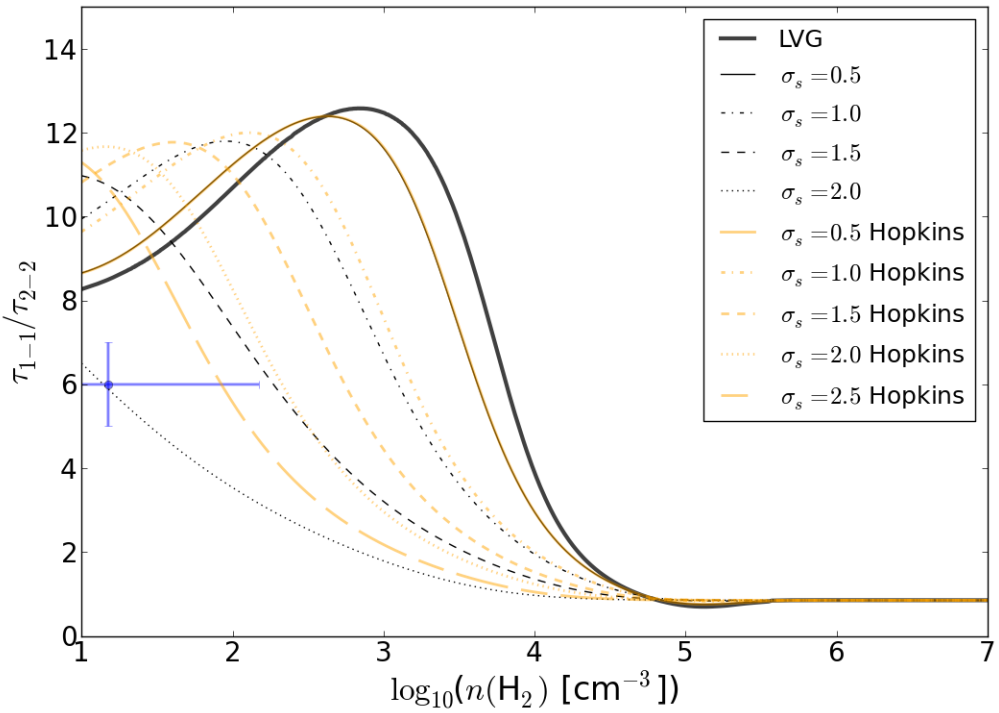

Figure 6.17 The predicted H_2CO $1_{10} - 1_{11}/2_{11} - 2_{12}$ ratio as a function of volume-weighted mean density for a fixed abundance relative to H_2 $X(\text{o-}H_2CO) = 10^{-9}$ and H_2 ortho/para ratio 1.0. The legend shows the effect of smoothing with different lognormal mass distributions as described in Equation 6.3. The solid line, labeled LVG, shows the predicted ratio with no smoothing (i.e., a δ-function density distribution). The blue errorbars show the G43.17 H_2CO measurement and the GSRMC 43.30-0.33 mean density.

entirely consistent with other measurements of $X_{\text{o-H}_2\text{CO}}$ and allow us to use Figure 6.17 for this analysis. The observed formaldehyde line ratio $\tau_{1-1}/\tau_{2-2} \sim 6$, while the volume averaged mean density of the cloud $8 \lesssim \rho_0 < 150$.

Assuming a temperature $T = 10$ K, consistent with both the H_2CO and CO observations (Plume et al., 2004), the sound speed in molecular gas is $c_s = 0.19$ km s^{-1}. The observed line FWHM in G43.17 is 0.95 km s^{-1} for H_2CO and 1.7 km s^{-1} for ^{13}CO 1-0, so the Mach number of the turbulence is $\mathcal{M} \approx 5.1 - 9.1$.

If we assume the density distribution is lognormal, we can determine the values of the 'compressibility coefficient' b from Equation 6.3. Assuming the thermal dominates the magnetic pressure ($\beta >> 1$), the allowed values of σ_s given the line-width based limits on $\mathcal{M}$ range from 1.8-2.1 for $b = 1$ and 1.2-1.5 for $b = 1/3$. If magnetic pressure is significant, the allowed values of σ_s drop.

Given that the observed mean cloud density is $n(H_2) \lesssim 10^2 \text{cm}^{-3}$, Figure 6.17 shows that only the most extreme values of σ_s can explain the mean density. Even if the cloud is extremely oblate, e.g. with a line-of-sight axis 0.1× the plane-of-sky axes, $\sigma_s > 1.5$ is required.

In order to achieve a self-consistent mass and volume PDF, we use the Hopkins (2013) distribution with the fitted relation $T = 0.25 \ln(1+0.25\sigma_s^4(1+T)^{-6}$. Using the $\sigma_s = 2.5$ distribution, which is just consistent with the observations, $T = 0.29$, and based on Hopkins (2013) Figure 3, the compressive Mach number $\mathcal{M}_c$ $20T \approx 5.8$. Compared to the mach number restrictions from the line width, this $\mathcal{M}_C$ implies a compressive-to-total ratio $b > 0.6$.

The restrictions on σ_s using either assumed density distribution are strong indications that compressive forcing must be a significant, if not dominant, mode in this molecular cloud. All of the systematic uncertainties tend to require a **greater** b value. Temperatures in GMCs are typically 10-20 K: warmer temperatures increase the sound speed, decrease the Mach number, and therefore decrease σ_s. Stronger (i.e. non-negligible) magnetic fields decrease σ_s.

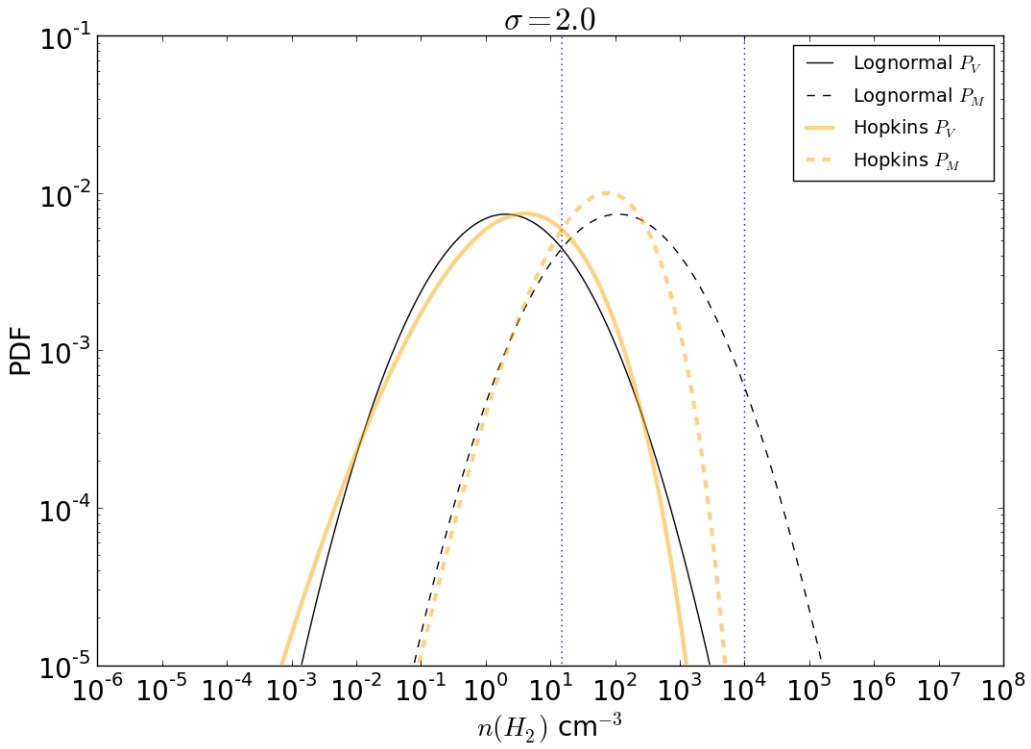

Figure 6.18 Example volume- and mass-weighted density distributions with $\sigma_s = 2.0$. The vertical dashed lines show $\rho = 15$ and $\rho = 10^4$, approximately corresponding to the volume-averaged mean density of GRSMC 43.30 and the H_2CO-derived density

6.16 Conclusions

We demonstrate the use of a novel method of inferring the shape of the density probability distribution in a molecular cloud using H_2CO densitometry in conjunction with ^{13}CO-based estimates of total cloud mass.

Our data show evidence for compressively driven turbulence in a non-star-forming giant molecular cloud. Such high compression in a fairly typical GMC indicates that compressive driving is probably a common feature of all molecular clouds.

Chapter 7

Software developed during this thesis

7.1 Preface

Software development is often underappreciated in astronomy. It is not particularly difficult for expert developers to make production-level codes useable by a large community, but that level of support is rarely provided to astronomers.

In this section, I summarize the codes I've written primarily for performing reduction of data not supported by any standard reduction software. The text is kept to brief summaries because, for most of these codes, there is extensive documentation available at the links provided.

7.2 The BGPS pipeline

`https://code.google.com/p/bgpspipeline/`

The BGPS pipeline is described in Chapter 3 and Aguirre et al. (2011). It was created to deal with bright 1.1mm emission in ways not well-supported by the original Bolocam pipeline. In the end, it did essentially the same things, but implemented a few new features. A great deal of time and effort went towards making the pipeline operate in memory instead of on disk; in retrospect, that was not a particularly wise use of my time. However, it allowed some signal-processing features to be added to the BGPS pipeline that could not be included in the original Bolocam pipeline.

7.2.1 Pyflagger

`http://agpy.googlecode.com/svn/trunk/agpy/pyflagger.py`

Pyflagger was originally intended as an interactive data-flagger for Bolocam data, and was used as such, but it ended up being a complete data visualization tool as well, implementing nearly the entire pipeline process within itself so that each step could be easily visualized. Much of the pipeline debugging and methodology development was performed using pyflagger. The interactive flagging involves key and mouse commands to the `matplotlib` GUI. Pyflagger uses the `idlsave` package to read IDL save files.

7.3 PySpecKit

`http://pyspeckit.readthedocs.org/`

PySpecKit was written in collaboration with Jordan Mirocha (Ginsburg & Mirocha, 2011). It grew from a need to perform interactive spectral plotting and fitting within python.

IRAF has very useful interactive plotting and fitting tools, specifically `splot`, but it is not easy to extend the fitting code to use models such as those generated from RADEX grids. It also does not readily yield publication-quality plots.

PySpecKit has been used in one form or another in all of my papers except Ginsburg et al. (2012). It provides a flexible interface for fitting arbitrarily models to data and plotting the models and fits in a sensible way.

7.4 TripleSpec Mapping Pipeline

`https://code.google.com/p/agpy/source/browse/trunk/iraf/pipeline_jhk.cl`

IRAF is still the only software capable of efficiently fitting and performing geometric transforms of images, which is necessary for both world coordinate corrections and two-dimensional spectroscopy. These limitations will, hopefully, be alleviated with new packages being built for astropy.

The standard TripleSpec pipeline is the SPEXTOOL data pipeline written by Michael Cush-

ing. This pipeline is useful for deep spectra of single objects, but not for spatially-resolved spectroscopy.

I created a data pipeline to reduce TripleSpec data entirely within IRAF. It produces a complete 2D spectrum that is wavelength and flux calibrated. It includes sky-line subtraction capabilities, but these are not as effective as in the IDL-based pipeline. This limitation is in part because the IRAF pipeline does not take advantage of (or require) the fast-switching approach typically used to acquire high-fidelity infrared data.

This approach is uniquely useful for mapping bright spectroscopic lines, in particular from outflows, as demonstrated in Ginsburg et al. (2009). Allison Youngblood has begun using this pipeline in conjunction with my map-making pipeline to make wide-field spectroscopic data cubes using the full NIR JHK spectrum in the W51 and Orion OMC 1 fields.

7.5 Arecibo and GBT mapping codes

`https://code.google.com/p/casaradio/source/browse/branches/gbtidl/ginsburg/`

`https://code.google.com/p/casaradio/source/browse/branches/aoidl/ginsburg/`

`https://code.google.com/p/casaradio/source/browse/branches/python/ginsburg/`

Making maps with Arecibo and GBT was not natively supported, but neither was it particularly difficult. The linked codes in this section are re-usable pipeline-like functions for calibrating and combining GBT and Arecibo spectra.

7.6 Image Registration

`http://image-registration.rtfd.org`

The problem of image registration in astronomical imaging and spectroscopy is well-studied, but the existing solutions are not all good. If you want to know the offset between two images that contain no point sources, it is straightforward to determine the peak of the cross-correlation between those images. However, if you need to know the offset to sub-pixel accuracy **and** you want to know the

error on that measurement, existing methods are either misleading or inaccurate.

A detailed demonstration of the different methods and their various (dis)advantages using monte-carlo experiments as a baseline for what the true errors on a measurement of a simulated map should be is shown at this URL: `http://nbviewer.ipython.org/urls/raw.github.com/keflavich/image_registration/master/examples/Cross%2520Correlation.ipynb`. The tests are not reproduced here for brevity.

7.7 Power-Law fitting

`https://plfit.readthedocs.org/en/latest/`

A maximum-likelihood approach to power-law distribution fitting for data with a lower cut-off (e.g., a completeness limit) was implemented by Clauset et al. (2007). I wrote a translation of his code into python (and fortran and c). It was used in most of the publications in this thesis.

7.8 Other codes

I am the maintainer for a few other significant code projects, some of which are specific to the University of Colorado and the Apache Point Observatory.

7.8.1 Astropy: Astroquery

`http://astroquery.readthedocs.org/en/latest/`

The `astroquery` project is an affiliate of the much larger `astropy` project. It implements python-based query tools for various astronomical data servers, e.g. IPAC, SIMBAD, Vizier, etc.

7.8.2 CASARADIO

`http://code.google.com/p/casaradio/`

Tools by and for radio astronomers at the Center for Astrophysics and Space Astronomy (CASA).

7.8.3 APO software

`https://code.google.com/p/aposoftware/`

The APO software page includes reduction tools for DIS, TripleSpec, and NICFPS. It also includes some observing preparation tools and observing scripts for TUI.

Chapter 8

Conclusions

The key conclusions of this thesis are divided into two components. The first centers on the Bolocam Galactic Plane Survey and its high-level results.

The BGPS has laid the grounds for an extensive study of dense gas within our Galaxy. It is the first blind survey of the Galactic plane at millimeter wavelengths, where optically thin dust emission dominates the observed signal.

- The BGPS has had two data releases and its pipeline has been well-characterized. The angular transfer function drops from 100% recovery at 100″ to $\sim$ 50% recovery at 300″.
- The BGPS map power spectra, when compared with Herschel Hi-Gal power spectra, indicate that in some portions of the galaxy, the smallest scales are **warmer** than the largest scales, hinting that internal heating by forming young stars is significant.
- There are 3 massive proto-clusters in the northern Galactic plane, G10.62, W49, and W51.
- There are about 20 'clumps' of mass $M \gtrsim 10^4\ M_\odot$ in the northern plane.
- All of these clumps are forming massive stars at present, implying that the starless timescale for the parent clumps is $\tau_{starless} < 0.5$ Myr.
- The BGPS and comparable ground-based surveys are excellent tools for identifying the precursors to massive clusters. Because the galaxy is transparent at 1.1 mm, the BGPS can be used for galaxy-wide population analyses

- Careful distance determination is crucial for population studies
- There is substantial free-free 'contamination' in the brightest BGPS sources, but these sources are nonetheless dust rich.

The second component is a study of gas density and turbulence. The probability distribution of gas density in the interstellar medium is generally thought to be governed by turbulence, which robustly delivers a lognormal probability distribution for density and velocity. Turbulence requires a driving force on large scales to maintain such a distribution, so I examined both its potential drivers and measures of the distribution.

Formaldehyde was used as a densitometer to examine the internal conditions of BGPS clumps. The density analysis yielded information about the distribution of density in active and quiescent clouds.

- The density of infalling gas around UCH II regions is comparable to the mean density observed in the interstellar media of starburst galaxies, with typical number densities $10^{4.5}\mathrm{cm}^{-3} \lesssim n \lesssim 10^{5.5}\mathrm{cm}^{-3}$
- The comparison of hydrogen and carbon radio recombination line velocities with H_2CO gas velocities can be used to determine the evolutionary state of individual UCH II regions
- The density of gas in quiescent GMCs is 1-2 orders of magnitude higher than typically assumed, with $10^{4}\mathrm{cm}^{-3} \lesssim n \lesssim 10^{4.5}\mathrm{cm}^{-3}$. This discrepancy indicates either an extreme failure of the spherical cloud assumption, such that the true densities within GMCs are uniformly higher over a smaller volume, or that the density distribution is not governed by normal turbulence.
- Study of the W5 region showed that molecular outflows from young and proto-stars do not drive the turbulence observed in this region. Instead, the turbulence is likely driven along the bubble edges by O-star winds and radiation.

Bibliography

Adams, F. C. & Fatuzzo, M. 1996, ApJ, 464, 256

Aguirre, J. E. et al. 2011, ApJS, 192, 4

Alexander, M. J. & Kobulnicky, H. A. 2012, ApJ, 755, L30

Anderson, L. D., Bania, T. M., Jackson, J. M., Clemens, D. P., Heyer, M., Simon, R., Shah, R. Y., & Rathborne, J. M. 2009, ApJS, 181, 255

André, P. et al. 2010, A&A, 518, L102

Araya, E., Hofner, P., Churchwell, E., & Kurtz, S. 2002, ApJS, 138, 63

Araya, E., Hofner, P., Linz, H., Sewilo, M., Watson, C., Churchwell, E., Olmi, L., & Kurtz, S. 2004, ApJS, 154, 579

Arce, H. G., Borkin, M. A., Goodman, A. A., Pineda, J. E., & Halle, M. W. 2010, ApJ, 715, 1170

Arvidsson, K., Kerton, C. R., Alexander, M. J., Kobulnicky, H. A., & Uzpen, B. 2010, AJ, 140, 462

Arzoumanian, D. et al. 2011, A&A, 529, L6

Bachiller, R. 1996, ARA&A, 34, 111

Bally, J. et al. 2010, ApJ, 721, 137

Bally, J., Walawender, J., Johnstone, D., Kirk, H., & Goodman, A. 2008, The Perseus Cloud, ed. Reipurth, B., 308–+

Barmby, P. et al. 2006, ApJ, 650, L45

Bastian, N. 2008, MNRAS, 390, 759

Battersby, C. et al. 2011, A&A, 535, A128

Beaumont, C. N. & Williams, J. P. 2010, ApJ, 709, 791

Benjamin, R. A. et al. 2003, PASP, 115, 953

Berriman, G. B. et al. 2004, in Astronomical Society of the Pacific Conference Series, Vol. 314, Astronomical Data Analysis Software and Systems (ADASS) XIII, ed. F. Ochsenbein, M. G. Allen, & D. Egret, 593

Bertoldi, F. & McKee, C. F. 1990, ApJ, 354, 529

Bonnell, I. A. 2008, in Astronomical Society of the Pacific Conference Series, Vol. 390, Pathways Through an Eclectic Universe, ed. J. H. Knapen, T. J. Mahoney, & A. Vazdekis, 26

Bonnell, I. A. & Bate, M. R. 2002, MNRAS, 336, 659

—. 2006, MNRAS, 370, 488

Bonnell, I. A., Vine, S. G., & Bate, M. R. 2004, MNRAS, 349, 735

Bourke, T. L. et al. 1997, ApJ, 476, 781

Bressert, E., Ginsburg, A., Bally, J., Battersby, C., Longmore, S., & Testi, L. 2012a, ApJ, 758, L28

Bressert, E., Ginsburg, A., Battersby, C., Bally, J., Longmore, S., & Testi, L. 2012b, ArXiv e-prints

Bretherton, D. E., Moore, T. J. T., & Ridge, N. A. 2002, in Hot Star Workshop III: The Earliest Phases of Massive Star Birth, Vol. 267, 347

Cabrit, S. & Bertout, C. 1990, ApJ, 348, 530

Cao, Y., Terebey, S., Prince, T. A., & Beichman, C. A. 1997, ApJS, 111, 387

Carey, S. J. et al. 2009, PASP, 121, 76

Chabrier, G. & Hennebelle, P. 2010, ApJ, 725, L79

Chapin, E. L., Berry, D. S., Gibb, A. G., Jenness, T., Scott, D., Tilanus, R. P. J., Economou, F., & Holland, W. S. 2013, ArXiv e-prints

Chen, X. et al. 2012, ApJS, 200, 5

Chernin, L. M. & Masson, C. R. 1991, ApJ, 382, L93

Cho, W. & Kim, J. 2011, MNRAS, 410, L8

Chomiuk, L. & Povich, M. S. 2011, AJ, 142, 197

Churchwell, E. 2002, Annual Review of Astronomy and Astrophysics, 40, 27

Churchwell, E. et al. 2009, PASP, 121, 213

Churchwell, E., Sievers, A., & Thum, C. 2010, A&A, 513, A9+

Churchwell, E., Walmsley, C. M., & Cesaroni, R. 1990, A&AS, 83, 119

Clauset, A., Rohilla Shalizi, C., & Newman, M. E. J. 2007, ArXiv e-prints

—. 2009, SIAM Review, 51, 661

Contreras, Y. et al. 2013, A&A, 549, A45

Correnti, M. et al. 2012, Ap&SS, 340, 263

Crossley, J. H., Sjouwerman, L. O., Fomalont, E. B., & Radziwill, N. M. 2008, in Society of Photo-Optical Instrumentation Engineers (SPIE) Conference Series, Vol. 7016, Society of Photo-Optical Instrumentation Engineers (SPIE) Conference Series

Curtis, E. I., Richer, J. S., Swift, J. J., & Williams, J. P. 2010, MNRAS, 408, 1516

Dame, T. M., Hartmann, D., & Thaddeus, P. 2001, ApJ, 547, 792

Darling, J. & Zeiger, B. 2012, ApJ, 749, L33

de Wit, W. J., Testi, L., Palla, F., & Zinnecker, H. 2005, A&A, 437, 247

Deharveng, L., Zavagno, A., Cruz-Gonzalez, I., Salas, L., Caplan, J., & Carrasco, L. 1997, A&A, 317, 459

Dickel, H. R. & Goss, W. M. 1987, A&A, 185, 271

Dickel, H. R., Goss, W. M., Rots, A. H., & Blount, H. M. 1986, A&A, 162, 221

Digel, S. W., Lyder, D. A., Philbrick, A. J., Puche, D., & Thaddeus, P. 1996, ApJ, 458, 561

Dunham, M. K., Rosolowsky, E., Evans, II, N. J., Cyganowski, C., & Urquhart, J. S. 2011, ApJ, 741, 110

Dunham, M. K. et al. 2010, ApJ, 717, 1157

Ellsworth-Bowers, T. P. et al. 2013

Elmegreen, B. G. 1998, in Astronomical Society of the Pacific Conference Series, Vol. 148, Origins, ed. C. E. Woodward, J. M. Shull, & H. A. Thronson Jr., 150–+

Elmegreen, B. G. & Lada, C. J. 1977, ApJ, 214, 725

Enoch, M. L., Glenn, J., Evans, II, N. J., Sargent, A. I., Young, K. E., & Huard, T. L. 2007, ApJ, 666, 982

Enoch, M. L. et al. 2006a, ApJ, 638, 293

—. 2006b, ApJ, 638, 293

Evans, N. J. et al. 2009, ApJS, 181, 321

Faúndez, S., Bronfman, L., Garay, G., Chini, R., Nyman, L.-Å., & May, J. 2004, A&A, 426, 97

Federrath, C., Chabrier, G., Schober, J., Banerjee, R., Klessen, R. S., & Schleicher, D. R. G. 2011, Physical Review Letters, 107, 114504

Federrath, C. & Klessen, R. S. 2013, ApJ, 763, 51

Federrath, C., Klessen, R. S., & Schmidt, W. 2008, ApJ, 688, L79

—. 2009, ApJ, 692, 364

Federrath, C., Roman-Duval, J., Klessen, R. S., Schmidt, W., & Mac Low, M. 2010a, A&A, 512, A81+

Federrath, C., Roman-Duval, J., Klessen, R. S., Schmidt, W., & Mac Low, M.-M. 2010b, A&A, 512, A81

Felli, M., Hjellming, R. M., & Cesaroni, R. 1987, A&A, 182, 313

Fish, V. L., Reid, M. J., Argon, A. L., & Menten, K. M. 2003, ApJ, 596, 328

Fujii, M. S., Saitoh, T. R., & Portegies Zwart, S. F. 2012, ApJ, 753, 85

Garden, R. P., Hayashi, M., Hasegawa, T., Gatley, I., & Kaifu, N. 1991, ApJ, 374, 540

Gieles, M., Heggie, D. C., & Zhao, H. 2011, MNRAS, 413, 2509

Ginsburg, A., Bressert, E., Bally, J., & Battersby, C. 2012, ApJ, 758, L29

Ginsburg, A., Darling, J., Battersby, C., Zeiger, B., & Bally, J. 2011a, ApJ, 736, 149

—. 2011b, ApJ, 736, 149

Ginsburg, A. & Mirocha, J. 2011, Astrophysics Source Code Library, 9001

Ginsburg, A. G. et al. 2013a, ApJS

—. 2013b, ApJS

Ginsburg, A. G., Bally, J., Yan, C., & Williams, J. P. 2009, ApJ, 707, 310

Glover, S. C. O., Federrath, C., Mac Low, M., & Klessen, R. S. 2010, MNRAS, 404, 2

Goldsmith, P. F. 1972, ApJ, 176, 597

Goodman, A. A. et al. 2013, in American Astronomical Society Meeting Abstracts, Vol. 221, American Astronomical Society Meeting Abstracts, 234.01

Green, S. 1991, ApJS, 76, 979

Green, S. 1994, ApJ, 434, 188

Gritschneder, M., Burkert, A., Naab, T., & Walch, S. 2010, ApJ, 723, 971

Guizar-Sicairos, M. & Fienup, J. R. 2008, Opt. Express, 16, 7264

Gwinn, C. R., Moran, J. M., & Reid, M. J. 1992, ApJ, 393, 149

Hachisuka, K. et al. 2006, ApJ, 645, 337

Harvey, P. M. et al. 2013, ApJ, 764, 133

Hatchell, J. & Dunham, M. M. 2009, A&A, 502, 139

Hatchell, J., Fuller, G. A., & Richer, J. S. 2007, Astronomy and Astrophysics, 472, 187

Helfand, D. J., Becker, R. H., White, R. L., Fallon, A., & Tuttle, S. 2006, Astronomical Journal, 131, 2525

Henkel, C., Walmsley, C. M., & Wilson, T. L. 1980, A&A, 82, 41

Henkel, C., Wilson, T. L., Walmsley, C. M., & Pauls, T. 1983, A&A, 127, 388

Hennebelle, P. & Chabrier, G. 2011, ApJ, 743, L29

—. 2013

Hennebelle, P. & Falgarone, E. 2012, ArXiv e-prints

Hennemann, M. et al. 2012, A&A, 543, L3

Heyer, M. H., Brunt, C., Snell, R. L., Howe, J. E., Schloerb, F. P., & Carpenter, J. M. 1998, ApJS, 115, 241

Hillenbrand, L. A. 1997, AJ, 113, 1733

Hopkins, P. F. 2012a, MNRAS, 423, 2016

—. 2012b, MNRAS, 423, 2037

Hopkins, P. F. 2013, Monthly Notices of the Royal Astronomical Society, 430, 1653

Ioannidis, G. & Froebrich, D. 2012, MNRAS, 421, 3257

Jackson, J. M. et al. 2006, ApJS, 163, 145

Jackson, J. M. et al. 2006, ApJS, 163, 145

Kainulainen, J., Beuther, H., Henning, T., & Plume, R. 2009, A&A, 508, L35

Kainulainen, J., Federrath, C., & Henning, T. 2013

Kainulainen, J. & Tan, J. C. 2012, ArXiv e-prints

Karr, J. L. & Martin, P. G. 2003, Astrophysical Journal, 595, 900

Kelly, B. C., Shetty, R., Stutz, A. M., Kauffmann, J., Goodman, A. A., & Launhardt, R. 2012, ApJ, 752, 55

Kennicutt, Jr., R. C. & Evans, II, N. J. 2012, ArXiv e-prints

Keto, E. 2002, ApJ, 580, 980

—. 2007, ApJ, 666, 976

Klein, R. I., Sandford, II, M. T., & Whitaker, R. W. 1983, ApJ, 271, L69

Klessen, R. S. 2000, ApJ, 535, 869

Klessen, R. S., Heitsch, F., & Mac Low, M.-M. 2000, ApJ, 535, 887

Koenig, X. P., Allen, L. E., Gutermuth, R. A., Hora, J. L., Brunt, C. M., & Muzerolle, J. 2008, Astrophysical Journal, 688, 1142

Konstandin, L., Girichidis, P., Federrath, C., & Klessen, R. S. 2012, ApJ, 761, 149

Kritsuk, A. G., Norman, M. L., Padoan, P., & Wagner, R. 2007, ApJ, 665, 416

Kritsuk, A. G., Norman, M. L., & Wagner, R. 2011, ApJ, 727, L20

Kruijssen, J. M. D., Pelupessy, F. I., Lamers, H. J. G. L. M., Portegies Zwart, S. F., & Icke, V. 2011a, MNRAS, 414, 1339

—. 2011b, MNRAS, 414, 1339

Krumholz, M. R., Klein, R. I., McKee, C. F., Offner, S. S. R., & Cunningham, A. J. 2009, Science, 323, 754

Krumholz, M. R. & McKee, C. F. 2005, ApJ, 630, 250

Krumholz, M. R., McKee, C. F., & Klein, R. I. 2005, Nature, 438, 332

Krumholz, M. R. & Tan, J. C. 2007, ApJ, 654, 304

Lada, C. J. & Fich, M. 1996, ApJ, 459, 638

Landsman, W. B. 1995, in Astronomical Society of the Pacific Conference Series, Vol. 77, Astronomical Data Analysis Software and Systems IV, ed. R. A. Shaw, H. E. Payne, & J. J. E. Hayes, 437

Lefloch, B., Lazareff, B., & Castets, A. 1997, Astronomy and Astrophysics, 324, 249

Lépine, J. R. D. et al. 2011, MNRAS, 417, 698

Leurini, S. et al. 2009, A&A, 507, 1443

Liu, H. B., Quintana-Lacaci, G., Wang, K., Ho, P. T. P., Li, Z.-Y., Zhang, Q., & Zhang, Z.-Y. 2012, ApJ, 745, 61

Lockman, F. J. & Brown, R. L. 1978, ApJ, 222, 153

Longmore, S. N. et al. 2012, ApJ, 746, 117

Lucas, P. W. et al. 2008, MNRAS, 391, 136

Mangum, J. G., Darling, J., Henkel, C., & Menten, K. M. 2013

Mangum, J. G., Darling, J., Menten, K. M., & Henkel, C. 2008, ApJ, 673, 832

Mangum, J. G. & Wootten, A. 1993, ApJS, 89, 123

Matthews, H. et al. 2009, AJ, 138, 1380

McKee, C. F. & Ostriker, E. C. 2007a, ARA&A, 45, 565

—. 2007b, ARA&A, 45, 565

McKee, C. F. & Tan, J. C. 2003, ApJ, 585, 850

Messier, C. 1764, Royal Society of London Philosophical Transactions Series I, 54, 68

Molina, F. Z., Glover, S. C. O., Federrath, C., & Klessen, R. S. 2012, MNRAS, 423, 2680

Molinari, S. et al. 2010, A&A, 518, L100

Motte, F., Bontemps, S., Schilke, P., Schneider, N., Menten, K. M., & Broguière, D. 2007, A&A, 476, 1243

Muenter, J. 1975, Journal of Molecular Spectroscopy, 55, 490, is always cited for $\mu = 0.122$ debye.

Natta, A., Walmsley, C. M., & Tielens, A. G. G. M. 1994, ApJ, 428, 209

Oey, M. S., Watson, A. M., Kern, K., & Walth, G. L. 2005, Astronomical Journal, 129, 393

Padoan, P., Haugbølle, T., & Nordlund, Å. 2012, ApJ, 759, L27

Padoan, P. & Nordlund, Å. 2002, ApJ, 576, 870

—. 2011, ApJ, 730, 40

Padoan, P., Nordlund, Å., Kritsuk, A. G., Norman, M. L., & Li, P. S. 2007a, ApJ, 661, 972

—. 2007b, ApJ, 661, 972

Pandian, J. D., Momjian, E., & Goldsmith, P. F. 2008, A&A, 486, 191

Pandian, J. D., Wyrowski, F., & Menten, K. M. 2012, ArXiv e-prints

Peters, T., Banerjee, R., Klessen, R. S., Mac Low, M., Galván-Madrid, R., & Keto, E. R. 2010, ApJ, 711, 1017

Plume, R. et al. 2004, ApJ, 605, 247

Portegies Zwart, S. F., McMillan, S. L. W., & Gieles, M. 2010, ARA&A, 48, 431

Price, S. D., Egan, M. P., Carey, S. J., Mizuno, D. R., & Kuchar, T. A. 2001, AJ, 121, 2819

Rathborne, J. M., Jackson, J. M., & Simon, R. 2006, ApJ, 641, 389

Reid, M. A., Wadsley, J., Petitclerc, N., & Sills, A. 2010, ApJ, 719, 561

Reid, M. J. et al. 2009, ApJ, 700, 137

Reipurth, B. & Bally, J. 2001, ARA&A, 39, 403

Reiter, M., Shirley, Y. L., Wu, J., Brogan, C., Wootten, A., & Tatematsu, K. 2011, ApJ, 740, 40

Rivera-Ingraham, A. et al. 2010, ApJ, 723, 915

Roman-Duval, J., Jackson, J. M., Heyer, M., Johnson, A., Rathborne, J., Shah, R., & Simon, R. 2009, ApJ, 699, 1153

Roman-Duval, J., Jackson, J. M., Heyer, M., Rathborne, J., & Simon, R. 2010a, ApJ, 723, 492

—. 2010b, ApJ, 723, 492

Roshi, D. A., Balser, D. S., Bania, T. M., Goss, W. M., & De Pree, C. G. 2005, ApJ, 625, 181

Rosolowsky, E. et al. 2010, ApJS, 188, 123

Sato, M., Reid, M. J., Brunthaler, A., & Menten, K. M. 2010

Sayers, J. et al. 2010, ApJ, 708, 1674

Schenck, D. E., Shirley, Y. L., Reiter, M., & Juneau, S. 2011, AJ, 142, 94

Schlingman, W. M. et al. 2011, ApJS, 195, 14

Schuller, F. 2012, in Society of Photo-Optical Instrumentation Engineers (SPIE) Conference Series, Vol. 8452, Society of Photo-Optical Instrumentation Engineers (SPIE) Conference Series

Schuller, F. et al. 2009, A&A, 504, 415

Sewilo, M., Watson, C., Araya, E., Churchwell, E., Hofner, P., & Kurtz, S. 2004, ApJS, 154, 553

Shepherd, D. S. & Watson, A. M. 2002, ApJ, 566, 966

Shetty, R., Kauffmann, J., Schnee, S., & Goodman, A. A. 2009a, ApJ, 696, 676

Shetty, R., Kauffmann, J., Schnee, S., Goodman, A. A., & Ercolano, B. 2009b, ApJ, 696, 2234

Shirley, Y. 2013

Shu, F. H., Adams, F. C., & Lizano, S. 1987, ARA&A, 25, 23

Simon, R., Jackson, J. M., Clemens, D. P., Bania, T. M., & Heyer, M. H. 2001, ApJ, 551, 747

Snell, R. L., Carpenter, J. M., & Heyer, M. H. 2002, ApJ, 578, 229

Stanke, T., McCaughrean, M. J., & Zinnecker, H. 1999, A&A, 350, L43

Stetson, P. B. 1987, PASP, 99, 191

Tan, J. C., Krumholz, M. R., & McKee, C. F. 2006, ApJ, 641, L121

Tang, X. D., Esimbek, J., Zhou, J. J., Wu, G., Ji, W. G., & Okoh, D. 2013, A&A, 551, A28

Taylor, A. R. et al. 2003, AJ, 125, 3145

Thompson, M. A., White, G. J., Morgan, L. K., Miao, J., Fridlund, C. V. M., & Huldtgren-White, M. 2004, Astronomy and Astrophysics, 414, 1017

Troscompt, N., Faure, A., Maret, S., Ceccarelli, C., Hily-Blant, P., & Wiesenfeld, L. 2009a, A&A, 506, 1243

Troscompt, N., Faure, A., Wiesenfeld, L., Ceccarelli, C., & Valiron, P. 2009b, A&A, 493, 687

—. 2009c, A&A, 493, 687

Tucker, K. D., Tomasevich, G. R., & Thaddeus, P. 1971, ApJ, 169, 429

—. 1972, ApJ, 174, 463

Turner, B. E., Richard, L. J., & Xu, L. 1989, ApJ, 344, 292

Urquhart, J. S. et al. 2012, MNRAS, 420, 1656

—. 2013, ArXiv e-prints

van der Tak, F. F. S., Black, J. H., Schöier, F. L., Jansen, D. J., & van Dishoeck, E. F. 2007a, A&A, 468, 627

—. 2007b, A&A, 468, 627

Vansevičius, V., Kodaira, K., Narbutis, D., Stonkutė, R., Bridžius, A., Deveikis, V., & Semionov, D. 2009, ApJ, 703, 1872

Vig, S., Cesaroni, R., Testi, L., Beltrán, M. T., & Codella, C. 2008, A&A, 488, 605

Wadiak, E. J., Rood, R. T., & Wilson, T. L. 1988, ApJ, 324, 931

Welsch, B. T., Fisher, G. H., Abbett, W. P., & Regnier, S. 2004, ApJ, 610, 1148

Whitehead, A. J., McMillan, S. L. W., Vesperini, E., & Portegies Zwart, S. 2013, ArXiv e-prints

Whitmore, B. C. 2009, Ap&SS, 324, 163

Wiesenfeld, L. & Faure, A. 2013, ArXiv e-prints

Williams, J. P., Blitz, L., & McKee, C. F. 2000, Protostars and Planets IV, 97

Williams, J. P., Blitz, L., & Stark, A. A. 1995, ApJ, 451, 252

Wilson, T. L., Rohlfs, K., & Hüttemeister, S. 2009, Tools of Radio Astronomy, ed. Wilson, T. L., Rohlfs, K., Huttemeister, S. (Springer-Verlag)

Wolfire, M. G., McKee, C. F., Hollenbach, D., & Tielens, A. G. G. M. 2003, ApJ, 587, 278

Xu, Y., Zheng, X.-W., & Jiang, D.-R. 2003, CJAA, 3, 49

Young, K. E., Lee, J.-E., Evans, II, N. J., Goldsmith, P. F., & Doty, S. D. 2004, ApJ, 614, 252

Yusef-Zadeh, F. et al. 2009, ApJ, 702, 178

Zeiger, B. & Darling, J. 2010, ApJ, 709, 386

Zylka, R., Guesten, R., Henkel, C., & Batrla, W. 1992, A&AS, 96, 525